Probing Magnetic Fields in Clusters of Galaxies

by

Tracy E. Clarke

A Thesis submitted in conformity with the requirements
for the degree of Doctor of Philosophy
Graduate Department of Astronomy
University of Toronto

Probing Magnetic Fields in Clusters of Galaxies

Tracy Clarke

Doctor of Philosophy, 1999

Department of Astronomy, University of Toronto

ABSTRACT

Galaxy clusters represent the largest gravitationally bound objects in the universe. Detailed morphological studies of galaxy clusters indicate that they are relatively young objects, currently in the formation process. Observations toward these objects reveal that the major components of the clusters are the galaxies, the diffuse, thermal cluster gas, and the dark matter. There is, however, evidence that the intracluster medium also contains magnetic fields distributed through the intracluster gas.

The presence of magnetic fields within the intracluster medium can lead to significant effects on the dynamics, and energy transport throughout the cluster. Embedded magnetic fields can modify the pressure of the intracluster medium, suppress thermal conduction, which may lead to the onset of cooling instabilities, and magnetic fields may even bias the initial mass function of star formation. Therefore, in order to understand the overall picture of the evolution of galaxy clusters, it is necessary to understand the role magnetic fields have played in this evolution.

The most direct method of probing intracluster magnetic fields relies on the Faraday rotation effect. As linearly polarized radiation passes through a magneto-ionic region, the rotation of the plane of polarization displays a characteristic wavelength dependence.

This thesis combines radio and X-ray observations, in a statistical study of Faraday rotation toward a sample of nearby galaxy clusters. A comparison of the Faraday rotation

measures of sources viewed through the intracluster medium, to the rotation measures of sources falling beyond the edge of the X-ray emitting gas, reveals the presence of excess Faraday rotation in the former sample. This excess rotation is interpreted as originating in the diffuse intracluster medium.

A detailed investigation of the Faraday rotating medium indicates that the Faraday screen is well represented by a model of Faraday cells distributed through the intracluster medium. An analysis of the cluster impact parameter distribution over the rotation measure sample indicates that the Faraday cell scales vary from < 1 kpc in the central regions of the clusters, to over 100 kpc at large impact parameter. Further, the rotation measure distribution indicates the widespread existence of intracluster magnetic fields out to the edges of the X-ray emitting gas. The overall distribution of magnetic field strengths inferred from the data suggests that the fields may play a dynamically important role in the evolution of galaxy clusters.

Acknowledgements

It seems only appropriate that thanks go first to my supervisor, Prof. Philipp Kronberg, who provided me with an enthusiasm for, and understanding of, the relevance of magnetic fields in astrophysics. This project began as Phil's vision and, through his encouragement for independence in research, has evolved into the current work as Phil provided me with the freedom to pursue my own vision of this project. I'd also like to thank Phil for providing me with numerous opportunities to attend conferences and workshops, and develop connections in the research community.

I would like to thank the members of my PhD examining committee for their interesting insights and clarifying suggestions on the thesis. Thanks Prof. Simon Lilly, Prof. Peter Martin, and Prof. Ernie Seaquist. I'd also like to particularly thank my external examiner, Dr. Gregory Taylor, for numerous suggestions and comments which have helped smooth out some of the bumps on the thesis.

In addition, I am particularly grateful to the staff at the Array Operations Center of the VLA in Socorro, New Mexico. During each visit to the VLA I was assured to be greeted with lots of friendly smiles and enthusiastic scientific discussion. In particular I would like to thank Michael Rupen for his patience in teaching me AIPS and his unwavering enthusiasm for all aspects of astronomy. I'd also like to thank Chris Carilli, Jean Eilek, and Frazer Owen for many interesting discussions which always left me thinking of new approaches to my work. A special thanks also to Dan Mertely for helping me to dodge RFI wherever possible. Finally, I'd like to thank NRAO for the generous allocation of VLA time to undertake this project.

This research has also greatly benefited from an extended stay at the Max-Planck-Institut für extraterrestrische Physik in Garching, Germany. I would like to thank Hans Böhringer for his patience and support as I learned the ropes of X-ray astronomy. I would also like to sincerely thank Thomas Reiprich for taking valuable time from his research schedule to provide extensive help and patience in teaching a radio astronomer how important each photon really is!

The Department of Astronomy at U of T has provided a wealth of knowledge, insight, and particularly friends which I will not forget. Although I'd like to thank all members

of the department for making my stay here enjoyable, there are a few fellow students who provided the majority of the laughter and companionship I relied on that I must single out. Whenever I lost sight of my enthusiasm for research, Mike Gladders always provided a bright reminder of the fascination that Astronomy holds. Felipe Barrientos was an endless source of humour and enthusiasm throughout my time at U of T, qualities which allowed me to overlook his dislike of chocolate. The pitfalls during my PhD always seemed less menacing after the words of support and encouragement from Marcin Sawicki. Marcin provided me with a role model both as a person and as a researcher. Mike Allen was essential to my sanity during the long days (and night) over the past year. His unique sense of humour and light heart made 1404 a fun place to work. Gabriela Mallén-Ornelas helped me to discover the beauty of Early Music through her love of music and extensive knowledge of the Toronto music scene. Gabriela also proved to be the ideal person to share the experiences of job searches and thesis completion with. With these people I have the strangest, and most enjoyable conversations possible over vast quantities of Chinese food and tea.

I'd also like to say a special thanks to Barbara Haynes and Elizabeth Rescher for providing much needed reality checks that there is a life outside the university. I also have to thank Kathy Durrell for sharing in an infinite number of strange conversations and boxes of Kraft Dinner, and *Boys in the Bright White Sportscar* for always knowing the proper distraction when I needed it. Thanks also to Sandra Scott for her advice on computers and life, and for her generous time spent reading this manuscript.

I would particularly like to thank my family for their support and encouragement during my many years in university. Although it was a long road from Moncton, New Brunswick to my PhD, they never doubted that I would be successful. In fact, I would like to dedicate my thesis to the memory of my grandmother, Olga Mae Richard, who recently passed away. Nan was a grandmother in every sense of the term, she was a beautiful, intelligent, and resourceful woman who always told me that I could accomplish anything I wanted to do, and who supported me with her love and strength throughout my life. Although I'm sad that I cannot share the joy of completing my PhD with her, I know how proud she would be.

I have made use of the ROSAT Data Archive of the Max-Planck-Institut für extraterrestrische Physik (MPE) at Garching, Germany. This research has also made use of the NASA/IPAC Extragalactic Database (NED) which is operated by the Jet Propulsion Laboratory, California Institute of Technology, under contract with the National Aeronautics and Space Administration.

This work was generously supported by scholarships from the National Sciences and Engineering Research Council of Canada, the province of New Brunswick, the I.O.D.E., the Sumner Foundation, the O'Brien Foundation, and the University of Toronto.

Contents

List of Figures

List of Tables

Chapter 1

Introduction

Magnetic fields (and their inevitable offspring fast particles) are found everywhere in the universe where we have the means to look for them.

E.N. Parker, *Cosmical Magnetic Fields* (1979)

The tendency for galaxies to cluster was noted in the late eighteenth century, although the significance of this clustering was not fully understood at that time. Systematic clustering studies, undertaken in the early to mid 20th century (e.g. Wolf 1906, Shapley & Ames 1932, Abell 1958, and Zwicky, Herzog & Wild 1968), catalogued cluster positions, richness and other optical properties, and showed that galaxy clusters are gravitationally bound systems. It was not until more recently, however, that the diffuse thermal and relativistic plasma components of galaxy clusters were identified through X-ray and radio observations.

Early X-ray observations toward galaxy clusters with the *Uhuru* satellite revealed that clusters are the most common bright sources of extended X-ray emission in the sky (Jones & Forman 1978). Subsequent X-ray spectra from various missions revealed that the emission is mainly from thermal gas at temperatures of $10^7 - 10^8$ K, and densities of $10^{-2} - 10^{-4}$ cm^{-3} (Sarazin 1992). The X-ray emission traces the cluster potential, and thus the surface brightness distribution can provide some information on the physical state of clusters (Jones & Forman 1992); relaxed, non-interacting clusters often reveal a profile which is strongly peaked in the central regions (cooling-flow), while the more disturbed, interacting galaxy clusters have a much shallower central X-ray profile. Since the majority of the X-ray emission is due to thermal bremsstrahlung, the X-ray surface brightness distribution reflects the

plasma density distribution within the cluster.

Radio observations toward galaxy clusters reveal the presence of both embedded radio galaxies as well as (occasionally) diffuse synchrotron halo emission. Embedded radio sources located in the central regions of galaxy clusters often show very distorted morphologies (Burns 1998) which indicate an interaction between the radio plasma and the thermal cluster gas. Radio halos, on the other hand, are characterized as fairly symmetric regions of extended (400-600 kpc), diffuse, steep spectrum synchrotron emission (Feretti & Giovannini 1996) located in the central regions of clusters. These rare, low surface brightness halos do not appear to be associated with a parent galaxy, but rather are associated with the intracluster medium (ICM) itself. The presence of this diffuse synchrotron component indicates *ipso facto* the co-existence of a relativistic electron population and magnetic fields within the ICM. The presence of relativistic electrons is further indicated by the detection of inverse Compton emission (Bagchi et al. 1998; Fusco-Femiano et al. 1999), and the presence of intracluster magnetic fields is revealed through their effects on polarized radio probes (Kim et al. 1991; Feretti et al. 1995).

As the polarized emission passes through a magnetized, ionized region, the plane of polarization of linearly polarized synchrotron emission is rotated through the Faraday effect. Radio polarimetry therefore provides a rotation measure estimate along lines of sight toward polarized radio sources. This rotation measure is proportional to the electron density weighted magnetic field along to line of sight to the radio source. Combining the rotation measure with the X-ray determined electron density in the intracluster medium, provides a measure of the line of sight component of the magnetic field in the Faraday rotating medium.

1.1 Why Study Intracluster Magnetic Fields?

Magnetic fields embedded in the intracluster medium can have strong effects on the cluster dynamics. These effects are due to the fact that the intracluster medium is composed of a plasma of free electrons and ions, whose motion is tied to magnetic field lines. A region of high magnetic field strength will effectively reflect electrons back into low field regions. Further, tangled magnetic fields will significantly alter the diffusion time for the electrons in the intracluster medium. This section briefly considers some of the dynamical effects

which are associated with the presence of intracluster magnetic fields.

In the hot dense cores of galaxy clusters, thermal conduction should result in an isothermal temperature distribution on timescales much shorter than the Hubble time. In contrast, X-ray observations toward galaxy clusters often reveal cooling flows, where the gas in the central regions of the clusters is cooler than the gas further out (Forman 1988). Due to the short timescale required by thermal conduction to erase these temperature gradients, there must be some mechanism in place which suppresses the thermal conduction. This suppression mechanism is generally considered to be tangled magnetic fields.

The motion of the electrons in the intracluster gas is tied to the magnetic field lines, thus thermal conduction perpendicular to the field lines is significantly reduced, even for very weak magnetic fields. The resulting thermal instabilities may, in fact, trigger the onset of the observed cooling flows (David & Bregman 1989). Further, the magnetic fields embedded within the cooling flow are expected to be stretched, and compressed by the inflowing gas (Soker & Sarazin 1990). Recent Faraday studies of extreme cooling flow clusters (Ge & Owen 1993) show that the magnetic fields within the cores of these clusters are amplified ($> 20\mu G$) over that in the outer regions. This magnetic field amplification may be the first direct evidence of motion within cooling flow cores.

Further implications of magnetic fields embedded in the intracluster gas are related to magnetic pressure support. Magnetic field estimates determined for the cores of cooling flow clusters (Ge & Owen 1993; Taylor & Perley 1993) often indicate that the magnetic pressure is in rough equipartition with the ambient gas pressure. This extra pressure support term has been invoked to explain the discrepancies in the measurements of the mass of galaxy cluster determined by lensing, as compared to X-ray determined cluster mass estimates (Loeb & Mao 1994; Miralda-Escude & Babul 1995; Makino 1997). An additional implication noted by Loeb & Mao is that the magnetic pressure support could shift the mass to light ratio to higher values, and thus increase the estimates of Ω.

One of the mysteries remaining about cooling flows is what happens to the gas which has piled up in the central regions of the cluster. Conversion of the material into massive stars would result in a detectable blue emission component in the cores of cooling flow clusters. Although there is some evidence of star formation activity in cooling cores (Allen 1995) the emission does not account for the amount of material which has been deposited into the cooling core. It has therefore been suggested that the star formation in these cooling flow

regions must be biased toward low mass stars. The role of intracluster magnetic fields in biasing the initial mass function (IMF) has been investigated by Friaça & Jafelice (1999). They conclude that magnetic fields embedded in cold star-forming clouds in the cooling flow can reproduce the observationally predicted radial bias in the IMF.

1.2 Overview of Previous Statistical Faraday Studies

One of the first statistical surveys of the Faraday rotation of a sample of Abell clusters was performed by Dennison (1979). In order to search for excess intracluster Faraday rotation measure, he examined the rotation measures of 16 sources located within and behind 16 galaxy clusters and compared this to the rotation measure sky at high Galactic latitudes. Unfortunately, due to the limited availability of polarized radio sources to probe the intracluster medium at the time of this study, no statistically significant conclusion could be drawn.

A larger Faraday sample of 24 sources was presented in Lawler & Dennison (1982), where a Faraday excess of ~ 50 rad m^{-2} was observed for sources viewed through the intracluster medium of 24 cluster, as compared to those beyond the influence of the cluster gas. Based on Monte Carlo simulations, Lawler & Dennison concluded that their results were consistent with an intracluster magnetic field strength of ~ 1 μG. Further, they suggested that these fields were tangled on scales of order 15 kpc.

Hennessy et al. (1989) studied a sample of high redshift radio probes behind relatively low redshift Abell clusters. This study determined the rotation measures for 16 radio galaxies which were viewed through the intracluster medium at impact parameters smaller than one-quarter of a modified Abell radius (equivalent to ~ 500 kpc). The determination of the source rotation measures for the Hennessy et al. sample was obtained from a fit to four 20 cm wavelengths which they selected to provide unambiguous rotation measures up to approximately 600 rad m^{-2}. A statistical comparison of their central radio probes, with radio sources at impact parameters beyond the edge of the cluster gas, placed an upper limit of 55 rad m^{-2} on any excess cluster-induced Faraday rotation. Hennessy et al. therefore concluded that there is no evidence for excess Faraday rotation attributable to the intracluster medium. As with the previous studies, however, these results suffered from a small sample size.

In contradiction to the Hennessy et al. analysis, the statistical Faraday study by Kim et al. 1991 indicated a clear excess Faraday rotation for radio sources viewed along lines of sight toward galaxy clusters compared to a control sample located beyond the edge of the intracluster gas. Their study examined the rotation measure distribution of 65 radio sources at impact parameters less than $\sim$ 700 kpc and compared it to the rotation measure distribution of sources falling at large cluster-centric radii. At a confidence level exceeding 99%, the Kim et al. results indicate the presence of an excess Faraday rotation of order 100 rad m^{-2} in the central regions of the clusters.

Note, however, that the cluster sample of Kim et al., although much larger than the Hennessy et al. sample, is dominated, in the central regions, by radio sources embedded within the intracluster medium. The possibility that this dependence on embedded sources may cause the observed Faraday excess led Goldshmidt & Rephaeli (1993) to re-examine the Kim et al. sample with an emphasis placed on examining the effects of potential biases in the sample. They concluded, however, that the presence of embedded radio sources did not affect the results presented by Kim et al. (1991).

A further, as yet unaddressed, complication with the Kim et al. sample is the unknown X-ray properties of many of the clusters probed. A re-examination of the Kim et al. clusters shows that a number of the clusters probed were not detected in X-rays by EINSTEIN. This lack of X-ray flux indicates that those clusters are either very poor clusters or are not gravitationally bound systems, but rather a line of sight projection of galaxies. In either case, the rotation measure toward these clusters would be much less than that toward clusters which contain a significant intracluster gas component. It is therefore important to limit statistical Faraday rotation measure studies to clusters which are known to be gravitationally bound systems, with a detectable intracluster gas component. The inclusion of "clusters" which have little or no intracluster gas, in a Faraday sample will tend to mask the true Faraday signal. The uncertainties introduced by the unknown intracluster gas distribution are therefore eliminated in this thesis through selection of a cluster sample with known X-ray properties.

1.3 This Thesis

This thesis undertakes a statistical Faraday study of magnetic fields in clusters of galaxies. The goal is to address some of the fundamental questions concerning the nature of intracluster magnetic fields. The main questions that are addressed are: Is there statistically significant evidence for the presence of excess Faraday rotation toward sources viewed through the intracluster gas? If so: What is the radial extent of the region of Faraday excess? What is the location of the Faraday rotating medium which gives rise to the Faraday excess? What is the structure of the magnetic fields within the Faraday rotating medium? Insights into the answers to these questions are determined from the combination of radio polarimetric, and X-ray observations.

Chapter 2 outlines the basic theory behind the radiation mechanisms which are used throughout this thesis. This Chapter also gives a brief overview of the properties of radio galaxies and the intracluster medium, and discusses the methods used to detect intracluster magnetic fields. In the final section of Chapter 2 interferometry theory is outlined, with emphasis placed on polarization.

The investigation of intracluster magnetic fields in this thesis is based on radio polarization observations of radio sources viewed toward a sample of 24 low redshift Abell clusters. The radio sample was selected to provide one set of (**cluster**) sources which probed the intracluster gas at a variety of radii, and a second set of (**control**) sources which are located beyond the influence of the cluster medium. The target selection and observing strategy for the radio sample are discussed in Chapter 3. This Chapter also presents an overview of the radio imaging process, and provides tables of the radio parameters of the polarization probes. The galaxy cluster sample probed in this thesis was selected based on X-ray data from the ROSAT satellite. As the Faraday effect requires the presence of both magnetic fields and free electrons, it is important to ensure that the clusters probed contain X-ray emitting (thermal) intracluster medium. The galaxy cluster selection criteria are presented in Chapter 4, together with an overview of the ROSAT satellite and X-ray observations. This Chapter also provides a detailed discussion of the X-ray analysis procedure, as well as the plots of the surface brightness profiles for the cluster sample, and tables of the cluster properties.

The rotation measure fitting procedure for the radio sample studied in this thesis is

presented in Chapter 5. This Chapter outlines the sources of error present in the observations and provides thumbnail images of the rotation measure fit for each source in the radio sample. Tables of the rotation measure fit parameters and radio source identifications are presented in Chapter 5, together with estimates of the Galactic contribution to the rotation measure toward each galaxy cluster.

The questions of the presence, extent, and location of the Faraday rotating medium are addressed in Chapter 6. Comparison of rotation measures of the sample of sources which are viewed through the intracluster medium, to those of sources beyond the influence of the cluster gas reveals a statistically significant Faraday excess in the former sample. This Faraday excess is traced to the outer edge of the thermal intracluster medium. Further, the rotation measure distribution indicates that the majority of the Faraday excess originates in the diffuse intracluster medium.

The nature of the magnetic field distribution is investigated in Chapter 7. This Chapter explores a range of models for the intracluster magnetic field distribution, and compares the model predictions to the observed properties of the radio sample. One of the predictions from this Chapter is that the coherence length of intracluster magnetic fields increases toward the outer regions of galaxy clusters. Faraday mapping of radio sources viewed through the intracluster medium of three Abell clusters indicates that the magnetic fields contain both large scale order, and small scale variations. These observations are consistent with the picture presented by the analysis of the rotation measure distribution.

Chapter 8 summarizes the main results from this thesis, and further develops the picture of the intracluster magnetic fields by fitting these results into the overall framework which has been developed in the literature. The final section of this Chapter outlines some of the fundamental issues which must still be addressed, and discusses some exciting prospects for future work.

Note that throughout this thesis the Hubble constant was taken to be 75 km s^{-1} Mpc^{-1}, and q=0.5.

Chapter 2

Theory

Overview: This chapter will provide a brief overview of the background theory on which this thesis is based. Section 2.1, on emission mechanisms, provides an overview of the synchrotron, thermal bremsstrahlung, and inverse Compton processes as they apply to the regimes of interest. The following section, § 2.2, provides a brief overview of the classification of extragalactic radio sources. The physical properties of the intracluster medium are outlined in § 2.3. The methods used to probe intracluster magnetic fields are discussed in § 2.4, while the following section, § 2.5, outlines the relevant interferometry theory that underlies much of the work in this thesis. The interferometry section covers the theory of total intensity observations and polarization observations. The polarization theory is written in terms of coefficients observed with the VLA interferometer, and includes a section on instrumental polarization specific to the VLA. Section 2.5 also develops the notation for understanding the Stokes parameters that are used throughout this work. Section 2.6 discusses instrumental depolarization effects which are relevant to VLA observations, and gives estimates of the magnitude of these effects on the data in this project.

2.1 Emission Mechanisms

2.1.1 Synchrotron Radiation

Synchrotron radiation (also known as magnetobremsstrahlung) is generated by charged particles gyrating about magnetic fields. The energy of the particle is distributed among the harmonics of the gyration frequency; for an ultra-relativistic population of electrons the

harmonics are so closely spaced that the spectrum is a continuum.

Synchrotron theory is described in detail by Pacholczyk (1970), Rybicki & Lightman (1979), and Longair (1981), and its application to extragalactic radio sources is discussed in Begelman, Blandford, & Rees (1984). A single charged particle moving relativistically in a magnetic field, has motion described by

$$\begin{aligned} \frac{d}{dt}(\gamma m\vec{v}) &= \frac{e}{c}\vec{v}\times\vec{\mathbf{B}} \\ \frac{d}{dt}(\gamma mc^2) &= e\vec{\mathbf{v}}\cdot\vec{\mathbf{E}} = 0, \end{aligned} \tag{2.1}$$

where $\gamma = \left(1-\frac{v^2}{c^2}\right)^{-1/2}$ is the Lorentz factor. These equations describe helical motion of the particles, which is a combination of uniform motion along the field lines and circular motion around the field lines.

Following the notation of Rybicki & Lightman (1979), for an isotropic distribution of pitch angles (angle between the magnetic field and the particle velocity), the total emitted radiation from each electron is given by

$$P = \frac{4}{3}\sigma_T c\beta^2\gamma^2 U_B, \tag{2.2}$$

where $\beta = v/c$, $\sigma_T = 8\pi r_o^2/3$ is the Thomson cross section, and $U_B = B^2/8\pi$ is the magnetic energy density. Individual electrons gyrate about the field lines with at the Larmor frequency

$$\nu_L = \frac{eB}{2\pi m_e c}. \tag{2.3}$$

Due to the relativistic nature of the particles, beaming effects cause the emitted radiation to be concentrated in a narrow cone, of width γ^{-1}, centered on the instantaneous velocity of the electron. A distant observer will see pulses of radiation with a characteristic frequency of

$$\nu_c = \frac{3}{4\pi}\gamma^2\frac{eB}{m_e}\sin\alpha, \tag{2.4}$$

where α is the pitch angle of the particle. The emitted spectrum from each electron is given by

$$P(\nu) = \sqrt{3}e^2\frac{B\sin\alpha}{m_e c^2}\mathcal{F}\left(\frac{\nu}{\nu_c}\right), \tag{2.5}$$

where $\mathcal{F}(\nu)$ is a dimensionless function discussed in Rybicki & Lightman (1979).

For a power-law distribution of electron energies, $N(E)dE = \kappa E^{-x}dE$, $E_1 < E < E_2$, and an isotropic distribution of pitch angles, the synchrotron emissivity can be approximated as (Longair 1981)

$$j(\nu) = \frac{2\sigma_T c}{3\mu_o(m_e c^2)^{2\alpha}} \left(\frac{e}{2\pi m_e}\right)^{(\alpha-1)} \kappa B^{(\alpha+1)} \nu^{-\alpha}. \tag{2.6}$$

The resulting synchrotron spectrum is thus a power-law with a spectral index α related to the particle distribution index by $\alpha = (x-1)/2$. A complete analysis yields

$$I(\nu) = 1.7 \times 10^{-21} a(x) \kappa V B^{(\alpha+1)} \left(\frac{6.26 \times 10^{18}}{\nu}\right)^{\alpha} \text{ ergs s}^{-1} \text{ Hz}^{-1}, \tag{2.7}$$

where V is the volume of the source, and the constant $a(x)$ is given in Table 18.1 of Longair (1981). The use of a power law energy spectrum of the relativistic electrons is generally justified by the fact that the observed radio spectra of many objects display a power law dependence. The characteristic spectral index for extragalactic radio sources is α =0.8 (Longair 1981).

Polarization

The emission from a single relativistic electron moving in a magnetic field is elliptically polarized, and the direction of rotation of the electric vector depends on the sign of the angle between the magnetic field and the line of sight (Rybicki & Lightman 1979). In the case of a large, incoherent, ensemble of electrons, as expected in astrophysical situations, the elliptical components of the emission will almost cancel out due to the distribution of pitch angles, and thus the observed radiation will be partially linearly polarized perpendicular to the magnetic field direction. The fractional polarization of the observed radiation will depend on the degree of order in the magnetic fields of the source. Well aligned magnetic fields produce a higher intrinsic fractional polarization than very disordered fields. For a general source containing both an ordered (B_o) and random (B_r) magnetic field, Burn (1966) gives the fractional polarization as

$$\Pi(x) = \frac{x+1}{x+\frac{7}{3}} \frac{B_o^2}{B_o^2 + B_r^2}. \tag{2.8}$$

In the case of a completely ordered magnetic field in an extragalactic source which has a spectral index of α=0.8, the fractional polarization reaches a maximum of 73%. Note that the polarization percentage has no frequency dependence, and depends only on the power-law index of the energy distribution of the electron population.

2.1.2 Thermal Bremsstrahlung

Bremsstrahlung, or free-free emission results from the acceleration of a charge in the Coulomb field of another charge. A complete understanding of bremsstrahlung emission requires a quantum treatment and is beyond the scope of this overview. Below is a brief outline of the classical treatment, together with the quantum corrections following the notation of Rybicki & Lightman (1979).

Electrons are the primary radiators in electron-ion bremsstrahlung since the relative accelerations of the particles are inversely proportional to the particle masses. The treatment below considers the electron to be moving in a fixed Coulomb field of the ion. In the small-angle scattering regime, the electron moves rapidly enough that it follows a straight line path. The change in velocity as an electron passes by an ion of charge Ze, with an impact parameter b, is

$$\Delta v = \frac{2Ze^2}{mbv}. \tag{2.9}$$

The electron interacts with an ion for a collision time of

$$\tau = \frac{b}{v}, \tag{2.10}$$

and the emission from a single collision can be given as

$$\frac{dW}{d\omega} = \begin{cases} \frac{8Z^2e^6}{3\pi c^3 m^2 v^2 b^2}, & b \ll v/\omega \\ 0, & b \gg v/\omega. \end{cases}$$

For a medium with an ion density n_i and electron density n_e, the total emission per unit time, volume, and frequency range is given as

$$\frac{dW}{d\omega dV dt} = \frac{16\pi e^6}{3\sqrt{3}c^3 m^2 v} n_e n_i Z^2 g_{ff}(v,\omega), \tag{2.11}$$

where the emission is from electrons of a fixed speed v, and $g_{ff}(v,\omega)$, called the Gaunt

factor, is the quantum correction to the classical formalism.

In the more general case of a thermal distribution of electron speeds, Rybicki & Lightman (1979) give the emissivity of thermal bremsstrahlung as

$$\varepsilon_\nu^{ff} = \frac{dL}{dV\,d\nu} \tag{2.12}$$

$$= \frac{2^5\pi e^6}{3m_e c^3}\left(\frac{2\pi}{3km_e}\right)^{1/2} Z^2 n_e n_i T^{-1/2} e^{-h\nu/kT}\bar{g}_{ff}, \tag{2.13}$$

in CGS units (ergs s^{-1} cm^{-3} Hz^{-1}), where $\bar{g}_{ff}$ is the velocity averaged Gaunt factor which varies slowly with frequency and temperature. The above equation shows that the emissivity due to thermal bremsstrahlung produces a roughly exponential continuum variation with ν, in the X-ray regime.

2.1.3 Inverse Compton

Inverse Compton (IC) emission results from energy transfer from very high energy electrons into a lower energy photon field. In the context of this work, the relevant mechanism is the scattering of cosmic microwave background photons off cosmic ray electrons, which produces X-ray photons (Felten & Morrison 1966).

In the case of an isotropic distribution of photons scattering off an isotropic distribution of electrons, Rybicki & Lightman (1979) express the expected inverse Compton power from a single scattering as

$$P = \frac{4}{3}\sigma_T c\gamma^2\beta^2 U_{ph}, \tag{2.14}$$

where $U_{ph} \equiv \int \epsilon v d\epsilon$ is the initial photon energy density, and ϵ is the photon energy. The average frequency of the scattered radiation ($\bar{\nu}$) can be related to the initial frequency of the photon field (ν_b), as

$$\bar{\nu} = \frac{4}{3}\gamma^2\nu_b \tag{2.15}$$

in the ultra-relativistic limit ($\gamma \gg 1$).

For a power law distribution of relativistic electrons $N_e(\gamma)d\gamma = \kappa\gamma^{-x}d\gamma, \gamma_1 < \gamma < \gamma_2$, the total Compton power per unit volume is given as

$$P_{tot} = \frac{4}{3}\sigma_T c U_{ph}(3-x)^{-1}(\gamma_2^{3-x} - \gamma_1^{3-x}). \tag{2.16}$$

The inverse Compton radiation spectrum from a power law distribution of relativistic electrons is given by Sarazin (1988) as

$$\frac{dL}{d\bar{\nu}} = 3\sigma_T hc 2^x \kappa \nu^{\alpha_x} \frac{x^2+4x+11}{(x+3)^2(x+1)(x+5)} \int \nu_o^{\alpha_x} n_o(\nu_o) d\nu_o, \tag{2.17}$$

where $n_o(\nu_o)$ is the number density of the background photons as a function of initial frequency. Note that the X-ray spectral index $\alpha_x = (x-1)/2$ is identical to the synchrotron spectral index α, due to Equation 2.15.

The above expression can be generalized for the 3K background radiation, by taking a blackbody radiation field of temperature T_{bb}, which gives

$$\frac{dL}{d\bar{\nu}} = \frac{3\pi\sigma_T}{h^2c^2} b(x) \kappa (kT_{bb})^3 \left(\frac{kT_{bb}}{h\bar{\nu}}\right)^{\alpha_x}. \tag{2.18}$$

This equation is valid for frequencies in the range $\gamma_1^2 \ll (h\bar{\nu}/kT_{bb}) \ll \gamma_2^2$, and

$$b(x) = 2^{x+3} \frac{x^2+4x+11}{(x+3)^2(x+5)(x+1)} \Gamma\left(\frac{x+5}{2}\right) \zeta\left(\frac{x+5}{2}\right), \tag{2.19}$$

where Γ is the gamma function, and ζ is the Riemann zeta function.

2.2 Radio Sources

Early observations of radio galaxies in the 1950's and 1960's revealed that the sources were composed of a core (generally associated with an optical counterpart), and two bright spots. Initial theories suggested that the outer regions were some form of ejecta from the core, but these theories required enormous energy densities in the initial ejection which were difficult to account for (Burbidge 1956). Higher resolution observations in the 1960's and 1970's revealed that the outer bright regions were connected to the core of the source by jets. These jets, predicted by Rees (1971) and Blandford & Rees (1974), provide a continuous energy supply from the nucleus to the outer hot spots.

Further detailed studies of large samples of radio galaxies by Fanaroff & Riley (1974) revealed that most extragalactic sources could be divided phenomenologically into two groups. The division point of the two populations is based on the radio source power at 1400 MHz; sources with $P_{1400} < 10^{24-25}$ W Hz^{-1} are called FR I type sources, while the more pow-

erful radio sources are called FR II. The FR I sources show bright emission in the cores and jets which fades outward toward the lobes, with no clear hot spots. Above the division point, the FR II sources are characterized by the presence of large, edge-brightened lobes, with clear hot spots. The remaining radio sources are generally compact sources which are characterized by their spectral properties as compact steep spectrum (CSS) or compact flat spectrum (CFS) sources. These sources account for ~20% of radio sources selected at 1400 MHz. Detailed reviews of extragalactic radio source properties and classification are given by Miley (1980), Bridle & Perley (1984), and Fanti et al. (1990).

2.3 Clusters of Galaxies

It has been well known for some time that the space between the galaxies within galaxy clusters is filled with a hot, diffuse gas, which radiates X-ray emission. Following the notation of Sarazin (1988), this section briefly outlines the physical properties of the intracluster medium, as well as the relation between the X-ray surface brightness distribution and the intracluster gas density.

2.3.1 Properties of the Intracluster Medium

For a plasma of electron temperature T_e, and electron density n_e, the mean free path for an electron that suffers energy exchanging collisions with another electron, is given by (Spitzer 1956)

$$\lambda_e = \frac{3^{3/2}(kT_e)^2}{4\pi^{1/2} n_e e^4 \ln\Lambda}, \tag{2.20}$$

where Λ is the ratio of the largest to the smallest impact parameters for the collision. For temperatures and densities representative of galaxy clusters, the Coulomb logarithm is $\ln\Lambda = 38$ (Sarazin 1988), and the electron mean free path can be written as

$$\lambda_e = 23 \left(\frac{T_e}{10^8 \text{ K}}\right) \left(\frac{n_e}{10^{-3} \text{ cm}^{-3}}\right)^{-1} \text{ kpc}. \tag{2.21}$$

For a plasma in thermal equilibrium, the electron and ion temperatures are equal to the gas temperature, $T_e = T_i = T_g$. In this situation, the mean free path of the ions will be much the same as that of the electrons. In general, these particle mean free paths are smaller than the length scales of interest within galaxy clusters, and the intracluster medium (ICM)

must be treated as a collisional fluid.

Consider the assumption above, that galaxy clusters are in thermal equilibrium at some time after the initial collapse of matter into the cluster's potential. An initial homogeneous plasma with a non-Maxwellian particle distribution will experience elastic collisions which will tend to relax the plasma to a Maxwellian distribution. This relaxation will occur on a timescale determined by the mean free path of each component of the plasma. The equipartition timescale for electrons is set by the ratio of the mean free path and the r.m.s. velocity of the electron:

$$\begin{aligned} t_{eq}(e,e) &= \frac{3m_e^{1/2}(kT_e)^{3/2}}{4\pi^{1/2}n_e e^4 \ln\Lambda} \\ &\approx 3.3\times 10^5 \left(\frac{T_e}{10^8\ \mathrm{K}}\right)^{3/2} \left(\frac{n_e}{10^{-3}\ \mathrm{cm}^{-3}}\right)^{-1}\ \mathrm{yr}. \end{aligned} \tag{2.22}$$

The timescale for the proton component to reach equilibrium is given by Sarazin (1988) as $t_{eq}(p,p) \approx (m_p/m_e)^{1/2} t_{eq}(e,e)$, which is approximately 43 $\times$ $t_{eq}(e,e)$. At the end of this time, the electrons and protons will be in equilibrium with their own species, but not with each other. The timescale for all components of the plasma to be in thermal equilibrium is set by the timescale for the proton and electron fluids to equilibrate, $t_{eq}(p,e) \approx (m_p/m_e) t_{eq}(e,e)$, which is roughly 1870 $\times$ $t_{eq}(e,e)$. Although this timescale is actually the proton-electron equilibrium timescale, it is generally appropriate also for the heavier ions in the plasma, as the increased charge on the ion compensates for the increased mass in relation to the equilibrium timescale. Typical ICM temperatures of $T_g \approx 10^8$K, and electron densities of $n_e \approx 10^{-3}$ cm^{-3} give a plasma equilibrium timescale of $t_{eq}(p,e) \approx 6\times 10^8$ yr. This equilibrium timescale is short compared to the typical cluster ages, $\tau_{cl} \approx 10^{10}$yr, which means that the cluster can be treated as a collisional fluid with a smooth radial pressure gradient (assuming $\partial\phi/\partial \mathrm{t} = 0$).

A hydrostatic gas distribution is characterized by

$$\nabla P = -\rho_g \nabla\phi(r), \tag{2.23}$$

where $P = \rho_g kT_g/\mu m_p$ is the gas pressure, ρ_g is the gas density, and $\phi(r)$ is the cluster's

gravitational potential. For a spherically symmetric cluster, this equation reduces to

$$\frac{1}{\rho_g}\frac{dP}{dr} = -\frac{GM(r)}{r^2}, \tag{2.24}$$

where $M(r)$ is the total cluster mass within radius r. Individual galaxies within the cluster will also respond to the same gravitational potential as the gas, thus, if the velocity distribution of the galaxies orbits is isotropic, the galaxies also satisfy a hydrostatic equation

$$\frac{1}{\rho_{gal}}\frac{d(\rho_{gal}\sigma^2)}{dr} = -\frac{GM(r)}{r^2}, \tag{2.25}$$

where ρ_{gal} is the number density of the galaxies, and σ is their one-dimensional velocity dispersion. Equations 2.24 and 2.25 can be combined to eliminate the total mass terms, which gives

$$\frac{1}{\rho}\frac{dP}{dr} = \frac{1}{\rho_{gal}}\frac{d(\rho_{gal}\sigma^2)}{dr}. \tag{2.26}$$

Under the assumption of an isotropic velocity distribution for the galaxies, Equation 2.26 can be solved to yield

$$\rho \propto \rho_{gal}^{\beta}, \tag{2.27}$$

where

$$\beta = \frac{\mu m_p \sigma^2}{kT_g} = 0.76\left(\frac{\sigma}{10^3 \text{ km s}^{-1}}\right)^2\left(\frac{T_g}{10^8 \text{ K}}\right)^{-1}. \tag{2.28}$$

The mean mass per particle in the gas is μ=0.63 in units of the proton mass. The parameter β is the square of the ratio of the average galaxy and gas particle speeds.

A convenient form for the gas distribution is the King analytic form

$$\rho(r) = \rho_o\left[1+\left(\frac{b}{r_c}\right)^2\right]^{-3\beta/2}, \tag{2.29}$$

where ρ_o is the central gas density, b is the impact parameter, and r_c is the cluster's core radius. This gas distribution can be used to parameterize the X-ray surface brightness in any spectral band

$$I_x(r) = I_x^o\left[1+\left(\frac{b}{r_c}\right)^2\right]^{-3\beta+1/2}. \tag{2.30}$$

This parameterization has been shown to provide a good fit to the radial surface brightness profiles of clusters by Jones & Forman (1984).

2.4 Detecting Intracluster Magnetic Fields

2.4.1 Synchrotron Halos: Equipartition

In addition to synchrotron emission from individual cluster galaxies, a few galaxy clusters reveal extended diffuse synchrotron emission, which does not appear to be associated with any optical counterpart (Feretti & Giovannini 1996). Although it is still a rare phenomenon, this diffuse emission appears to fall within two distinct morphological categories, which are correlated with the location of the emission within the cluster. Diffuse synchrotron emission within the central regions of galaxy clusters has a fairly relaxed morphology, appearing as a central synchrotron *halo* with typical sizes of order 500 kpc. The prototypical example of a synchrotron halo is Coma-C in the Coma cluster. In the outer regions of galaxy clusters, the diffuse synchrotron emission often appears very irregular and elongated. This peripheral emission has a similar scale to that of the central halos. The elongation of the emission has led to the hypothesis that these outer synchrotron sources are *relics* of currently inactive radio galaxies. The prototype for this class of synchrotron emission is 1253+275, also in the Coma cluster. Both the halo and relic synchrotron sources are observed to have very steep spectral indices, $\alpha \gtrsim 1.0$, however they differ significantly in their polarization properties. The central halos show little or no polarized radio flux, while the outer relic sources are often very highly polarized. A recent review of the properties of synchrotron halo and relic sources is given by Feretti & Giovannini (1996).

A convenient method of estimating the strength of the magnetic field with these synchrotron sources is to consider equipartition between the relativistic particles and the magnetic fields within the source. Minimizing the total energy within the synchrotron source, the corresponding magnetic energy is given by (Pacholczyk 1970)

$$E_B = \frac{3}{4}(1+k)E_e, \tag{2.31}$$

where k is the ratio of the energy in the heavy particles to that in the electrons, and $E_e = \kappa \int E^{-x+1} dE$ is the total energy in the electrons. The minimum total energy is attained at a magnetic field strength of

$$B_{eq} = (4.5)^{2/7}(1+k)^{2/7} c_{12}^{2/7} \phi^{-2/7} R^{-6/7} L^{2/7}, \tag{2.32}$$

where the function c_{12} is tabulated in Appendix 2 of Pacholczyk (1970), ϕ is the fraction of the source's volume occupied by magnetic fields and relativistic particles, R is the radius of the source, and L is the radio luminosity of the source. Note that the equipartition estimate of the magnetic field relies on the *unknown* filling factor, ϕ, and energy ratio parameter, k. The standard assumption used for calculations are $\phi = 1$, and k=1, which provide lower limit estimates on the equipartition field strength. The magnetic field strengths determined from these estimates are discussed in § 8.2.1.

2.4.2 Synchrotron Haloes and Inverse Compton Radiation

In § 2.1, the equations describing the synchrotron and inverse Compton (IC) losses for relativistic electrons were outlined. This section will consider how the two emission mechanisms can be used to constrain the magnetic field strength in clusters of galaxies.

Comparing Equations 2.2 and 2.14, it can be seen that the ratio of the radiation losses for electrons in the intracluster medium

$$\frac{P_{IC}}{P_S} = \frac{U_{rad}}{U_B} \tag{2.33}$$

is determined by the ratio of the energy density in the cosmic microwave background radiation, and in the magnetic field. This relation holds for arbitrary values of the electron velocity, not just the ultra-relativistic regime, but relies on the assumption that Thomson scattering is valid in the electron's rest frame (Felten & Morrison 1966; Rybicki & Lightman 1979).

In terms of observational quantities, Sarazin (1988) gives the ratio of the single-frequency synchrotron and inverse Compton fluxes as

$$\left(\frac{f_x}{f_s}\right)\left(\frac{\nu_x}{\nu_s}\right)^{\alpha_x} = \frac{2.47e-19 T_{bb}^3 b(x)}{B a(x)} \left(\frac{4960 T_{bb}}{B}\right)^{\alpha_x}, \tag{2.34}$$

where

$$a(x) = 2^{(x-7)/2}\left(\frac{3}{\pi}\right)^{1/2} \frac{\Gamma\left(\frac{3x-1}{12}\right)\Gamma\left(\frac{3x+19}{12}\right)\Gamma\left(\frac{x+5}{4}\right)}{(x+1)\Gamma\left(\frac{x+7}{4}\right)}, \tag{2.35}$$

and $b(x)$ is given by Equation 2.19. Since the temperature of the cosmic microwave background is known at any epoch, ($T_{bb}(z) = 2.74(1+z)$; Mather et al. 1990), Equation 2.34 gives the magnetic field strength, B, in a region containing relativistic electrons. While the

majority of the X-ray emission from galaxy clusters appears to be thermal bremsstrahlung in origin, recent measurements with BeppoSAX (Fusco-Femiano et al. 1999) claim to detect a hard X-ray excess due to inverse Compton. Section 8.2.1 describes the magnetic field strengths derived from these combined synchrotron and IC measurements as well as the limits placed on the intracluster fields from upper limits on intracluster IC emission.

2.4.3 Faraday Rotation

A more direct method to measure intracluster magnetic fields is through their effects on the propagation of linearly polarized radiation, as it passes through a magnetized plasma (Faraday rotation). The signature of this Faraday rotation depends on the location of the magneto-ionic plasma in relation to the source of polarized emission. Below, three possible situations are briefly outlined. In the simplest case, the rotating medium can be assumed to be completely outside the polarized source, forming an external screen between the polarized emission and the observer. The second situation considers internal rotation, which assumes that the polarized emission and the Faraday medium come from the same location. The most complicated situation is mixed internal and external Faraday rotation. The basic theory of Faraday rotation in different media is covered in a classic paper by Burn (1966).

External

External Faraday rotation results from a Faraday screen, composed of a magnetized, ionized plasma, located between the polarized radio source and the observer. As the polarized emission travels through the magneto-ionic medium, the plane of polarization of the radiation will be rotated. This rotation of the plane of polarization can be understood by considering a linearly polarized wave to be resolved into equal components of two opposite hand elliptical polarizations. In the limit where the gyrofrequency, ν_g, is much less than the observing frequency, ν, the refractive indices for the two polarized modes are (Longair 1981)

$$n^2 = 1 - \frac{(\nu_p/\nu)^2}{(1 \pm (\nu_g/\nu)\cos\theta)}, \tag{2.36}$$

where ν_p =9.1×10^{3}N$_e^{1/2}$ Hz is the plasma frequency, and θ is the angle between the wave propagation direction and the magnetic field. As the two waves propagate through the magneto-ionic media, they will have different phase velocities, which results in a rotation of

the plane of polarization of the radiation as the two orthogonal modes are added together after some propagation distance $d\ell$. In the regimes of interest to this research, the difference in the refractive indices is

$$\Delta n = \frac{\nu_p^2 \nu_g}{\nu^3} \cos\theta, \tag{2.37}$$

which results in a phase difference between the polarization modes of

$$\Delta\phi = \frac{2\pi\nu\Delta n}{c}. \tag{2.38}$$

After a propagation distance $d\ell$, the two orthogonal polarizations are recombined, to reveal a rotation of the plane of polarization of

$$\Delta\chi = \frac{\pi\nu_p^2\nu_g}{c\nu^2} \cos\theta \; d\ell, \tag{2.39}$$

where χ is the position angle of the polarized emission. Integrating this equation, and re-writing it in terms of useful astronomical units, gives the amount of rotation of the polarization angle as

$$\Delta\chi = \chi - \chi_o = 811.9\lambda^2 \int_0^L n_e B_{||} d\ell = RM\lambda^2 \text{ radians}, \tag{2.40}$$

where RM is the rotation measure in radians m^{-2}, χ_o is the intrinsic polarization angle of the radiation, n_e is the (thermal) electron density in cm^{-3}, $B_{||}$ is the line of sight component of the magnetic field in μG, and L is the path length through the rotating medium in kpc. Through a set of polarization observations at a minimum of three wavelengths, the RM of a source can be determined by plotting the polarization angle versus the square of the wavelength, and performing a linear least squares fit. By standard convention, a positive rotation measure corresponds to a magnetic field pointed toward the observer.

Internal

Another possible origin for Faraday rotation is when thermal electrons are mixed with the synchrotron emitting relativistic electrons within the radio source. The simple slab model, considered below, follows the notation of Dreher, Carilli, & Perley (1987) for an optically thin synchrotron plasma. A more general development of the theory can be found in Burn

(1966), and Pacholczyk (1970).

The total intensity, I, and complex polarized flux density, P=Q+iU, change with path $d\ell$ through the source as

$$\frac{dI}{d\ell} = -\kappa I + \epsilon \tag{2.41}$$

$$\frac{dP}{d\ell} = 2i\mathcal{R}P - \kappa P + \Pi(x)\epsilon e^{2i\chi_B}, \tag{2.42}$$

where κ is the absorption coefficient, ϵ is the mean emission coefficient, $\mathcal{R} = \Delta\chi_o/d\ell = 811.9\lambda^2 n_e B_{||}$ is the rate of rotation of the polarization angle per element $d\ell$, and χ_o is the intrinsic polarization angle of the radiation. In a medium with a uniform magnetic field direction ($\Delta\chi_o = 0$) no thermal absorption (κ=0) and no random magnetic field component ($B_r = 0$) integration of the above equation, through a source of depth L, yields

$$I = \epsilon L, \tag{2.43}$$

and

$$P = \frac{\Pi(x)\epsilon}{2i\mathcal{R}}(1 - e^{-2i\mathcal{R}L}), \tag{2.44}$$

where the reference frame has been rotated so that $\chi_o = 0°$. The degree of polarization, $m = |P|/I$, is given by

$$m = \Pi(x)\left|\frac{\sin(\mathcal{R}L)}{\mathcal{R}L}\right|. \tag{2.45}$$

Physically, Equations 2.44 and 2.45 show that the polarized flux density will vary sinusoidally with depth through the source, since the radiation emitted from different regions within the source will interfere as they will be rotated by different amounts. Note, however, that the total flux density, I, does not vary with source depth, thus the degree of polarization will drop with increasing wavelength! This behaviour of the degree of polarization with wavelength is shown by the solid lines in Figure 2.1, and gives meaning to the term "Faraday depth".

In the uniform slab model, the polarization angle (Equation 2.64) follows the relation

$$\chi = \frac{1}{2}\left(\frac{1 - \cos|2\mathcal{R}L|}{\sin|2\mathcal{R}L|}\right), \tag{2.46}$$

which indicates that, relative to the intrinsic polarization angle χ_o, the observed polarization angle can be rotated from 0 to $\pi/2$ as a function of λ^2. When $\mathcal{R}L$ reaches π, the source

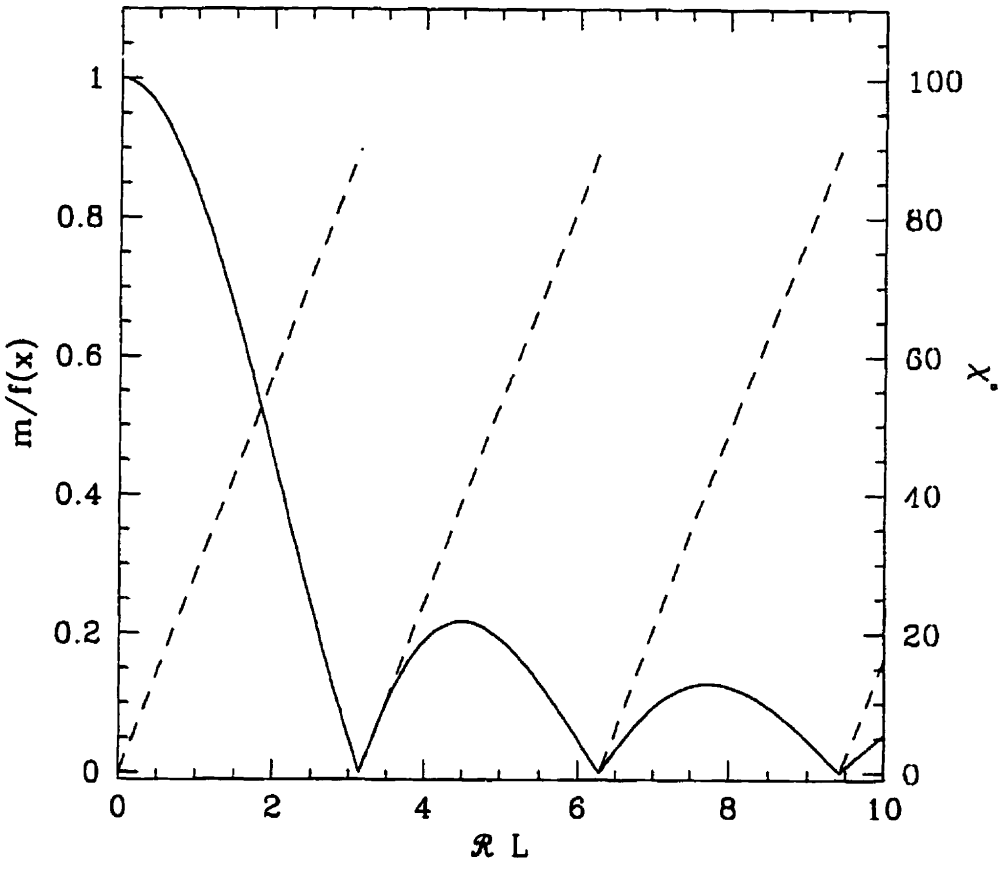

Figure 2.1: This plot shows the variation of the degree of polarization, m/f(x), and the polarization angle, χ, as a function of the Faraday depth $\mathcal{R}$L. The degree of polarization, solid line, drops from the intrinsic value toward long wavelengths. The polarization angle, dashed line, follows a λ^2 relation with increasing wavelength to the point at which the polarization degree reaches zero. At this Faraday depth, the polarization angle jumps discontinuously from $\pi/2$ to zero.

will be completely depolarized, m=0, and the polarization angle will change discontinuously from the maximum of $\pi/2$ back to 0 radians. This discontinuous behavior, as a function of increasing λ^2, produces a characteristic sawtooth plot shown by the dashed lines in Figure 2.1. This polarization angle signature can then be used to diagnose the presence of internal Faraday rotation in sources. It is important to sample a sufficient range of λ^2 space, that one expects the polarization angle to rotate by more than $\pi/2$ radians.

Mixed Internal and External

Radio sources which are embedded in a thermal medium, such as the intracluster medium, may be subject to a mixture of internal and external Faraday effects. If the thermal electrons from the ICM mix into the magnetized relativistic plasma within the radio source, there will be a region of internal Faraday rotation which would likely take on the form of a sheath surrounding the radio source. The degree of polarization, and the polarization angle measured for lines of sight toward the radio source would reveal a mixture of internal Faraday rotation from the sheath, and external Faraday rotation from the foreground intracluster medium.

Taylor (1991) considered a situation where the synchrotron source was divided into two regions. The first, most distant, region contained only relativistic electrons and a uniform magnetic field. In the second region, the relativistic electrons are mixed with thermal electrons and a uniform magnetic field. Each element in the second region will emit synchrotron emission, which will then experience Faraday rotation through the remainder of the path out of the source. The second region will also serve as an external Faraday screen for the emission from the first region. Taylor conducted simulations in which the fraction of thermal material in the source ranged from 0.2 to 0.8. The varying fraction of thermal material was obtained by increasing the size of the region containing only relativistic electrons so that the thermal region would have a fixed size, and thus the rotation measure would be constant. Taylor found that in the limit of a small amount of thermal material, the position angle follows the λ^2 behaviour of an external screen fairly closely. A large thermal fraction produces a polarization angle which displays significant deviations from a λ^2 law, which should be visible in multi-frequency observations. The large thermal fraction also produces strong depolarization of the source. In all simulations containing a fraction, F_t, of thermal material, the fractional polarization at long wavelengths approaches $(1 - F_t)$,

and the polarization angle deviations from λ^2 become less severe. Further models of mixed internal and external Faraday rotation are considered by Gardner & Whiteoak (1966).

$n\pi$ Ambiguities

The above statement, that the rotation measure can be determined from a set of observations at a minimum of three wavelengths, is not completely true. While it is possible to determine a rotation measure from three observations, the wavelengths of these observations must be carefully selected to prevent ambiguities in the rotation measure. The ambiguity results from the fact that the observed position angle of the polarization is only a pseudo-vector lying in the range of $0 < \chi < \pi$ radians. A measurement of this angle is uncertain by a factor of $\pm n\pi$, which allows for an unknown number of half rotations of the polarization plane along the line of sight between the source and the observer. An additional constraint on the selected wavelenghts is the limited range of rotation measures that they are sensitive to. For any particular line of sight to a source, there must be a unique rotation measure and intrinsic polarization angle. The key to recovering the correct rotation measure is to choose two closely spaced wavelengths to provide a range of rotation measures which has no ambiguity. These measurements can then be combined with one or more measurements at a more widely spaced wavelength, to pin down an accurate rotation measure.

To understand the rotation measure ambiguity, and method to avoid it, consider Figures 2.2 and 2.3 drawn from the work of Ruzmaikin & Sokoloff (1979). The first figure represents observed measurements of the polarization angle (solid lines) at three uniformly spaced points in wavelength squared space. Each measurement of the polarization angle has an associated uncertainty of an integer number of half rotations, represented by the dotted lines. A set of linear least square fits to the polarization angles is shown by the dashed lines. The associated set of possible rotation measures for this particular source are given by the slopes of the lines, and the set of intrinsic polarization angles are given by the intercepts of the lines. In this situation, a determination of the best rotation measure of the source requires an assumption about the nature of the expected magnitude of the rotation measure, an unenviable situation for a researcher. A more acceptable situation is shown in Figure 2.3 where the observations have been undertaken at a carefully selected set of points in wavelength squared space. Although the measured polarization angles are still uncertain by $\pm n\pi$, the two points closely spaced in wavelength squared space can provide

an unambiguous determination of the rotation measure up to some maximum value set by the spacing of the points. The measured polarization angles will have associated measurement errors which can be used to construct an error cone (dashed lines) within which the source rotation measure lies. A least squares fit to these points and observations at one or more wavelengths with a larger separation in lambda squared space provides an unambiguous determination of the source rotation measure (solid line). Details of observational considerations for this method are described in Ruzmaikin & Sokoloff (1979).

2.4.4 Summary

This section discussed the methods available to measure, or place limits on the magnetic field strength in clusters of galaxies. These methods involve two basic approaches. First, the presence of cluster-wide synchrotron emission originating within the intracluster medium indicates the presence of magnetic fields throughout the synchrotron emitting volume. The strength of these magnetic fields can be estimated through minimum pressure arguments, § 2.4.1. Alternatively, upper limits on inverse Compton emission for the synchrotron halo clusters places lower limits on the intracluster magnetic fields strength, § 2.4.2. The second approach to measuring intracluster magnetic fields relies on Faraday rotation measures. Section 2.4.3 discusses internal, external, and mixed internal plus external origins of Faraday rotation, and their associated Faraday characteristics. This section also outlines the ambiguities associated with measurements of the position angle of the polarized emission.

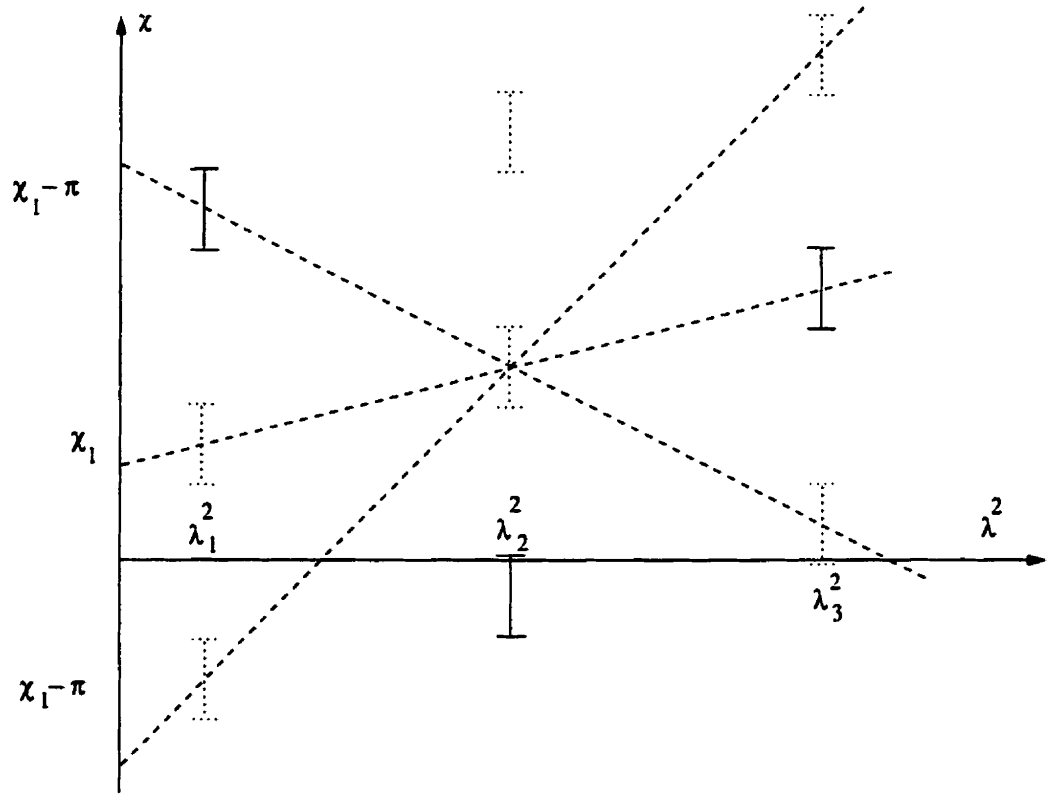

Figure 2.2: For a set of position angle measurements at three equally spaced wavelengths, λ_1–λ_3, the $n\pi$ uncertainty allows for a number of shifts by $\pm\pi$ radians along the position angle axis. These shifts are represented by the dotted error bars in the plot. The three dashes lines indicate three possible fits to the set of position angles. The slope of each line gives a different rotation measure for the source in question.

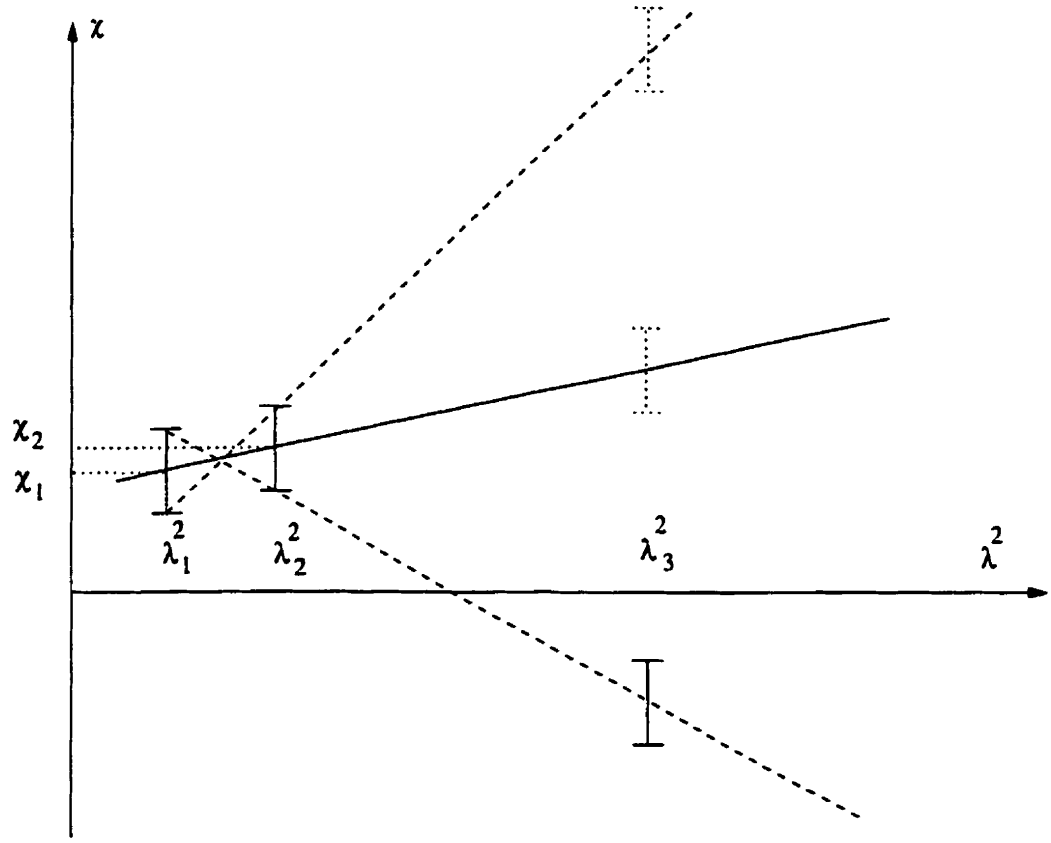

Figure 2.3: This figure shows a set of position angle measurements at non-uniformly spaced points in λ^2 space. The two points at closely spaced points in λ^2 set a cone of rotation measure values which are constrained to fall within the dashed lines. The addition of a measurement at a widely spaced point in λ^2 fixes the rotation measure of the source, solid line.

2.5 Interferometry

2.5.1 Total Intensity Observations

The correlator output from any two elements in an interferometer array observing a point on the celestial sphere, will provide an instantaneous measure of the visibility function $V(u,v)$[1] at two points in the u-v plane. The rotation of the Earth will cause the u and v components of the baseline to trace an elliptical locus, which is the projection onto the u-v plane of the circular locus traced by the baseline vector. An array of antennas produces an ensemble of such elliptical loci known as the sampling function $S(u,v)$, which is a function of the antenna spacings, and the source declination. This sampling function indicates the values of u and v at which the visibility function is sampled. Under certain approximations (described in Clark 1994, and Thompson 1994), the visibility function is related to the source intensity distribution $I(l,m)$ (multiplied by the primary beam of the array elements) through a two-dimensional Fourier transform:

$$V(u,v) = \int\int I(l,m) e^{-2\pi i(ul+vm)} dl\, dm \tag{2.47}$$

where the integral is taken over the entire sky. The direct inversion of this equation gives the intensity distribution on the sky:

$$I(l,m) = \int\int V(u,v) e^{2\pi i(ul+vm)} du\, dv. \tag{2.48}$$

In practice, an interferometer only measures a finite number of noise-weighted samples of the visibility function, thus the source intensity distribution cannot be recovered directly. Inserting the sampling function into the Fourier inversion equation provides an inferior image called the *dirty image*:

$$I^D(l,m) = \int\int V(u,v) S(u,v) e^{2\pi i(ul+vm)} du\, dv. \tag{2.49}$$

[1]The visibility or spatial coherence function is evaluated at projected baselines u and v measured in units of wavelength.

The *dirty image* is related to the true image $I(l, m)$ through:

$$I^D = I * B, \tag{2.50}$$

where * denotes convolution, and

$$B(l, m) = \int\int S(u, v) e^{2\pi i(ul+vm)} du\, dv \tag{2.51}$$

is the synthesized beam, or point spread function, corresponding to the sampling function. The true surface brightness distribution on the sky can be recovered through the use of a Direct Fourier Transform (DFT), although the DFT requires a large investment in CPU time since the number of multiplications required increases as N^4. The Fast Fourier Transform (FFT) on the other hand uses the periodic nature of the exponential to reduce the number of operations to $N^2 \log_2 N$. This increase in efficiency is obtained by gridding the visibilities before applying the FFT. The sensitivity and resolution in the final image are controlled by applying sampling and weighting to the measured visibilities before the Fourier transform process (Sramek et al. 1994). The limited sampling of the visibilities results in defects in the final image formed by a simple Fourier transform of the sampled visibilities. Non-linear deconvolution, in the form of the 'CLEAN' algorithm or the Maximum Entropy Method, is required to correct for the sampling effects. These deconvolution methods are described in more detail by Cornwell & Braun (1994), and are the standard methods employed for most radio synthesis images. The application of non-linear deconvolution to the calibrated data for this thesis is described in § 3.4.

2.5.2 Polarization Observations

The polarization state of electromagnetic radiation is characterized by the motion of the tip of the electric field vector. This motion is generally described in terms of orthogonal linear, orthogonal circular, or elliptical polarization as shown in Figure 2.4. Elliptical polarization is a more general description of the polarization state, and is a combination of the circular and linear components.

In general, emission from astrophysical phenomena are incoherent, with the emission containing a mix of different polarization states. A source is labeled polarized if there is statistically more of one polarization component present. Measurements of source polariza-

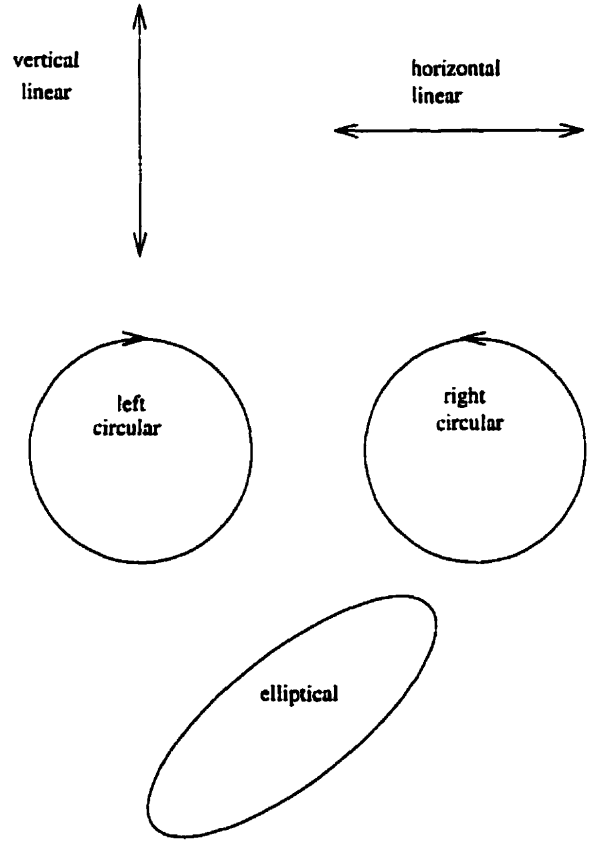

Figure 2.4: The polarization state of electromagnetic radiation is determined by the locus that the tip of the electric vector traces out in the plane perpendicular to the direction of propagation (out of the page in the above figure). The polarization of a source is generally characterized in terms of linear, circular, or elliptical polarization, where elliptical polarization is a combination of the linear and circular polarization states.

tion are generally expressed in terms of Stokes parameters I, Q, U, and V which represent the total intensity, two orthogonal linear polarization components, and the circular polarization component, respectively.

Stokes Parameters

Following the notation of Kraus (1986), for a completely polarized wave, referring to Figure 2.5, one can write:

$$\begin{aligned} E_x &= E_1 \sin(\omega t - \delta_1) \\ E_y &= E_2 \sin(\omega t - \delta_2) \end{aligned} \tag{2.52}$$

where $\delta_1 - \delta_2$ is the phase difference of E_x and E_y, and

$$\begin{aligned} E_1 &= E_0 \sqrt{\cos^2 \epsilon \cos^2 \chi + \sin^2 \epsilon \sin^2 \chi} \\ E_2 &= E_0 \sqrt{\cos^2 \epsilon \sin^2 \chi + \sin^2 \epsilon \cos^2 \chi}. \end{aligned} \tag{2.53}$$

The magnitude of the total Poynting vector or flux density (watts m^{-2}) of the electromagnetic wave is

$$S = S_x + S_y = \frac{E_1^2 + E_2^2}{Z} = \frac{E_0^2}{Z}, \tag{2.54}$$

where Z is the intrinsic impedance of the medium (ohms). S_x and S_y represent the Poynting vectors for the wave components polarized in the x and y direction respectively, and are given by:

$$\begin{aligned} S_x &= \frac{E_1^2}{Z} = S(\cos^2 \epsilon \cos^2 \chi + \sin^2 \epsilon \sin^2 \chi) \\ S_y &= \frac{E_2^2}{Z} = S(\cos^2 \epsilon \sin^2 \chi + \sin^2 \epsilon \cos^2 \chi) \end{aligned} \tag{2.55}$$

The Stokes parameters I, Q, U, and V are defined as (Stokes 1852):

$$\begin{aligned} I &= S = S_x + S_y = \frac{E_1^2}{Z} + \frac{E_2^2}{Z} \\ Q &= S_x - S_y = \frac{E_1^2}{Z} - \frac{E_2^2}{Z} = S \cos 2\epsilon \cos 2\chi \\ U &= (S_x - S_y) \tan 2\chi = S \cos 2\epsilon \sin 2\chi = 2\frac{E_1 E_2}{Z} \cos(\delta_1 - \delta_2) \end{aligned}$$

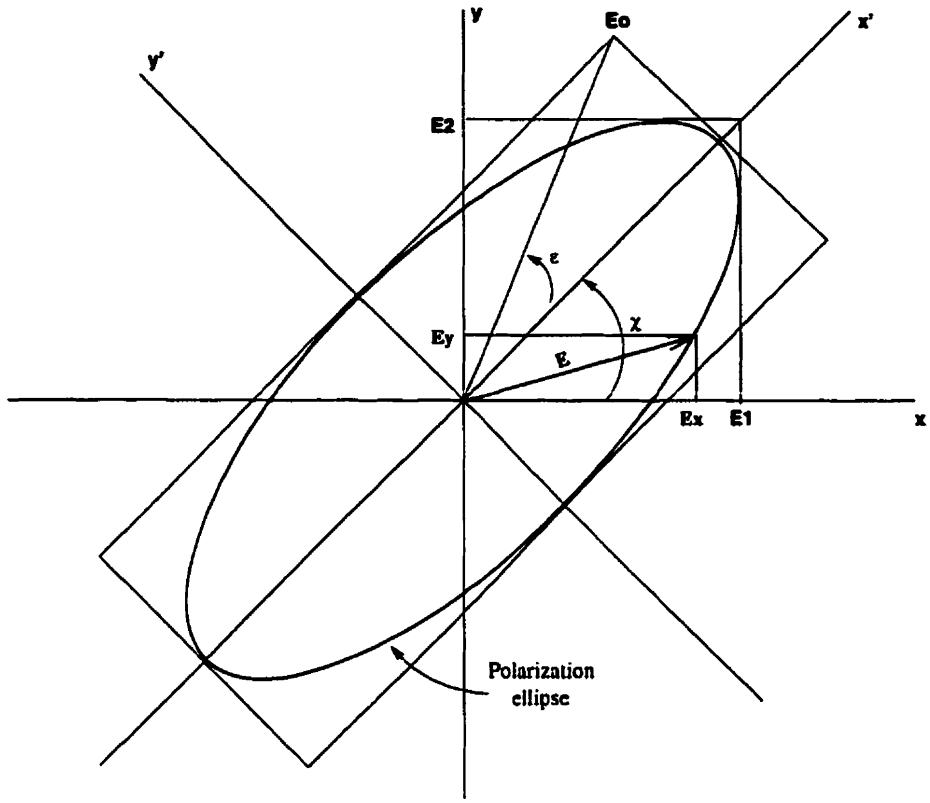

Figure 2.5: Relation of electric vector amplitudes E_1 and E_2 to polarization axes.

$$V = (S_x - S_y)\tan 2\epsilon \sec 2\chi = S \sin 2\epsilon = 2\frac{E_1 E_2}{Z}\sin(\delta_1 - \delta_2). \tag{2.56}$$

For a completely polarized wave, it follows that

$$\begin{aligned} I^2 &= Q^2 + U^2 + V^2 \\ \frac{U}{Q} &= \tan 2\chi \\ \frac{V}{S} &= \sin 2\epsilon = \frac{V}{\sqrt{Q^2 + U^2 + V^2}}. \end{aligned} \tag{2.57}$$

More generally, for a partially polarized wave, the $\vec{x}$ and $\vec{y}$ components of the electromagnetic wave can be written as

$$\begin{aligned} E_x &= E_1(t)\ \sin[\omega t - \delta_1(t)] \\ E_y &= E_2(t)\ \sin[\omega t - \delta_2(t)]. \end{aligned} \tag{2.58}$$

In this case, the Stokes parameters must be time averaged so that

$$\begin{aligned} I &= \frac{< E_1^2 >}{Z} + \frac{< E_2^2 >}{Z} = S_x + S_y = S \\ Q &= \frac{< E_1^2 >}{Z} - \frac{< E_2^2 >}{Z} = S_x - S_y = S < \cos 2\epsilon \cos 2\chi > \\ U &= 2\frac{< E_1 E_2 \cos(\delta_1 - \delta_2) >}{Z} = S < \cos 2\epsilon \sin 2\chi > \\ V &= 2\frac{< E_1 E_2 \sin(\delta_1 - \delta_2) >}{Z} = S < \sin 2\epsilon >, \end{aligned} \tag{2.59}$$

where <...> indicates a time average, and

$$I^2 \geq Q^2 + U^2 + V^2. \tag{2.60}$$

Each of the six standard receivers on the VLA is designed to record orthogonal right-hand circular (RCP) and left-hand circular (LCP) polarizations. In this coordinate system, the left and right hand circularly polarized components, E_L and E_R, can be written as

$$\begin{aligned} E_L &= E_l\, e^{i\omega t} \\ E_R &= E_r\, e^{-i(\omega t + \delta)} \end{aligned} \tag{2.61}$$

where E_l, and E_r are constants, and δ is the phase difference between the two components. The Stokes parameters can be expressed as

$$\begin{aligned} I &= E_L E_L^* + E_R E_R^* = E_r^2 + E_l^2 \\ Q &= E_L E_R^* + E_R E_L^* = 2E_r E_l \cos\theta \\ U &= i(E_L E_R^* - E_R E_L^*) = 2E_r E_l \sin\theta \\ V &= E_L E_L^* - E_R E_R^* = E_l^2 - E_r^2 \end{aligned} \tag{2.62}$$

where * denotes complex conjugation. The advantage of Equations 2.62 is that the Stokes parameters are now represented in term of quantities that are measured by the interferometer. Note that Stokes I and V depend on the parallel hand correlator products, while Stokes Q and U depend on the cross-hand correlator products.

Two main results which will be relevant throughout this thesis are the definitions of the

polarized intensity of the radiation

$$P = \sqrt{Q^2 + U^2}, \tag{2.63}$$

and the polarization angle

$$\chi = \frac{1}{2}\arctan\frac{U}{Q}. \tag{2.64}$$

2.5.3 Instrumental Polarization

Due to the polarization leakage, the antenna receiver system responds to polarization signals other than the nominal component. These instrumental polarization terms can be corrected if the deviations are known. Inverting Equations 2.62, one can recover the true visibilities (Conway & Kronberg 1969)

$$\begin{aligned} E_L E_L^* &= \frac{1}{2}(I+V) = V_{jkLL} \\ E_R E_R^* &= \frac{1}{2}(I-V) = V_{jkRR} \\ E_L E_R^* &= \frac{1}{2}(Q-iU) = V_{jkLR} \\ E_R E_L^* &= \frac{1}{2}(Q+iU) = V_{jkRL} \end{aligned} \tag{2.65}$$

in terms of the measured correlations. Following the notation of Hjellming (1992), the complex voltages of the j^{th} antenna, before cross-correlation, can be written as

$$\begin{aligned} R_j &= G_{jR}(E_R e^{-i\phi_P} + D_{jR} E_L e^{i\phi_P}) \\ L_j &= G_{jL}(E_L e^{i\phi_P} + D_{jL} E_R e^{-i\phi_P}), \end{aligned} \tag{2.66}$$

where G_{jR} and G_{jL} are the complex gains describing all the amplification and phase modification aspects of the j^{th} antenna, E_R and E_L are the right and left circularly polarized components of the electromagentic radiation, D_{jR} and D_{jL} describe the coupling between the polarizations (polarization leakage), and ϕ_P is the parallactic angle.

The parallactic angle is a result of the altitude-azimuth mount system employed at the VLA. This type of antenna mount results in a time-dependent rotation of the sky relative to the fixed reference system of the antenna. This angle is defined as the angle between the

source meridian and the elevation of the great circle of the antennas:

$$\phi_P = \tan^{-1}\left[\frac{\cos(\lambda_{\rm lat})\sin H}{(\sin(\lambda_{\rm lat})\cos\delta - \cos(\lambda_{\rm lat})\sin\delta\cos H)}\right]. \quad (2.67)$$

The VLA latitude is given by $\lambda_{\rm lat}$, δ is the source declination, and H is the source hour angle.

The measured correlator visibilities are represented by

$$\begin{aligned} V'_{jkLL} &= L_j L_k^* \\ V'_{jkRR} &= R_j R_k^* \\ V'_{jkLR} &= L_j R_k^* \\ V'_{jkRL} &= R_j L_k^*. \end{aligned} \quad (2.68)$$

Expanding this equation gives

$$\begin{aligned} V'_{jkRR} &= G_{jR}G_{kR}^*(E_R E_R^* + E_L E_R^* D_{jR} e^{2i\phi_P} + E_R E_L^* D_{kR} e^{-2i\phi_P} + E_L E_L^* D_{jR} D_{kR}^*) \\ V'_{jkLL} &= G_{jL}G_{kL}^*(E_L E_L^* + E_R E_L^* D_{jL} e^{-2i\phi_P} + E_L E_R^* D_{kL} e^{2i\phi_P} + E_R E_R^* D_{jL} D_{kL}^*) \\ V'_{jkRL} &= G_{jR}G_{kL}^*(E_R E_L^* e^{-2i\phi_P} + E_R E_R^* D_{kL}^* + E_L E_R^* D_{jR} D_{kL}^* e^{2i\phi_P} + E_L E_L^* D_{jR}) \\ V'_{jkLR} &= G_{jL}G_{kR}^*(E_L E_R^* e^{2i\phi_P} + E_L E_L^* D_{kR}^* + E_R E_L^* D_{jL} D_{kR}^* e^{-2i\phi_P} + E_R E_R^* D_{jL}). \end{aligned}$$

In practice, the D terms are found to be generally less than ten percent, and the linear polarization of sources is generally under ten percent (Bignell 1982). In this situation, the cross terms in the above equation are of order one percent of the parallel terms, thus the second order and higher terms are neglected. Dropping these terms, and using Equations 2.65, the relation between the true and measured visibilities can then be written as

$$\begin{aligned} V'_{jkLL} &= G_{jL}G_{kL}^* V_{jkLL} \\ V'_{jkRR} &= G_{jR}G_{kR}^* V_{jkRR} \\ V'_{jkRL} &= G_{jR}G_{kL}^*(V_{jkRL} e^{-2i\phi_P} + V_{jkRR} D_{kL}^* + V_{jkLL} D_{jR}) \\ V'_{jkLR} &= G_{jL}G_{kR}^*(V_{jkLR} e^{2i\phi_P} + V_{jkLL} D_{kR}^* + V_{jkRR} D_{jL}). \end{aligned} \quad (2.69)$$

Polarization calibration (discussed in more detail in § 3.3.3) consists of observing a calibrator

source with known Stokes parameters. Applying Equations 2.65 to the calibrator source provides a measure of the true source visibilities. Using Equations 2.69, the true and measured visibilities for the calibrator source provide a measure of the complex constants (G_{jR}, G_{jL}, D_{jR}, and D_{jL}) for each antenna. Defining

$$\begin{aligned} g_{jR} &= \frac{1}{G_{jR}} \\ g_{jL} &= \frac{1}{G_{jL}}, \end{aligned} \tag{2.70}$$

and rearranging Equations 2.69, gives

$$\begin{aligned} V_{jkLL} &= g_{jL} g^*_{kL} V'_{jkLL} \\ V_{jkRR} &= g_{jR} g^*_{kR} V'_{jkRR} \\ V_{jkLR} &= (g_{jL} g^*_{kR} V'_{jkLR} - D_{jL} V_{jkRR} - D^*_{kR} V_{jkLL})\, e^{-2i\phi_P} \\ V_{jkRL} &= (g_{jR} g^*_{kL} V'_{jkRL} - D_{jR} V_{jkLL} - D^*_{kL} V_{jkRR})\, e^{2i\phi_P}. \end{aligned} \tag{2.71}$$

From Equation 2.71, the true source visibilities can be determined from the measured visibilities and the complex antenna constants determined from the calibrator. A more detailed description of the VLA's on-line correction and calibration systems can be found in Hjellming (1992).

2.6 Instrumental Depolarization

Observations of radio sources at a number of wavelengths often show a variation in the degree of polarization measured. The standard method used to measure this depolarization is through the depolarization ratio

$$DP = \frac{m_{high}}{m_{low}} \tag{2.72}$$

where m_{high} and m_{low} represent the fractional polarization at the high and low frequency respectively. One source of depolarization, discussed in § 2.4.3, is internal Faraday rotation, which is an intrinsic property of a source. Depolarization can also result from a specific choice of instrumental parameters. The two instrumental effects discussed below are beamwidth depolarization, and bandwidth depolarization.

2.6.1 Beamwidth Depolarization

Beamwidth depolarization results from a side-to-side averaging of different polarization angles within the beam of the telescope. This effect is a result of having a rotation measure gradient within the source on scales smaller than the telescope beam. In the limit of a linear gradient in rotation measure across the beam, the depolarization will follow the same pattern as that for internal Faraday rotation. It should, however, be possible to distinguish between these types of depolarization, as the magnitude of the internal Faraday depolarization depends on the magnitude of the rotation measure through the term $\mathcal{R}$L in Equation 2.45, while the beamwidth depolarization will depend on the size of the rotation measure gradient, and should not be correlated with the magnitude of the rotation measure.

The effects of beamwidth depolarization will become severe when the position angle of the radiation varies by more than $\pi/2$ radians across the observing beam. The change in rotation measure associated with a polarization angle variation of $\Delta\chi$ is $\Delta\mathrm{RM} = \Delta\chi/\lambda^2$. For the wavelengths of interest in this work, a polarization angle variation of $\pi/2$ radians corresponds to a rotation measure gradient of 40 rad m^{-2} at 20 cm, and 440 rad m^{-2} at 6 cm. Although rotation measure gradients have been observed across kiloparsec regions by Feretti et al. (1999) for a source in the central regions of a cooling flow cluster, these large rotation measure gradients are generally confined to the cooling cores of clusters (Ge & Owen 1994). The sources observed for this work are generally probing regions of galaxy clusters which are beyond the cooling radius, and thus should not be affected by large rotation measure gradients. More detailed examinations of the effects of foreground depolarization on radio sources can be found in Burn (1966), Tribble (1991), and Sokoloff et al. (1998).

2.6.2 Bandwidth Depolarization

Bandwidth depolarization is important for observations of sources with very large rotation measures and/or observations using very wide bandwidths. The depolarization results from a variation in the polarization angle across the observing bandwidth. This effect follows a similar `sinc` function to that of the depolarization resulting from internal Faraday rotation.

It is, however, fairly simple to estimate the expected rotation of the polarization angle across the observing bandwidth, by considering the expected maximum rotation measure

of the radio source. Considering Equation 2.40 one finds that the amount of rotation of the polarization angle, across a bandwidth $\Delta\nu$, centered on frequency ν, is

$$\Delta\chi = -RM\lambda^2\frac{2\Delta\nu}{\nu}. \tag{2.73}$$

In theory, the VLA is capable of observing with a bandwidth of 50 MHz within one observing band. In practice, however, the maximal available bandwidth for continuum observations in the 20 cm band is set by the width of the radio frequency interference (RFI) free region around any particular frequency of interest, and is generally limited to a maximum bandwidth of 25 MHz. At a frequency of 1400 MHz, a rotation of $\pi/2$ radians, across a bandwidth of 25 MHz, will occur for sources whose rotation measure is 1100 rad m^{-2}, much larger than the rotation measures which are found in the regions outside cooling flow cores probed in this research.

2.7 Summary

This chapter concentrated on outlining the relevant theory which is applied in the remainder of this thesis. The first section discusses the radiation mechanisms for radio sources and the intracluster medium. The next two sections briefly discuss the properties of radio sources and the diffuse cluster gas. Section 2.4 provides the fundamentals for the methods which are used to probe intracluster magnetic fields. In particular, the Faraday effect is discussed in some detail, as many of the results presented within this thesis rely on calculating, and interpreting, the Faraday effect. The final two sections of this chapter present an overview of the instrument theory; § 2.5 outlines the background to interferometry, with emphasis on polarization observations, and § 2.6 examines the effects of instrumental depolarization on the observations.

Chapter 3

Radio Observations and Data Reductions

Overview: All radio polarimetric observations for this thesis were undertaken between October 1995 and September 1997 at the National Radio Astronomy Observatory (NRAO) Very Large Array (VLA)[1]. This chapter discusses the target selection and observing strategy, followed by a complete description of the data reduction procedure, with specific emphasis placed on the details of the polarization calibration procedures. Section 3.4 provides an overview of the imaging process for the data, and § 3.5 provides tables of the measured radio source fluxes.

3.1 The Very Large Array

The Very Large Array is a connected-element interferometer consisting of 27 antennas, each of diameter 25 meters, located on the plains of San Augustin, approximately 80 km west of Socorro, New Mexico. Each element is a fully steerable antenna on an altitude-azimuth mount with a Cassegrain feed system. The feed system consists of five receivers, centered on λ 20, 6, 3.6, 2 and 1.3 cm, located on a ring of radius 98 cm at the Cassegrain focus. All antennas are also equipped with a 90 cm feed which consists of a crossed dipole mounted near the prime focus. Additional receivers at 0.7 cm are currently (1999) mounted on thirteen antennas, and removable dipoles for observations at 400 cm are also available.

[1]The NRAO is operated by Associated Universities, Inc., under contract with the National Science Foundation.

Elements of the VLA are mounted on a railroad track which runs along each of the three arms of the instrument. The arms are arranged in a 'Y' shaped pattern with 9 antennas along each arm. Moving the elements to a set of fixed pads along the arms provides different configurations (standard: A through D) for the instrument. The most extended configuration (highest resolution) is A-array with a maximum antenna separation of 36 km; the most compact array (D-array) has a maximum antenna separation of 1 km. The diffraction limited resolution of the VLA can be approximated as

$$\theta_{HPBW} = \frac{250}{D} \quad \text{arcsec} \tag{3.1}$$

where D is the maximum antenna spacing in kilowavelengths. The precise shape of the synthesized beam depends on the source declination and the details of the u-v coverage. The VLA remains within a particular configuration for approximately four months. An overview of the theory of total intensity and polarization observations with an interferometer is given in § 2.5. The overview provides VLA-specific information, and also provides an introduction to the Stokes parameters which are used throughout this work. Detailed technical information on the VLA can be found in Perley (1998), and references therein.

3.2 Observations

As discussed in § 1.3, one of the goals of this research is to examine the radial distribution of the strength and structure of intracluster magnetic fields. These fields cannot be directly observed (see § 2.4), and are generally probed through their Faraday effects on polarized radiation propagating through the magneto-ionic cluster medium.

This thesis relies primarily on compact polarized radio sources to probe the intracluster magnetic fields at a variety of cluster impact parameters. Although the X-ray emitting intracluster medium generally extends to ~ 2 Mpc from the cluster center, currently available levels of sensitivity in radio astronomy are such that a particular galaxy cluster rarely has more than one or two strong polarized radio sources located (in projection) within its perimeter. There is, therefore, an insufficient density of sources on the sky to undertake a detailed probe of the radial Faraday distribution for individual clusters with the current VLA in a reasonable integration time. Thus the Faraday distribution must be studied through a large sample of radio sources viewed along the line of sight to a number of galaxy

clusters.

3.2.1 Target Planning

Compiling a statistical sample of objects requires careful consideration of source properties in order to build a database of a uniform population of targets. For the purposes of this thesis, the target cluster population was selected from rich, low redshift, weak or non-cooling flow Abell clusters. The parameter space selected for this research was optimized to provide a subset of clusters which would have the best possibility of tracing the intracluster magnetic fields from the central regions of clusters to the outer edges of the X-ray emitting gas. Radio sources probing the central regions of strong cooling flow clusters were avoided since these regions have been fairly well studied (Taylor & Perley 1993; Ge & Owen 1994; Taylor et al. 1999), and can be used for comparison purposes.

Another issue is the realistic availability of telescope observing time. As discussed in § 2.4.3, Faraday studies require polarimetry observations at three or more wavelengths in order to unambiguously determine the source rotation measure. Although the VLA is capable of recording two simultaneous wavelengths within a single observing band, it is still time consuming to add the extra observing time for each supplementary pair of wavelengths (six wavelengths in total for most observations in this work). Additional observing time must also be allocated for calibration at each of the observed wavelength. For polarimetry, calibrations generally total an extra 30% overhead on the observing time. In order to maximize the scientific use of observing time, the NRAO VLA Sky Survey (NVSS) was used to preselect polarized radio source targets for the follow-up polarimetry. This step eliminated the need to undertake an initial snapshot survey to find the polarized targets.

The NVSS survey (Condon et al. 1998), begun in September 1993, is a radio continuum survey which covers the entire sky north of $-40°$ declination, at a frequency of 1.4 GHz. The survey consists of a set of over 200 000 overlapping snapshots[2], and has a resolution of $45''$. The principal survey products are a set of $4° \times 4°$ continuum data cubes which contain image planes of Stokes I, Q, and U, a survey catalog of discrete radio sources, and a calibrated u-v data set. In the context of this thesis, it is important to point out that the NVSS is unique in that it is the only radio survey to date that provides simultaneous polarimetry

[2]A VLA observation with an integration time of less than 5 minutes is termed a snapshot.

of all target sources. The total intensity images have r.m.s. brightness fluctuations of order $\sigma_I \simeq 0.45$ mJy beam^{-1}, while the Stokes Q and U images have $\sigma \simeq 0.29$ mJy beam^{-1}. The survey was undertaken in stages during D-configurations between 1993 and 1997, when most of the final coverage gaps were filled. All NVSS data products were made publicly available as they were verified.

General Outline of Target Selection

The development of the radio source target list proceeded in several stages which are briefly outlined in this section. The basic procedure involved compiling a list of galaxy clusters which were observed by ROSAT, then selecting polarized radio sources which are viewed through these clusters. A more detailed description of the complete radio source target selection process, including details of the selected source parameter space, follows the target outline.

1. An initial list of all potential target clusters was compiled from the Abell (1958) and Abell, Corwin & Olowin (1989) cluster lists. This preliminary target list contained all high Galactic latitude clusters ($|b| > 20°$) which have known redshifts below z=0.1.

2. This cluster list was then compared to the ROSAT All Sky Survey, and ROSAT Pointed Source catalogs to produce a secondary subset list of high X-ray flux clusters. At this stage, the X-ray emission from each cluster was also analyzed for the presence of extended soft X-ray emission (indicating an intracluster medium). Any cluster showing only compact, active galactic nuclei- (AGN) type X-ray emission was excluded from the secondary list.

3. The secondary cluster list was then cross-correlated with the positions of the currently complete NVSS fields to provide a final list of all potential clusters falling within these completed radio fields. In the initial stages of this work, the available fraction of the sky for target selection was very small as only a fraction of the NVSS data products had been verified and released. Figure 3.1 shows the fields publicly available at the end of September 1995 which were used to select the targets for the October 1995 observing run.

4. The NVSS maps were then used to extract a list of all the strong ($I_{1.4} > 100$ mJy),

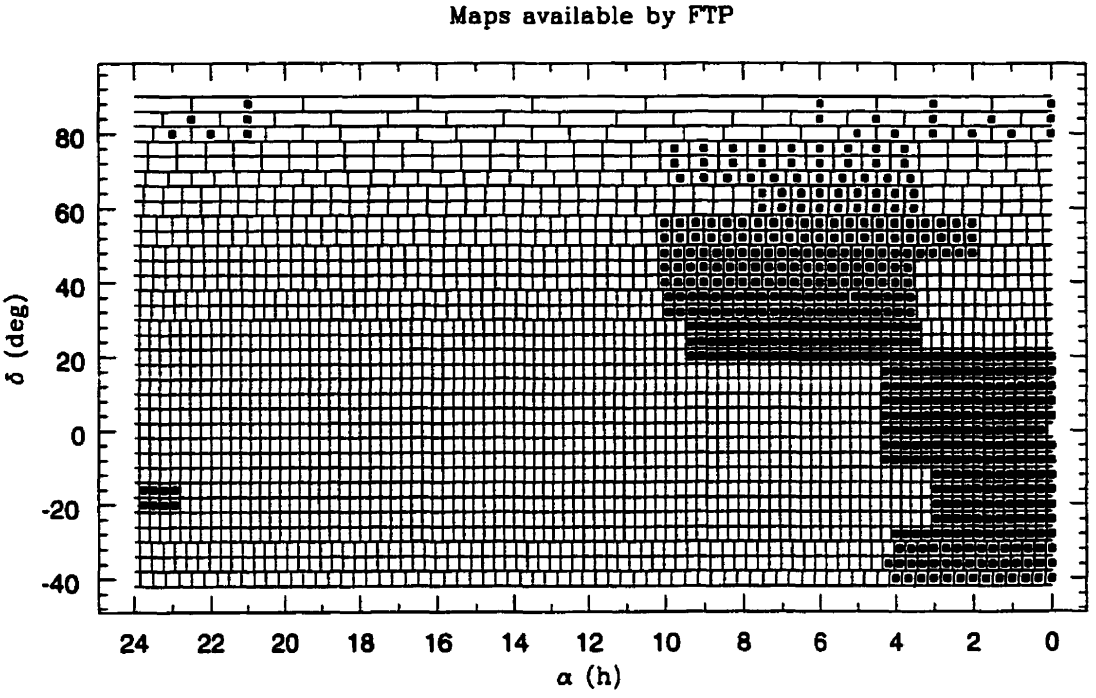

Figure 3.1: Gridded right ascension α and declination δ plot of the survey region to be covered by the NRAO VLA Sky Survey (NVSS). Each gridded element represents one 4° x 4° map. The elements that contain a filled in region represent NVSS fields that were verified and publicly available at the end of September 1995, just before the first observing run for this thesis. The figure is taken from NRAO's NVSS website.

linearly polarized (P > 1%) radio sources that are viewed through the intracluster gas. This list, referred to as the **cluster** list, generally contained one or two target sources per cluster. A second list of radio targets with similar total intensity and polarization fractions was selected to include sources at larger radii around each cluster. This list is known as the **control** list, and contains the radio targets which will be used to verify the Galactic rotation measure corrections as well as provide a "baseline" for the intrinsic scatter in the rotation measure of sources which are not viewed through a dense intracluster medium.

5. Finally, a list of target radio sources for the observing session was selected from the **cluster** list to provide a fairly uniform distribution of radio sources probing impact parameters from the cluster core regions to the edge of the X-ray emitting gas (~ 2–4 Mpc, Böhringer 1995). Further, a subset of radio sources around each cluster was selected from the **control** list and added to the target lists for each observing

run. Tables 5.6 and 5.7 present the positions and identifications for the **cluster** and **control** samples, respectively.

The goal of the target selection was to produce a follow-up target list of radio sources which could be used to radially probe magnetic fields from the central regions to the outskirts of a uniform sample of galaxy clusters. The **control** list of radio galaxies provides both a measure of the scatter in intrinsic source properties, as well as a measure of large-scale Galactic Faraday features which may exist in the direction of the galaxy cluster. These **control** sources could then be used to correct for any Galactic contamination which may be present in the Faraday rotation of the **cluster** sources (see § 5.4).

Source Details

Radio galaxy probes selected for this Faraday analysis must be particularly radio bright to permit the use of the VLA in snapshot mode. As discussed below (§ 3.2.2), snapshot observations involve integration times of less than five minutes at the VLA. To determine a minimum acceptable total intensity flux density for target sources, consider the theoretical noise reached in a 5 minute snapshot with 27 antennas at the VLA. The expected r.m.s. noise level due to thermal fluctuations in a full synthesis observation can be calculated from the following formula:

$$\sigma_I = \frac{K}{\sqrt{N(N-1)N_{IF}\Delta T_{\rm int}\Delta\nu}} \quad \text{mJy beam}^{-1} \tag{3.2}$$

where N represents the number of individual interferometer elements, N_{IF} is the total number of IFs to be combined in the final image, $\Delta T_{\rm int}$ is the total on-source integration time in hours, and $\Delta\nu$ is the effective continuum bandwidth in MHz. The system constant, K, expressed in terms of system temperature ($T_{\rm sys}$), and antenna efficiency (η_a) is given by

$$K = \frac{0.12 T_{\rm sys}}{\eta_a} \tag{3.3}$$

which yields 8.0 and 7.8 for the 20, and 6 cm bands respectively (Perley 1998). For a 5 minute on-source integration of a radio source with all VLA antennas (N=27), at 20 cm, a bandwidth of 25 MHz, and two IFs combined in the final image, Equation 3.2 predicts a theoretical noise level of 0.15 mJy beam^{-1}. To obtain a minimum signal-to-noise level of

10, the peak polarized intensity of the radio source must be greater than 1.5 mJy beam^{-1}. A typical extragalactic radio source at 20 cm is generally found to be polarized at the few percent level (Wright 1973), thus a peak polarized intensity of 1.5 mJy beam^{-1} on average corresponds to a peak total intensity of 50 mJy beam^{-1}. This minimum peak intensity flux estimate is actually a best case scenario since snapshot observations rarely reach theoretical noise level due to confusion. Analysis of the NVSS fields predicts $\sim$ 1 source per cluster at this flux level.

3.2.2 Observing Considerations

The majority of the observations for this thesis were undertaken in one of the compact VLA configurations to provide full sensitivity to large scale structure for the target radio sources with a single observation. The multi-wavelength observations were undertaken in a single epoch of observing. This method of simultaneous wavelength coverage provides a sample of sources which are uncontaminated by intrinsic variability. In addition, the selection of fairly powerful radio galaxies for this analysis provides sufficient signal to noise to use the snapshot mode of observation at the VLA.

Snapshot Mode

With its 'Y' configuration of 27 antennas, the VLA can produce a reasonable synthesized beam within a very short integration time. Although the beam contains fairly high sidelobes, it is possible to use the snapshot mode to observe relatively bright, unconfused sources with integration times as short as one minute. Unfortunately the high sidelobes severely limit the sensitivity in the compact arrays, at long wavelengths, due to confusion with bright off-center sources. An additional problem associated with the sparse u-v coverage of the snapshots is the restricted range of angular sizes which are recoverable. In order to correctly reconstruct the true sky brightness distribution, the u-v plane must be sampled sufficiently to satisfy the sampling theorem. Both the high confusion noise level, and restricted angular sizes can be reduced by splitting observations into two or more snapshots separated by at least one hour. This technique takes advantage of the Earth's rotation to fill in a larger fraction of the u-v plane. Figure 3.2 shows the typical u-v snapshot coverage for radio sources at 20 cm and 6 cm for each of the VLA arrays used in this survey. The largest baselines determine the resolution of the array in the image plane, and the shortest baselines

determine the scale of the largest structure which a particular configuration will be sensitive to.

Short observing runs make it very difficult to determine the proper instrumental polarization calibration properties. Polarization calibration requires several observations of a polarization calibrator over the course of the observing run. The parallactic angle of the polarization calibrator must change by more than 90° over the observing session (see § 3.3.3 for details). This parallactic angle requirement constraints the observing runs to extend over at least three hours.

Specific Strategy

To compensate for the sparse u-v coverage of snapshot observations, all radio source integrations were split into two snapshots, separated by at least one hour, and optimally as close to two hours as possible. The u-v coverage of these split hour angle snapshots can be seen in Figure 3.2. Although splitting the on-source time made planning the details of the observing schedule more difficult, it greatly enhanced the sensitivity of the final data through increased sampling of the u-v plane. Due to the short antenna move times between sources within a single cluster (generally covering 1° on the sky), observations were designed to point at all sources in the vicinity of a cluster, then move on to several other clusters before returning for the second snapshot pass at a different hour angle. Each individual pointing cycled through all observing frequencies during each snapshot. Through this technique, observations maximized the use of telescope time for polarimetry of a large sample of target sources of varying morphologies, while also maximizing the output signal-to-noise on each source.

As discussed in § 2.4.3, the degree of rotation of the position angle of linearly polarized radiation depends on the product of the rotation measure (RM) and the wavelength squared. The wavelength selection for these observations was designed to provide both closely spaced points in wavelength squared space to constrain $n\pi$ ambiguities, and widely spaced points in wavelength squared space to pin down an accurate rotation measure. Based on these requirements, and the VLA's ability to simultaneously observe two wavelengths within an observing band, observations undertaken in 1995 covered two wavelengths in the 20 cm band and two wavelengths in the 6 cm band. Subsequent analysis of that data showed that there was contamination from radio frequency interference (RFI) in at least one of the

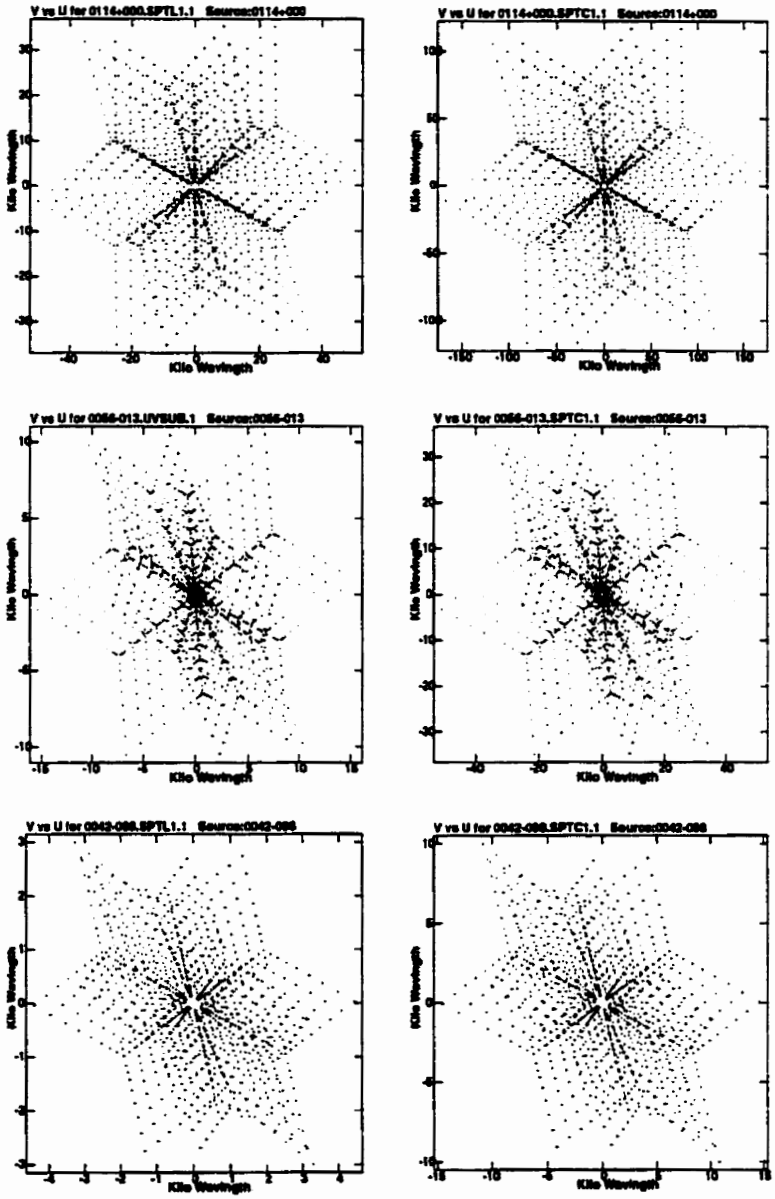

Figure 3.2: Typical u-v coverage for split hour-angle VLA snapshots. The left panels from top to bottom show the snapshot coverage at 20 cm in B, CS, and D arrays respectively. The right panels display the 6 cm u-v coverage for each array.

20 cm wavelengths for much of the observing run. This RFI resulted in significant data loss and large errors on the extracted rotation measures in this observing session. Further observing runs in 1996, and 1997 were designed with four wavelength coverage in the 20 cm band, and two in the 6 cm band to minimize the impact of time-variable interference in one or more bands. Table 3.1 summarizes the configurations, run lengths, cluster targets and calibrators used in this work. Individual cluster details and calibration procedures are described elsewhere in this thesis.

Date	Config	Obs. Length (Hours)	Target Abell Clusters	Polarization Calibrator(s)	Phase Calibrators (J2000)
09Oct95	B	10	A168, A399, A400, A401, A576	3C48, 3C286	0059+001, 0242+110, 0259+077, 0238+166 0735+478
21Dec95	B	10	A119, A194, A569 A576, A779	3C48, 3C286	0059+001, 0713+438, 0614+607, 0920+446
04Aug96	D	12	A85, A496, A1185	3C138, 3C286	0059+001, 0423-013, 1125+261
05Aug96	D	8	A76, A147, A754, A1314	3C138, 3C286	0022+002, 0108+015, 0902-142, 1219+484
08Aug96	D	8	A76, A147, A754 A1314	3C138, 3C286	0022+002, 0108+015, 0902-142, 1219+484
16Sep97	CS	12	A75, A119, A194, A262, A376, A426, A1060, A1367, A1383, A2247	3C138, 3C286	0029+349, 0059+001, 0137+331, 0237+288, 0303+472, 1018-317, 1150+242, 1146+539, 1800+784

Table 3.1: Observing dates, configurations, Abell clusters, and calibrators for each of the observing session for this thesis. Observations undertaken in 1995 involved two wavelengths around 20 cm, and two around 6 cm. The remainder of the observations involved four wavelengths around 20 cm, and two around 6 cm.

Wavelength Coverage

The Faraday rotation measure (RM) can be written in terms of observational parameters as:

$$RM = \frac{\Delta\chi}{\lambda^2} \quad \text{rad m}^{-2} \tag{3.4}$$

where $\Delta\chi$ is the position angle through which the polarized emission has been (Faraday) rotated at wavelength λ. Through observations at three or more carefully selected wavelengths, Equation 3.4 can be used to recover the rotation measure introduced along the line of sight between the source of the polarized emission and the observer.

For the purposes of this research, polarimetry has been undertaken at wavelengths ranging between 20 cm and 6 cm. Specifically, during the first observing session, polarimetry

was undertaken at 21.978 cm, 18.018 cm, 6.615 cm, and 6.141 cm. As discussed above, radio frequency interference was fairly severe in one data set (18 cm), and resulted in significant data loss in most sources at this wavelength during the first observing session. Attempts to determine the best fit rotation measure for the remaining three wavelengths showed that the resulting fits had fairly large associated errors. Based on these findings, subsequent observing sessions relied on four wavelengths in the 20 cm band (21.978, 20.906, 20.478, and 18.072 cm), and two wavelengths in the 6 cm band (6.615, and 6.141 cm). The complete wavelength coverage permits the *unambiguous* determination of the rotation measure of target sources up to a maximum of 2600 rad m^{-2}, well above the expected Faraday rotation outside of the cooling cores in galaxy clusters.

Calibration Strategy

Radio polarimetry observations require three to four individual sets of calibrators. The observational setup for each calibration step, as applied to observing runs for this thesis, is briefly outlined below. The application of the calibration solutions is discussed in § 3.3.

1. **Absolute flux:** Absolute flux calibration requires at least one observation of a primary flux calibrator at each wavelength during each observing session. The primary flux calibrators for the VLA are 3C295, 3C48, 3C286, 3C147, and 3C138. Although 3C286 was used as the primary flux calibrator for each observing run, observations of 3C48, or 3C147 were also generally undertaken during the observing session. These extra calibrator observations served both as a backup in case of the loss of 3C286, as well as a redundancy check on the flux calibration.

2. **Phase referencing:** Proper phase calibration requires frequent observations of a calibrator source which is located near the target source, preferably close enough to be within the same isoplanatic patch. Unfortunately there is no *a priori* way to estimate the size of the isoplanatic patch on any given day, or at any given time. The phase calibration strategy undertaken for this thesis was to select a phase calibrator near each galaxy cluster. These calibrators, listed in Table 3.1, are generally located within ten degrees of the target cluster. Observing runs were designed to bracket the cluster radio sources in the CALIBRATOR-TARGETS-CALIBRATOR sequence such that all target sources (**cluster** and **control**) were located between observations of

the cluster's phase calibrator, and the maximum time between observations of the phase calibrator was approximately 30 minutes.

3. **Feed polarization:** Due to polarization leakage, the measured polarization of a source will be a sum of the source polarization plus an instrumental term. Observations of a calibrator source which covers more than 90° of parallactic angle can be used to separate source and instrumental polarization terms. The requirement for a large parallactic angle coverage places constraints on the length of a particular observing session: generally polarimetric observing runs require at least 3 hours to provide the parallactic angle coverage to determine the instrumental polarization calibrations. Observing sessions undertaken for this thesis spanned an average of 10 hours per session. These long sessions covered observations of several galaxy clusters, and provided the parallactic angle coverage necessary to determine the instrumental polarization terms.

4. **Calibration of the origin of position angle:** Phase referencing calibration provides independent calibration of the right- and left-handed receiver systems and thus leaves a systematic phase difference between the two orthogonal polarization systems. This phase offset is determined through calibration on a source of known polarization properties. This calibrator source is generally observed once or twice during each observing session. The recommended R-L/L-R phase (or absolute polarization angle) calibrators for the VLA at frequencies of interest to this thesis are 3C286 and 3C138, although 3C48 is also available for wavelengths of 6 cm and shorter. Since 3C286 was observed during each session as a primary flux calibrator, it was also used as the R-L/L-R phase calibrator. Due to the importance of proper polarization calibration for this thesis, one of 3C138 or 3C48 was also generally observed during each session, particularly during the interval when 3C286 was not available. These redundant calibrators provided the opportunity to monitor the stability of the right minus left phase through each observing session.

3.3 Data Reductions

All imaging, deconvolution, and calibration were undertaken within the NRAO Astronomical Image Processing System (AIPS). The major steps in the data reduction process are

briefly described below with specific references to the AIPS tasks employed.

3.3.1 Absolute Flux Calibration

The absolute flux density scale for an observing run is determined through observations of an unresolved reference source, of known brightness, at all observed frequencies. The standard flux density scale for calibrator sources is the Baars et al. scale (Baars et al. 1977), although careful measurements in the VLA's D configuration show that these coefficients are slightly in error. The follow-up calibrator measurements, undertaken by Perley & Taylor (1996), provide an updated set of calibrator coefficients. For the purposes of this thesis, all flux densities are tied to the 1995.2 epoch calibrator coefficients.

The absolute flux calibration for all observing runs undertaken for this thesis was determined through observations of 3C286 or 3C48. Both of these primary calibrators are unresolved at 20 cm and 6 cm in the compact configurations but require special restrictions to be placed on the u-v range for proper flux bootstrapping in the more extended VLA configurations (see Perley & Taylor 1996). Although these sources are well studied, and their flux densities are fairly well known, recent measurements (Ott et al. 1994) indicate that 3C48 is variable, and in fact has become brighter at short wavelengths. In contrast, 3C286 does not show variability in excess of ~1% over the last couple of decades, thus, wherever possible, 3C286 was used as the absolute flux calibrator with 3C48 employed for redundancy checking. The best current estimates of the calibrator coefficients can be determined through the analytic expression:

$$\log S = A + B \times \log \nu + C \times (\log \nu)^2 + D \times (\log \nu)^3 \tag{3.5}$$

where S is the flux density of the source in Jy and ν is the frequency in MHz. The 1995.2 epoch constants for the two calibrators of interest are listed in Table 3.2.

Calibrator	A	B	C	D
3C48	1.16801	+1.07526	-0.42254	+0.02699
3C138	1.97498	-0.23918	+0.01333	-0.01389
3C286	0.50344	+1.05026	-0.31666	+0.01602

Table 3.2: Calibrator constants determined by Perley & Taylor (1996) for the 1995.2 epoch.

The absolute flux density scale for a VLA observing run is set using the AIPS task SETJY

on the primary calibrator. In addition to the primary calibrator, observing programs also include secondary calibrators for purposes of phase calibration and polarization calibration. The program CALIB is used to determine the antenna gain solutions for both the primary and secondary calibrators. Once the best set of gain solutions is found (generally through an iterative process of calibrating and data editing), the task GETJY is used to determine the flux density of the secondary calibrators from the flux density of the primary flux calibrator and the antenna gain solutions. These calibrator solutions can then be interpolated through the target sources to determine the target source flux densities on the absolute flux scale.

3.3.2 Phase and Amplitude Calibration

Amplitude and phase variation of radio antennae are due to a combination of slowly varying instrumental effects and more rapidly varying atmospheric propagation effects. The instrumental variation is fairly easy to correct through calibration but, as discussed in § 3.2.2, proper calibration of atmospheric effects requires that the calibrator be located in the same isoplanatic patch as the program source. The phase calibrators are therefore selected as close to the program sources as possible (generally within 10°).

All phase calibrators observed for this research are listed in Table 3.1 and were selected from the VLA Calibrator Manual (Perley & Taylor 1996). Since the Abell clusters are spread over a large range in right ascension, it was necessary to select a separate phase calibrator for most clusters. During the observing sessions, the phase calibrators were observed for a few minutes every half hour, and scheduled so that they bracketed all target sources for the cluster of interest.

3.3.3 Polarization Calibration

There are two aspects to consider in polarization calibration for VLA observing sessions. The first calibration addresses the non-ideal response of the antenna feed system. Any particular feed will respond to polarizations other than the nominal one, adding a spurious instrumental response to the source term. The second aspect of polarization calibration is designed to calculate the phase difference between the two orthogonally polarized antenna feeds. This R-L phase difference results from the fact that the phase referencing calibration (described in § 3.3.2) is determined independently for each of the parallel hand systems, which allows for an arbitrary offset between the two systems. This offset term is not

important for total intensity observations since Stokes I only depends on the parallel hand correlations, but, as seen from Equations 2.62, the polarized Stokes parameters (Q and U) depend on the correlation of the cross-hand components, so any phase offset between these systems must be removed for polarimetry. Both aspects of polarization calibration are discussed in more detail below.

Instrumental Leakage Terms

In practice, an antenna feed will respond to polarizations other than the nominal one. This polarization leakage is parameterized through the D terms in Equation 2.66, which represent the instrumental leakage into the opposite orthogonal polarization. In the limit of weakly polarized sources and near perfect feed/antenna combinations, the second order terms in D can be ignored to produce Equations 2.69.

The instrumental polarization term will add vectorially to the source polarization terms, as shown in Figure 2.5. For altitude-azimuth mounted antennas like the VLA, the source and instrumental polarizations can be separated due to varying parallactic angle. As the antennas track a source through different parallactic angles, the component of the interferometer response from the radio source will rotate, while the instrumental term will remain constant. Calibration of the instrumental leakage terms normally requires observations of a calibrator source which spans more than 90° in parallactic angle, in order to separate the source and instrumental terms.

Many observing programs are able to make use of the phase calibrator for calibration of the instrumental term, as the only requirements on the calibrator are that the source be unresolved and observed over more than 90° in parallactic angle. Due to the nature of the observations for this thesis, there are several different phase calibrators observed through each session, although none cover the desired parallactic angle range. It was therefore necessary to include a parallactic angle calibrator into each observing session, to be observed at each frequency. The effective feed parameters for each antenna were determined using the AIPS task PCAL. These feed parameters are then applied to the data during the imaging stage.

R-L Phase Calibration

The phase referencing procedure described in § 3.3.2 relies on independently referencing all right- and left-hand antenna phases to that of a single *reference* antenna. The underlying assumptions of this technique are that the phase difference between the two orthogonal systems is stable over time for the reference antenna, and that the complex gain terms of the other antennas are determined with sufficient frequency that any time-variable phase changes can be calibrated out. In this case, the calibration of the right-left (R-L) phase offset is determined through a single observation of a calibration source, with known Stokes parameters (I, Q, U, and V), which provides a measure of the relative phase between the orthogonal systems for the reference antenna.

In selecting a reference antenna for phase referencing, it is important to first check the overall R-L phase stability of the antenna over the entire observing period. The R-L phase stability of any antenna has been found to be fairly good over a period of up to twelve hours. During this period one can expect to find phase changes of around 10°. The exception to this R-L phase stability is seen as a phase jump in an antenna which is visible as a discontinuous change in the antenna R-L phase, and can result in phase differences of over 100°. Antennas displaying these R-L phase jumps must be excluded from the list of possible reference antennas.

Correction of the phase offset between the right- and left-hand systems was determined for calibration observations of 3C286. During each observing run, this source was observed at two different hour angles for each wavelength. After applying standard total intensity calibration procedures (§ 3.3.1 and § 3.3.2) to the data, the scan-averaged right minus left phase angles for 3C286 was examined for signs of any large phase differences, indicating corrupted data. Once all corrupted data had been removed, and any necessary calibration steps had been re-applied, the average right minus left phase angle was determined for each of the calibrator scans. These measurements of the phase difference were then averaged to determine the phase offset term. The phase offset correction was then calculated from the expected value (66° for 3C286) minus the measured phase values. This correction was applied to all sources in the observing run using the task CLCOR.

After application of the phase correction, a visual inspection of the right minus left phase matrix for 3C286 revealed phase variations of order 2°. For cases where the phase

fluctuations were significantly larger than this, the data was further edited and re-calibrated. Once the final right-left phase calibration stage was completed, the phase stability through the night was examined by comparing the measured and expected phases for 3C138. The total amplitude of the fluctuations of the matrix-averaged phases about the expected value were generally found to be less than 5° at both the 20 cm, and 6 cm bands. The matrix-averaged phases of 3C138 after right-left phase correction are shown in Table 3.3.

Time	Frequency (MHz)					
UT	1365	1435	1465	1660	4535.1	4885.1
	AC461 — August 4, 1996					
11:23	-25.8	-23.9	-24.9		-24.3	-23.4
	SUNRISE					
12:52	-25.4	-23.3	-22.7		-26.2	-22.6
14:28	-23.6	-22.6	-21.2		-26.9	-22.2
15:36	-20.8	-20.3	-19.6		-21.3	-20.8
17:25	-19.5	-18.4	-18.9		-24.1	-21.7
19:45	-18.9	-17.0	-19.0		-21.1	-20.3
	AC461 — August 5, 1996					
11:20	-23.5	-23.0	-22.1		-27.0	-24.1
	SUNRISE					
13:44	-21.0	-21.1	-18.3		-24.4	-23.0
14:52	-14.3	-15.0	-16.5		-26.8	-24.0
17:14	-15.4	-15.0	-14.7		-22.5	-22.8
18:47	-15.1	-16.5	-15.5		-25.1	-20.0
	AC461 — August 8, 1996					
11:08	-16.5	-18.0	-20.8	-20.7	-21.1	-23.2
	SUNRISE					
13:28	-15.7	-17.4	-18.7	-19.4	-18.6	-22.3
14:43	-16.5	-16.5	-17.7	-18.3	-25.6	-26.5
16:36	-15.5	-17.8	-15.6	-15.7	-25.7	-23.6
18:31	-16.2	-16.9	-15.4	-16.9	-25.9	-22.9
	AC483 — September 16, 1997					
07:46	-23.7		-24.2		-24.5	-21.7
09:28	-23.8		-24.6		-20.2	-18.9
11:44	-23.8		-22.8		-22.2	-22.7
	SUNRISE					
13:58	-19.5		-20.1		-23.0	-20.7
16:06	-18.7		-18.8		-21.1	-19.2
18:25	-19.5		-18.6		-22.3	-19.2

Table 3.3: Calibrated position angles for 3C138. Errors in the matrix-averaged position angles listed are 0°.1 for each time and frequency.

3.3.4 Ionospheric Faraday Rotation

At heights between 50 and 300 km in the Earth's atmosphere solar ultraviolet rays and X-rays dissociate molecules such as oxygen and nitrogen to produce a layer of free electrons called the ionosphere. In this region, peak electron densities can reach 10^6 cm^{-3}. As the polarized source signal passes through the Earth's atmosphere on its way to the radio telescope the magneto-ionic plasma in the ionosphere will rotate the plane of polarization of the incident radiation through the Faraday effect (see § 2.4.3). This ionospheric Faraday rotation will be seen as a source- and time-variable right-left phase difference.

The amount of rotation depends on the path length through the ionosphere, the free electron density, and the longitudinal component of the Earth's magnetic field in the direction of the radio source. The Faraday rotation induced for a particular source will therefore vary strongly with observing geometry. The ionospheric Faraday rotation also shows diurnal variations due to solar heating effects on the free electron density, and is also affected by the solar cycle. Near times of solar maximum, the ionospheric Faraday rotation can reach levels of tens of radians m^{-2}. At $\lambda = 20$ cm this can amount to a rotation in the position angle of linearly polarized emission of up to 50°.

Observations for this thesis were undertaken between October 1995 and September 1997. During these observing sessions, ionospheric Faraday rotations were expected to have been fairly small as solar minimum occurred around July 1996, and the next solar maximum is predicted to be in late 2000 or early 2001. During this time of fairly low solar activity, a correspondingly low ionospheric effect of a few radians m^{-2} is expected (Perley, private communication). For the observations near 20 cm this corresponds to a polarization angle rotation of around 6°, while at 6 cm this effect results in less than 1° of rotation.

Until fairly recently, the ionospheric contribution to the rotation measure at the VLA could be determined through the AIPS task FARAD. This task relies on total electron count (TEC) information from the (nearby) Boulder ionospheric monitoring station to determine the ionospheric rotation measure during a particular observing session. Unfortunately, as of 1992, the TEC data are no longer available from Boulder. FARAD also provides the flexibility of determining the ionospheric rotation measure from an empirical model using the monthly mean Zurich sunspot number. This empirical model is very crude, however, and was not applied to the data as it was found to provide limited information for times

near solar minimum.

A more appealing approach to determining the ionospheric rotation measure during observations involves the use of recently installed Global Positioning System (GPS) receivers at the VLA site. The receivers measure GPS delay information between adjacent GPS channels during an observing session. The AIPS tasks LDGPS and GPSDL are then used to load the delay data and calculate the ionospheric rotation measure using a simple model that takes the TEC measurement at the zenith, and models the sky TEC distribution assuming a linear gradient is present. Unfortunately, due to technical difficulties beyond the control of the observers[3], the GPS delay data were unavailable during the observing sessions for this thesis.

In the absence of TEC data for the VLA, the presence of variable Faraday rotation was constrained through the redundant polarization angle observations of 3C138. Table 3.3 shows the mean polarization angle at each frequency during observations of 3C138, which were undertaken approximately every two hours during the observing sessions. The table also indicates the times of sunrise, when large fluctuations are expected in the ionospheric electron densities, and hence large associated phase differences. The expected polarization angle of 3C138 is $-18°$. Through the night, the variation in the calibrated polarization angle was generally less than 5°, completely consistent with the predicted ionospheric effects of 6° or less during solar minimum. The polarization angle variations at C-band were found to be generally below 5°($|RM|< 20$ rad m^{-2}). These ionospheric contributions result in errors of $< 10\%$ in the RMs of sources viewed through the central regions of galaxy clusters.

3.4 Imaging

The calibration procedures described in § 3.3 produce a final set of completely calibrated u-v data which can then be imaged. The basic premise behind imaging is that the visibilities and the true sky brightness distribution form a Fourier pair, thus permitting the recovery of the sky brightness distribution from Equation 2.48.

Although it is not within the scope of this work to give a detailed treatise on the imaging process, a brief outline of the basic procedure is given below. A detailed description of the

[3]A severe lightning strike in 1997 disabled the GPS receivers as well as the computer containing the stored delay data.

imaging process can be found in Sramek et al. (1994), and references therein.

3.4.1 Deconvolution

Ideally the u-v plane would be completely and uniformly sampled across all baselines relevant to the structure present within the radio source of interest. A Fourier inversion of these measured visibilities would produce an ideal image of the source containing information at all spatial frequencies while simultaneously being free of image defects. Unfortunately, such an ideal instrument would be prohibitively difficult to construct for all radio frequencies and sources of interest.

The next best approach is to use an interferometer to sample the u-v plane. Unfortunately the process of sampling of the u-v plane results in the loss of spatial information due to missing baselines (*e.g.* the unsampled central region of the u-v plane), as well as image defects due to the non-uniform sampling. As discussed in § 2.5.1, the image recovered from the Fourier transform of the sampled visibilities is known as the *dirty image*. This image is simply a convolution of the true image with the *dirty beam* (Equation 2.50). Fortunately, the precise shape of the *dirty beam* is known from the sampling function, thus the effects of the beam can be corrected for through routines that attempt to interpolate for the missing u-v samples.

The deconvolution routine used for all data in this research was the CLEAN algorithm (Hogbom 1974). This algorithm attempts to describe the image as a set of delta functions convolved with the *dirty beam*. Briefly, the CLEAN routine searches the image for positive and negative peaks, and subtracts a *dirty beam* of suitable amplitude centered on the peak. This process removes the sidelobes of this peak from the map, and reveals other sources within the map, if present. This iterative process of removing the peaks from the map is continued until some user defined threshold is reached. At this point, the final map is reconstructed by adding the components convolved with the point-spread function (*clean beam*) back into the map. A detailed description of the deconvolution process and the associated routines is given by Cornwell & Braun (1994).

3.4.2 Self-Calibration

The deconvolution routine described above will produce final images that are often sufficient for scientific analysis, however these images will still be limited by residual phase and

amplitude errors which serve to lower the dynamic range of the image. These residual errors are due in part to the fact that the external calibration of atmospheric phase and amplitude fluctuations, discussed in § 3.3.2, is only effective if the target source and calibrator fall within the same atmospheric cells. As was previously mentioned, calibration based on a source that does not fall within the same isoplanatic patch as the target source can actually serve to deteriorate the target signal since the atmospheric variations traced by the calibrator will not be following those induced in the target source. For high dynamic range imaging, the most reliable method to remove the effects of the residual atmospheric fluctuations is to calibrate the phase and amplitude based on the target source itself, *self-calibration* (Pearson & Readhead 1984).

Self-calibration can only be undertaken for very bright sources as it requires the data to have a high signal to noise on very short time intervals so that the antenna gains can be determined on time scales similar to that of the coherence time of the atmospheric screen, τ_{atm}. The r.m.s. noise in the determination of the phase gain for a single VLA antenna using self-calibration on a point source is given by

$$\phi_{rms} = \frac{13\Delta S}{S_{sc}\sqrt{\Delta\nu\tau_{sc}}} \quad \text{degrees}, \tag{3.6}$$

where ΔS is the sensitivity in Jy $s^{-1}MHz^{-1}$, S_{sc} is the flux density of the source in Jy, $\Delta\nu$ is the observing bandwidth in MHz, and τ_{sc} is the averaging time used in the gain solutions. In general, self-calibration will improve the data if $\phi_{rms} \ll 60°$ on timescales of $\tau_{sc} = \tau_{atm}$. Once new antenna gain solutions are determined they are then applied to the source data, and a new, hopefully improved, image is formed. This improved image can then be used in the iterative process of self-calibration and imaging until the solutions no longer improve on the previous iteration.

For the purposes of this thesis, iterative self-calibration was applied to all target sources. The AIPS task SCMAP was used to undertake multiple iterations of self-calibration and imaging. The self-calibration routine was restricted to phases only, as tests on amplitude self-calibration did not reveal improvements in the final output map's signal to noise ratio; in fact the signal to noise generally deteriorated after amplitude self-calibration. In general, convergence was found after three phase-only self-calibration loops. Following each self-calibration loop, the clean component table was merged so that all clean components

corresponding to a given position were summed in the final table. The next self-calibration loop was then restarted using all merged components that were brighter than 8 times the r.m.s. residual of the previous CLEAN. In addition to these constraints, acceptable self-calibration solutions were restricted to those with a signal-to-noise ratio greater than three. The final output u-v data set obtained from the self-calibration process is properly calibrated for all Stokes parameters.

3.5 Radio Source Fluxes

The deconvolution and self-calibration routine described above provides a final u-v data set where all Stokes images are fully calibrated. The Q and U maps were used to create the polarized intensity map, $P = \sqrt{Q^2 + U^2}$, which was corrected for the positive Ricean bias introduced by the quadrature combination of the two linear polarization maps (Wardle & Kronberg 1974). The AIPS task TVSTAT was then used to determine the I, Q, U, and P fluxes for each source. Tables 3.4 – 3.7 present the total intensity and polarized fluxes (in mJy), where measurable, for the sources at each of the observed wavelengths. Although all sources were observed at all wavelengths, the presence of time- and location-variable radio frequency interference occasionally resulted in a loss of data at one or more wavelengths in the 20 cm observing band. Additional loss of data occurred in the 6 cm observing band are generally due to spectral index effects which reduced the polarized signal-to-noise to undetectable levels for a number of sources.

3.6 Summary

This chapter discussed the target selection, observations, and reductions of the polarized radio galaxies selected to probe the intracluster medium. Specific emphasis was placed on the planning of observing parameters and calibration strategy. Tables 3.3 to 3.7 summarize the basic angle calibration data, and list the flux density and polarization results for all sources and frequencies.

Source	S_{1365}	σ_S	S_{1665}	σ_S	S_{4535}	σ_S	S_{4885}	σ_S
	P_{1365}	σ_P	P_{1665}	σ_P	P_{4535}	σ_P	P_{4885}	σ_P
0108−006	922.45	2.66	886.14	1.66	640.84	0.71	621.70	0.73
	55.64	0.32	50.86	0.29	20.63	0.25	20.55	0.21
0113+024	500.08	4.18	529.32	2.74	680.76	0.86	691.23	0.90
	23.96	0.34	22.20	0.27	10.96	0.29	8.29	0.20
0114+000	341.93	1.97	305.55	1.77	161.06	0.90	158.55	0.93
	21.62	0.35	20.12	0.46	8.79	0.41	9.50	0.38
0115+000	36.89	0.67	38.40	0.69	13.53	0.43	7.16	0.24
	4.09	0.20	3.04	0.23	0.93	0.26	1.11	0.16
0125−000U	105.29	6.54	89.11	4.52	33.58	1.22	33.05	1.06
	10.28	0.43	7.88	0.44	3.56	0.32	2.90	0.30
0125−000L	52.97	5.37	50.09	3.84	21.12	1.07	19.14	0.85
	5.89	0.41	4.67	0.42	2.64	0.26	1.71	0.27
0238+049	114.51	1.42	92.18	1.64	38.94	0.68	34.59	0.47
	7.62	0.21	5.80	0.62	2.17	0.25	1.50	0.20
0251+062U	744.39	1.49	644.20	2.59	225.94	0.61	206.09	0.46
	81.45	0.31	62.18	0.35	21.48	0.27	20.11	0.27
0251+062L	297.48	1.40	252.81	2.39	72.05	0.45	65.60	0.36
	26.78	0.24	22.27	0.31	8.28	0.24	7.50	0.24
0257+130	45.66	0.20	45.21	0.21	34.45	0.43	33.33	0.38
	1.95	0.18	3.57	0.24	2.45	0.16	2.63	0.15
0259+008	335.29	2.51	277.61	3.38	96.58	1.47	76.51	1.02
	25.55	0.34	24.63	0.45	9.67	0.56	3.84	0.24
0259+077	667.86	2.23	680.26	1.06	629.82	0.47	620.87	0.46
	26.39	0.24	21.03	0.19	36.56	0.27	38.58	0.24
0259+139	692.46	3.68	584.49	2.90	233.96	1.14	218.59	1.25
	33.63	0.53	31.60	0.66	15.34	0.42	14.10	0.33
0301+074	745.28	2.68	640.38	2.46	293.93	0.98	275.69	1.11
	36.86	0.32	41.32	0.35	33.78	0.65	33.61	0.51
0305+056	109.78	2.61	81.37	2.30	35.93	0.60	70.59	1.04
	21.41	0.22	18.73	0.25	9.37	0.21	9.21	0.22
0318+053L	124.16	3.70	111.90	1.66	54.68	0.94	47.92	0.71
	10.10	0.30	10.40	0.42	1.03	0.15	1.18	0.16
0318+053R	40.95	2.21	77.77	1.81	20.31	0.53	14.43	0.37
	1.63	0.16	4.20	0.32	0.48	0.13	0.37	0.14
0723+548	92.58	0.86	77.99	0.81	33.68	0.51	32.02	0.53
	10.72	0.30	9.86	0.24	3.90	0.28	3.85	0.27

Table 3.4: Total intensity (S) and polarized (P) flux in mJy for each source at each wavelength obtained during the October 1995 observing session. The table also contains the errors associated with each flux measurement.

Source	S_{1365}	σ_S	S_{1665}	σ_S	S_{4535}	σ_S	S_{4885}	σ_S
	P_{1365}	σ_P	P_{1665}	σ_P	P_{4535}	σ_P	P_{4885}	σ_P
0048−022L	256.03	2.29	227.01	2.42	93.99	1.06	99.29	0.91
	10.46	0.51	10.01	0.56	3.49	0.24	3.57	0.24
0048−022R	34.08	1.22	41.81	1.76	...	...	10.21	0.44
	3.86	0.28	6.25	0.49	...	...	1.57	0.23
0049−027	1306.10	3.19	1106.10	2.52	374.23	0.68	351.38	0.77
	113.92	0.71	100.33	0.89	41.82	0.54	41.78	0.52
0050−033L	256.23	2.06	205.59	1.87	71.80	0.52	65.07	0.42
	12.93	0.20	14.01	0.27	7.15	0.21	7.09	0.21
0050−033R	152.87	1.86	126.59	1.69	37.87	0.42	38.26	0.52
	7.30	0.21	7.29	0.28	1.56	0.21	1.54	0.20
0052−011L	78.80	1.18	64.19	0.95	19.43	0.90	22.16	0.86
	6.08	0.22	4.98	0.31	1.54	0.20	1.73	0.20
0052−011U	78.28	1.04	66.39	0.94	25.60	0.80	24.67	0.80
	2.61	0.17	4.73	0.35	3.95	0.27	3.42	0.21
0057−013	4104.40	22.68	4981.00	27.69	...	...	...	...
	892.60	7.63	876.52	7.76	...	...	...	...
0106−019	689.55	1.44	664.24	1.34	485.75	0.65	475.04	0.69
	47.87	0.25	52.54	0.65	33.13	0.29	32.17	0.31
0122−063	328.50	2.74	283.24	2.50	123.53	0.73	110.76	0.55
	29.38	0.29	27.76	0.47	20.24	0.42	20.22	0.41
0125−001	1565.40	9.23	1646.70	8.05	1629.40	1.42	1612.50	1.51
	52.75	0.42	52.20	1.61	44.25	0.27	48.66	0.25
0139+015	1141.20	2.30	1062.30	3.06	520.57	1.45	480.70	1.07
	106.61	0.79	88.70	1.19	59.23	0.67	63.21	0.73
0654+503	434.16	2.31	370.40	1.89	137.33	1.83	119.86	1.42
	25.00	0.38	29.00	0.49	8.77	0.60	8.89	0.48
0658+492U	94.65	1.65	71.44	1.14	16.29	0.28	15.54	0.22
	9.36	0.28	9.20	0.33	1.34	0.18	1.35	0.18
0701+497	324.78	1.57	274.89	1.42	103.14	0.72	94.21	0.52
	18.38	0.32	17.82	0.31	7.24	0.40	7.38	0.39
0706+425B	546.75	10.97	400.67	8.59	50.72	0.92	49.71	1.31
	48.40	1.20	47.69	1.20	4.91	0.43	3.37	0.39
0709+486	282.16	2.19	259.85	2.25	153.24	1.03	125.19	0.47
	15.51	0.36	18.49	0.50	1.85	0.30	1.34	0.35
0712+565	199.06	1.09	169.03	0.75	66.54	0.74	61.36	0.66
	15.09	0.28	14.88	0.29	7.57	0.36	7.81	0.34
0713+488	544.86	2.44	448.02	1.69	168.22	1.29	153.91	1.06
	27.40	0.34	27.57	0.47	11.97	0.63	11.63	0.51
0713+579L	84.07	2.35	71.50	1.72	21.47	0.30	22.20	0.41
	2.98	0.18	4.76	0.23	3.19	0.19	3.48	0.18
0713+579R	182.87	2.01	161.39	1.62	60.93	0.37	57.82	0.35
	4.25	0.17	8.25	0.19	3.98	0.21	3.83	0.20
0714+456	1233.40	13.70	1024.30	13.25	351.22	1.69	352.86	1.84
	109.17	0.95	111.11	1.13	28.49	0.50	38.39	0.70
0728+505	1034.30	3.32	931.42	3.25	311.78	3.44	281.00	3.00
	165.22	1.79	143.64	1.67	22.18	0.70	26.34	0.81
0915+320	190.06	1.43	162.45	1.13	66.11	1.03	57.95	0.69
	14.20	0.23	13.78	0.27	6.00	0.25	6.12	0.30
0919+334	193.69	1.55	202.21	1.59	219.86	0.50	220.29	0.51
	14.27	0.18	16.18	0.20	19.78	0.25	20.63	0.20
0921+368L	107.92	2.81	81.04	1.74	26.77	0.70	22.83	0.69
	10.75	0.22	9.17	0.23	1.57	0.19	2.46	0.19
0921+368R	99.04	2.93	80.59	1.84	27.28	1.05	27.91	1.07
	4.71	0.19	5.08	0.22	2.83	0.19	2.86	0.17

Table 3.5: Total intensity (S) and polarized (P) flux in mJy for each source at each wavelength obtained during the December 1995 observing session. The table also contains the errors associated with each flux measurement. Entries containing "..." indicate wavelenghts at which the source flux could not be measured due to low signal to noise.

Source	S_{1365}	σ_S	S_{1435}	σ_S	S_{1465}	σ_S	S_{4535}	σ_S	S_{4885}	σ_S
	P_{1365}	σ_P	P_{1435}	σ_P	P_{1465}	σ_P	P_{4535}	σ_P	P_{4885}	σ_P
0033+064	792.43	2.26	751.32	2.50	732.73	1.82	208.02	0.38	190.42	0.37
	38.35	0.38	40.44	0.35	40.40	0.30	21.44	0.19	20.53	0.17
0035+067	152.88	1.63	151.97	1.46	147.65	1.45	59.23	0.42	52.70	0.32
	13.22	0.35	12.59	0.31	11.45	0.34	5.41	0.24	4.66	0.19
0038+071A	125.20	1.85	123.19	1.76	115.97	1.21	47.79	0.50	44.94	0.48
	18.35	0.19	18.42	0.26	18.03	0.24	6.00	0.22	6.20	0.24
0038+071B	170.59	2.08	164.47	1.92	153.01	1.29	67.36	0.56	64.93	0.39
	6.70	0.18	6.84	0.21	6.67	0.21	2.86	0.16	3.04	0.16
0040+072	165.11	2.16	163.39	1.94	160.70	1.68	62.72	0.52	59.07	0.52
	7.66	0.30	7.31	0.23	7.30	0.25	1.66	0.16	1.81	0.18
0040−098	361.80	3.10	340.72	2.56	339.10	2.44	95.16	0.66	89.30	0.57
	14.96	0.30	15.24	0.32	14.72	0.27	2.83	0.23	2.78	0.24
0041+069	570.66	2.89	548.63	1.99	534.65	1.83	181.11	0.48	171.58	0.51
	26.91	0.24	28.76	0.28	28.22	0.27	12.85	0.24	12.02	0.22
0041+076	193.25	1.13	187.97	0.93	187.50	0.89	119.59	0.39	116.61	0.36
	11.54	0.28	9.79	0.24	10.83	0.23	5.45	0.16	5.55	0.16
0042−078	156.25	3.83	152.78	3.13	145.61	2.44	95.17	0.66	91.84	0.69
	6.55	0.37	7.57	0.40	6.69	0.38	4.59	0.35	3.51	0.31
0042−080A	106.46	2.00	110.77	1.95	112.14	2.03	35.65	0.48	37.01	0.59
	7.59	0.36	7.58	0.31	7.53	0.28	2.93	0.21	3.22	0.21
0042−080B	115.48	2.25	110.65	1.96	111.94	1.96	36.91	0.37	37.83	0.53
	7.33	0.36	7.17	0.31	6.50	0.28	2.44	0.20	2.66	0.19
0042−092	174.00	2.20	174.22	1.99	175.08	1.95	76.36	0.66	74.46	0.66
	8.36	0.24	7.57	0.31	8.43	0.27	5.13	0.24	5.34	0.25
0042−098	158.73	1.47	150.47	1.41	149.88	1.31	48.27	0.52	45.71	0.53
	8.35	0.29	9.13	0.24	9.98	0.30	4.67	0.25	4.67	0.25
0043+060	132.95	1.49	125.27	1.20	121.83	1.11	45.17	0.28	42.66	0.27
	7.68	0.23	7.16	0.27	7.76	0.32	3.21	0.16	2.26	0.12
0047−095	198.07	1.96	195.28	2.44	192.40	2.41	87.77	0.40	84.63	0.43
	18.20	0.33	17.86	0.37	16.89	0.25	7.13	0.20	6.41	0.18
0059+001	2471.00	1.86	2411.00	1.96	2386.80	2.37	1378.10	0.93	1328.30	0.84
	92.44	0.29	87.41	0.29	88.11	0.30	109.81	0.27	96.45	0.22
0102+020A	746.96	1.75	700.74	1.70	690.02	1.82	223.49	0.39	208.56	0.34
	76.10	0.40	73.19	0.35	76.32	0.44	28.54	0.23	28.36	0.21
0102+020B	70.75	1.23	61.22	1.13	60.00	1.21	...	...	...	...
	3.17	0.27	1.75	0.18	2.50	0.24	...	...	...	...
0107+015	52.15	1.87	46.71	2.40	...	...	17.56	0.52	16.50	0.43
	2.31	0.31	1.54	0.27	...	...	1.20	0.15	0.66	0.13
0108+015	2493.10	4.05	2463.80	3.65	2450.90	3.44	2012.30	1.80	2006.60	2.42
	88.79	0.26	86.12	0.28	83.91	0.28	41.04	0.20	41.15	0.19
0108+028	156.11	2.09	149.24	1.74	152.75	2.04	62.43	0.37	58.16	0.28
	13.19	0.31	12.82	0.26	12.81	0.32	9.57	0.17	10.46	0.19
0110+015	97.91	3.42	91.76	2.61	91.76	2.76	39.86	0.40	37.01	0.41
	3.57	0.35	5.63	0.28	4.19	0.34	1.46	0.14	1.79	0.15
0110+018	134.00	1.50	128.81	1.41	125.69	1.81	50.16	0.53	47.81	0.47
	8.49	0.27	7.54	0.27	6.78	0.29	3.19	0.21	2.79	0.23
0113+027	74.41	1.93	69.79	1.88	71.26	1.78	24.75	0.50	24.17	0.45
	8.34	0.32	7.62	0.36	7.31	0.29	3.35	0.15	3.10	0.16
0427−116	354.34	5.90	326.56	3.86	328.51	2.21	129.65	0.89	122.29	0.95
	17.95	0.46	17.21	0.39	18.28	0.32	9.63	0.33	9.13	0.25
0430−130	268.21	4.65	240.12	3.51	228.39	2.58	87.75	1.31	82.36	0.44
	11.29	0.36	10.85	0.27	10.80	0.30	2.13	0.22	2.37	0.21
0434−131	1659.00	14.95	1564.00	12.58	1564.50	13.53	544.42	0.92	507.23	1.13
	152.04	1.01	148.28	1.05	146.29	1.43	77.19	0.40	72.93	0.34

Table 3.6: Total intensity (S) and polarized (P) flux in mJy for each source at each wavelength obtained during the 1996 observing session. The table also contains the errors associated with each flux measurement. Entries containing "..." indicate wavelenghts at which the source flux could not be measured due to low signal to noise.

Source	S_{1365}	σ_S	S_{1435}	σ_S	S_{1465}	σ_S	S_{4535}	σ_S	S_{4885}	σ_S
	P_{1365}	σ_P	P_{1435}	σ_P	P_{1465}	σ_P	P_{4535}	σ_P	P_{4885}	σ_P
0434−133	755.41	12.58	752.60	14.21	687.27	9.59	252.76	1.85	238.07	1.76
	36.60	0.72	43.77	0.84	40.08	0.82	25.30	0.50	23.23	0.40
0436−133	116.40	2.84	102.40	2.85	96.80	2.92	30.75	0.61	29.42	0.61
	6.28	0.27	7.70	0.39	6.96	0.29	2.81	0.33	2.21	0.20
0439−113	105.52	2.33	96.98	2.23	94.96	1.54	29.99	0.50	...	...
	6.09	0.32	7.40	0.41	13.11	0.45	1.56	0.16	...	...
0444−135	302.77	4.12	283.83	3.04	268.67	2.64	89.04	0.98	80.45	0.83
	10.15	0.44	9.98	0.46	9.25	0.37	2.84	0.29	3.01	0.25
0906−090	75.07	3.49	...	...	...	...	93.77	0.61	95.71	0.52
	4.78	0.91	...	...	...	...	4.50	0.21	4.00	0.20
0906−103	146.71	2.41	126.52	2.04	147.80	2.46	41.44	0.37	38.63	0.37
	9.09	0.62	7.36	0.48	16.37	1.26	2.06	0.18	1.80	0.16
0908−100	337.69	11.16	...	...	...	...	172.17	1.59	166.00	1.47
	19.70	3.21	...	...	...	...	6.24	0.39	6.51	0.36
0908−107	422.79	4.17	402.17	3.90	380.36	6.46	162.11	0.44	149.18	0.36
	54.92	0.88	51.52	0.82	44.30	1.54	24.00	0.19	23.32	0.19
0909−093	394.73	13.73	...	...	...	...	180.48	1.23	173.74	1.11
	14.39	1.80	...	...	...	...	11.36	0.46	10.86	0.50
0913−092	158.85	5.40	155.68	3.36	...	...	61.73	0.31	57.87	0.29
	5.07	1.33	6.46	0.64	...	...	5.25	0.16	4.55	0.15
1059+283	210.23	2.58	196.62	3.41	...	...	61.83	0.55	57.68	0.56
	11.81	1.00	11.49	1.02	...	...	8.36	0.29	7.54	0.31
1106+300	326.79	2.97	277.71	2.32	287.59	2.75	92.26	0.57	84.52	0.61
	24.14	0.61	16.48	0.48	23.72	0.86	5.48	0.25	4.41	0.19
1107+288	80.54	1.88	71.64	1.84	...	...	26.99	0.48	23.98	0.36
	3.30	0.26	3.43	0.29	...	...	2.25	0.24	2.08	0.20
1108+279	76.77	2.21	80.51	2.40	77.12	1.65	37.91	0.39	35.34	0.38
	4.54	0.25	6.02	0.32	3.73	0.41	2.11	0.20	2.43	0.18
1108+292A	56.40	2.47	49.82	1.83	47.69	1.75	17.75	0.50	17.78	0.45
	1.80	0.40	0.83	0.31	2.52	0.36	2.00	0.22	1.76	0.19
1108+292B	53.44	2.36	41.43	1.71	51.51	1.85	19.60	0.44	17.45	0.43
	4.07	0.43	4.20	0.41	5.74	0.35	2.46	0.23	2.12	0.17
1109+289	67.59	2.77	65.93	1.83	65.65	2.03	21.85	0.52	21.16	0.42
	2.57	0.43	4.73	0.24	3.22	0.34	0.91	0.20	1.17	0.23
1110+293	161.69	2.81	151.82	3.63	149.49	1.97	48.77	0.42	44.23	0.36
	4.66	0.28	3.58	0.56	4.32	0.39	1.60	0.18	1.87	0.19
1118+279A	480.44	5.91	487.53	4.32	470.72	4.82	110.65	3.14	103.41	2.06
	23.12	0.82	22.78	0.86	25.76	1.40	4.74	0.25	5.27	0.27
1118+280B	68.96	2.86	70.90	2.99	77.07	2.02	28.12	0.66	25.68	0.57
	6.96	0.46	5.98	0.67	8.21	0.79	3.48	0.28	3.81	0.25
1121+501	149.26	2.42	148.21	2.10	143.27	2.30	51.34	0.33	48.00	0.34
	22.82	0.46	20.82	0.68	20.04	0.52	7.53	0.19	7.04	0.17
1125+261	922.41	1.34	937.13	1.07	947.07	1.68	1089.40	0.84	1075.20	0.82
	17.95	0.30	17.49	0.38	18.17	0.35	8.07	0.20	5.27	0.15
1133+490	834.45	6.76	788.71	8.79	797.98	5.31	427.13	1.72	403.19	1.76
	14.33	0.40	11.33	0.91	14.25	0.50	26.64	0.53	30.14	0.59
1134+489A	395.21	6.84	362.48	4.87	368.62	6.34	155.23	0.62	149.76	0.44
	7.31	0.71	9.88	0.47	7.20	0.65	5.74	0.20	5.00	0.19

Table 3.6 – *Continued*

Source	S_{1365}	σ_S	S_{1435}	σ_S	S_{1465}	σ_S
	P_{1365}	σ_P	P_{1435}	σ_P	P_{1465}	σ_P
0039+212	153.47	2.02	122.14	2.54	125.87	2.09
	10.31	0.41	11.44	0.53	10.36	0.43
0040+212	49.50	0.88	48.00	1.11	45.10	0.87
	2.42	0.16	2.50	0.20	1.78	0.21
0056−013	1080.30	7.25	1098.30	10.76	1083.50	6.22
	20.39	0.62	24.11	0.83	26.81	0.82
0126−013a	947.55	5.72	599.41	4.50	580.60	4.31
	108.16	1.26	62.57	0.98	67.54	1.04
0154+364	212.80	1.39	204.23	1.60	202.20	1.28
	14.74	0.44	14.58	0.47	13.41	0.41
1650+815U	158.43	2.01	163.30	2.23	125.11	1.32
	3.43	0.19	4.66	0.31	4.04	0.21
1650+815L	89.47	1.64	120.95	2.38	76.28	1.34
	10.37	0.38	11.00	0.53	8.98	0.41
0245+368	54.22	0.89	54.97	1.46	50.21	0.91
	3.78	0.23	3.55	0.19	3.27	0.18
0316+412	627.54	6.02	482.61	5.94	450.07	6.80
	39.62	1.06	32.46	1.78	19.79	0.99
0318+419	6393.50	30.90	6364.60	25.31	6560.40	20.65
	492.48	7.26	660.99	8.68	618.44	6.80
0319+415[a]	23905.00	21.36	24790.00	44.09	25047.00	32.08
	19.11	0.82	29.36	0.99	18.95	1.15
0317+440L	183.01	1.10	...	...	175.32	1.31
	25.29	0.23	...	...	24.05	0.27
0317+440R	196.68	1.08	...	...	191.66	1.33
	36.39	0.24	...	...	34.57	0.28
1036−267	131.00	1.96	119.59	2.11	118.85	1.58
	8.30	0.66	9.92	0.43	8.19	0.55
1037−281	89.79	1.53	84.48	1.89	...	...
	1.76	0.30	1.18	0.23	...	...
1037−270	202.54	2.48	196.61	2.17	...	...
	6.64	0.51	8.41	0.41	...	...
1039−273	67.47	1.26	67.54	1.19	...	...
	6.44	0.43	5.28	0.45	...	...
1039−272	68.74	1.29	64.83	1.53	...	...
	4.24	0.44	2.97	0.27	...	...
1023−278	261.46	1.66	...	...	233.25	2.03
	19.54	0.47	...	...	17.68	0.48
1145+196	5694.70	44.46	5134.50	25.12	5305.40	38.89
	55.05	6.22	80.73	3.03	22.56	2.97
1147+545	85.55	1.28	80.75	1.24	74.76	0.91
	5.45	0.30	4.66	0.32	4.59	0.28

[a]Note that the measured polarization for this source falls at the limit of the VLA's capabilities (~0.1%). Results determined for this source should therefore be regarded with extreme caution.

Table 3.7: Total intensity (S) and polarized (P) flux in mJy for each source at each wavelength obtained during the 1997 observing session. The table also contains the errors associated with each flux measurement. Entries containing "..." indicate wavelenghts at which the source flux could not be measured due to low signal to noise.

Source	S_{1660}	σ_S	S_{4535}	σ_S	S_{4885}	σ_S
	P_{1660}	σ_P	P_{4535}	σ_P	P_{4885}	σ_P
0039+212	98.40	1.92	...	...	...	...
	11.70	0.47	...	...	...	...
0040+212	43.81	0.84	...	...	...	...
	1.70	0.22	...	...	...	...
0056−013	971.36	5.36	391.76	1.15	379.52	1.40
	28.46	0.96	39.79	0.88	32.89	0.83
0126−013a	642.01	5.40	...	...	...	...
	96.17	1.53	...	...	...	...
0154+364	195.28	1.33	136.24	0.69	134.34	0.60
	16.19	0.54	6.18	0.34	5.95	0.36
1650+815U	76.65	0.66	44.36	0.26	41.31	0.29
	4.25	0.32	2.65	0.20	1.77	0.17
1650+815L	57.02	0.83	23.25	0.33	23.3	0.46
	6.23	0.34	4.32	0.36	1.80	0.22
0245+368	46.22	0.85	18.11	0.32	17.78	0.36
	2.73	0.23	1.38	0.20	0.62	0.16
0316+412	...	...	229.75	1.18	227.54	1.07
	...	...	15.70	0.64	13.80	0.76
0318+419	5665.50	13.44	...	...	...	...
	801.19	9.86	...	...	...	...
0319+415	...	...	...	...	...	...
	...	...	...	...	...	...
0317+440L	...	...	59.81	0.37	53.15	0.46
	...	...	8.04	0.33	6.37	0.29
0317+440R	...	...	68.46	0.38	61.85	0.48
	...	...	11.06	0.32	10.17	0.30
1036−267	103.84	1.58	31.4	0.41	29.21	0.43
	7.75	0.53	2.49	0.23	1.20	0.19
1037−281	...	...	33.26	0.37	...	...
	...	...	0.56	0.16	...	...
1037−270	190.44	3.35	240.12	0.73	242.98	0.68
	10.00	0.78	3.99	0.22	3.60	0.20
1039−273	53.10	1.34	29.28	0.33	29.2	0.29
	3.28	0.39	1.06	0.16	2.01	0.28
1039−272	56.36	1.59	27.81	0.45	24.44	0.36
	1.86	0.38	1.33	0.16	1.29	0.13
1023−278	...	...	83.99	0.42	81.15	0.45
	...	...	6.60	0.32	6.27	0.20
1145+196	4611.00	33.43	1484.3	4.16	1329.8	4.12
	114.24	7.09	259.11	2.30	247.67	2.29
1147+545	71.77	1.14	...	...	...	...
	3.46	0.29	...	...	...	...

Table 3.7 – *Continued*

Chapter 4

X-ray Observations and Data Reductions

Overview: Each of the 24 galaxy clusters included in this analysis have been imaged by the ROSAT X-ray satellite. This chapter presents an overview of the X-ray observations and data reductions for these clusters. Section 4.1 outlines the relevant parameters, and history of the ROSAT satellite. The cluster images analyzed in this thesis were extracted from both the ROSAT pointed observations, and all-sky survey archives. The detailed target selection process for the galaxy clusters is described in § 4.2, and the X-ray reductions of the cluster data is discussed in § 4.3. The X-ray fits to the clusters are presented in § 4.4, together with tables of the fit parameters.

4.1 ROSAT

The initiative for the Röntgensatellit, or ROSAT satellite, came from the Max-Planck-Institut für extraterrestrische Physik (MPE) in 1975. The initial proposal suggested undertaking an all-sky survey with a resolution of less than an arcminute. During the planning stages, the concept of the satellite expanded to include an international collaboration with a Wide Field XUV Camera (WFC), through the University of Leicester, and a high resolution imager (HRI) for the focal plane of the X-ray telescope (XRT), through NASA. The other XRT focal plane instruments are the two Position Sensitive Proportional Counters (PSPCs), each with a filter wheel carrying a boron filter, which were developed at MPE. The WFC is described in detail by Kent et al. (1990), and Wells et al. (1990) and will not

be discussed here.

The satellite was launched into a nearly circular 575 km orbit on June 1, 1990. The first phase of the ROSAT mission was to conduct an all-sky X-ray imaging survey (RASS) during the first six months of operation. Following the all-sky survey, the satellite was designed to take deeper pointed observations of individual targets proposed by observers. A detailed overview of the ROSAT mission can be found in Trümper (1983). ROSAT operated the XRT with both the PSPC and HRI as focal plane detectors until September 1994, when the PSPC detector was taken off-line due to the depletion of the gas supply. The satellite continued to successfully operate the HRI until September 1998 when it was damaged by an accidental slew across the Sun. The satellite was de-commissioned on February 12, 1999.

4.1.1 ROSAT's XRT

The imaging mirror assembly of ROSAT's XRT consisted of a fourfold nested Wolter type I mirror. This assembly combines parabolic and hyperbolic surfaces to enable proper focusing of the incoming photons (Wolter 1952) which strike the mirror surface at typical grazing angles between 1° and 2°. The effective aperture of the XRT was 83 cm, and the focal length was 240 cm. The instrument was designed to be sensitive to photons in the soft X-ray range of 0.1 to 2.4 keV, and had a total collecting area of 1141 cm^2 and a focal plane plate scale of 11.64 μm $arcsec^{-1}$. A detailed description of the mirror assembly and performance is given by Aschenbach (1988).

The XRT was operated with one of the three focal plane detectors. Two of the detectors were identical position sensitive proportional counters (PSPCs), and the third detector was a high resolution imager (HRI), similar to the one flown on the EINSTEIN observatory[1]. With the HRI as the focal plane detector for the XRT, the field of view was 36′, with a spatial resolution of 1.7″ (FWHM) at 1 keV. The PSPC + XRT combination resulted in a field of view of 2°, and a spatial resolution of 25″ (FWHM) at 1 keV. The large angular diameter subtended by low redshift galaxy clusters made the XRT + PSPC combination the natural choice for studies of extended emission from galaxy clusters.

The PSPC was developed at the Max-Planck-Institut für extraterrestrische Physik, and is described in detail in Briel & Pfeffermann (1986). In addition to the position and

[1]A significant improvement of the ROSAT HRI was the increased quantum efficiency (to 30 %) at 1 keV.

energy sensing counter, the PSPC also contained a lower layer which acted as an anti-coincidence counter for the rejection of background events. Figure 4.1 shows that the angular resolution of the detector was only a weak function of the photon energy in the

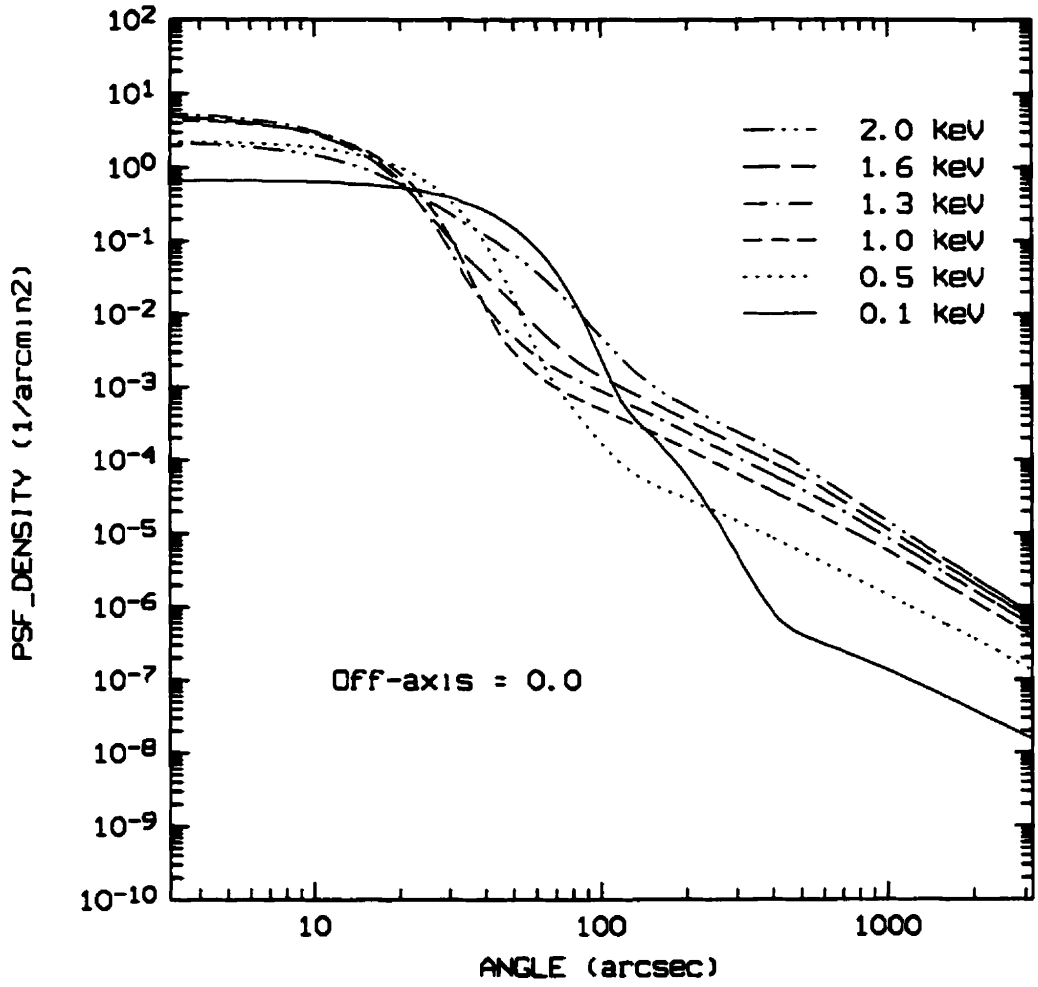

Figure 4.1: This plot shows the radial dependence of the on-axis PSPC pointing PSF density as a function of photon energy. In the hard X-ray region used in this work, 0.5-2.4 keV, the PSF density is only a weak function of photon energy.

4.1.2 ROSAT All Sky Survey

The first two months after the launch of the ROSAT satellite were devoted to the calibration and verification of the instrument package. Following this period, ROSAT began the six month all-sky survey during which nearly the entire sky was covered in scans consisting of 2° strips centered on great circles through the ecliptic poles in the plane perpendicular to the Earth-Sun axis. This survey was designed so that no Earth occultation occurred, and the zenith angle was minimized. The survey, begun in August 1990, was designed to be

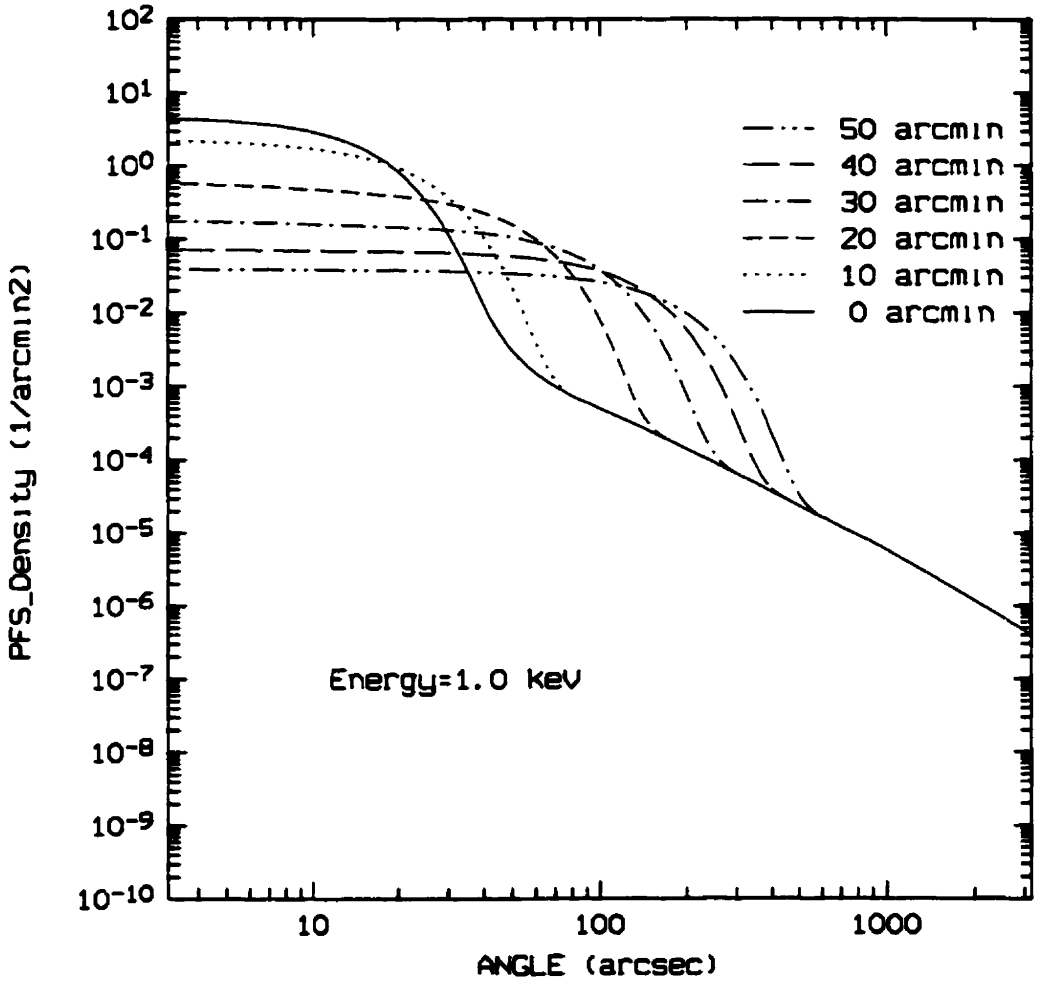

Figure 4.2: This plot shows the radial dependence of the PSPC pointing PSF density at a photon energy of 1 keV as a function of increasing off-axis angle. Note the increase in the width of the point spread function at large off-axis angles.

completed at the end of January 1991. Unfortunately about a week prior to the nominal completion date of the survey, the satellite's attitude control suffered a catastrophic failure which sent the satellite into a tumbling orbit. As a result of the failure, the solar panels were no longer capable of drawing power from the Sun and satellite was forced to switch to its backup batteries for power. After a few hours the battery power was drained and the satellite switched into an enforced hibernation state which made the ground controller's task of re-establishing contact very difficult. Fortunately, for this thesis (and many other research projects!), contact was re-established with the satellite. As the satellite tumbled, however, the telescopes slewed across the Sun which destroyed the focal plane detector (PSPC-C) which was being used for the survey. The payload, however, included a spare detector (PSPC-B) which was used to complete the unobserved regions of the survey during observing periods in February and August 1991.

The primary products derived from the RASS are the source catalog, and maps of the diffuse X-ray background (Snowden et al. 1995; Snowden et al. 1997). The source catalog contains 18,811 sources which have a PSPC count rate above 0.05 counts/second (cts/s) in the 0.1-2.4 keV energy band. All catalogued sources contain at least 15 photons. For a brightness limit of 0.1 cts/s there are 8547 sources, and the catalogue represents a sky coverage of 92%, with a typical position accuracy of 30″. The catalog, presented in Voges et al. (1999), lists the source positions in equatorial co-ordinates, the positional error, the source count rate and associated error, the background count rate, the on-source exposure time[2], the hardness-ratio and error, the extent and likelihood of extent, and the likelihood of detection of the source. An earlier pass through the RASS (Voges et al. 1996) found that of the 40% of sources having a counterpart in SIMBAD, 53% were stars, 16% were galaxies, 31% were clusters of galaxies, AGNs, quasars, and miscellaneous (known) objects[3]. Nine of the galaxy clusters analyzed for this thesis are taken from the RASS observations. The remainder of the cluster sample was observed during ROSAT's pointed observation phase.

[2]Due to the scanning process used for the RASS, the exposure time varies from $\sim$ 100 seconds at the ecliptic equator, to $\sim$ 40 000 seconds at the ecliptic poles.

[3]The coincidental association error was estimated to be 15% for these identification.

4.1.3 Pointed Observations

Following the six-month all-sky survey, ROSAT entered into the pointed observation phase of the mission. During this phase, the guest observer program provided the opportunity for researchers to carry out observations with either the PSPC, while available, or the HRI as the focal plane detector. The average exposure time during the pointed observations phase was 13 kiloseconds (ksec). Investigators retained proprietary use of their data for 12 months, after which time the data became publicly available.

During this second phase of operation, the telescope's pointing direction was generally moved slowly back and forth a distance of ± 3 arcminutes in a period of 400 seconds. This motion was in a direction diagonal to the coarse wire mesh of the PSPC window support structure. This wobbling of the telescope prevented unwanted shadowing of X-ray sources which fell behind the mesh by providing a method of smoothing out the mesh when it was projected in sky coordinates.

4.2 Galaxy Cluster Targets

The general properties of the galaxy cluster targets selected for this analysis are briefly touched upon in § 3.2.1. The main goal of that section was to provide a detailed description of the targeting procedure used to select the polarized radio sources. Below is an outline of the considerations taken into account in the selection of target galaxy clusters. Table 4.1 provides the relevant selection parameters for the galaxy cluster sample selected for this work.

- **Location:** A positional limit on the available galaxy clusters is set by the declination limits of the VLA. Although the interferometer is capable of observing sources down to declinations of $-40°$, the foreshortened u-v coverage, even for hybrid configurations, at these low declinations makes recovery of the source structure of the radio probes difficult. The selection of galaxy clusters was therefore limited to those at declinations greater than $-15°$, with the exception of Abell 1060, which falls at a declination of $-27°$. Further restrictions on the position of galaxy cluster candidates were set by i) the requirement of obtaining radio probes at high Galactic latitudes, $|b| > 20°$, to avoid contamination from Galactic Faraday rotation, and ii) the sky coverage of the NVSS available at the time of observations.

The Galactic latitude restriction was determined from detailed maps of the Faraday sky (Simard-Normandin & Kronberg 1980) which revealed enhanced Faraday rotation at low Galactic latitudes in the disk of the Milky Way. Rotation measures in the plane of the Galaxy were found to be of order 100 rad m^{-2}, which is the same order of magnitude as expected from non-cooling flow regions of galaxy clusters. At higher Galactic latitudes, the Faraday sky maps show typical rotation measures are of order 10 rad m^{-2}. These small Galactic contributions are easily corrected for using the method described in § 5.4.

- **Redshift:** Analysis of the fields available from the initial release of the NVSS survey products revealed that there are approximately three strong (I> 100 mJy) radio sources per square degree with polarized radio flux greater than 1.1 mJy[4], the approximate polarized flux limit for a three sigma detection in the VLA's snapshot mode. Further, the X-ray emission within relatively rich galaxy clusters is generally found to extend to radii of 2 Mpc from the cluster cores (Böhringer 1995). At a redshift of 0.1, a rich cluster, which has X-ray emission extending to a radius of 2 Mpc, covers an angular region of 0.36 square degrees. Galaxy clusters selected for this study have therefore been restricted to redshifts below z=0.1, to provide a large angular extent on the sky for the selection of polarized radio probes.

- **Richness:** Faraday rotation of polarized emission will occur if there is a co-spatial distribution of magnetic fields and thermal electrons. In order to use this effect to probe the intracluster magnetic fields, sufficiently rich galaxy clusters must be selected to ensure a relatively high thermal electron density within the cluster.

  Ebeling et al. (1996) present the properties of the X-ray-bright Abell-type clusters of galaxies (XBACs) from the ROSAT All-Sky Survey. This cluster sample is limited to high Galactic latitude ($|b| > 20°$) ACO clusters at redshifts of less than 0.2, and X-ray fluxes above 5.0×10^{-12} erg cm^{-2} s^{-1} in the 0.1-2.4 keV band. All but four galaxy clusters within the thesis sample are drawn from the X-ray flux-limited XBACs sample. The four clusters outside the XBACs sample fall below the flux cutoff. Two of the galaxy clusters were observed prior to the release of XBACs, Abell 569 and Abell 779, and were selected based on EINSTEIN IPC luminosities. The other two

[4]Flux estimate at the NVSS frequency of 1.4 GHz.

clusters, Abell 1383 and Abell 2247, were selected based on the presence of polarized radio probes at small cluster impact parameter. The lower limit on the rest frame 0.1-2.4 keV X-ray luminosity of the galaxy clusters selected for analysis in this thesis is 0.1×10^{44} ergs s^{-1}.

- **Morphology:** X-ray images of the hot intracluster gas trace the potential of the galaxy cluster. In the case of a relaxed virialized system, the X-ray emission will be spherically symmetric. Many clusters, however, display very distorted X-ray morphologies which have been associated with the merging of clusters or subclusters of galaxies. In the case of a merger situation, it is very difficult to model the X-ray emission in the region affected by the merger, due to the (unknown) variations in the gas density and temperature. These uncertainties lead to an increased error in the determination of the electron column density through the intracluster medium toward polarized radio probes. On the other hand, clusters which display relaxed morphologies often reveal an X-ray surface brightness profile which is strongly peaked in the central regions of the cluster, suggesting the presence of some amount of a cooling-flow. As discussed in § 1.3, one of the goals of this thesis is to probe the underlying intracluster magnetic field in non-cooling flow regions of galaxy clusters, and to compare this to the results of work by other researchers which concentrated on the magnetic field in the central cooling flow regions of galaxy clusters. This goal, therefore, makes selection on morphology somewhat difficult.

  The majority of galaxy clusters selected for this analysis which do have fairly relaxed X-ray profiles are known to have cooling rates below 50 $M_{\odot}$ yr^{-1}. The remainder of the cluster sample contains several galaxy clusters whose X-ray surface brightness profiles reveal various stages of cluster merger events. In these clusters, the X-ray surface brightness profiles are fit for both the entire galaxy cluster, and for an angular region of the cluster covering the radio probe. These profiles are then compared to determine the best-fit parameters.

  One additional morphological consideration was the presence of extended X-ray emission. All target clusters were examined to ensure that the cluster X-ray emission was indeed extended, and not simply dominated by compact AGN-type X-ray emission.

- **Central cooling time:** As discussed above, the majority of galaxy clusters selected

for this analysis are weak or non-cooling flow clusters. Although the cooling rate for the target clusters was initially taken from the (unpublished) cooling flow catalog of Arnaud 1988, the numbers presented in Table 4.1 are extracted from the EINSTEIN analysis by White et al. (1997), where available. The four clusters with cooling rates above 50 $M_{\odot}$ yr^{-1}, Abell 85, Abell 376, Abell 426, and Abell 496, have radio galaxy probes which fall beyond the cooling radius of the cluster. The cooling radius is defined as that at which the cooling time for the gas is equal to the age of the galaxy cluster. Typical values of the cooling radius are $\sim$ 100 kpc.

- **Polarized radio probe:** Of course, in addition to the above constraints on the target galaxy clusters, one of the most important constraints was that there must be a polarized NVSS radio probe viewed through the intracluster medium at an impact parameter interior to the edge of the X-ray emitting gas.

Abell	RA (J2000)[a]	Dec (J2000)[b]	z[c]	R[d]	RS[e]	$\dot{M}$[f]	R_{cool}[g]
	h m s	° m s				$M_\odot$ yr^{-1}	Mpc
75	00 39 35.7	21 13 23.5	.0626	0	L a	...	...
76	00 40 01.8	06 50 44.0	.0416	0	L a	0	0
85	00 41 50.9	-09 18 26.0	.0518	1	cD	81	.07
119	00 56 15.6	-01 14 56.0	.0440	1	C	0	0
147	01 08 11.9	02 10 53.0	.0438	0	I s	...	...
168	01 15 11.3	00 20 41.0	.0452	2	I c	0	0
194	01 25 49.3	-01 23 40.5	.0178	0	L a	0	0
262	01 52 47.2	36 09 24.0	.0161	0	C	9.4	.04
376[h]	02 46 02.6	36 53 28.5	.0489	0	C	92	.08
399	02 57 51.6	13 02 52.5	.0715	1	cD	0	0
400	02 57 38.8	06 00 41.5	.0232	1	I c	0	0
401	02 58 57.3	13 34 48.5	.0748	2	cD	0	0
426	03 19 49.3	41 30 51.0	.0183	2	L	283	.1
496	04 33 38.0	-13 15 34.5	.0320	1	cD	134	.09
569	07 09 08.3	48 36 47.0	.0196	0	B	>5.2	>.06
576	07 21 29.1	55 47 03.0	.0381	1	I c	17	.05
754	09 09 14.2	-09 40 41.5	.0528	2	cD s	0	0
779	09 19 46.6	33 45 01.5	.0226	0	cD sp	3.1	.03
1060	10 36 41.6	-27 31 46.5	.0114	1	C	8	.05
1185	11 10 33.5	28 43 00.0	.0304	1	C	0	0
1314	11 34 45.7	49 05 28.4	.0341	0	C	0	0
1367	11 44 53.2	19 43 13.5	.0215	2	F	2.3	.03
1383	11 47 56.1	54 42 42.9	.0603	1	I c	...	...
2247	16 50 17.7	81 39 02.6	.0392	0	L	...	...

[a]Right ascension of X-ray centroid in J2000 coordinates as determined by the author.

[b]Declination of X-ray centroid in J2000 coordinates as determined by the author.

[c]Redshift from Abell, Corwin & Olowin (1989).

[d]Richness class from Struble & Rood (1987).

[e]Revised Rood-Sastry type from Struble & Rood (1987).

[f]Cooling rate in solar masses per year from White et al. (1997) unless otherwise indicated.

[g]The radius as determined by White et al. (1997) at which the cooling time reaches 2×10^{10} yrs.

[h]Cooling rate and radius from Arnaud 1988.

Table 4.1: General observational parameters of the target Abell clusters.

4.3 Reductions

As discussed above, fifteen of the galaxy clusters selected for analysis were observed by the ROSAT satellite during the Pointed Observation phase of the mission. The X-ray data on these target clusters were extracted from the ROSAT Data Archive. The other nine clusters were observed during the All-Sky Survey phase of the ROSAT mission, and the data were extracted from the survey database through collaboration with H. Böhringer of the Max-Planck-Institut für extraterrestrische Physik. The relevant ROSAT observational parameters for the cluster sample are listed in Table 4.2. The reduction of the ROSAT X-ray data was undertaken within the Extended X-ray Scientific Analysis Software (EXSAS) package under the European Southern Observatory's (ESO's) Munich Image Data Analysis System (MIDAS). The analysis of the ROSAT X-ray emission was undertaken for each of the three PSPC energy bands: the broad band (0.1-2.4 keV), the soft band (0.1-0.4 keV), and the hard band (0.5-2.0 keV). The main results, however, concentrate on the hard X-ray band, since the majority of the X-ray emission from gas at typical intracluster medium temperatures ($10^7 - 10^8$K) falls above the carbon Kα break in Figure 4.3. In addition, the soft ROSAT band is also strongly contaminated by Galactic emission. Below is a brief outline of the steps involved in the analysis of the extended cluster emission. A detailed technical description of the reduction techniques for extended ROSAT sources is given by Snowden et al. (1994).

4.3.1 Calculating the Radial Surface Brightness Profile

As discussed in § 2.3.1, the intracluster gas density can be traced by the surface brightness profile of the X-ray emission. This section outlines the process of determining the radial distribution of the intracluster surface brightness. The first step toward determining a proper background subtracted cluster surface brightness profile is to determine the emission center of the cluster. Although the analysis presented below assumes spherical symmetry for the clusters, it is often the case that the X-ray emission from galaxy clusters is elongated. It is, therefore, important to consider the distribution of the cluster photons to sufficiently large radii that the true center of mass of the photons can be determined. In the case of elongated cluster emission, which is not intrinsic to the individual cluster under study, but, rather, is due to a merging sub-cluster component, it is desirable to determine the

emission center after masking the sub-cluster component. The masking of the sub-cluster emission is possible through either excision of the photons from a region around the sub-cluster, or, for sub-cluster components at large radii, through restriction of the centering to a cluster radius interior to that of the sub-cluster component. The latter approach was employed for the current cluster sample. Note that, although the differentiation between intrinsic X-ray elongation, and X-ray elongation due to a sub-cluster component is somewhat ambiguous, for the purposes of determining an X-ray emission centroid, the X-ray excess is attributed to a sub-cluster component if it clearly disobeys the emission gradient in its general vicinity. Therefore an elongated cluster with a smoothly varying radial emission profile will be considered intrinsically elongated.

Briefly described, the centering program begins with an initial estimate of the emission-weighted center of the cluster, usually the map center. The program then begins an iterative loop through all photon events in the ROSAT hard X-ray band, 0.5-2.0 keV, to determine the center of mass of the photons within a radius of $3'$ to an accuracy of $2''$. When convergence occurs the programs continues with an iterative loop to determine the centroid of the photon emission within $5'$, and a final loop for the center of mass of photons within $7'.5$.

The next step is to determine the background level in the image. This first requires an estimate of the outer significant radius (R_{out}) of the cluster emission. This radius is defined as the point at which the (Poisson) error curve rises faster than the integrated hard band count rate. The background level is then determined by examining 12 individual sectors which lie in an annulus beyond R_{out}. Specifically, the count rate is determined in each annular sector for the broad, hard, and soft energy bands. The clipping algorithm then examines each energy band individually to exclude any sector where the count rate is more than 2σ off the median value for that energy band. The background surface brightness and associated error are then determined for each band from the sectors remaining after clipping. This method of determining the background properly excludes any regions which are contaminated by neighbouring X-ray sources.

The final step is to determine the hard-band radial profile of the cluster. Each cluster image is examined for the presence of X-ray emission from discrete sources. All photons in an area surrounding these sources are removed from the photon event table before the radial profile is calculated. Note that the photon event table contains information on the arrival time, detector location and energy of all PSPC photon events. The projected radial

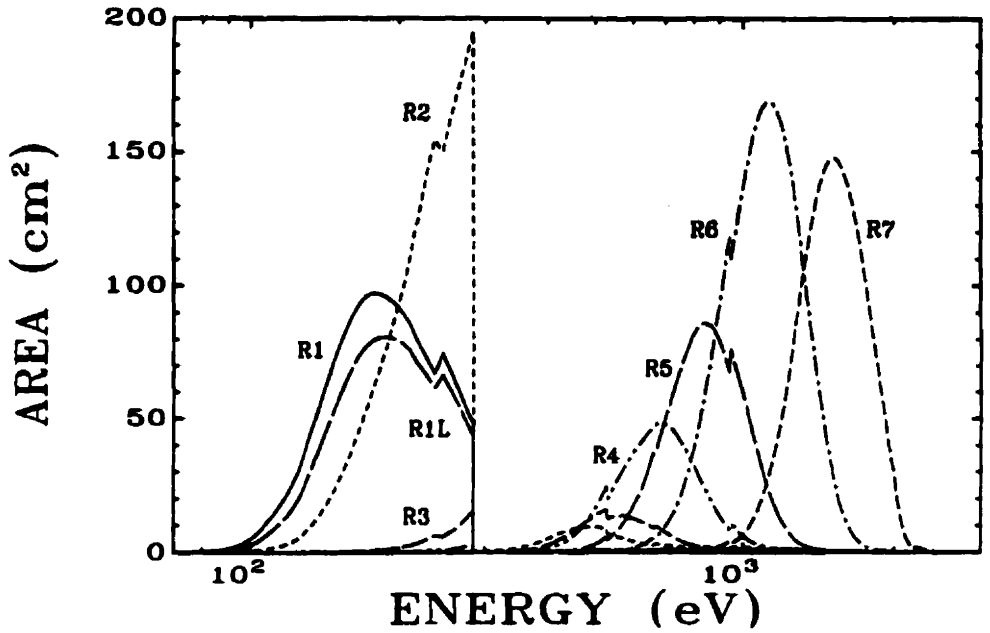

Figure 4.3: This plot shows the on-axis response curve for the pulse-height band definitions suggested by Snowden et al. (1994). The sharp edge at 0.284 keV is caused by the carbon Kα absorption edge of the PSPC entrance window. Bands falling below the Kα edge cover the ROSAT soft energy band (0.1-0.4 keV), while bands above the edge cover the ROSAT hard energy band (0.5-2.0 keV). The ROSAT bands R4 to R7 cover the energy range relevant to intracluster X-ray emission.

profile of the X-ray surface brightness is then obtained by averaging over all remaining photons in radially increasing annular regions of 15″ width, centered on the center of mass of the photon distribution. This averaging process neglects any deviations from spherical symmetry in the cluster and should therefore be used with caution. For a few clusters which showed a deviation from spherical symmetry, the radial profile was determined for both the entire cluster, and also for the sub-portion of the cluster containing the radio source of interest.

Abell	ROSAT[a] Phase	Sequence[b] number	Exposure ksec	count[c] rate s^{-1}	PI
75	RASS	...	0.422	0.17	...
76	PO	800317p	1.697	0.63	S. Murray
85	PO	800250p	10.238	3.51	C. Jones
119	PO	800251p	15.197	1.90	C. Jones
147	RASS	...	0.425	0.20	...
168	RASS	...	0.426	0.42	...
194	PO	800316p	24.482	0.52	S. Murray
262	PO	800254p	8.686	2.50	L. David
376	RASS	...	0.560	0.55	...
399	PO	800235p	7.457	0.94	J. Henry
400	PO	800226p	23.615	1.11	F. Owen
401	PO	800235p	7.457	1.93	J. Henry
426[d]	PO	...	...	...	...
496	PO	800024p	8.857	3.54	G. Kriss
569	PO	800575p	4.176	0.06	W. Voges
576	RASS	...	0.275	0.99	...
754	PO	800550p	8.156	3.33	U. Briel
779	PO	600547p	17.860	0.35	T. Maccacaro
1060	PO	800200p	15.764	4.16	G. Stewart
1185	RASS	...	0.260	0.33	...
1314	PO	800392p	2.932	0.44	R. Schwarz
1367	PO	800153p	18.745	3.65	W. Forman
1383	RASS	...	0.441	0.09	...
2247	RASS	...	1.397	0.09	...

[a]Phase of the ROSAT mission during which the cluster was observed: RASS - ROSAT All-Sky Survey, or PO - Pointed Observation

[b]ROSAT Data Archive sequence number for pointed observations.

[c]X-ray count rate in the ROSAT hard band, 0.5-2.4 keV

[d]Due to the large angular extent of this cluster, the final ROSAT image is a mosaic of multiple pointings.

Table 4.2: General ROSAT observational parameters for the target Abell clusters.

4.3.2 Fitting the β Model

As discussed in § 2.3.1, the X-ray surface brightness of the intracluster gas can be parameterized by a hydrostatic isothermal model of the form

$$S(r) = S_0 \left(1 + \left(\frac{r}{r_c}\right)^2\right)^{-3\beta+1/2} + S_b \tag{4.1}$$

where S_0 is the central surface brightness, r_c is the core radius, S_b is the background, and β is the ratio of the galaxy to gas temperature. The central surface brightness is initially determined for each cluster from the count rate in the central bin of the radial profile, with the final central surface brightness being determined from the best fit model. Similarly the background surface brightness is initially determined from the outer regions of the X-ray image, with the final background level being determined by the best fit model. The best-fit parameters for S_0, r_c , β, and S_b are determined by minimizing the χ^2 difference between the model, and the observed surface brightness profiles. The χ^2 minimization follows the Levenberg-Marquardt method (Press et al. 1988).

The fitting procedure provides the flexibility to exclude the inner or outer region of the observed surface brightness profile during the model fitting. This feature is particularly useful for clusters which display excess central emission, which can be due to a cooling flow, or a central point source. Attempts to fit a β model to the entire radial profile for clusters where there is excess central emission, result in fits that produce artificially small core radii, and β values. The artificially small values can be understood, since a decreased core radius provides a better fit of the central regions of the cluster, while a decreased β parameter compensates for small core radius by providing an increase in the emission at larger radii. It is important to be careful, however, when selecting regions for exclusion in the central parts of the cluster, as a selection of too large an exclusion region will result in an increased uncertainty in the determination of the cluster's core radius. The core radius in such a situation will also be biased toward larger values.

An additional flexibility that the program provides is the ability to fix one or more of the fit parameters. In a situation where the radial profile of the cluster under study is well determined through a large signal-to-noise throughout the cluster, the data are sufficient to constrain all four fit parameters for the β model. If, however, the signal-to-noise within the cluster is fairly low, as in the case of clusters observed during the All-Sky Survey, then the

data are often insufficient to accurately determine all four fit parameters. In this situation it is often necessary to fix either the central surface brightness or the background based on the observed radial profile.

4.3.3 Extracting the Cluster Gas Distribution

The final step in the analysis of the intracluster gas distribution is to convert the fitted count rates to an estimate of the X-ray flux in the rest-frame of the cluster. This conversion assumes the emission is due to an appropriately redshifted Raymond-Smith thermal spectrum (Raymond & Smith 1977) from intracluster gas at a given emission weighted mean ICM temperature. Although it is known that the temperature of the intracluster gas has a radial dependence, the assumption of a single temperature component for the ROSAT analysis appears to provide an adequate constraint on the ICM density distribution (Mohr et al. 1999). This reasonable fit is due to the fact that the spectrum of a thermal plasma has very little variation as a function of temperature within the spectral range of the ROSAT PSPC. This spectral variation is shown in Figure 4.4, where the PSPC count rate for a Raymond-Smith thermal spectrum is plotted as a function of the plasma temperature. The abundance of heavy elements is fixed at a value of 35% of solar for the thermal emission. The flux conversion also takes into account the absorption of soft X-ray emission due to the foreground Galactic neutral hydrogen. The neutral hydrogen column density toward each galaxy cluster was determined from the maps of Stark et al. (1992), and Cleary et al. (1979).

4.4 The Cluster Fits

Figure 4.5 displays the smoothed X-ray contour map of each cluster in our sample in J2000 coordinates in the left panel. Note that Abell 399 and Abell 401 are in shown in the same contour plot, with Abell 399 located in the lower right of the panel. The right-hand panels of Figure 4.5 show the radially binned X-ray surface brightness profile of each cluster. This profile displays the binned count rate as a function of radial distance from the cluster centroid in arcmin, where $1'$=120 detector pixels. Overlaid on each surface brightness plot is the best-fit β profile for the cluster. The profile for Abell 401 is displayed in the panel beside the contour plot, while that for Abell 399 is displayed below the Abell 401 profile.

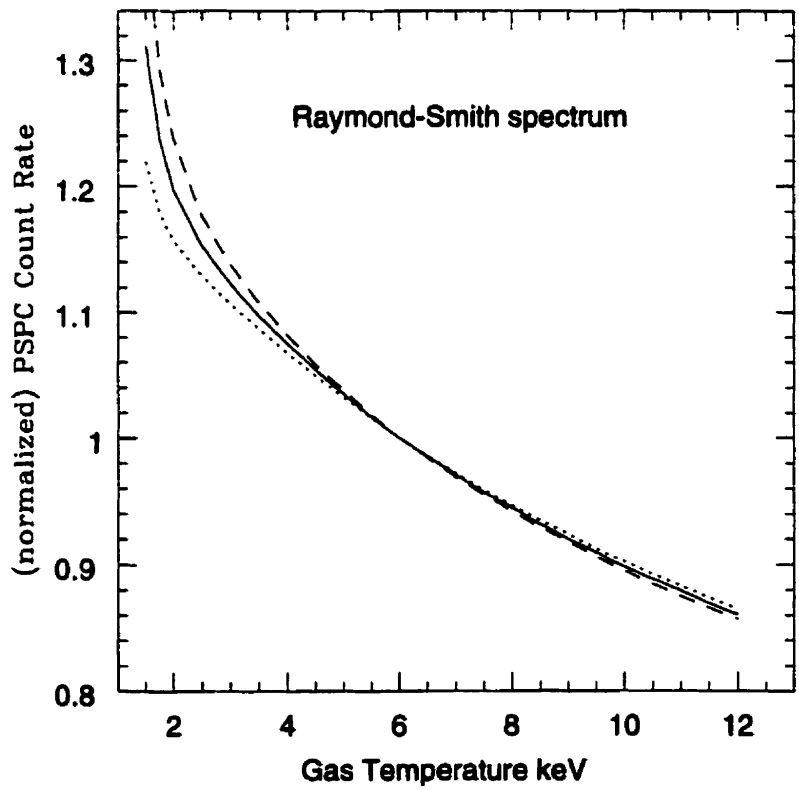

Figure 4.4: Plot of the normalized (at 6.0 keV) PSPC count rate in the 0.5-2.0 keV band as a function of plasma temperature for the ROSAT PSPC detector. The emission model is a Raymond-Smith thermal model. Note that above 4 keV, the PSPC count rate shows a variation of less than 10% with gas temperature. The solid line represents 35% solar abundance in the emitting plasma, as used in the analysis. For comparison, the dotted line represents 20% solar abundance and the dashed line is for 50% solar abundance. Note also that there is very little variation in the count rate with abundance for temperatures above 4 keV.

Following the cluster plots, there is a section containing notes on the fits for individual clusters. Table 4.3 lists the Galactic Hydrogen column density toward each cluster, the emission-weighted mean gas temperature of the cluster, physical scale at the redshift of the cluster, and the radial bin size in arcseconds for the surface brightness profile. Table 4.4 provides the best-fit values of the central surface brightness, core radius, β, background surface brightness, the associated reduced χ^2, and the total X-ray luminosity and flux of the cluster in the rest-frame 0.1-2.4 keV band.

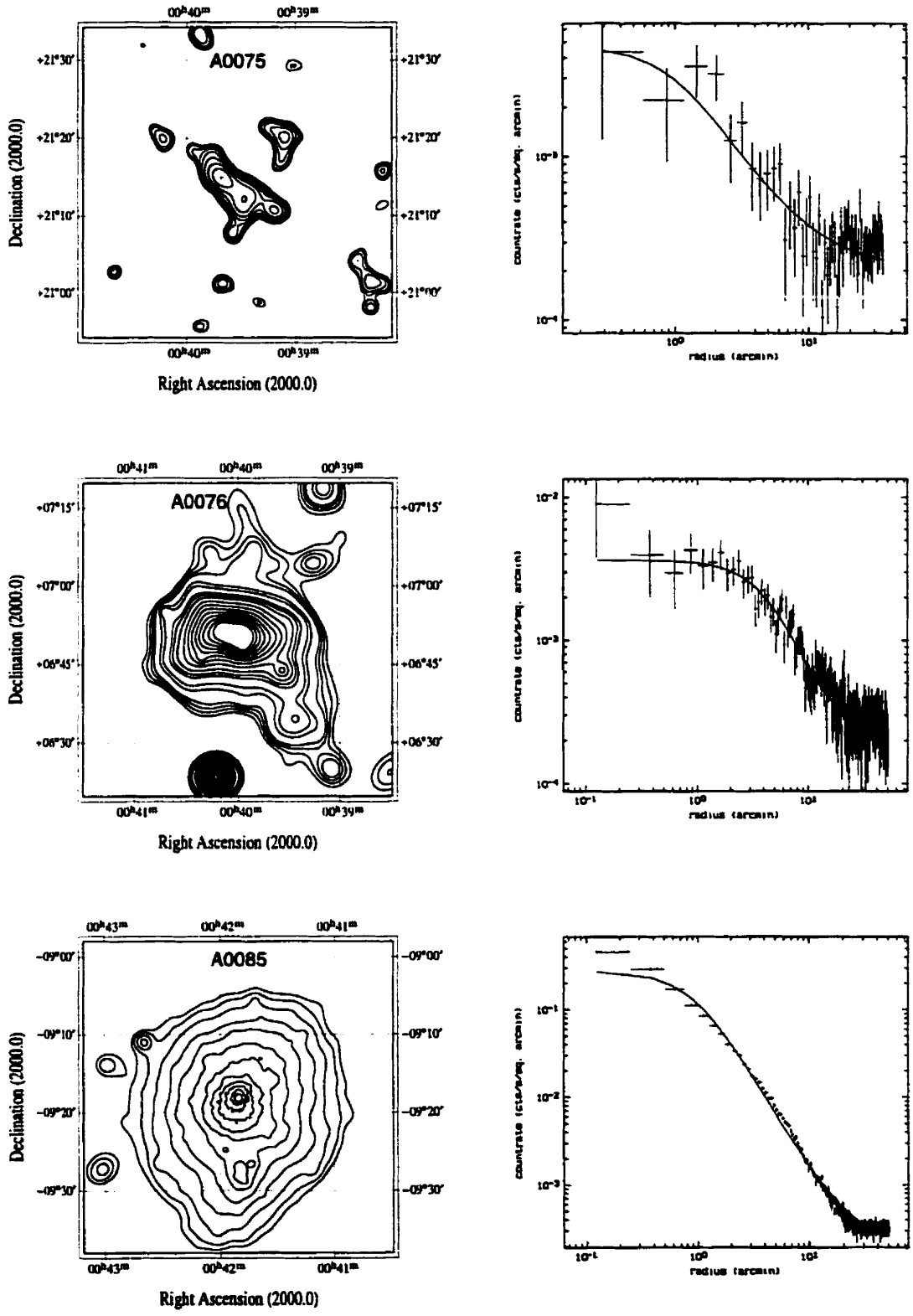

Figure 4.5: ROSAT hard band contour maps of Abell clusters are shown in the left panels. The right panels show the binned surface brightness profile in counts s^{-2} $arcmin^{-2}$ versus distance in arcmin. The solid line indicates the β fit model.

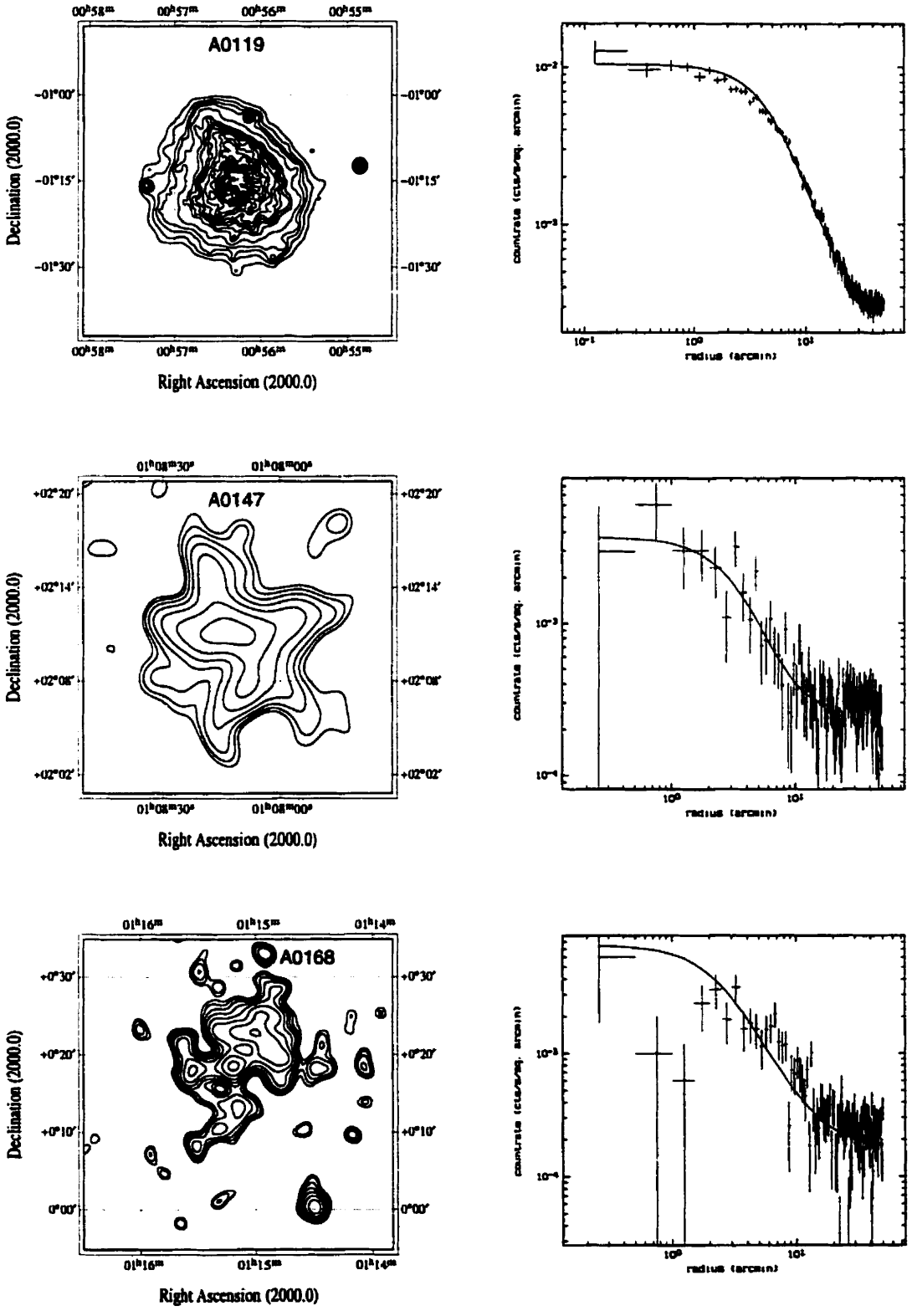

Figure 4.5 – *Continued*

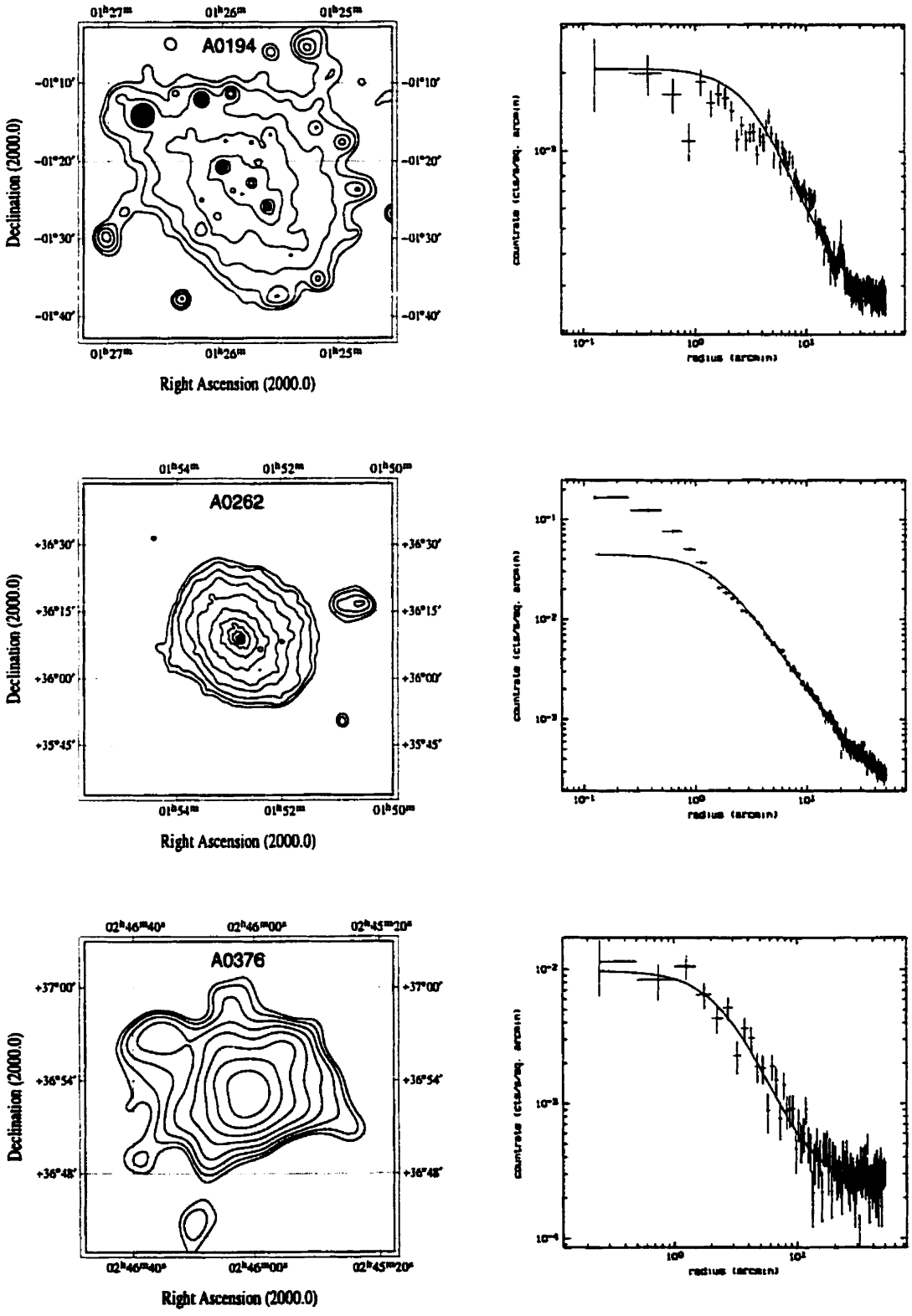

Figure 4.5 - *Continued*

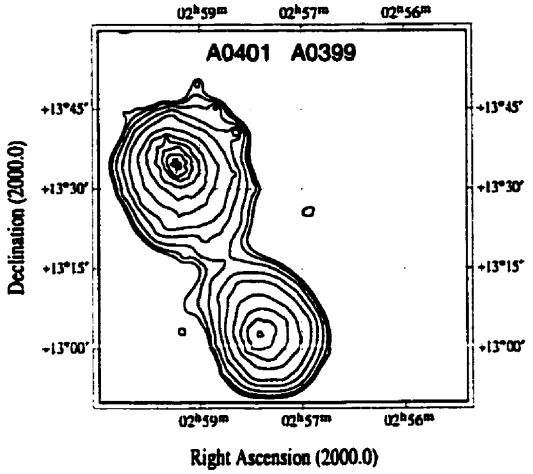

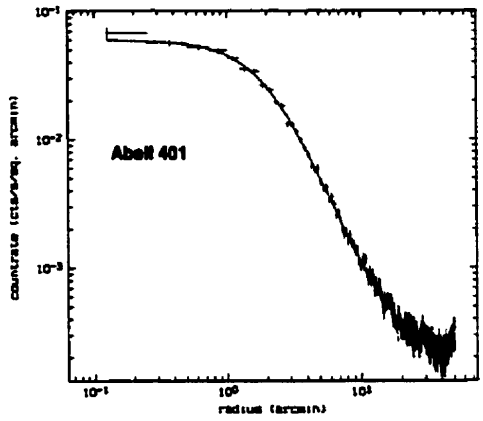

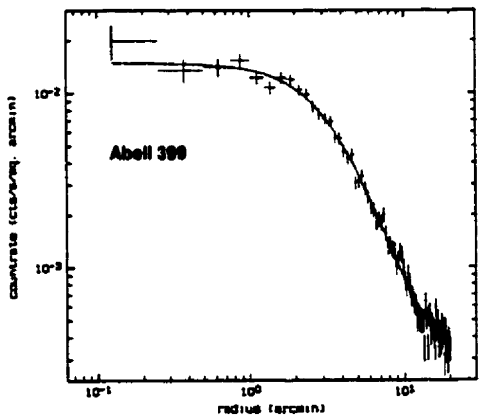

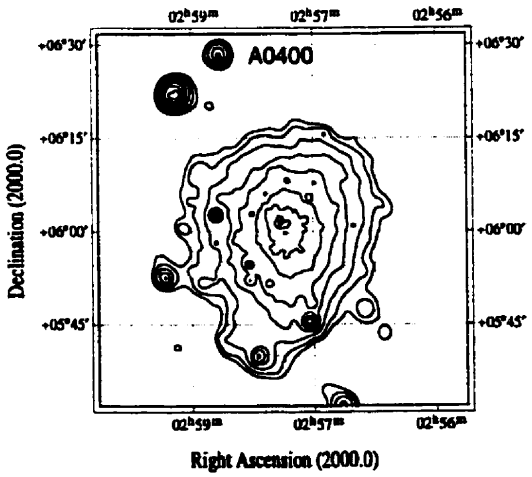

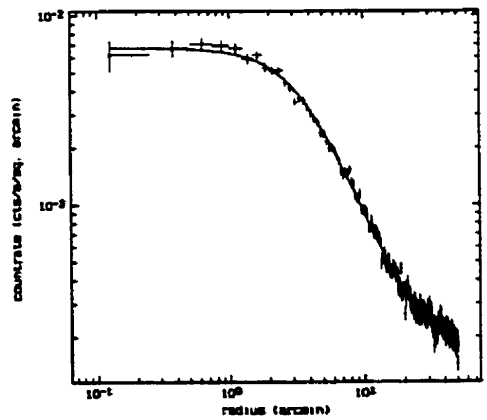

Figure 4.5 – *Continued*

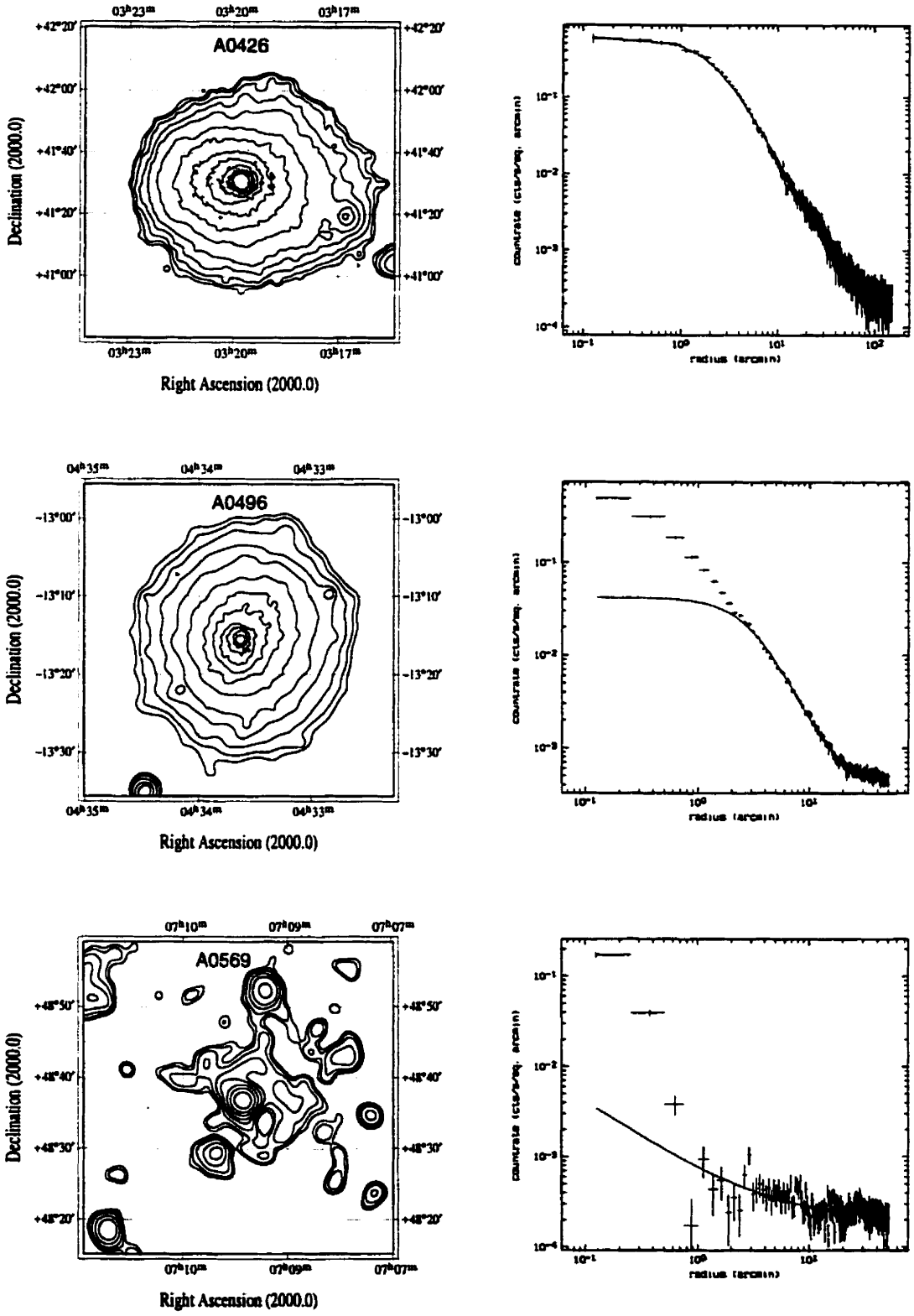

Figure 4.5 – *Continued*

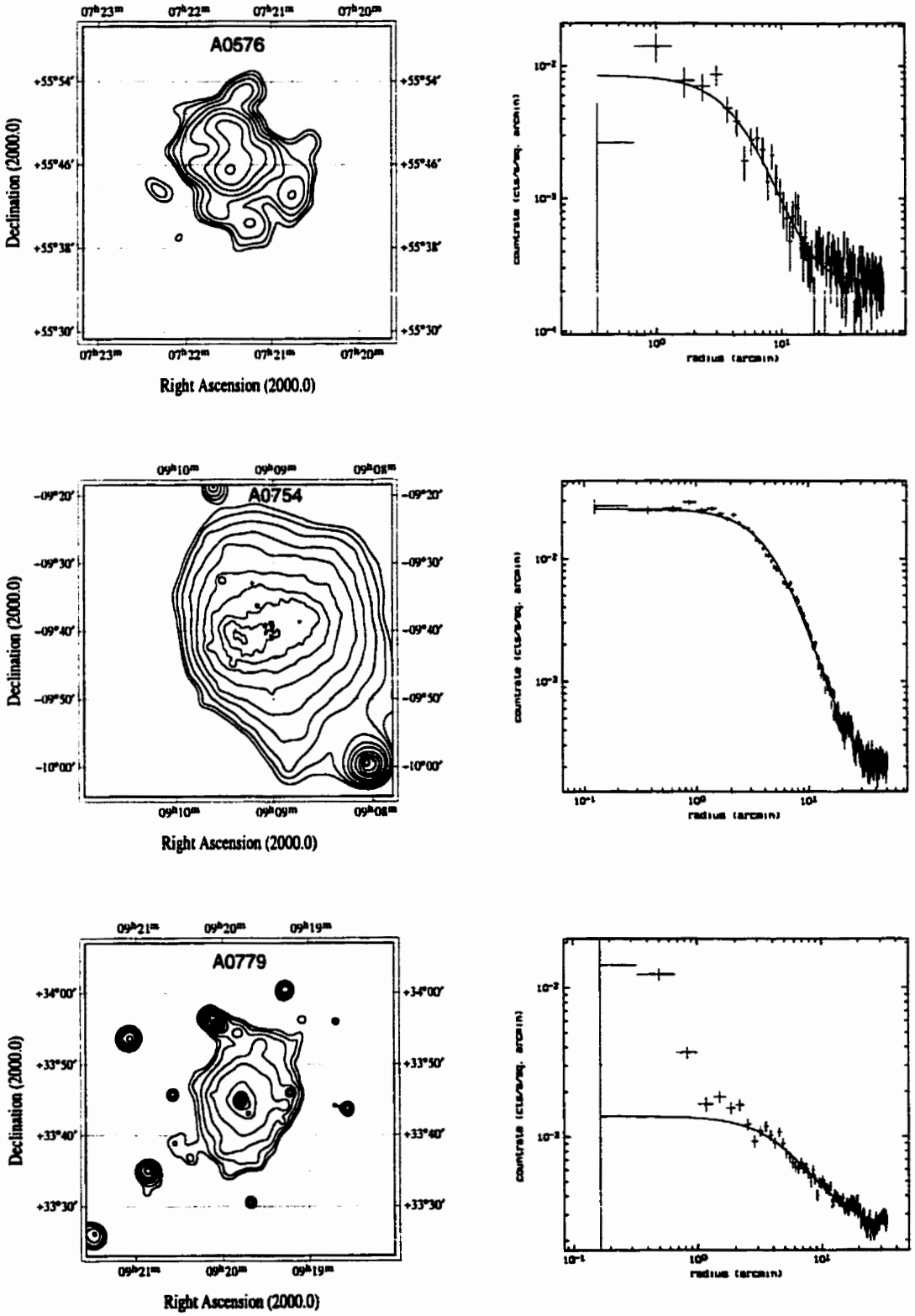

Figure 4.5 - *Continued*

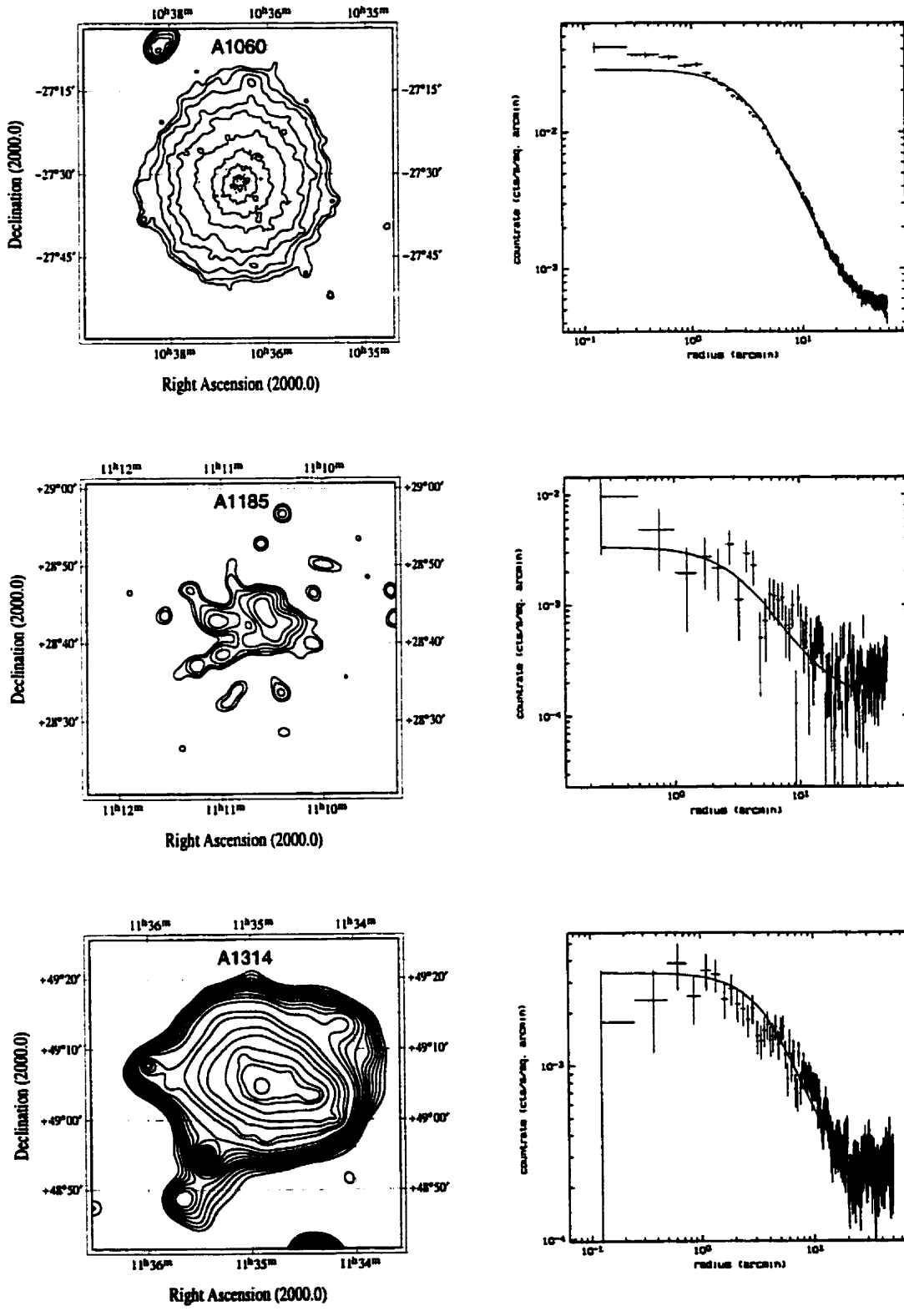

Figure 4.5 – *Continued*

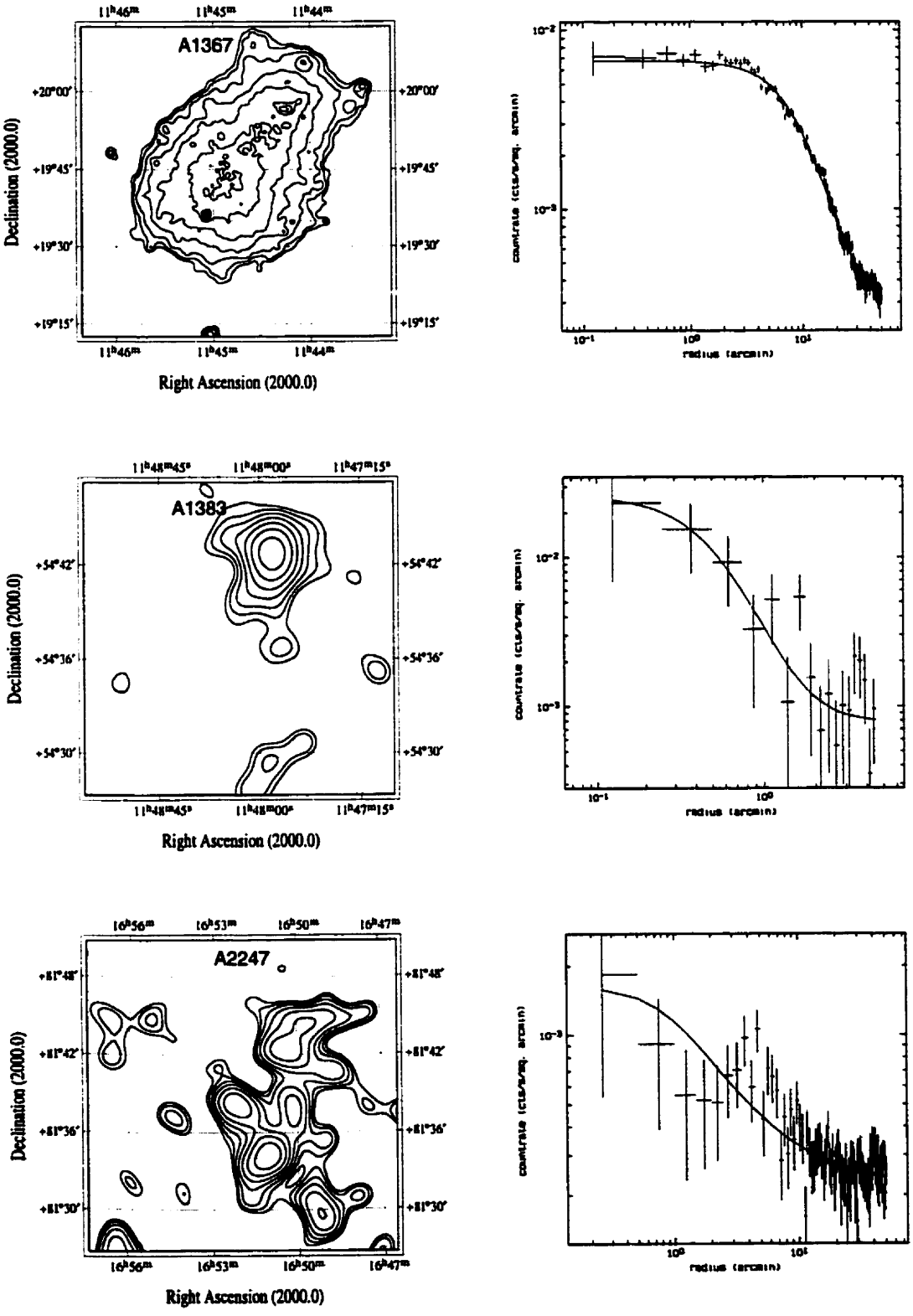

Figure 4.5 – *Continued*

Notes on individual clusters

- **Abell 75** The elongated nature of the X-ray emission from this cluster, together with the short exposure time from the RASS pointing make it difficult to provide an accurate fit to the surface brightness profile. Due to the sparse information available on this cluster, the best fit was determined by fixing the background level for the cluster, and allowing the central surface brightness, core radius, and β parameters to be fitted.

- **Abell 76** This boxy cluster contains several embedded X-ray point sources which were masked before binning the surface brightness profile. Despite the flattened nature of this cluster, the β model was found to be a reasonable approximation to the cluster emission.

- **Abell 85** This cluster displays fairly regular X-ray emission with a slight extension to the south, and a couple of X-ray point sources in the outer periphery of the diffuse X-ray emission. These regions were masked before determining the radial surface brightness profile.

- **Abell 119** The diffuse X-ray emission for this cluster contains several embedded X-ray point sources which were removed before determining the radial surface brightness profile of the cluster. The profile was determined both for the entire angular region of the cluster, as well as for a region excluding the X-ray extension to the North. There was no significant difference within the errors in the best-fit beta model to these two profiles. The profile displayed in Figure 4.5 is the fit to the entire angular region of the cluster.

- **Abell 147** The sparse data available for this RASS cluster results in a poorly constrained fit to the surface brightness profile.

- **Abell 168** The amorphous nature of this cluster results in a radial profile which drops in the two bins around 50″ from the cluster centroid. Although the best-fit β model cannot recover this radial variation, due to the spherical symmetry involved, the β model does provide a good fit to the outer regions of the cluster where the radio probes lie.

- **Abell 194** There are several X-ray point sources embedded within the diffuse cluster emission which were masked before determining the radial profile of this cluster.

- **Abell 262** This cluster displays very symmetric, diffuse X-ray emission. Note, however, that the high central count rate of 10^{-5} photons pixel^{-2} s^{-1} suggests the presence of an X-ray point source. This dominant central emission is, in fact, associated with the central D galaxy of this cluster (Amram et al. 1994). The best-fit β model was constructed by removing the central excess, and fitting the remaining diffuse cluster emission.

- **Abell 376** The contour plot for this RASS cluster displays fairly smooth X-ray emission.

- **Abell 399** This cluster is located in the outer regions of the PSPC image of its companion cluster Abell 401. The X-ray contours of Abell 399 display smooth, spherically symmetric X-ray emission, and the cluster is well fit by a β model.

- **Abell 400** Abell 400 contains several point X-ray sources embedded within the diffuse cluster emission. The surface brightness profile, excluding these sources, is well fit by a β model.

- **Abell 401** There are three point X-ray sources visible in the western periphery of the X-ray emission for this cluster. They were masked out prior to the determination of the X-ray surface brightness profile.

- **Abell 426** Although this cluster, also known as Perseus, contains the largest cooling flow of the sample, it is well fit through the entire profile by a single component β model.

- **Abell 496** The central region of this cluster is dominated by X-ray emission from the cooling flow. As the radio probes for this cluster are located beyond the cooling radius, the surface brightness profile fit is determined from a single β model fit to the data outside the cooling radius.

- **Abell 569** There is very little diffuse X-ray emission visible in the RASS image of this cluster. The X-ray emission is mainly dominated by compact X-ray sources. In fact, the central radio probe for this cluster lies within the central compact X-ray clump.

Due to the dominance of the X-ray emission from the central compact clump, it is not possible to obtain a reasonable fit to the radial profile through a single β model. The sparse RASS data also excludes the possibility of fitting this cluster through a two-component β model. For a spherical clump of free-free emitting gas, the X-ray luminosity, L_x, between energies E_1 and E_2 is related to the electron density, n_e, by (Rybicki & Lightman 1979)

$$L_x = 1.96 \times 10^{-27} g_{ff} n_e^2 R_{clump}^3 T^{1/2} \left(e^{-E_1/kT} - e^{-E_2/kT}\right) \text{ ergs s}^{-1}, \qquad (4.2)$$

where $g_{ff} \simeq 1.2$ is the Gaunt factor, and R_{clump} is the radial extent of the clump. A one-dimensional slice through the X-ray clump provides a radial extent of $\sim$38 kpc. The ROSAT X-ray luminosity between 0.1 and 2.4 keV for the clump was found to be 2.3×10^{42} ergs s^{-1}, yielding an electron density of $0.016^{+0.010}_{-0.007}$ cm^{-3} for the clump. The error associated with the electron density of the clump was determined from the error associated with the measurement of the radial extent of the clump.

- **Abell 576** The X-ray contours for this cluster reveal a compact, fairly symmetric, diffuse X-ray component. Although the surface brightness profile displays an X-ray deficit in the central bin (1′), the outer regions of the cluster appear to be well fit by a β model.

- **Abell 754** This cluster shows a very prominent central east-west elongation which is a result of the fact that the cluster is in the late stages of a merger event (Henriksen & Markevitch 1996; Roettiger et al. 1998). Additionally, the X-ray peak of the cluster emission is offset from the central region of the cluster. The best-fit β model was determined by varying the selected X-ray centroid and determining the model with the lowest overall reduced χ^2.

- **Abell 779** The diffuse X-ray emission from this cluster contains several embedded point X-ray sources in the outer periphery. The central region of the cluster also appears to be dominated by a compact X-ray source. This central excess, together with the outer point sources, was masked prior to fitting the surface brightness profile. This removal of the central excess will not affect the results at the position of the radio probe as the radio source lies well beyond the excised central region.

- **Abell 1060** This nearby galaxy cluster contains a weak cooling flow which is visible as a slight excess in the central 50″ of the surface brightness profile. The best-fit β model was determined from the binned profile outside this radius as the radio probes lie well beyond it.

- **Abell 1185** This cluster displays very patchy X-ray emission with slight extensions to the east. Note that the sparse nature of the RASS data is clearly visible in the binned X-ray surface brightness profile.

- **Abell 1314** The X-ray emission for this cluster is elongated in the east-west direction, and contains several embedded point X-ray sources. It is also interesting to note that the X-ray contours in the outer regions of this cluster show a very steep edge to the emission.

- **Abell 1367** The X-ray emission from the cluster displays a clear elongation to the north-west. This extended X-ray emission coincides with the location of a peripheral radio relic in this cluster. The extension to the north-west was masked during the determination of the surface brightness profile as the radio probe for this cluster lies in the central symmetric region of emission.

- **Abell 1383** Although the central region of this cluster contains a fairly high count rate, the surface brightness profile is sparsely sampled due to the combination of the compact nature of this cluster, and the fact that the data are obtained from the RASS archive.

- **Abell 2247** The RASS image for this cluster shows a patchy, extended region of X-ray emission. Due to the sparse nature of the available data, the best-fit β model was determined by holding the central surface brightness fixed and allowing the fitting routine to determine the best fit values of the core radius, β and X-ray background.

4.4.1 Estimating the Fit Errors

The uncertainties associated with the best-fit values of β, and r_c are determined by examining the χ^2 surface associated with these two fit parameters. The error surface is constructed by taking the central surface brightness, and background surface brightness as free parameters, and calculating the χ^2 values between the model and data on a grid of β and r_c. This

χ^2 surface is then used to calculate the 1σ errors on the β and r_c which are presented in Table 4.4.

4.5 Summary

This chapter presented the details of the X-ray observations and reductions for the galaxy cluster sample. The details of the cluster selection criteria were also outlined. The final sections of the chapter presented the X-ray determined cluster gas properties which will be used in the analysis in the remainder of this thesis.

Abell	z	N_H	T_g	kpc/′	R_{bin}	R_{out}[a]
		10^{20} cm^{-2}	keV		″	kpc
75	0.0626	3.45	3.0[b]	65	30	620
76	0.0416	4.02	1.5	45	15	990
85	0.0518	3.82	6.2	55	15	1410
119	0.0440	4.15	5.9	47	15	1640
147	0.0438	3.21	2.4[b]	47	30	400
168	0.0452	3.20	2.6	49	30	660
194	0.0178	3.44	1.4[b]	20	15	560
262	0.0161	5.78	2.4	18	15	660
376	0.0489	6.61	5.0	52	30	660
399	0.0715	13.90	5.8	74	15	1220
400	0.0232	10.80	2.5	26	15	840
401	0.0748	13.90	7.8	77	15	1650
426	0.0183	14.45	6.3	21	...	3000
496	0.0320	4.37	3.9	35	15	1000
569	0.0196	8.50	1.4[c]	22	...	330[d]
576	0.0381	5.51	4.3	42	40	650
754	0.0528	4.49	9.1	56	15	1740
779	0.0262	1.83	1.5[c]	25	15	570
1060	0.0114	5.03	3.9	13	15	650
1185	0.0304	1.62	3.9	34	30	400
1314	0.0314	1.45	5.0	37	15	750
1367	0.0215	3.16	3.7	24	15	1050
1383	0.0603	1.07	1.0[c]	63	30	250
2247	0.0392	4.52	4.4	43	30	430

[a]Outer radius of X-ray emission as traced by ROSAT observations.

[b]Ebeling et al. 1996

[c]White et al. (1997)

[d]Estimate based on radial slices through the ROSAT images

Table 4.3: Input parameters for cluster fits, Galactic hydrogen column density N_H from Stark et al. (1992), and Cleary et al. (1979), emission weighted gas temperature T_g from David et al. (1993) except where noted otherwise.

Abell	S_o	R_c	β	B_o	χ^2/ν	L_x [0.1 – 2.4]	f_x [0.1 – 2.4]
	10^{-13}			10^{-15}		10^{44}	10^{-12}
	ergs/s/cm^2/□′	kpc		ergs/s/cm^2/□′		ergs/s	ergs/s/cm^2
75	0.92	63^{+65}_{-14}	$0.40^{+.059}_{-.023}$	4.14	1.00	0.26	3.39
76	0.68	223^{+76}_{-30}	$0.59^{+.12}_{-.046}$	4.48	1.04	0.43	12.61
85	58.95	50^{+1}_{-1}	$0.53^{+.003}_{-.002}$	4.68	6.28	3.96	75.16
119	2.21	248^{+1}_{-6}	$0.59^{+.008}_{-.007}$	5.41	1.99	1.55	41.01
147	0.69	180^{+149}_{-41}	$0.68^{+.41}_{-.11}$	5.28	0.91	0.15	4.08
168	1.49	117^{+25}_{-12}	$0.53^{+.057}_{-.028}$	3.53	2.08	0.34	8.62
194	0.36	74^{+3}_{-3}	$0.41^{+.012}_{-.009}$	4.13	2.41	0.06	9.97
262	9.88	27^{+1}_{-1}	$0.44^{+.007}_{-.000}$	3.19	4.85	0.28	55.32
376	2.15	147^{+80}_{-19}	$0.59^{+.14}_{-.028}$	5.75	1.11	0.57	12.26
399	3.99	301^{+31}_{-19}	$0.72^{+.059}_{-.032}$	7.53	1.10	2.60	25.66
400	1.65	101^{+5}_{-4}	$0.53^{+.009}_{-.009}$	4.19	1.53	0.29	27.94
401	16.31	160^{+6}_{-4}	$0.60^{+.006}_{-.007}$	5.87	1.47	5.85	52.76
426	164.49	43^{+2}_{-1}	$0.55^{+.003}_{-.002}$	4.82	1.22	...	...
496	9.00	115^{+5}_{-6}	$0.63^{+.010}_{-.009}$	9.63	1.35	1.52	76.46
576	1.80	228^{+137}_{-11}	$0.72^{+.29}_{-.023}$	5.05	1.00	0.61	21.61
754	5.57	308^{+12}_{-6}	$0.72^{+.018}_{-.008}$	3.88	2.08	3.98	72.73
779	0.21	129^{+33}_{-21}	$0.50^{+.085}_{-.038}$	4.25	1.82	0.07	6.56
1060	6.16	50^{+1}_{-1}	$0.54^{+.005}_{-.005}$	9.85	2.14	0.23	91.33
1185	0.63	113^{+297}_{-103}	$0.53^{+1.0}_{-.12}$	2.75	1.37	0.12	6.54
1314	0.63	176^{+15}_{-13}	$0.60^{+.047}_{-.032}$	4.61	1.43	0.20	8.78
1367	1.35	262^{+10}_{-10}	$0.71^{+.025}_{-.017}$	5.84	2.00	0.68	76.24
1383	3.72	38^{+115}_{-35}	$0.74^{+1.1}_{-.022}$	11.46	0.87	0.09	1.31
2247	0.30	39^{+26}_{-10}	$0.34^{+.065}_{-.021}$	4.69	1.26	0.06	1.94

Table 4.4: Central surface brightness, core radius, β, and background surface brightness determined from the ROSAT X-ray fits. The associated reduced χ^2 for each fit is also listed. Note that the errors in R_c and β are 1σ. The last two columns in the table show the X-ray luminosity and flux for each cluster in the rest-frame 0.1–2.4 keV energy band.

Chapter 5

Rotation Measure Fitting

Overview: This chapter describes the method of determining the radio source rotation measures. Section 5.1 outlines the potential sources of error associated with the measured position angle of the polarized radiation. Some concerns which must be addressed during the determination of the rotation measure are discussed in § 5.2, together with the fitting routine used for the rotation measure determination. Section 5.3 provides the regression plots for the best-fit rotation measure of each radio source. At the end of this section, there are notes on the rotation measure fits of a few of the individual sources. The determination of the Galaxy-corrected rotation measure (residual rotation measure) for each radio source is discussed in § 5.4, and the radio source identifications are given in § 5.5.

5.1 Determining the Polarization Angle Error

The rotation measure induced along the line of sight between a polarized radio source and an observer is determined through observations of the position angle of the polarized emission at three or more wavelengths (§ 2.4.3), RM = $\Delta\chi/\lambda^2$. Before discussing the method of determining the rotation measure for each source in the radio sample, it is necessary to consider the errors associated with the measured position angle, χ. Recall that the position angle of the polarized emission is $\chi = \frac{1}{2}\arctan\frac{U}{Q}$, Equation 2.64. Formally, the error in the position angle, due to the (Gaussian) noise in the Stokes Q and U maps, is

$$\sigma_{\chi'} = \frac{1}{2P^2}(Q^2\sigma_U^2 + U^2\sigma_Q^2)^{1/2} \text{ radians,} \tag{5.1}$$

where $P = (Q^2 + U^2)^{1/2}$ is the polarized intensity. In the limit of ideal calibration and zero ionospheric contributions, Equation 5.1 would accurately represent the error associated with the position angle measurement. In reality, however, there are several other sources of error which must be taken into account, as they will affect the measured position angle of the polarized emission. Briefly, these contributions are:

- **Intrinsic:** The error in the intrinsic position angle of the emission from any source can be traced to the error associated with determining the right minus left phase offset correction. As discussed in § 3.3.3, the phase corrected matrix for 3C286 showed variations of approximately $\sigma_{\rm int}$=±2° in phase around the expected value.

- **Instrumental:** Polarization spill-over in antenna feeds results in an instrumental error term, which is vectorially added to the polarization percentage of the radio source, $\sigma_{\rm ins} = 0.1/\%P$.

- **Ionospheric:** Section 3.3.4 discusses the magnitude of the ionospheric Faraday rotation measure contribution to the measured position angles. Due to the timing of the observations near solar minimum, it was found that the ionospheric contribution ($\sigma_{\rm ion}$) to the position angles in the 20 cm band was less than 5°, while at 6 cm the ionospheric contribution is expected to be of order 1°. Note, however, that the measured polarization angle of 3C138 at 6 cm, listed in Table 3.3, displays variability at the level of 5°. Although the source of this variation is not completely understood, the effect is similar to ionospheric fluctuations at the level of 5°, and was thus included as such in the position angle error analysis.

The final error in the position angle measurements is determined from the summation in quadrature of each of the above sources of error:

$$\sigma_\chi = (\sigma_{\chi'}^2 + \sigma_{\rm int}^2 + \sigma_{\rm ins}^2 + \sigma_{\rm ion}^2)^{1/2}. \tag{5.2}$$

5.2 Rotation Measure Fitting

As discussed in § 2.4.3, the determination of a reliable rotation measure from a set of position angle observations at a number of wavelengths is complicated by the presence of $n\pi$ ambiguities in the measured position angle. It is therefore necessary to investigate a suite

of solutions to Equation 3.4, each of which provides a range of $n\pi$ rotations for the source data. The 'best' solution can then be determined through use of a regression coefficient. It must be noted, however, that as the number of $n\pi$ rotations increases, the goodness of fit to extreme values of rotation measure becomes artificially high due to the simplicity of fitting the data to a nearly vertical line. This tendency toward extreme rotation measure fits must be kept in mind when performing the regression analysis.

An additional consideration to keep in mind during the rotation measure fitting procedure is the variation of the degree of polarization of the radio source at different wavelengths. Depolarization of radio sources at long wavelengths is discussed briefly in § 2.6, and the depolarization ratio, DP, is given by Equation 2.72. Care must be taken in the analysis of sources which display large variations in the degree of polarization between short and long wavelengths, as this depolarization may be accompanied by non-linearities in the χ-λ^2 plot. In general, the data at any wavelength could be considered potentially corrupted when the degree of polarization drops below 25% of the maximum polarization (i.e. DP$\geq$ 4). The choice of the 25% level is suggested by the internal depolarization models of Burn (1966), and Gardner & Whiteoak (1966). In these models, the χ-λ^2 plot begins to deviate from a linear relation when the polarization drops below 25% of the maximum polarization. Note, however, the clear exception provided by the Crab nebula, where high depolarization ratios are not associated with significant deviations from a linear χ-λ^2 law (Burn 1966). Figure 5.1 shows a histogram of the depolarization ratio for the radio sources in the thesis sample. Note that there are 8 sources in the sample that do not have a depolarization ratio calculated due to a lack of 6 cm data. The mean depolarization ratio for the sources below the 25% limit is $\overline{DP} = 1.2$. Although there are five sources whose depolarization ratio is above the cutoff at DP=4, four of these are only slightly above the cutoff. The rotation measure fitting of these sources is discussed individually at the end of this section. Figure 5.2 shows a histogram of the maximum polarization percentage for the radio source sample.

Although sources displaying a high depolarization ratio have been specifically singled out in the fitting procedure for careful visual follow-up, it should be noted that all fits were verified individually and generally tested for robustness of fit through the variation of the combinations of wavelengths fitted, and multiple regression searches described below.

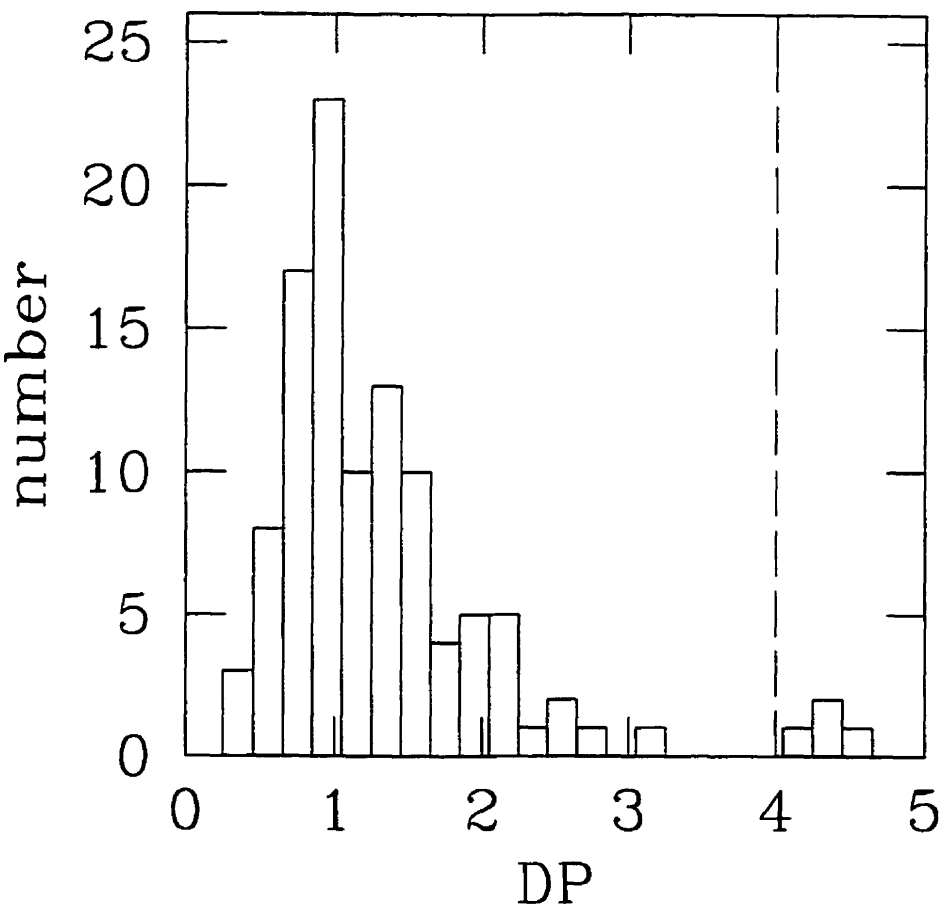

Figure 5.1: Histogram of the depolarization ratio for the radio source sample. Note that the depolarization ratio was calculated only for those sources which were detected in polarized flux at both 6 cm and 20 cm. There are 8 sources which were not detected at 6 cm, and thus do not have calculated depolarization ratios. In addition, one source, 1145+196, has a depolarization ratio of 19, and is not represented in the histogram. The data at long wavelength for sources whose depolarization ratio is above the dashed vertical line (DP=4) must be carefully examined during the rotation measure fitting procedure. The radio source sample contains a total of 5 sources, including 1145+196, which fall above this cutoff.

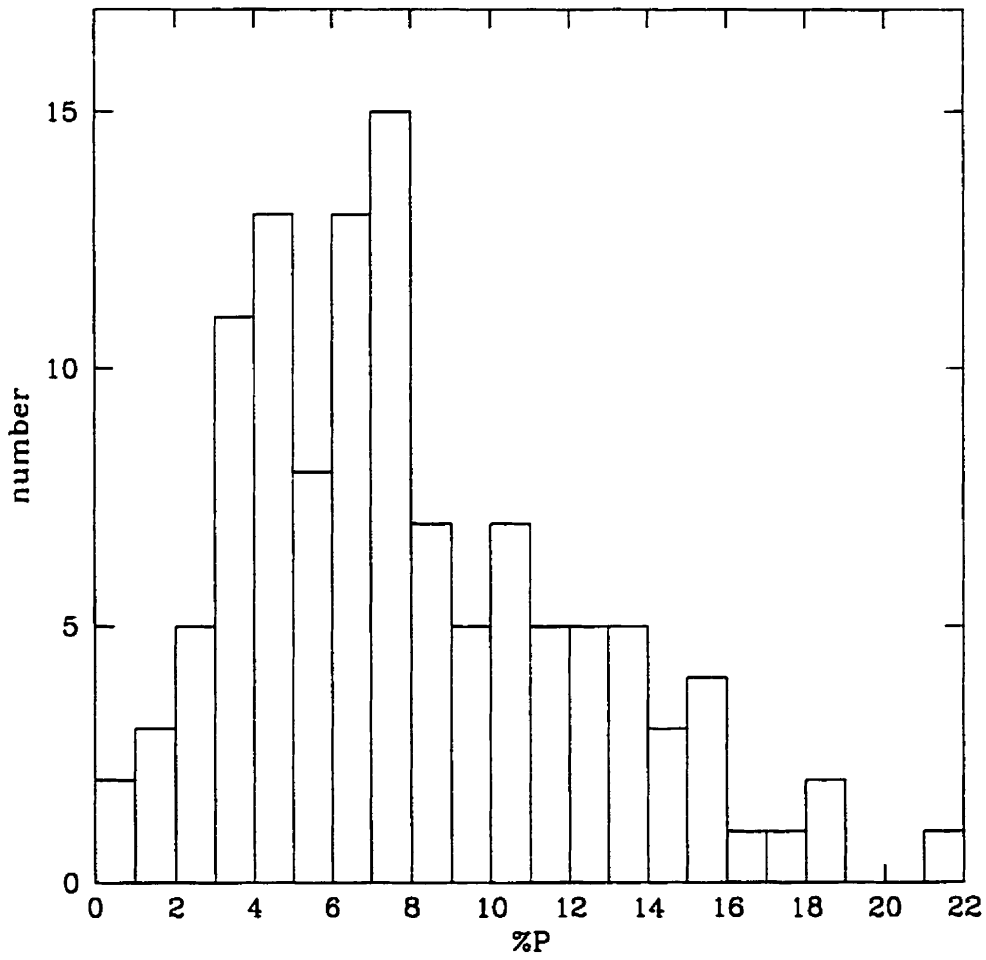

Figure 5.2: This histogram displays the maximum polarization percentage observed for the radio sample. The polarization percentage for the 8 sources, which were not observed at 6 cm, was calculated from the 20 cm data.

5.2.1 nπ Fitting Routine

The regression analysis routine used in the determination of the rotation measures is based on a routine developed under the supervision of P.P. Kronberg at the University of Toronto. Each session of the nπ program runs twice through a set of six searches for the best fit rotation measure. The first run through the program considers only the input data and associated errors during the fitting procedure, while the second performs a wavelength weighted fit to the data. The wavelength weighted fit depends heavily on the short-wavelength data and was only used as a tool to examine the robustness for the best-fit rotation measure. The rotation measure presented in this thesis are determined solely from data gathered during the course of this thesis. There is, however, additional polarimetry available in the literature on several of the sources studied. As a robustness check of the best fit rotation measure, a second session of nπ, which included all available data, was undertaken. In general, the best fit rotation measure from the second session was in fairly good agreement with that of the first session. Note, however, that the rotation measure determined from multiple epoch observations should be regarded with extreme caution due to the potential time variability of sources. For this reason, the multi-epoch fits are not considered further in this thesis.

The six search routines followed for the analysis are:

1. All input observations have an associated flag to indicate the reliability of the polarization data for a particular source. This flag also takes into account measurements which are only for part of a source so that they will not be combined with full source data when fitting the rotation measure. The first step in the fitting routine is to throw out all unreliable data based on the polarization flag. Although cutting on this flag is not necessary for the data obtained for this thesis, it was helpful for the robustness check which included polarization observations from the literature. At this stage, the program also rejects all data from wavelengths longer than 31 cm as these data are almost certainly corrupted by source depolarization and Galactic background contamination of the polarization. The remaining data set is then used in a least squares regression analysis which allows for nπ ambiguities in the polarization angle measurements. The rotation measure fit is constrained by upper and lower limits to avoid the problem of arbitrarily good fits to extremely high values of rotation measure. For the

purposes of this work, the rotation measure limits were set to $\pm$ 1000 rad m^{-2}. The best fit plots in Figures 5.3 and 5.4 show the result of this search.

2. Using the data set from Step 1, the program then searches for nearby data points which have $\Delta\lambda^2 < 10$ cm^{-2}. Points satisfying this criterion are averaged together, and the regression analysis is performed on these data plus the remaining unaveraged points. In the case of observations undertaken for this thesis, the two 6 cm points are averaged for this second rotation measure fit.

3. Again using the unaveraged data from Step 1, all data points with polarized flux below 25% of the maximum observed polarization are cut from the dataset. The remaining points are then used in a regression analysis to determine the rotation measure.

4. The fourth search takes the database from Step 3 and performs an average of nearby wavelengths as in Step 2. The regression analysis is then performed on the averaged data.

5. In this rotation measure search, all measurements from Step 1, at wavelengths shorter than that displaying the maximum polarization for the source, are removed. The regression analysis is then performed on the remaining data.

6. The final search involves averaging nearby wavelengths in the data from Step 5, and performing the regression analysis.

Note that in all six steps of the rotation measure fitting, the regression analysis is only performed if there are three or more wavelengths present after all selection cuts.

The best-fit rotation measure selected from each of the six searches is determined through the associated F ratio, which is the ratio of the mean variance from the fit to the mean variance calculated from the uncertainties associated with the polarization angles, an F ratio of 1 therefore represents a perfect fit. Following the completion of the fitting procedure, all output rotation measure fits were visually inspected to determine the quality of the fit. This visual inspection involved individually comparing the rotation measure fits, and F ratios calculated from each of the six steps. As mentioned above, the final rotation measure estimate was selected from the best-fit result from Step 1. The error associated

with the best-fit rotation measure is given by

$$\sigma_{RM} = \sqrt{\frac{1}{\sum_{i=1}^{N}\frac{1}{\sigma_i^2}\left(\lambda_i^2 - \frac{\sum_{i=1}^{N}\frac{\lambda_i^2}{\sigma_i^2}}{\sum_{i=1}^{N}\frac{1}{\sigma_i^2}}\right)^2}}, \tag{5.3}$$

where N is the number of position angle measurements, and σ_i is the error associated with each position angle measurement.

5.3 The Fits

This section presents the plots of the best-fit regression analysis to the χ-λ^2 data for all radio sources which had data at three or more wavelengths. The source plots are split between two separate figures depending on the impact parameter of the radio source with the nearest Abell cluster centroid. Figure 5.3 shows the rotation measure fits to sources which are viewed through the intracluster gas, while Figure 5.4 shows the fits for sources which fall beyond the edge of the intracluster gas. The distinction between these two samples is discussed in detail in § 6.1. For each source, the rotation measure plot contains four axes, and two sets of points: the left axis, associated with the solid points, shows the position angle of the polarized emission, while the right axis, associated with the open points, shows the polarization percentage for the source at each of the given wavelengths. The bottom and top axes of each graph are the wavelength (cm), and wavelength squared (cm^2), respectively, associated with the polarization angle measurement. The source name in J2000 coordinates is shown in light grey within each plot, and the best-fit regression is shown by the solid line. Near the top of each graph, the best-fit rotation measure and its error, and the intrinsic position angle at the source (χ_0) and its error are listed. The F ratio values are also listed for each of the fits. Note that the rotation measure fit for a resolved source is derived from the integrated polarization measurements at each wavelength. Following the rotation measure plots, there is a brief section containing notes on a few of the rotation measure fits.

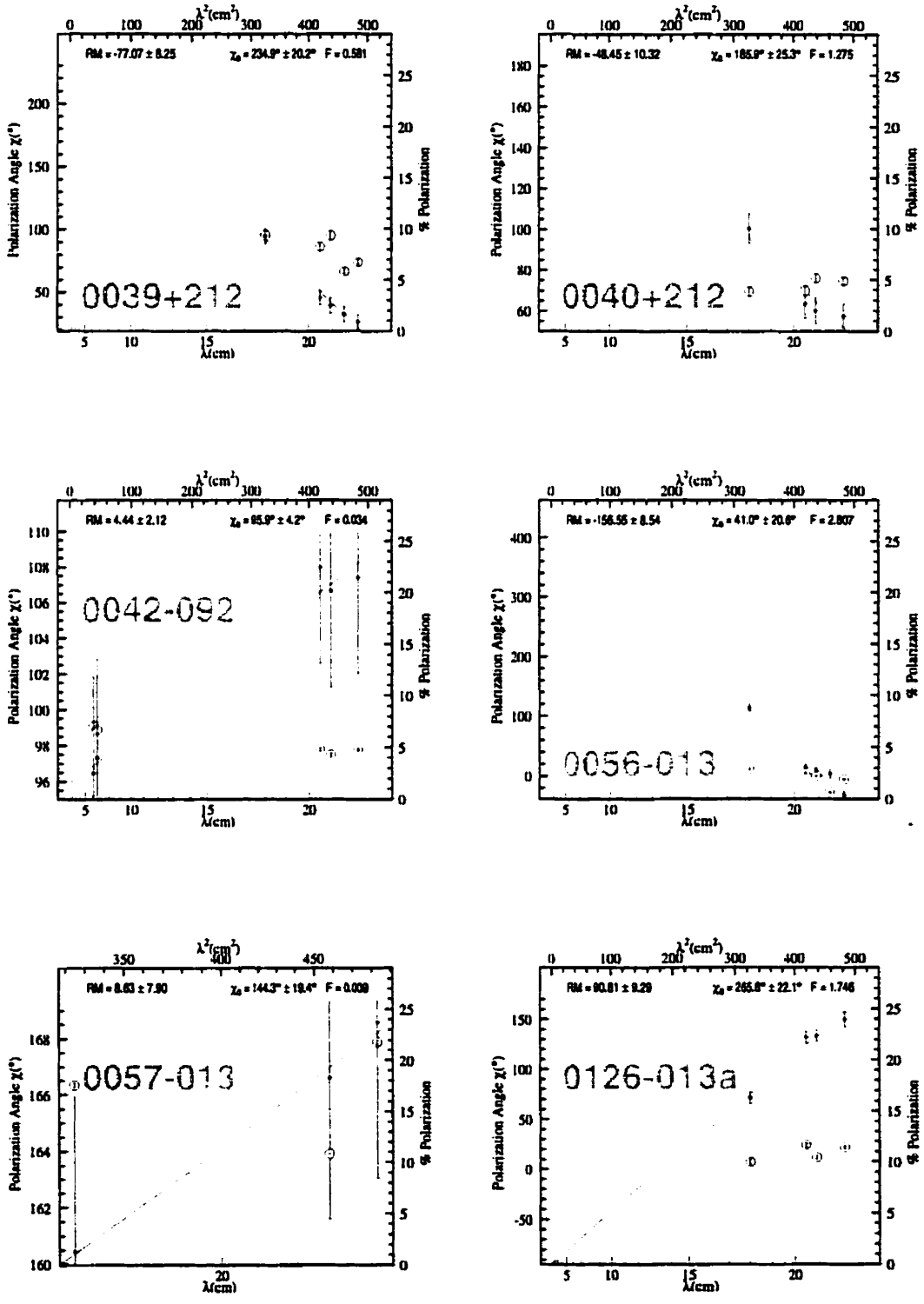

Figure 5.3: Polarization angle (closed points) versus wavelength squared for sources in the cluster sample. The slope of the best-fit line is the rotation measure, RM. Open circles indicate polarization percentage at the associated wavelength.

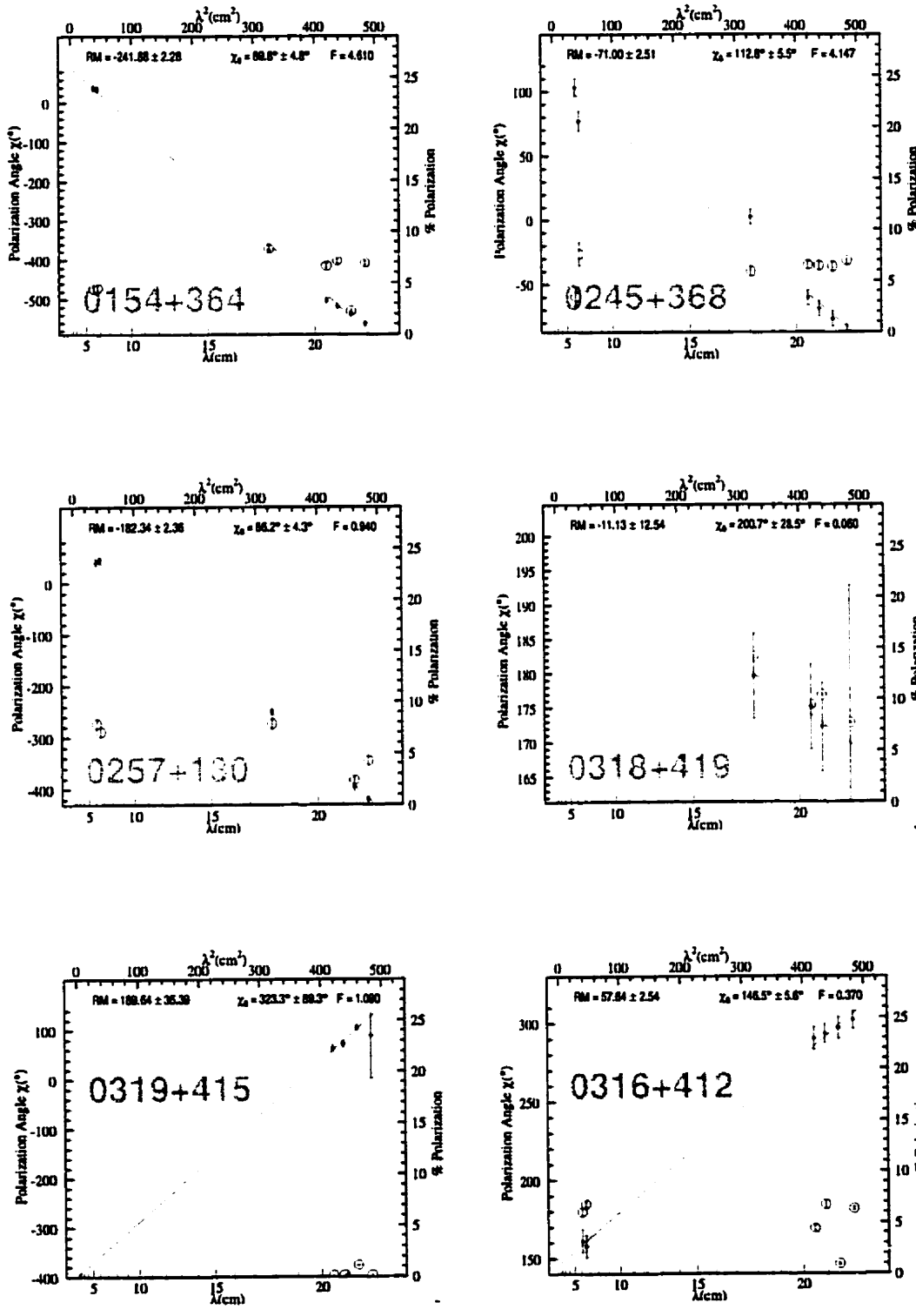

Figure 5.3 – *Continued*

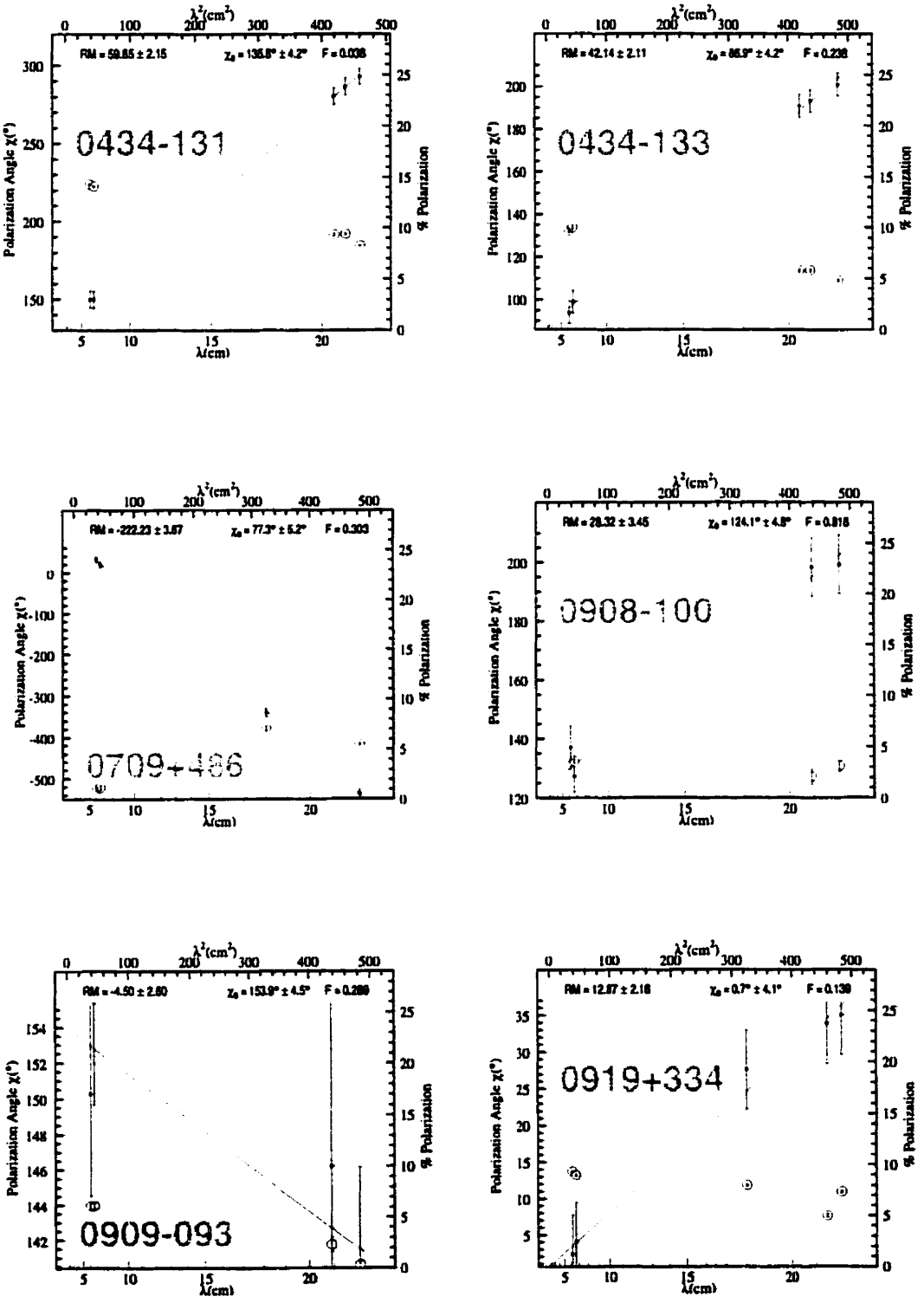

Figure 5.3 – *Continued*

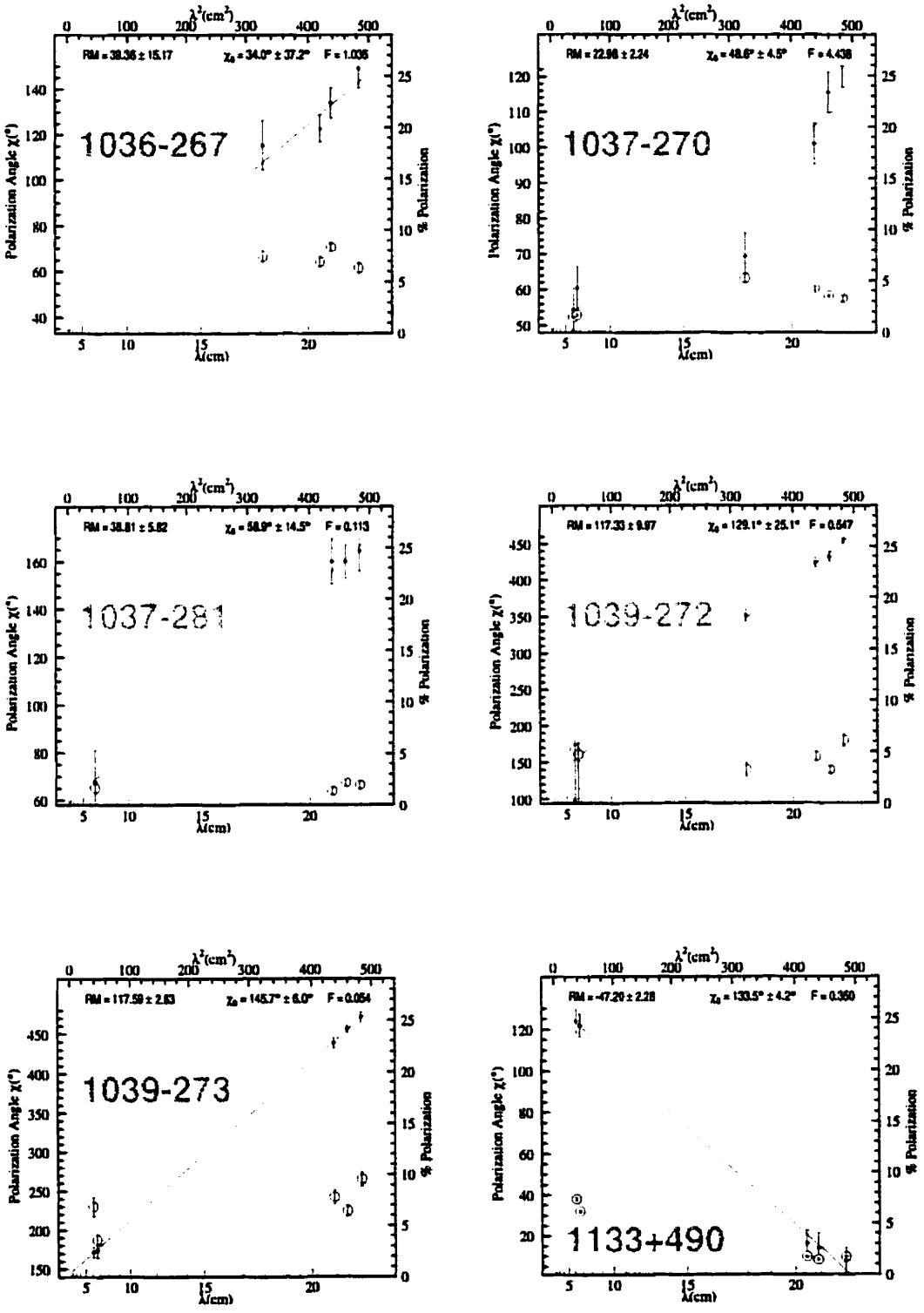

Figure 5.3 – *Continued*

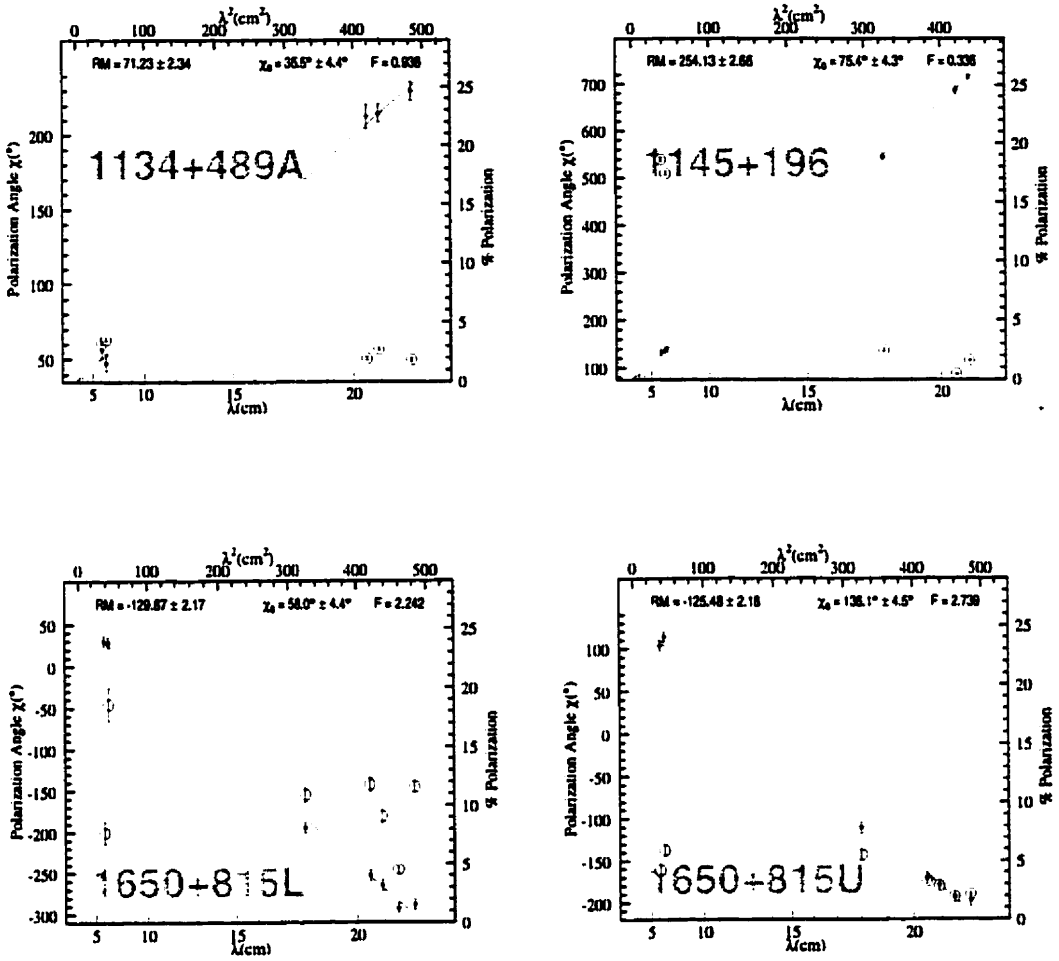

Figure 5.3 - *Continued*

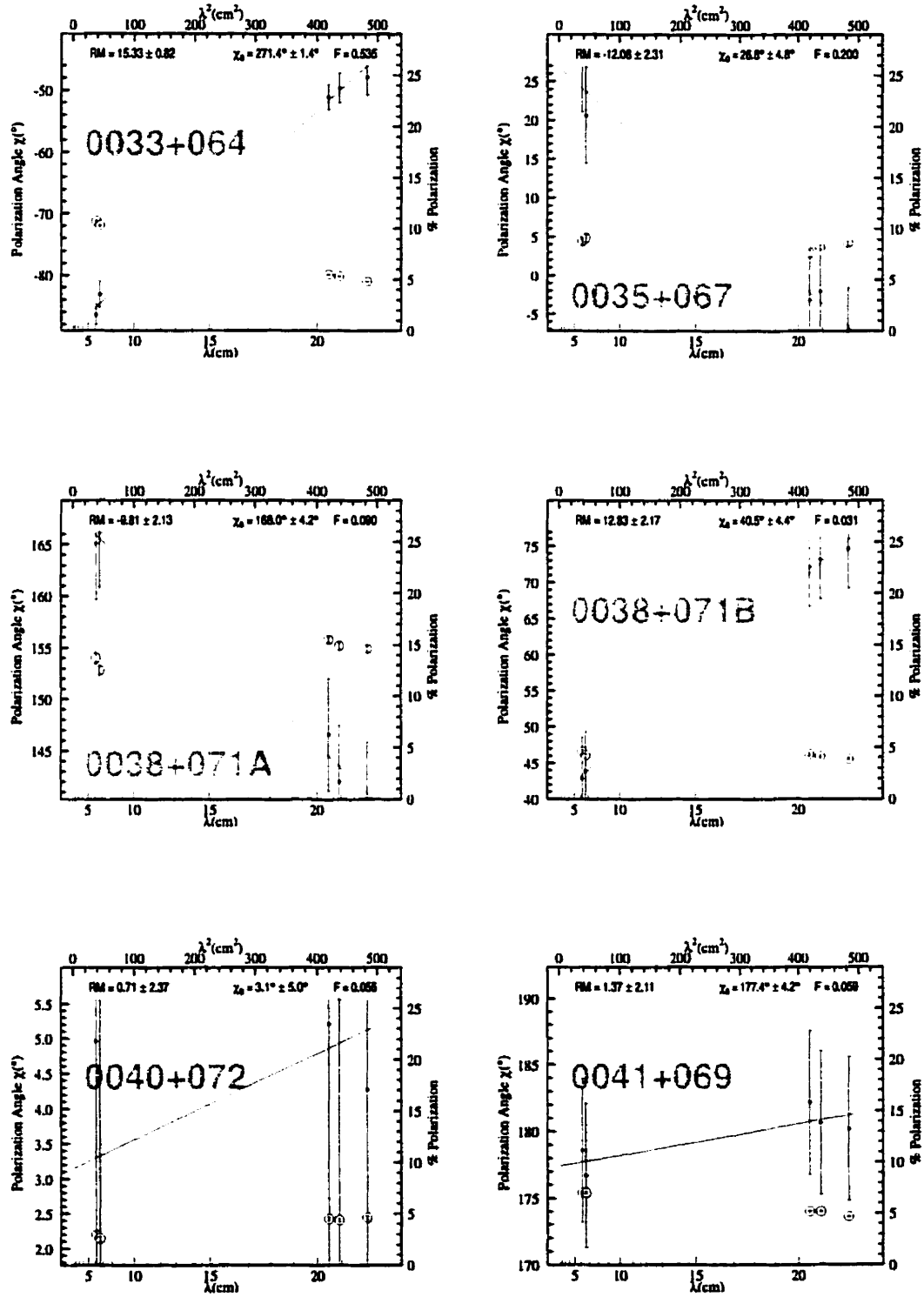

Figure 5.4: Polarization angle (closed points) versus wavelength squared for sources in the control sample. The slope of the best-fit line is the rotation measure. Open circles indicate the polarization percentage at the associated wavelength.

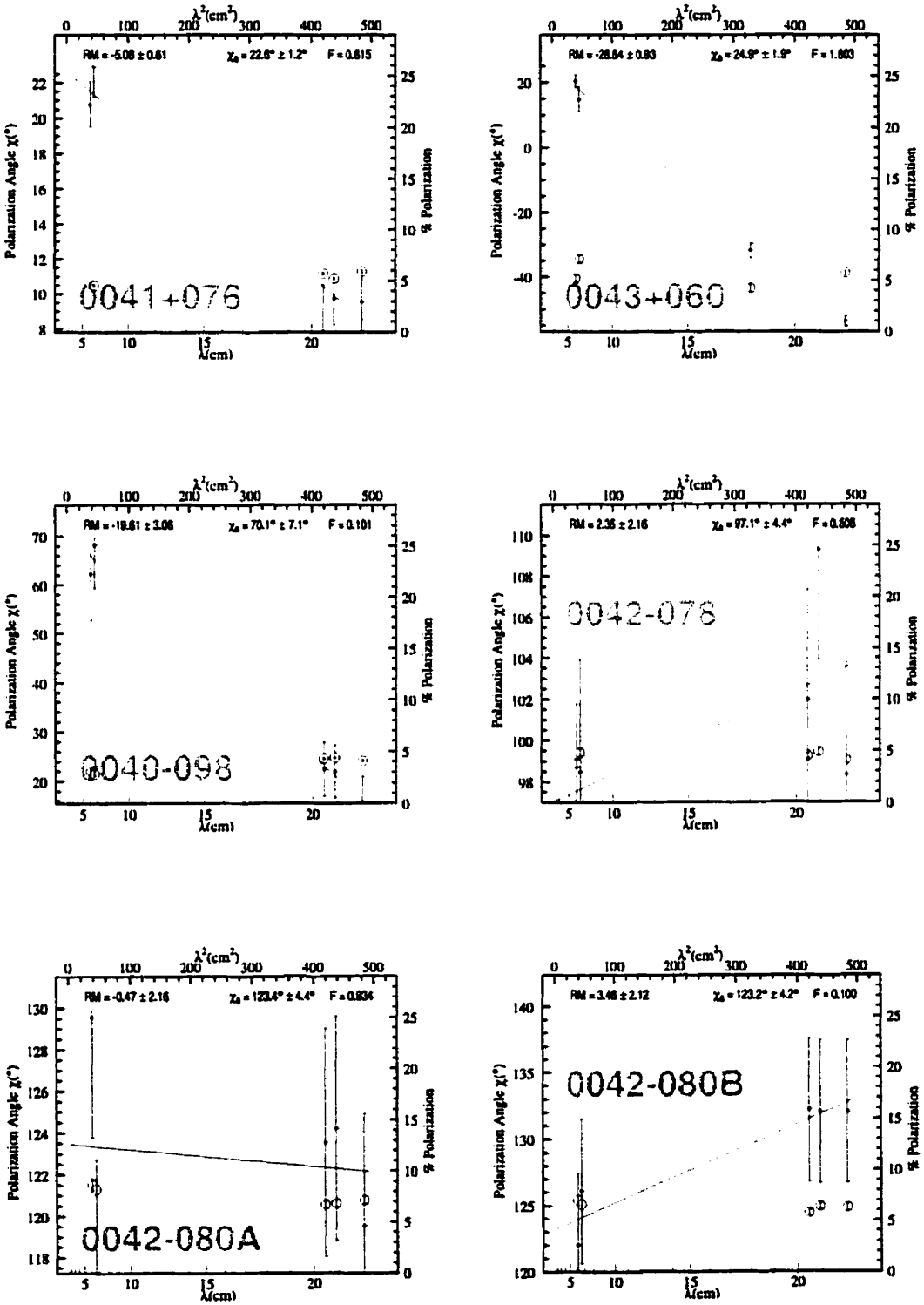

Figure 5.4 – *Continued*

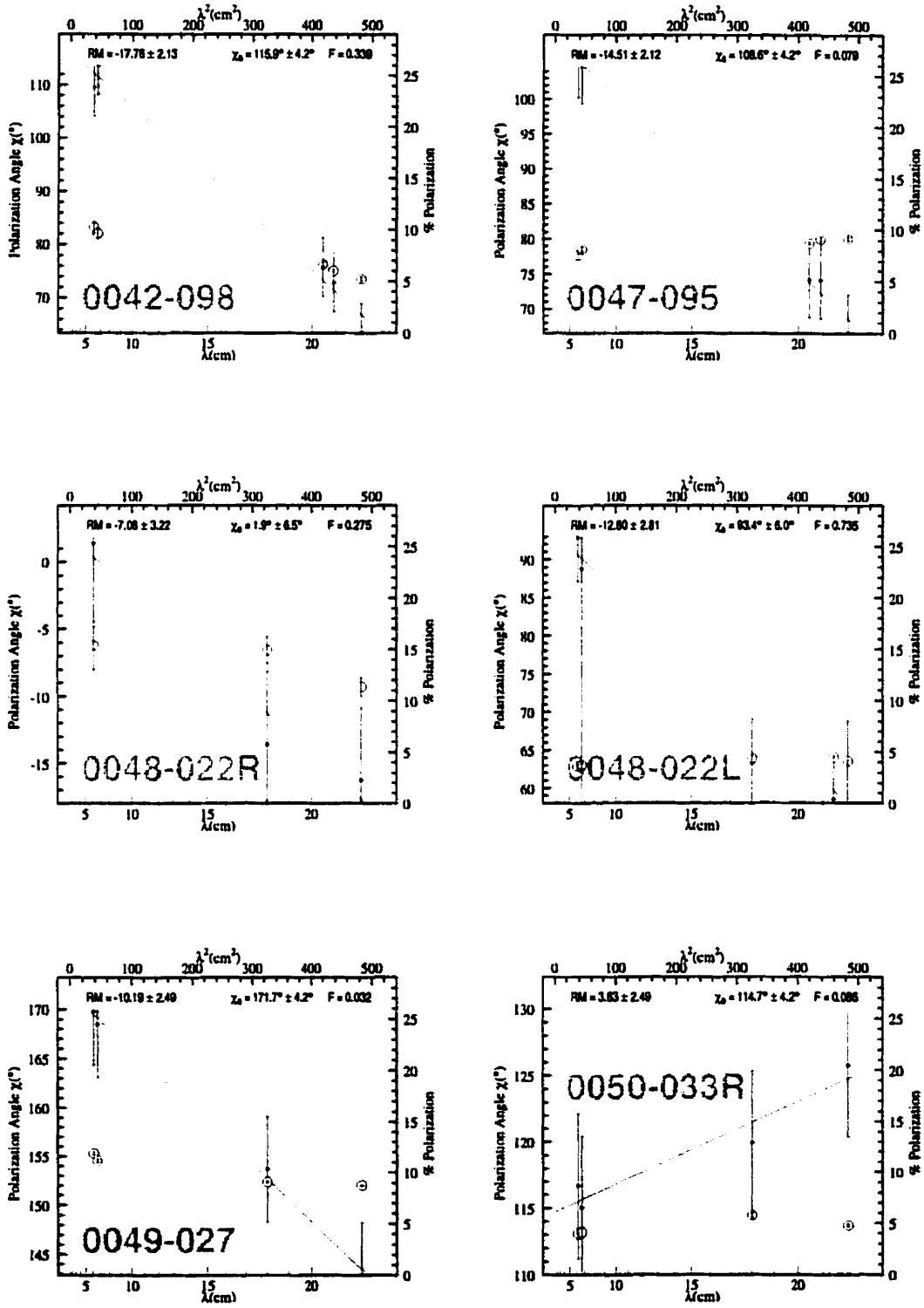

Figure 5.4 – *Continued*

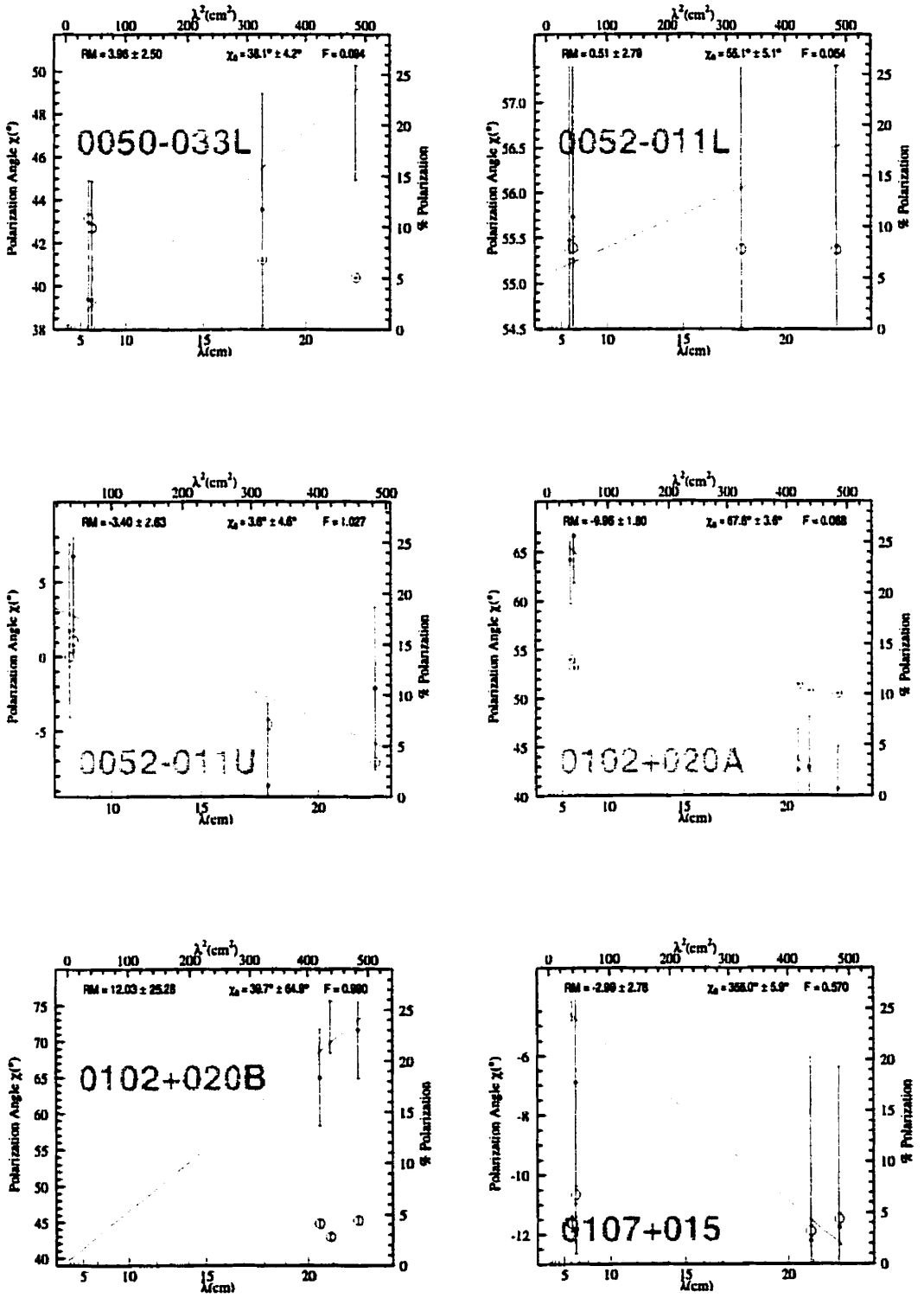

Figure 5.4 – *Continued*

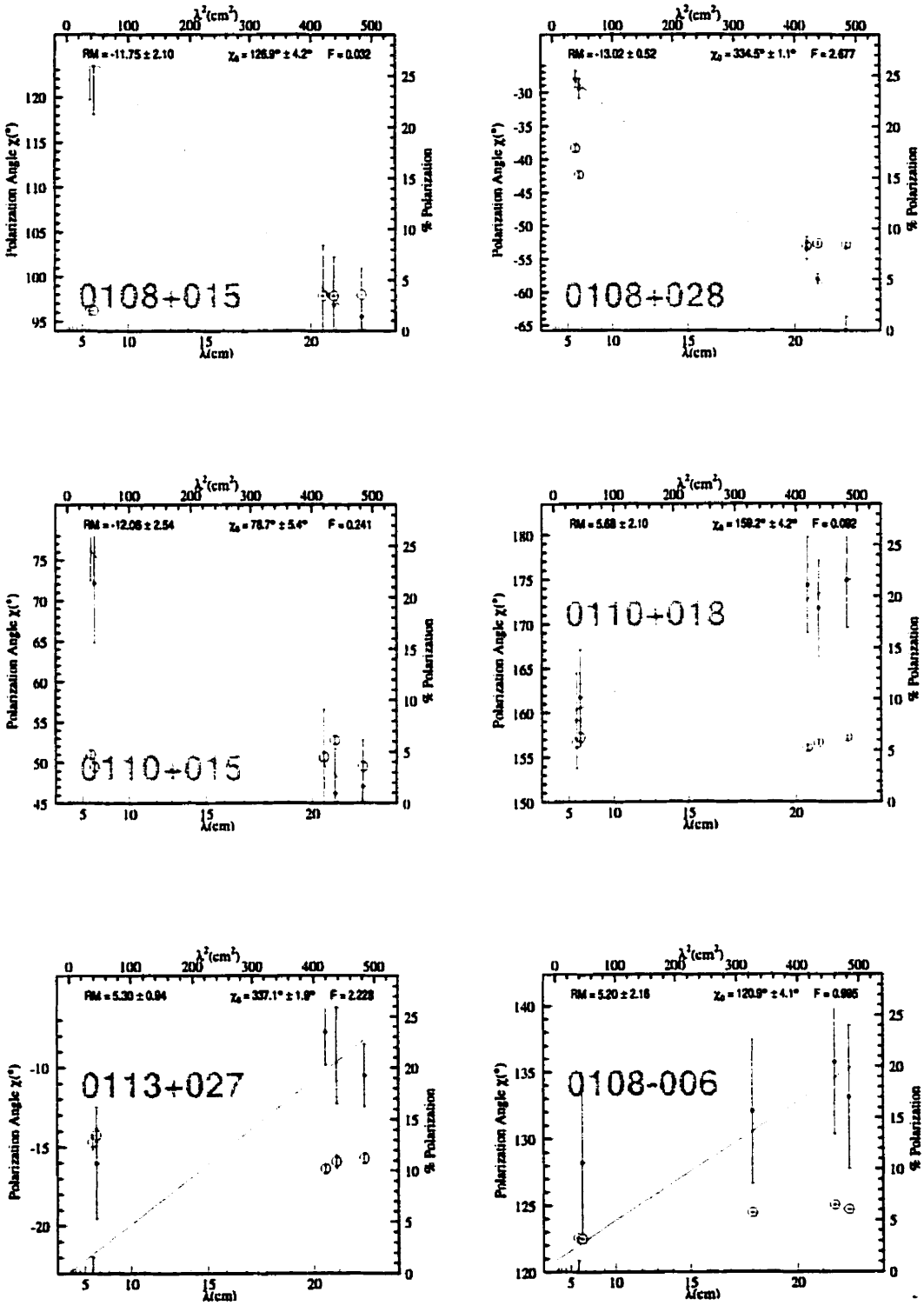

Figure 5.4 – *Continued*

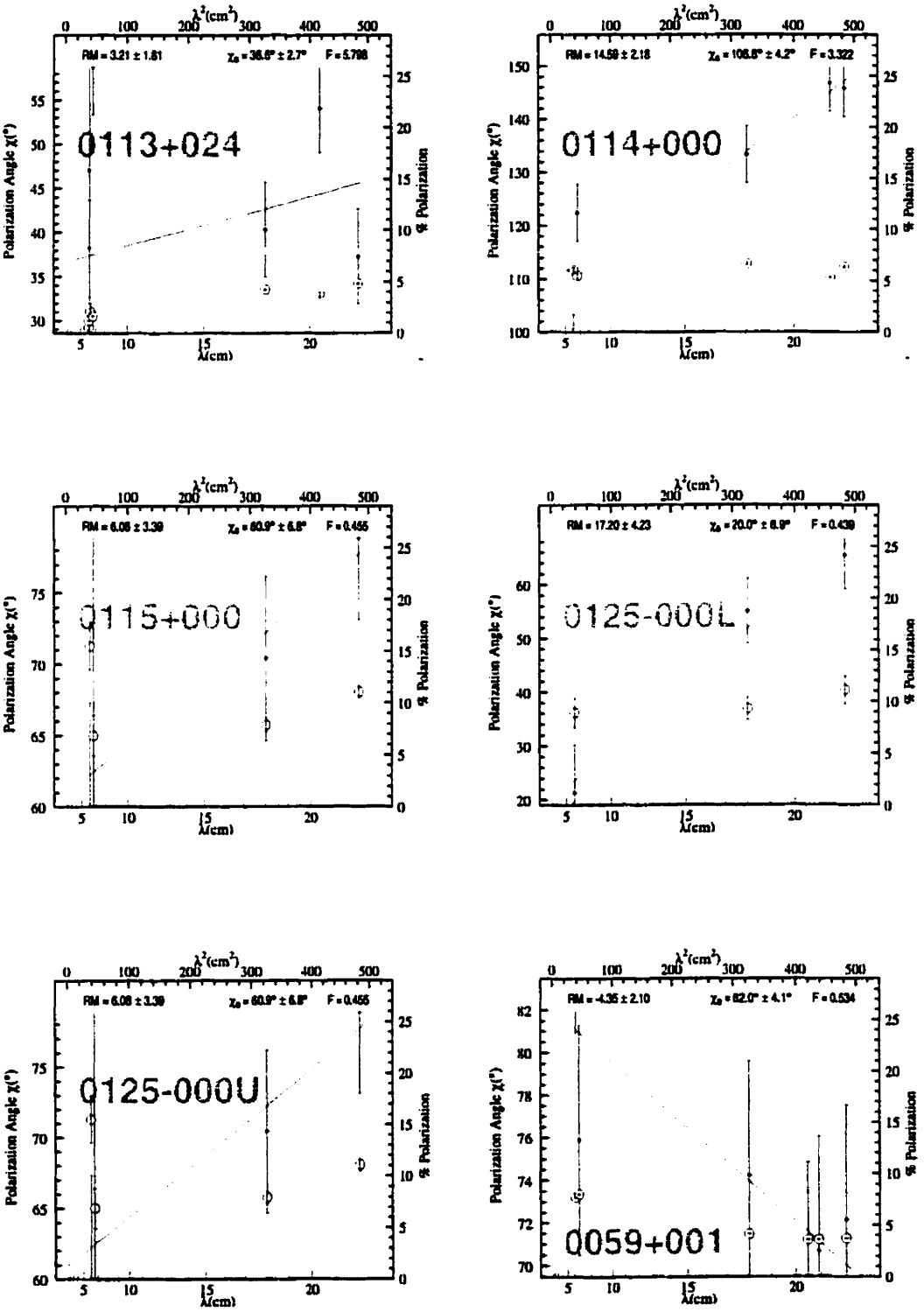

Figure 5.4 – *Continued*

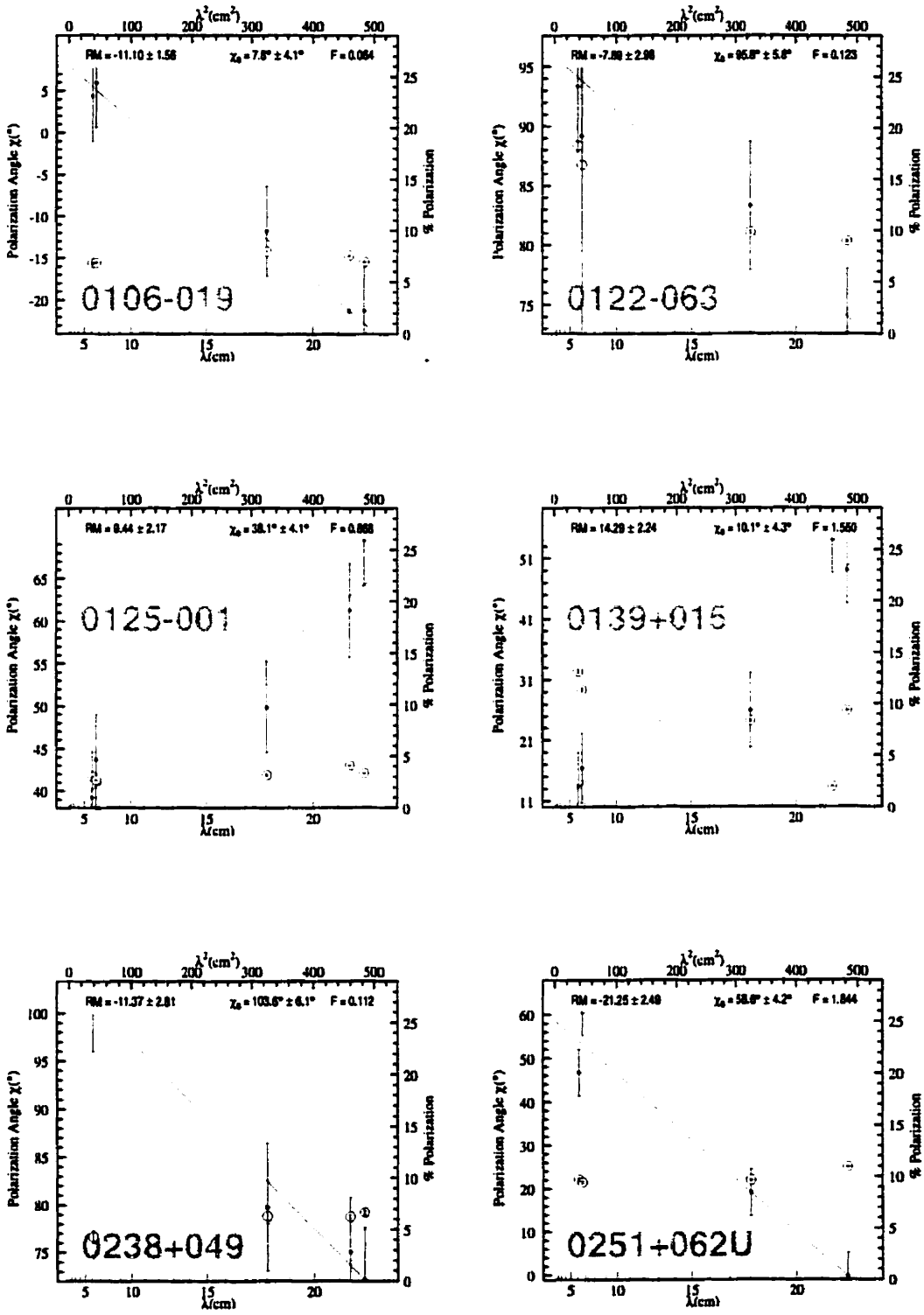

Figure 5.4 – *Continued*

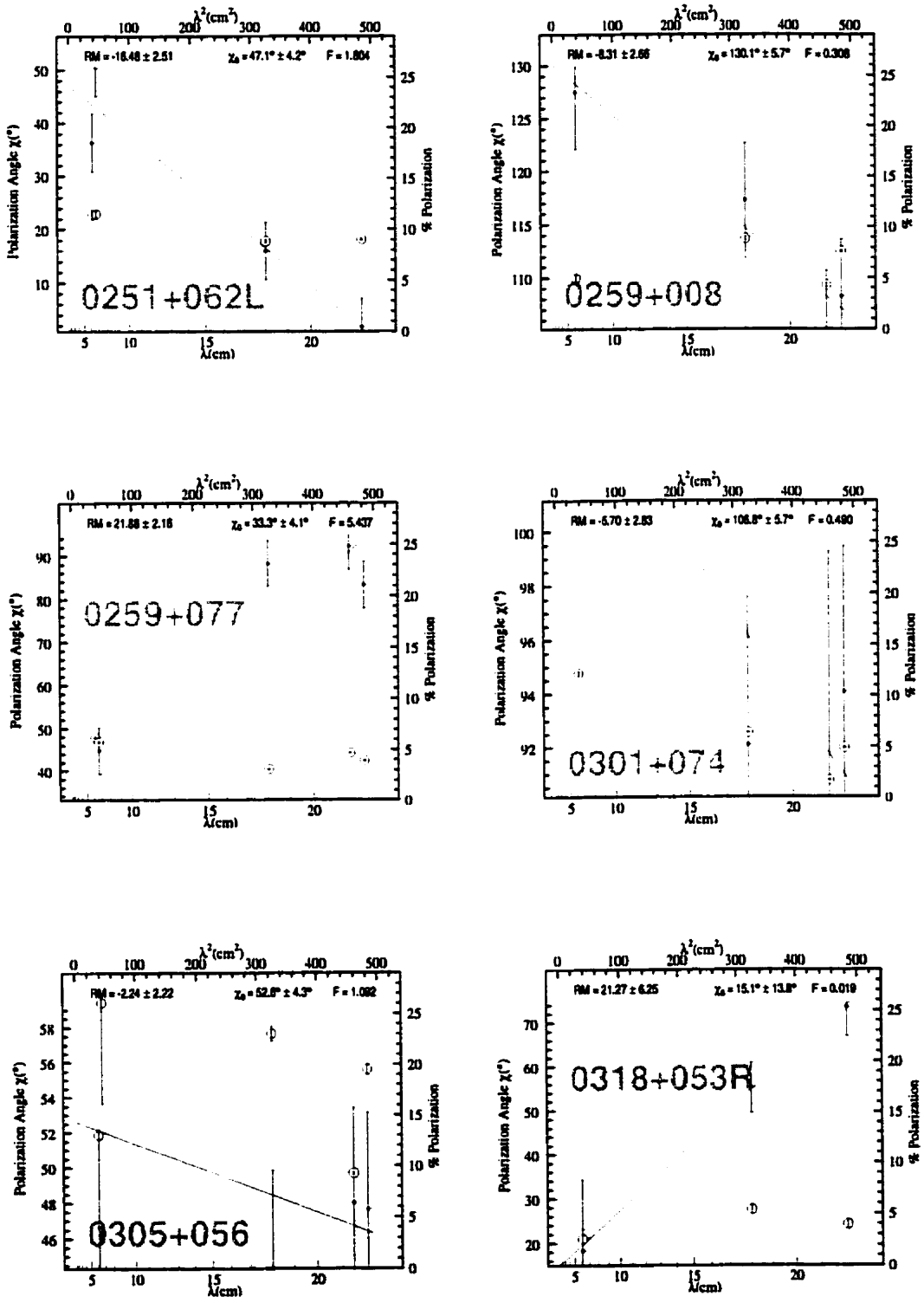

Figure 5.4 – *Continued*

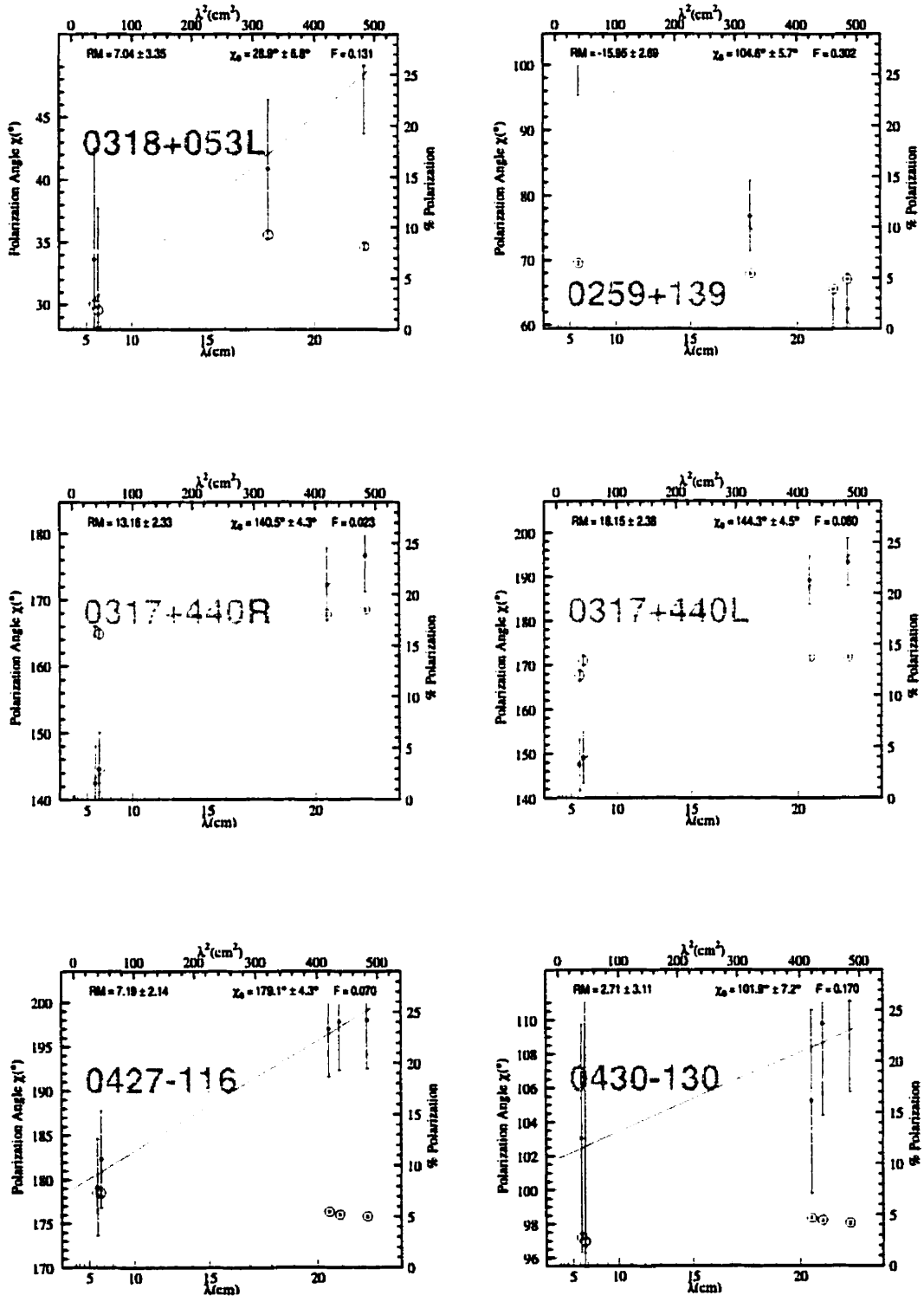

Figure 5.4 – *Continued*

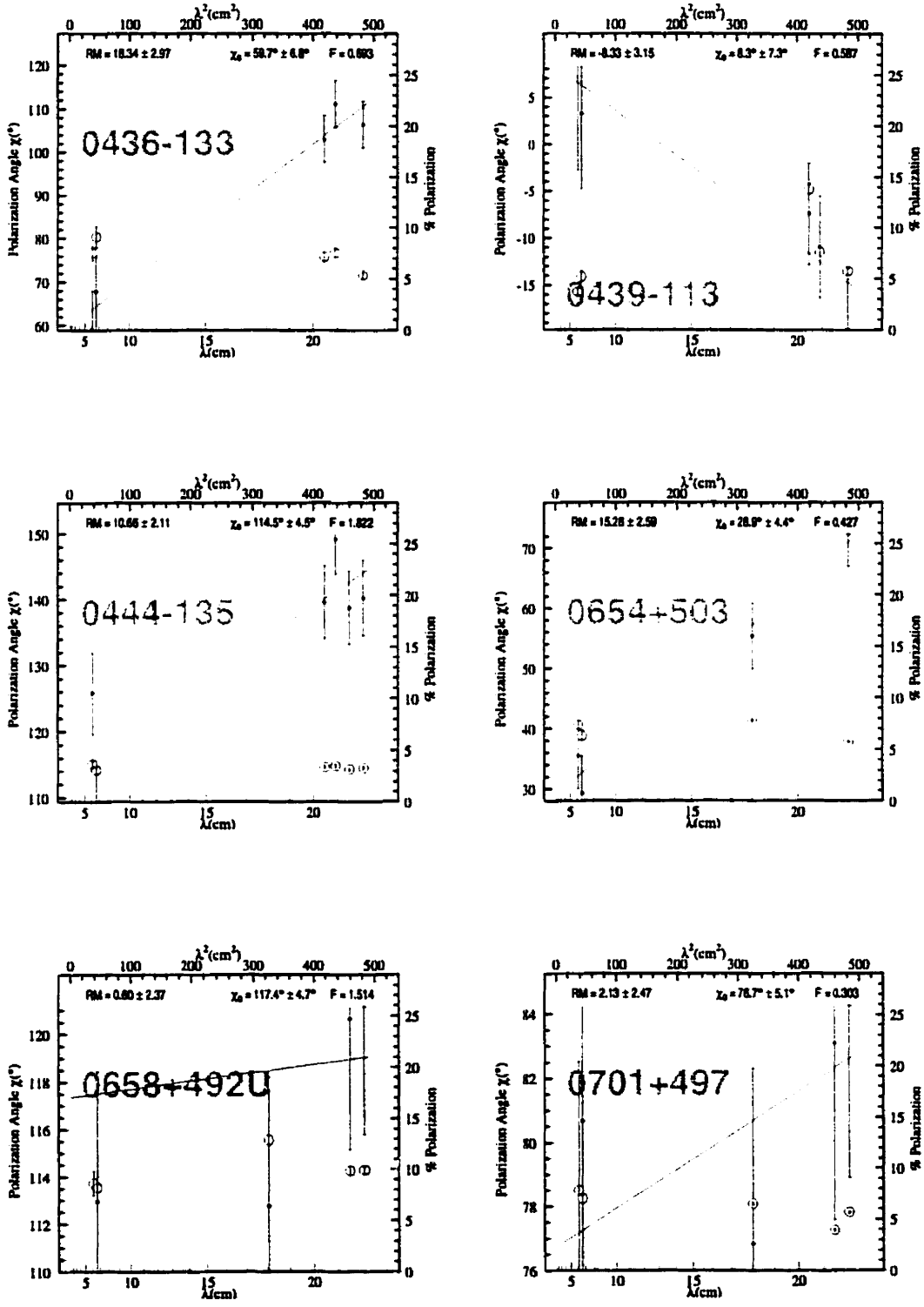

Figure 5.4 – *Continued*

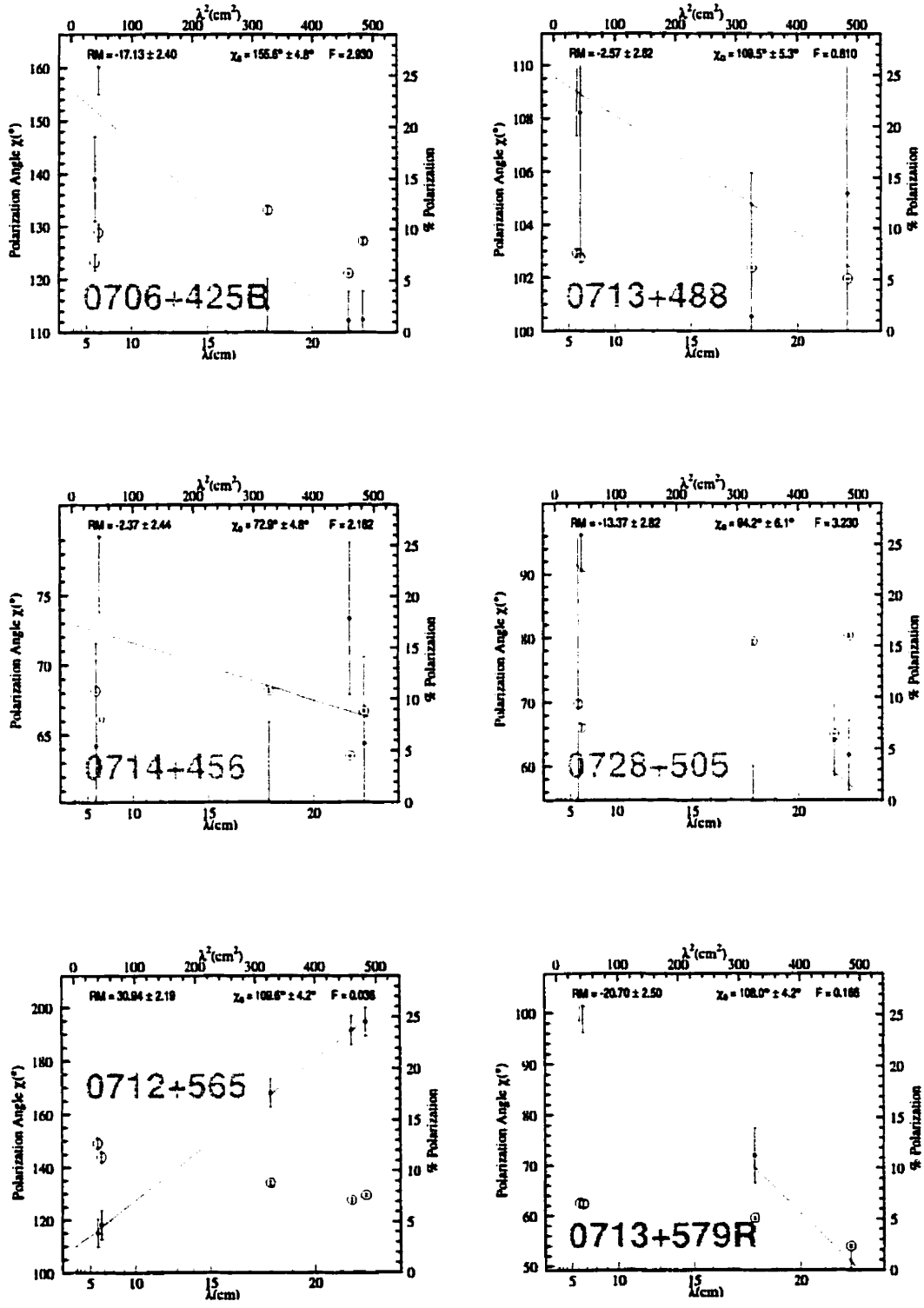

Figure 5.4 – *Continued*

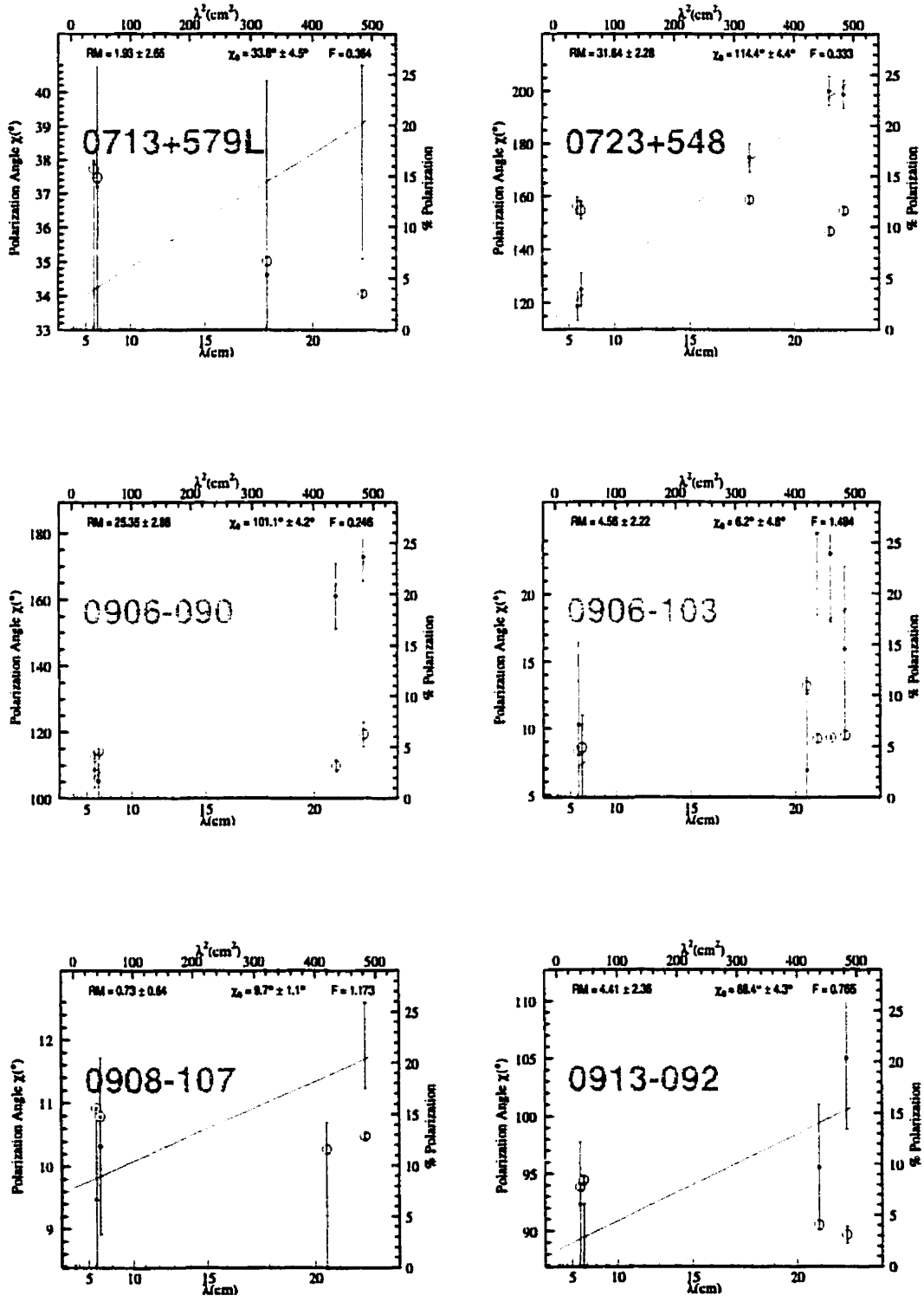

Figure 5.4 – *Continued*

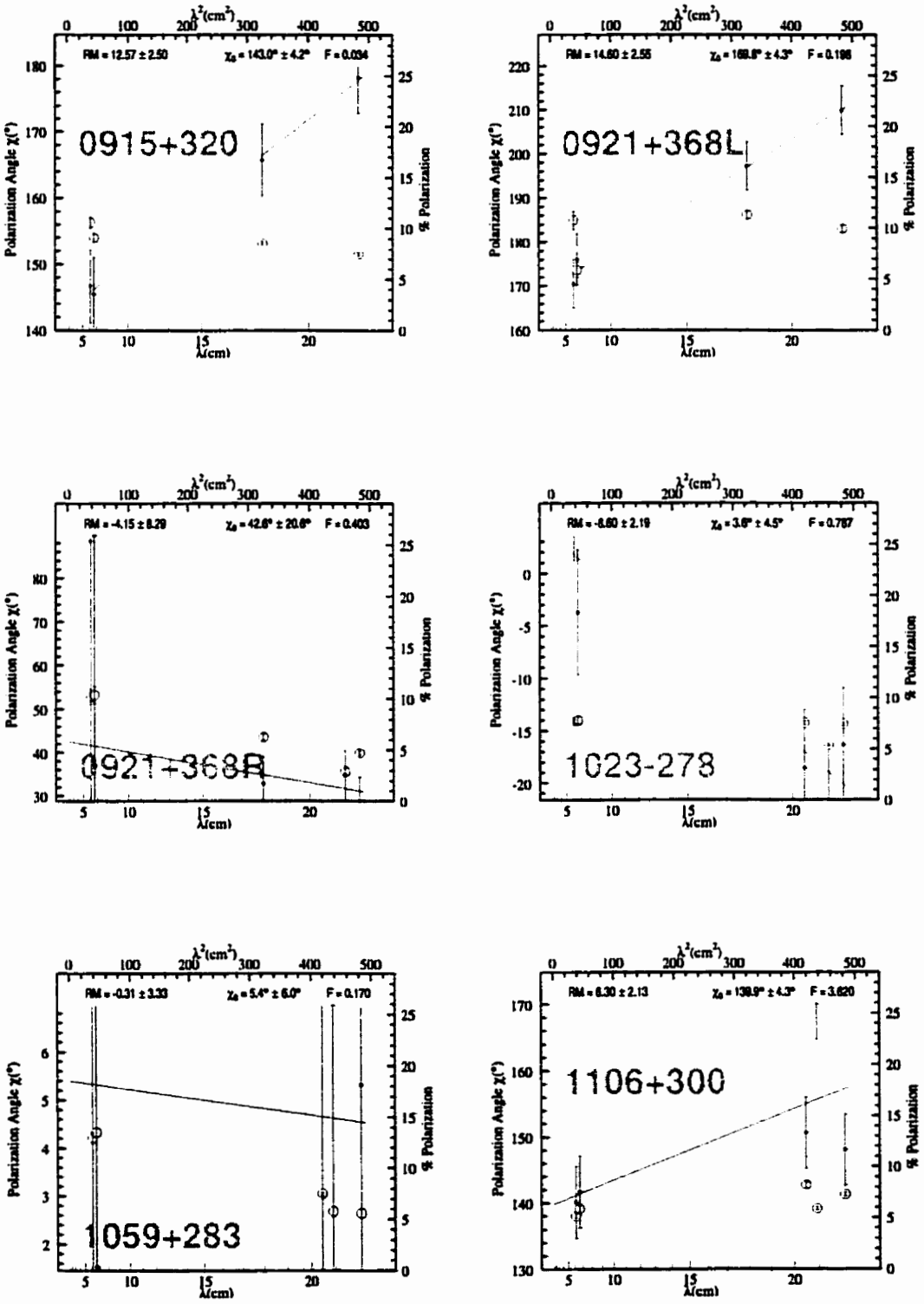

Figure 5.4 – *Continued*

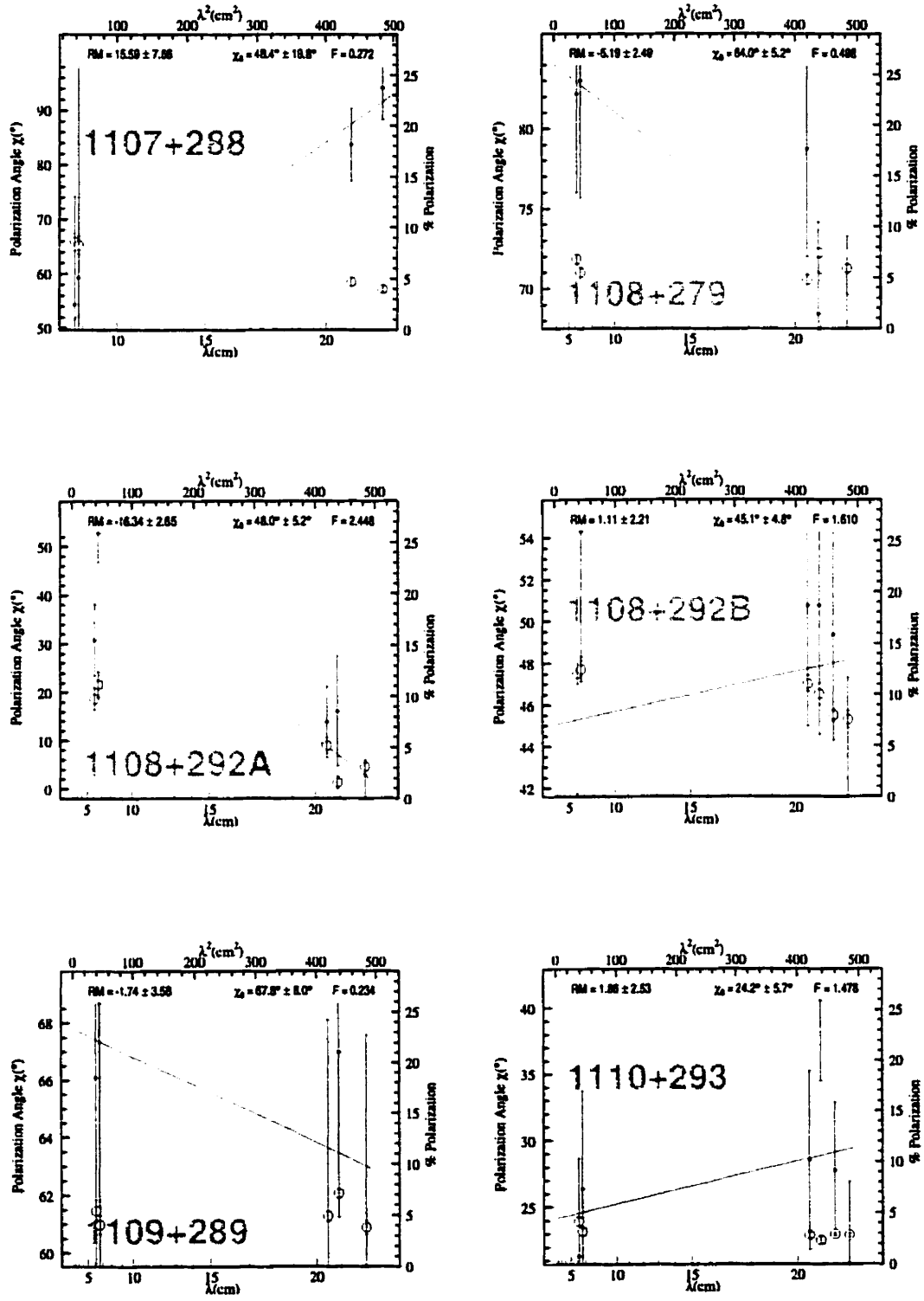

Figure 5.4 – *Continued*

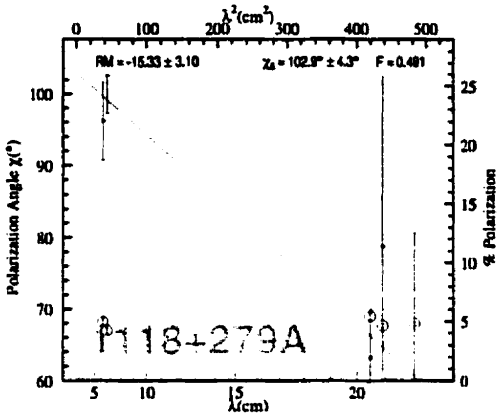

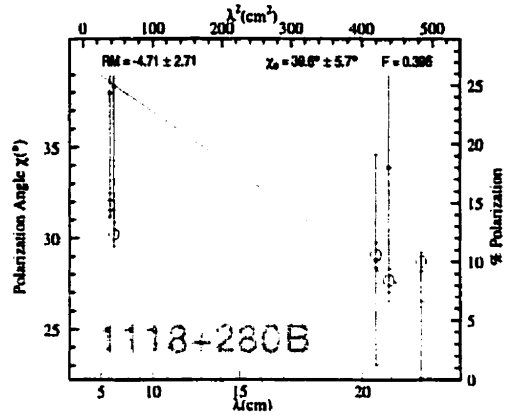

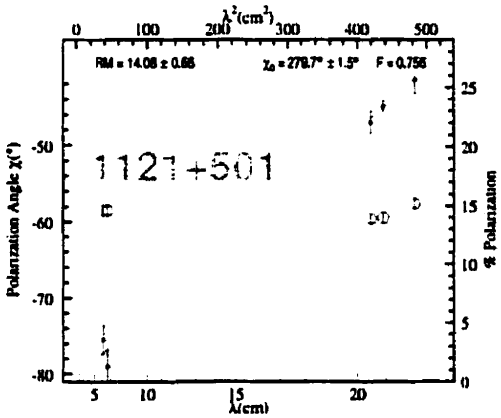

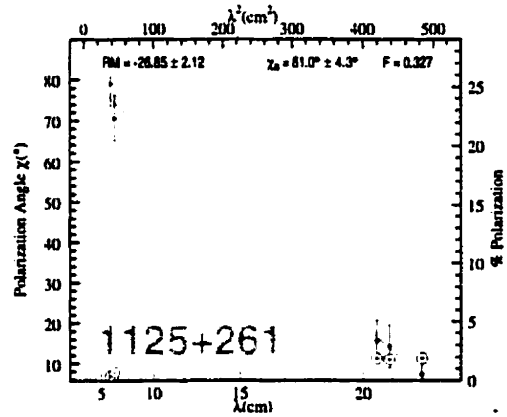

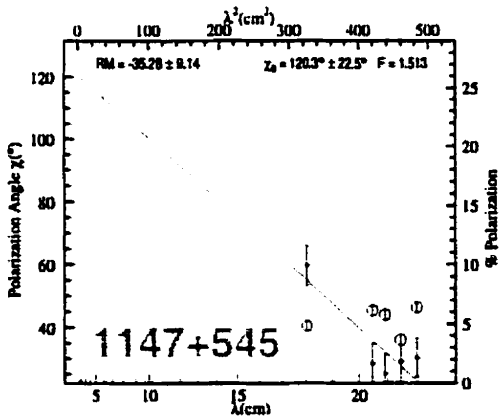

Figure 5.4 – ***Continued***

Notes on individual sources

- **0052−011U** The depolarization ratio of 4.2 for this source places it in the regime of potential non-linearities in the χ-λ^2 relation. Although it is possible that χ-λ^2 plot may flatten to long wavelength, this flattening cannot be verified with the current data which contains two 6 cm, and two 20 cm measurements. Despite the high depolarization ratio for this source, a visual inspection of the rotation measure fit shows that it is a reasonable fit. It is also interesting to note that the nearby, although apparently unrelated, source, 0052−011L, has a much smaller depolarization ratio of 1.0.

- **0056−013** Although the rotation measure fit in Figure 5.4 only contains data within the 20 cm band, there is data available at one 6 cm wavelength for this source. This 6 cm measurement provides a depolarization ratio of 4.6 for this source. Fitting the data to the 20 cm measurements of the polarization angle results in a good fit to the χ-λ^2 data. Including the 6 cm data point in the fit increases the fitted rotation measure from -157 rad m^{-2} to -197 rad m^{-2}. The lower of the two rotation measures was selected for the analysis as any bias introduced will lead to lower estimates of the intracluster magnetic field strength.

- **0319+415** The measured polarization percentage of this source is at the limits of the instrumental polarization error of the VLA, and thus the results for this source should be regarded with extreme caution. In fact, the locations of this source in the cooling core of Perseus (Abell 426) suggests that the rotation measure is likely to be in the range of several thousand radians m^{-2}. This prediction is based on observed rotation measures toward other cooling cores (Ge & Owen 1993; Taylor et al. 1999). Therefore, the rotation measure of $\sim$ 190 rad m^{-2} presented herein likely significantly underestimates the true rotation measure. The associated magnetic field calculated from this rotation measure should therefore be considered a lower limit. Note that although this source is included in the sample for the analysis, the results presented in this thesis are not affected by the removal of 0319+415.

- **0713+579L** This source is similar to 0052−011U in that the effects of the relatively high depolarization ratio, DP=4.4, cannot be determined with the limited data avail-

able (four wavelengths). An additional parallel is the presence of a nearby source, 0713+579R in this case, whose depolarization ratio is much smaller (2.9). In contrast, it appears that the 0713+579L and its companion may represent the outer hot-spots in a double lobed system. There is, however, no current optical identification of this system. It is also interesting to note that the more depolarized source is the weaker of the two sources.

- **1133+490** An analysis of this source reveals a depolarization ratio of 4.4. Although the 18 cm observation of this source was lost due to RFI, the remaining five wavelengths show no visible deviations for a linear χ-λ^2 fit. Due to the potential flattening of the fit at long wavelengths for this source, the fit was also determined with the 6 cm wavelengths removed. The rotation measure from the 20 cm measurements alone fell within the errors of the fit to all available data.

- **1145+196** This source has the distinction of being both the most highly polarized source, %P=18.6, and the source with the highest depolarization ratio, DP=19.3, in the radio sample. It is not surprising, however, that these distinctions fall on the same source, since a source of lower polarization percentage with such high depolarization ratio would not be visible in polarized flux at 20 cm (§ 6.3). A visual inspection of the fit to all measurements for this source shows a linear χ-λ^2 behaviour, with a best fit RM of 254 rad m^{-2}. To test the robustness of the rotation measure, the fit was was also determined from the data near 20 cm only. The resulting rotation measure of 264 rad m^{-2} is found to be consistent within the associated errors to the previous best-fit value. Although basically meaningless, the fit to the two 6 cm measurements provides a rotation measure of 160 rad m^{-2}. The rotation measure selected was the best-fit value to all available data.

Fit Results

The best-fit rotation measures and their associated error estimates are listed in Tables 5.1 and 5.2. The tables also list the intrinsic position angle of the polarized emission, χ_o, and its associated error, as well as the depolarization ratios and maximum percent polarizations for the sources. The depolarization ratio is only calculated for those sources which had measurements at both 20 cm and 6 cm. The tables are split, as in Figures 5.3 and 5.4,

to show the parameters for sources viewed through the intracluster gas, and sources falling beyond the edge of the cluster gas, respectively.

Source	DP	σ_{DP}	%P	$\sigma_{\%P}$	RM	σ_{RM}	χ_o	σ_{χ_o}
					rad m^{-2}		degrees	
0039+212	...	...	6.7	0.3	-77.07	8.25	234.9	20.2
0040+212	...	...	4.9	0.3	-48.45	10.32	185.9	25.3
0056−013	4.59	0.23	8.7	0.2	-154.55	8.54	41.0	20.6
0057−013	...	...	21.8	0.2	8.63	7.90	144.3	19.4
0126−013a	...	...	11.4	0.1	90.81	9.29	265.8	22.1
0154+364	0.64	0.05	4.4	0.3	-241.90	2.30	89.8	4.8
0245+368	0.50	0.14	3.5	0.9	-71.00	2.51	112.8	5.5
0257+130	1.85	0.26	7.9	0.5	-182.34	2.36	86.2	4.3
0318+419	...	...	7.7	0.1	-11.13	12.54	200.7	28.5
0319+415[a]	...	...	0.1	0.0	189.64	35.95	323.3	89.3
0316+412	0.96	0.06	6.1	0.3	57.64	2.40	146.5	5.6
0434−131	1.57	0.02	14.4	0.1	59.16	1.99	135.8	4.2
0434−133	2.01	0.07	9.8	0.2	42.14	2.11	86.9	4.2
0709+486	0.19	0.05	1.1	0.2	-222.23	3.67	77.3	5.2
0908−100	0.67	0.16	3.9	0.2	28.32	3.45	124.1	4.8
0909−093	1.72	0.31	6.3	0.3	-4.50	2.60	153.9	4.5
0919+334	1.27	0.03	9.4	0.1	12.87	2.18	0.7	4.1
1036−267	0.65	0.13	4.1	0.7	39.36	15.17	34.0	37.2
1037−270	0.45	0.06	1.5	0.1	22.98	2.24	48.6	4.5
1037−281	0.86	0.32	1.7	0.5	38.81	5.82	58.9	14.5
1039−272	0.86	0.15	5.3	0.5	117.33	9.97	129.1	25.1
1039−273	0.72	0.12	6.9	1.0	117.59	2.63	145.7	6.0
1133+490	4.35	0.19	7.5	0.1	-47.20	2.28	133.5	4.2
1134+489A	1.80	0.26	3.3	0.1	71.23	2.34	35.5	4.4
1145+196	19.27	3.08	18.6	0.2	254.13	2.34	75.4	4.3
1650+815L	0.67	0.09	7.7	1.0	-129.87	2.17	58.0	4.4
1650+815U	1.98	0.25	4.3	0.4	-125.48	2.18	136.1	4.5

[a]Note that the polarization determined for this source is at the limit of the VLA's capabilities. Results from this source should be regarded with extreme caution.

Table 5.1: Depolarization ratio, maximum polarization percentage, rotation measure, and intrinsic position angle calculated for each source in the cluster sample.

Source	DP	σ_{DP}	%P	$\sigma_{\%P}$	RM	σ_{RM}	χ_o	σ_{χ_o}
					rad m^{-2}		degrees	
0033+064	2.23	0.04	10.8	0.1	15.35	2.11	271.4	1.4
0035+067	1.02	0.06	8.8	0.4	-12.08	2.31	26.8	4.8
0038+071A	0.94	0.04	13.8	0.6	-9.81	2.13	168.0	4.2
0038+071B	1.19	0.08	4.7	0.2	12.83	2.17	40.5	4.4
0040+072	0.66	0.07	3.1	0.3	0.71	2.37	3.1	5.0
0041+069	1.49	0.03	7.0	0.1	1.37	2.11	177.4	4.2
0041+076	0.80	0.04	4.8	0.1	-5.07	2.14	22.6	1.2
0043+060	0.92	0.06	5.3	0.3	-26.97	2.19	24.9	1.9
0040−098	0.75	0.07	3.1	0.3	-19.61	3.08	70.1	7.1
0042−078	0.91	0.11	3.8	0.3	2.35	2.16	97.1	4.4
0042−080A	1.22	0.12	8.7	0.6	-0.47	2.16	123.4	4.4
0042−080B	1.11	0.11	7.0	0.5	3.46	2.12	123.2	4.2
0042−092	1.49	0.09	7.2	0.3	4.44	2.12	95.9	4.2
0042−098	1.94	0.14	10.2	0.6	-17.76	2.13	115.9	4.2
0047−095	0.82	0.03	7.6	0.2	-14.51	2.12	108.6	4.2
0048−022R	1.36	0.25	15.4	2.3	-7.08	3.22	1.9	6.5
0048−022L	0.88	0.09	3.6	0.2	-12.80	2.81	93.4	6.0
0049−027	1.36	0.02	11.9	0.2	-10.19	2.49	171.7	4.2
0050−033R	0.84	0.12	4.0	0.5	3.63	2.49	114.7	4.2
0050−033L	2.16	0.08	10.9	0.3	3.96	2.50	38.1	4.2
0052−011L	1.01	0.13	7.8	1.0	0.51	2.79	55.1	5.1
0052−011U	4.16	0.48	13.9	1.0	-3.40	2.63	3.6	4.6
0102+020A	1.33	0.01	13.6	0.1	-9.51	2.12	67.6	3.6
0102+020B	...	...	4.5	0.4	12.03	25.28	37.9	64.9
0107+015	0.90	0.25	4.0	0.8	-2.99	2.78	356.0	5.9
0108+015	0.58	0.00	2.1	0.1	-11.75	2.10	126.9	4.2
0108+028	2.13	0.08	18.0	0.3	-13.53	2.12	334.5	1.1
0110+015	1.33	0.21	4.8	0.4	-12.06	2.54	78.7	5.4
0110+018	0.92	0.09	5.8	0.5	5.68	2.10	159.2	4.2

Table 5.2: Depolarization ratio, maximum polarization percentage, rotation measure, and intrinsic position angle calculated for each source in the control sample.

Source	DP	σ_{DP}	%P	$\sigma_{\%P}$	RM	σ_{RM}	χ_o	σ_{χ_o}
					rad m^{-2}		degrees	
0113+027	1.14	0.09	12.8	0.7	5.46	2.12	337.1	1.9
0108−006	0.55	0.01	3.3	0.1	5.20	2.16	120.9	4.1
0113+024	0.25	0.01	1.2	0.1	3.21	1.81	36.6	2.7
0114+000	0.95	0.04	6.0	0.2	14.59	2.18	106.8	4.2
0115+000	1.40	0.23	15.5	2.3	6.08	3.39	60.9	6.8
0125−000L	0.80	0.15	8.9	1.5	17.20	4.23	20.0	8.9
0125−000U	0.90	0.11	8.8	1.0	17.34	2.99	60.9	6.8
0059+001	1.94	0.01	7.3	0.1	-4.35	2.10	82.0	4.1
0106−019	0.97	0.01	6.8	0.1	-10.42	2.11	7.8	4.1
0122−063	2.04	0.05	18.3	0.4	-7.89	2.98	95.8	5.8
0125−001	0.90	0.01	3.0	0.1	9.44	2.17	38.1	4.1
0139+015	1.41	0.02	13.1	0.2	14.29	2.24	10.1	4.3
0238+049	0.65	0.09	4.3	0.6	-11.37	2.81	103.6	6.1
0251+062U	0.89	0.01	9.8	0.1	-21.25	2.49	58.6	4.2
0251+062L	1.27	0.04	11.4	0.4	-16.48	2.51	47.1	4.2
0259+008	0.66	0.04	5.0	0.3	-8.31	2.66	130.1	5.7
0259+077	1.57	0.02	6.2	0.1	21.88	2.16	33.3	4.1
0301+074	2.46	0.05	12.2	0.2	-5.70	2.83	106.8	5.7
0305+056	0.67	0.02	13.0	0.4	-2.24	2.22	52.6	4.3
0318+053R	0.64	0.26	2.6	1.0	21.27	6.25	15.1	13.8
0318+053L	0.30	0.04	2.5	0.3	7.04	3.35	28.9	6.8
0259+139	1.33	0.04	6.5	0.2	-15.95	2.69	104.6	5.7
0317+440R	0.89	0.03	16.4	0.5	13.16	2.33	140.5	4.3
0317+440L	0.87	0.04	12.0	0.6	18.15	2.38	144.3	4.5
0427−116	1.47	0.07	7.5	0.2	7.19	2.14	179.1	4.3
0430−130	0.68	0.07	2.9	0.3	2.71	3.11	101.9	7.2
0436−133	1.39	0.15	7.5	0.7	18.34	2.97	59.7	6.8
0439−113	0.90	0.12	5.2	0.5	-8.33	3.15	8.3	7.3
0444−135	1.12	0.12	3.7	0.3	10.66	2.11	114.5	4.5
0654+503	1.29	0.08	7.4	0.4	15.28	2.59	28.9	4.4

Table 5.2 – *Continued*

Source	DP	σ_{DP}	%P	$\sigma_{\%P}$	RM	σ_{RM}	χ_o	σ_{χ_o}
					rad m^{-2}		degrees	
0658+492U	0.88	0.12	8.7	1.2	0.60	2.37	117.4	4.7
0701+497	1.38	0.08	7.8	0.4	2.13	2.47	76.7	5.1
0706+425B	0.77	0.10	6.8	0.8	-17.13	2.40	155.6	4.8
0713+488	1.50	0.07	7.6	0.3	-2.57	2.82	109.5	5.3
0714+456	1.23	0.03	10.9	0.2	-2.37	2.44	72.9	4.8
0728+505	0.59	0.02	9.4	0.3	-13.37	2.82	94.2	6.1
0712+565	1.68	0.09	12.7	0.6	30.86	2.50	109.6	4.2
0713+579R	2.85	0.22	6.6	0.3	-20.70	2.50	108.0	4.2
0713+579L	4.42	0.45	15.7	0.9	1.93	2.65	33.8	4.5
0723+548	1.04	0.09	12.0	0.9	31.64	2.28	114.4	4.4
0906−090	0.66	0.18	4.2	0.2	25.35	2.88	101.1	4.2
0906−103	0.75	0.10	4.7	0.4	4.56	2.22	6.2	4.8
0908−107	1.20	0.03	15.6	0.1	0.38	2.13	9.7	1.1
0913−092	2.46	0.92	7.9	0.3	4.41	2.36	88.4	4.3
0915+320	1.41	0.08	10.6	0.5	12.57	2.50	143.0	4.2
0921+368L	1.08	0.10	10.8	0.9	14.60	2.55	169.8	4.3
0921+368R	2.15	0.20	10.2	0.7	-4.15	8.29	42.6	20.6
1023−278	1.03	0.05	7.7	0.3	-8.60	2.19	3.6	4.5
1059+283	2.33	0.29	13.1	0.6	-0.31	3.33	5.4	6.0
1106+300	0.71	0.04	5.2	0.2	6.30	2.13	139.9	4.3
1107+288	2.12	0.31	8.7	0.8	15.60	7.70	48.4	19.8
1108+279	1.16	0.13	6.9	0.5	-5.19	2.49	84.0	5.2
1108+292A	3.10	1.03	9.9	1.1	-16.34	2.65	48.0	5.2
1108+292B	1.59	0.27	12.1	1.0	1.11	2.21	45.1	4.8
1109+289	1.45	0.45	5.5	1.1	-1.74	3.58	67.8	8.0
1110+293	1.47	0.20	4.2	0.4	1.86	2.53	24.2	5.7
1118+279A	1.06	0.08	5.1	0.3	-15.33	3.10	102.9	4.3
1118+280B	1.47	0.17	14.8	1.0	-4.71	2.71	39.6	5.7
1121+501	0.96	0.04	14.7	0.4	14.13	2.30	279.7	1.5
1125+261	0.25	0.01	0.5	0.0	-26.85	2.12	81.0	4.3
1147+545	...	...	6.4	0.4	-35.28	9.14	120.3	22.5

Table 5.2 – *Continued*

5.4 Determining the Intracluster Contribution to the Rotation Measure

The observed rotation measure for a radio source is a linear combination of all sources of Faraday rotation along the line of sight between the source and the observer. Polarized radiation from a typical extragalactic radio source may be influenced by some combination (or all) of the following Faraday rotating regions:

- **Intrinsic:** Intrinsic Faraday rotation may result from a mixture of thermal plasma in the environment surrounding the radio source with the synchrotron plasma of the source. This internal Faraday rotation, discussed in § 2.4.3, produces a characteristic signature whereby the position angle of the polarized emission will obey a λ^2 law over at most 90°. As can be seen from the plots of χ-λ^2 for the source sample, the linear nature of the fit is generally extended well beyond 90° of rotation, thus indicating the dominance of another source of rotation. The small depolarization ratios associated with the sample also argue for an external source of rotation.

- **Local galactic:** The parent galactic environment around radio sources can induce substantial Faraday rotation. An example of this is shown in the work of Venturi & Taylor (1999) which shows that the observed rotation measure of ~700 rad m^{-2} in 3C216 results from interactions between the radio jets and the local galactic environment. This source of Faraday rotation cannot, in general, be dominant in extragalactic radio sources as the observed rotation measures for the **control** are consistent with zero with very little scatter.

- **Intercluster:** An intercluster contribution to the observed rotation measure might be expected for sources at high redshift which have a very long path length through intercluster space to a radio telescope. A limit on any possible intercluster contribution can be placed by examining a large sample of rotation measures at various redshifts and looking for a correlation between the rotation measure and redshift (Kronberg & Simard-Normandin 1976; Welter et al. 1984). An examination of the rotation measure catalog of Broten et al. (1988) by Vallée (1990) found no significant Faraday rotation in a sample of high redshift radio sources.

- **Intracluster:** The intergalactic region within galaxy clusters is known to be filled with a tenuous X-ray emitting plasma bound to the potential well of the cluster. If magnetized, such a thermal plasma provides an ideal environment for Faraday rotating polarized emission. It is, of course, this component of the rotation measure that is targeted by this thesis.

- **Galactic:** This is the overwhelming non-cluster contribution to RMs. An examination of a plot of the Faraday sky in Galactic coordinates, Figure 5.5, displays a clear trend of large rotation measure in the galactic plane, and much smaller values at high latitudes. The rotation measure sky at low Galactic latitudes is well fit by a large-scale ordered field located within the disk of the Milky Way (Simard-Normandin & Kronberg 1980). In order to minimize the possible effect of the Galactic Faraday rotation, the source sample selected for this thesis was restricted to high latitudes where the Galactic contribution is found to be on the order of a few rad m^{-2}.

- **Ionospheric:** The magnitude of the ionospheric contribution to the observed rotation measure is discussed in § 5.1. Due to the timing of the observations near solar minimum, the ionospheric contribution is expected to be very small, and has thus been included as an uncertainty in the measured polarization angles.

Based on the above arguments, the main intervening Faraday rotation component to consider when searching for an intracluster contribution to the rotation measure, is the Galactic component. The cluster contribution of the rotation measure, or the residual rotation measure (RRM), is therefore defined to be the observed rotation measure minus the Galactic contribution:

$$RRM = RM_o - RM_G. \tag{5.4}$$

The error in the residual rotation measure

$$\sigma_{RRM} = \sqrt{\sigma^2_{RM} + \sigma^2_{GRM}}, \tag{5.5}$$

is determined from the quadrature summation of the error in the fitted rotation measure, Equation 5.3, and the error associated with the Galactic rotation measure.

The Galactic contribution to the rotation measure, Table 5.3, was determined by taking the median rotation measure of all sources located within 15° of each cluster, after outliers

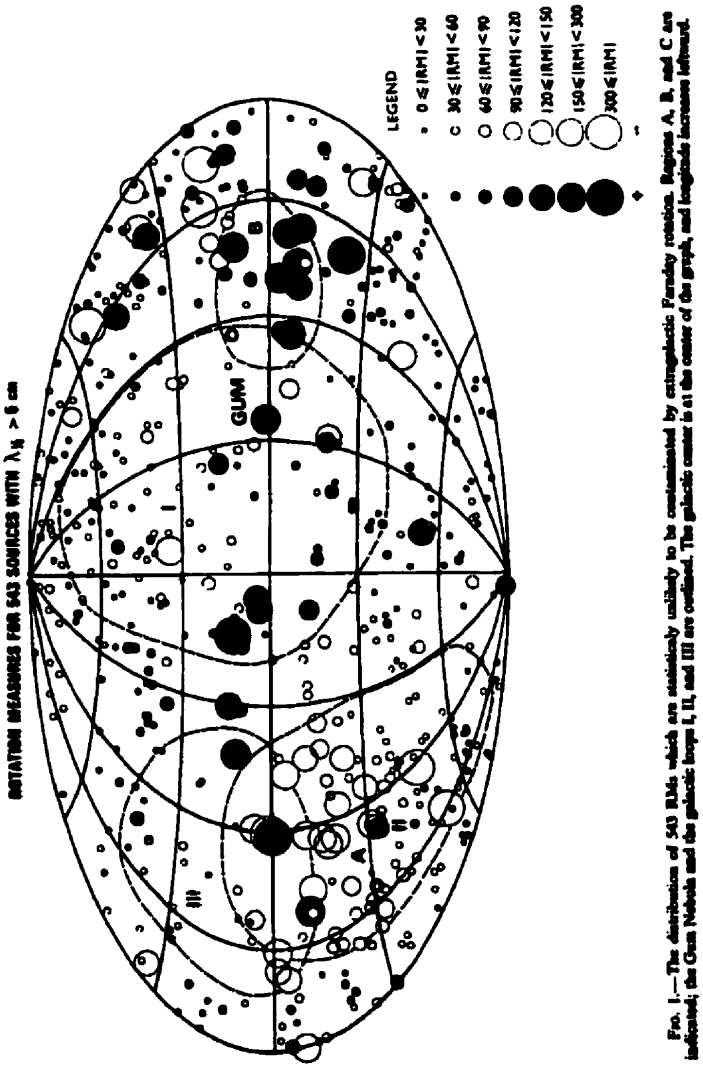

FIG. 1.—The distribution of 543 RMs which are statistically unlikely to be contaminated by extragalactic Faraday rotation. Regions A, B, and C are indicated; the Gum Nebula and the galactic loops I, II, and III are outlined. The galactic center is at the center of the graph, and longitude increases leftward.

Figure 5.5: Plot of the rotation measure sky in Galactic coordinates, Simard-Normandin & Kronberg (1980). Note the decrease in the magnitude of the rotation measures away from the Galactic plane.

($> 2\sigma$) had been removed. The source sample used in determining the Galactic rotation measure was a combination of the control sample obtained from this thesis, and sources from the literature.

Abell	l°	b°	GRM	σ_{GRM}
			rad m^{-2}	
75	119.33	-41.53	-14.45	3.66
76	117.76	-55.98	-7.97	6.05
85	115.06	-72.06	-0.44	9.54
119	125.76	-64.11	-5.39	6.41
147	131.44	-60.43	-7.58	6.16
168	135.67	-62.04	-5.96	5.92
194	142.07	-63.10	-3.41	7.98
262	136.59	-25.09	-39.54	3.64
376	147.08	-20.59	-22.94	5.36
399	164.38	-39.47	3.55	6.02
400	170.25	-44.93	10.95	5.72
401	164.19	-38.87	4.42	6.52
426	150.39	-13.38	-17.30	8.94
496	209.58	-36.48	6.25	6.39
569	168.58	22.81	7.51	6.83
576	161.42	26.24	2.40	7.60
754	239.26	24.76	15.97	8.78
779	191.07	44.41	-3.68	8.09
1060	269.64	26.51	13.60	5.76
1185	203.05	67.75	-3.88	12.93
1314	151.84	63.57	3.18	5.98
1367	234.81	73.03	-3.33	11.49
1383	141.44	60.17	-2.03	6.74
2247	114.49	31.22	1.88	8.28

Table 5.3: The median Galactic rotation measure (GRM) calculated from all sources located within 15° of the respective Abell cluster.

Finally, the residual rotation measure for the radio sources are provided in Tables 5.4, and 5.5. The separation of the radio sample into two populations (**cluster**, and **control**) is based impact parameter of the radio source, compared to the radial extent of the intracluster

gas. Each table presents the J2000 epoch source name according to IAU convention, the radial impact parameter to the nearest Abell cluster, the name of the nearest Abell cluster, and the Galaxy-corrected rotation measure (RRM) and its 1σ error. Additionally, Table 5.4 contains the electron density, and its 1σ error at the impact parameter of the radio source calculated assuming spherical symmetry of the cluster gas distribution. The error in the electron density was determined from the χ^2 error surface as described in § 4.4.1, through Equation 2.29. Note, however, that it was not possible to fit a β model to Abell 569. The method of determining the electron density, and associated error, at the impact parameter of the radio source for this cluster is discussed in § 4.4.

The impact parameter for each radio source was determined from the ROSAT X-ray centroids of the clusters, Table 4.1, and the radio source positions, Tables 5.6 and 5.7. In general, the angular separation between two sources is given by

$$b = \cos^{-1}[\sin\ \delta_1\ \ \sin\ \delta_2\ \ + \cos\ \delta_1\ \ \cos\ \delta_2\ \ \cos\ (\alpha_1 - \alpha_2)]\,, \tag{5.6}$$

where α_1 and δ_1 are the right ascension and declination of the cluster, and α_2 and δ_2 are those of the radio source. Note, however, that the above equation breaks down when the angular separation is very near 0° (or 180°), due to the fact that |cos b| is very close to one. Therefore, for angular separations of less than $\sim 10'$, the impact parameter was determined from (Meeus 1991)

$$b = \sqrt{[(\alpha_1 - \alpha_2)\ \cos\ \delta'\ ]^2 + (\delta_1 - \delta_2)^2}, \tag{5.7}$$

where δ' is the average of the declinations of the galaxy cluster and radio source.

5.5 Radio Source Identifications

Identification of sources within the radio sample was mainly undertaken through the use of NASA's Extragalactic Database. For previously unidentified radio sources which fell near galaxies of known redshift, the candidate galaxy and the radio source were further examined in an image overlay for potential identification. In addition to the source name and position in J2000 coordinates, Tables 5.6 and 5.7 provide alternate source names and redshifts, where available, for the **cluster** and **control** samples respectively. The final column in Table 5.6 contains a flag to indicate the line of sight position of the radio source,

compared to the relevant galaxy cluster. An 'e' in the flag column indicates that the source is a cluster member which is embedded within the ICM, while a 'b' indicates that the source is identified as a high redshift, background source. Sources which have no identification do no contain an entry in the flag column.

Source	Abell	b	RRM	σ_{RRM}	$n_e(b)$
		kpc	rad m^{-2}		10^{-3} cm^{-3}
0039+212	75	100	-62.62	9.03	$1.01^{+0.55}_{-0.22}$
0040+212	75	480	-34.00	10.95	$0.19^{+0.17}_{-0.05}$
0042−092	85	960	4.88	9.77	$0.20^{+0.000}_{-0.009}$
0056−013	119	280	-149.16	10.68	$0.96^{+0.007}_{-0.017}$
0057−013	119	1020	14.02	10.17	$0.16^{+0.000}_{-0.004}$
0126−013a	194	140	94.22	12.25	$0.43^{+0.007}_{-0.011}$
0154+364	262	570	-202.36	4.31	$0.19^{+0.001}_{-0.002}$
0245+368	376	630	-48.06	5.92	$0.66^{+0.22}_{-0.08}$
0257+130	399	280	-185.89	6.47	$1.40^{+0.07}_{-0.04}$
0318+419	426	550	6.17	15.40	$0.11^{+0.006}_{-0.000}$
0319+415[a]	426	10	206.94	37.04	$6.94^{+0.021}_{-0.001}$
0316+412	426	740	74.94	9.26	$0.07^{+0.003}_{-0.000}$
0434−131	496	310	52.91	6.69	$0.80^{+0.03}_{-0.05}$
0434−133	496	360	35.89	6.73	$0.62^{+0.02}_{-0.04}$
0709+486[b]	569	3	-229.74	7.75	$16.0^{+10.0}_{-7.0}$
0908−100	754	1460	12.35	9.43	$0.11^{+0.001}_{-0.002}$
0909−093	754	1010	-20.47	9.16	$0.22^{+0.004}_{-0.004}$
0919+334	779	560	16.55	8.38	$0.08^{+0.006}_{-0.008}$
1036−267	1060	640	25.76	16.23	$0.11^{+0.001}_{-0.002}$
1037−270	1060	410	9.38	6.18	$0.22^{+0.003}_{-0.003}$
1037−281	1060	510	25.21	8.19	$0.16^{+0.002}_{-0.002}$
1039−272	1060	620	103.73	11.51	$0.11^{+0.002}_{-0.002}$
1039−273	1060	530	103.99	6.33	$0.15^{+0.002}_{-0.002}$
1133+490	1314	310	-50.38	6.40	$0.35^{+0.01}_{-0.02}$
1133+489A	1314	270	68.05	6.42	$0.42^{+0.01}_{-0.02}$
1145+196	1367	170	257.46	11.73	$1.06^{+0.01}_{-0.02}$
1650+815L	2247	270	-131.75	8.56	$0.18^{+0.05}_{-0.03}$
1650+815U	2247	200	-127.36	8.56	$0.25^{+0.08}_{-0.04}$

[a]The location of this source in the core of a cooling flow cluster, combined with the low fractional polarization suggests that the RRM listed severely underestimates the true RRM.

[b]The error associated with n_e is determined from the uncertainty in the determination of the X-ray clump size.

Table 5.4: This table presents the calculated residual rotation measures (RRMs) and associated error for each source in the cluster sample. The table also indicates the cluster probed, the source impact parameter and the projected electron density at that impact parameter for each source.

Source	Abell	b	RRM	σ_{RRM}
		kpc	rad m^{-2}	
0033+064	76	4660	23.32	6.41
0035+067	76	2770	-4.11	6.48
0038+071A	76	1600	-1.84	6.41
0038+071B	76	1200	20.80	6.43
0040+072	76	1190	8.68	6.50
0041+069	76	1070	9.34	6.41
0041+076	76	2220	2.90	6.42
0043+060	76	3270	-19.00	6.43
0040−098	85	1860	-19.17	10.02
0042−078	85	4810	2.79	9.78
0042−080A	85	4360	-0.03	9.78
0042−080B	85	4290	3.90	9.77
0042−098	85	1950	-17.32	9.77
0047−095	85	4380	-14.07	9.77
0048−022R	119	6200	-1.69	7.17
0048−022L	119	6160	-7.41	7.00
0049−027	119	6230	-4.80	6.88
0050−033R	119	7180	9.02	6.88
0050−033L	119	7170	9.35	6.88
0052−011L	119	2380	5.90	6.99
0052−011U	119	2390	1.99	6.92
0102+020A	147	4230	-1.93	6.51
0102+020B	147	4090	19.61	26.02
0107+015	147	1840	4.59	6.76
0108+015	147	1720	-4.17	6.51
0108+028	147	1850	-5.95	6.51
0110+015	147	2260	-4.48	6.66
0110+018	147	2000	13.26	6.51
0113+027	147	3640	13.04	6.51
0108−006	168	5670	11.16	6.30
0113+024	168	6010	9.17	6.19
0114+000	168	1100	20.55	6.31
0115+000	168	1000	12.04	6.82
0125−000L	168	7390	23.16	7.28
0125−000U	168	7370	23.30	6.63
0059+001	194	8250	-0.94	8.25

Table 5.5: This table presents the calculated residual rotation measures and associated error for each source in the control sample. Also indicated is the nearest Abell cluster and source impact parameter to that cluster.

Source	Abell	b	RRM	σ_{RRM}
		kpc	rad m^{-2}	
0106−019	194	5880	-7.01	8.25
0122−063	194	6030	-4.48	8.52
0125−001	194	1560	12.85	8.27
0139+015	194	5520	17.70	8.29
0238+049	400	7540	-22.32	6.38
0251+062U	400	2570	-32.20	6.25
0251+062L	400	2570	-27.43	6.26
0259+008	400	8080	-19.26	6.32
0259+077	400	2860	10.93	6.12
0301+074	400	2720	-16.65	6.39
0305+056	400	3120	-13.19	6.15
0318+053R	400	8120	10.32	8.48
0318+053L	400	8140	-3.91	6.64
0259+139	401	1720	-20.37	7.05
0317+440R	426	3060	30.46	9.24
0317+440L	426	3080	35.45	9.25
0427−116	496	4650	0.94	6.74
0430−130	496	1670	-3.54	7.11
0436−133	496	1600	12.09	7.05
0439−113	496	5160	-14.58	7.12
0444−135	496	5560	4.41	6.73
0654+503	569	3920	7.77	7.30
0658+492U	569	2390	-6.91	7.23
0701+497	569	2280	-5.38	7.26
0706+425B	569	8030	-24.64	7.24
0713+488	569	980	-10.08	7.39
0714+456	569	4070	-9.88	7.25
0728+505	569	4820	-20.88	7.39
0712+565	576	3470	28.46	8.00
0713+579R	576	5800	-23.10	8.00
0713+579L	576	5790	-0.47	8.05
0723+548	576	2150	29.24	7.93
0906−090	754	3120	9.38	9.24
0906−103	754	3460	-11.41	9.06
0908−107	754	3610	-15.59	9.03

Table 5.5 – *Continued*

Source	Abell	b	RRM	σ_{RRM}
		kpc	rad m^{-2}	
0913−092	754	3930	-11.56	9.09
0915+320	779	3020	16.25	8.47
0921+368L	779	4860	18.28	8.48
0921+368R	779	4850	-0.47	11.58
1023−278	1060	2480	-22.20	6.16
1059+283	1185	4930	3.57	13.35
1106+300	1185	3180	10.18	13.10
1107+288	1185	1590	19.48	15.05
1108+279	1185	1810	-1.31	13.17
1108+292A	1185	1430	-12.46	13.20
1108+292B	1185	1430	4.99	13.12
1109+289	1185	700	2.14	13.42
1110+293	1185	1260	5.74	13.18
1118+279A	1185	4080	-11.45	13.30
1118+280B	1185	3880	-0.83	13.21
1125+261	1185	8550	-22.97	13.10
1121+501	1314	4990	10.95	6.41
1147+545	1383	610	-33.25	11.36

Table 5.5 - *Continued*

Source J2000	ID	R.A. h m s	Dec. ° m s	z	Flag
0039+212	MCG +03-02-021	00 39 42.58	+21 14 08.20	0.0579	e
0040+212	...	00 40 07.04	+21 13 46.49	...	
0042−092	PMN J0043-0913	00 42 58.89	-09 13 43.26	0.0766	b
0056−013	CGCG 384-032	00 56 02.70	-01 20 01.10	0.0425	e
0057−013	3C 029	00 57 34.90	-01 23 27.50	0.0448	e
0126−013a	NGC 547/545	01 26 05.24	-01 18 09.90	0.0184	e
0154+364	73W200	01 54 51.44	+36 27 48.20	...	
0245+368	...	02 45 05.06	+36 49 55.70	...	
0257+130	...	02 57 37.18	+13 00 49.30	...	
0318+419	NGC 1265	03 18 15.41	+41 51 26.89	0.0251	b
0319+415	NGC 1275	03 19 48.18	+41 30 41.80	0.0176	e
0316+412	IC 310	03 16 43.16	+41 19 32.08	0.0189	e
0434−131	...	04 34 10.37	-13 11 41.81	...	
0434−133	GIN 190	04 34 09.15	-13 22 32.87	0.0346	e
0709+486	NGC 2329	07 09 07.95	48 36 56.49	0.0193	e
0908−100	NPM1G -09.0307	09 08 04.21	-10 00 14.72	0.0533	e
0909−093	A0907-0910	09 09 30.27	-09 22 60.00	0.0585	e
0919+334	MG2 J091909+3324	09 19 08.80	+33 24 42.20	...	
1036−267	...	10 36 36.04	-26 46 26.00	...	
1037−270	...	10 37 39.79	-27 05 24.50	...	
1037−281	...	10 37 18.99	-28 06 51.10	...	
1039−272	...	10 39 41.08	-27 12 55.72	...	
1039−273	...	10 39 23.69	-27 22 07.17	...	
1133+490	IC 0708	11 33 55.79	+49 03 54.23	0.0320	e
1134+489A	IC 0711	11 34 39.47	+48 58 18.96	0.0324	e
1145+196	NGC 3862	11 45 04.78	+19 36 45.59	0.0214	e
1650+815L	UGC 10638	16 50 38.85	+81 32 38.48	0.0382	e
1650+815U	UGC 10638	16 50 58.46	+81 34 28.88	0.0382	e

Table 5.6: Radio source positions for each source in the cluster sample. For each radio position, the source identification and redshift is listed, where available. The flag column indicates the line of sight location of the identified sources relative to the cluster probed, 'e' indicates that the source is embedded within the intracluster medium, and 'b' indicates that the source is a background probe.

Source	ID	R.A.	Dec.	z
J2000		h m s	° m s	
0033+064	4C +06.02	00 33 15.02	+06 28 16.25	...
0035+067	...	00 35 55.40	+06 45 07.80	...
0038+071A	PMN J0038+0712	00 38 08.44	+07 12 32.66	...
0038+071B	PMN J0038+0706	00 38 36.93	+07 07 08.66	...
0040+072	PMN J0040+0716	00 40 23.33	+07 16 38.87	...
0041+069	4C +06.03	00 41 32.54	+06 57 47.20	...
0041+076	PMN J0041+0736	00 41 12.32	+07 36 54.50	...
0043+060	...	00 43 37.88	+06 02 00.75	...
0040−098	MRC 0038−100	00 40 48.75	-09 48 33.91	...
0042−078	PMN J0042−0753	00 42 57.62	-07 52 47.62	...
0042−080A	PMN J0042−0800	00 42 16.48	-07 59 35.16	...
0042−080B	PMN J0042−0800	00 42 03.83	-08 00 39.16	...
0042−098	...	00 42 35.52	-09 52 03.58	...
0047−095	PMN J0047−0932	00 47 08.54	-09 32 07.33	...
0048−022R	PMN J0048−0212	00 48 18.02	-02 13 07.80	0.5350
0048−022L	PMN J0048−0212	00 48 22.18	-02 13 08.70	0.5350
0049−027	4C -03.02	00 49 45.74	-02 42 59.40	...
0050−033R	PMN J0050−0322	00 50 49.24	-03 22 23.60	...
0050−033L	PMN J0050−0322	00 50 50.48	-03 22 19.40	...
0052−011L	PKS 0050-014	00 52 56.56	-01 09 15.90	...
0052−011U	PKS 0050-014	00 52 55.70	-01 08 42.90	...
0102+020A	4C +01.01	01 02 15.03	+02 03 10.30	...
0102+020B	4C +01.01	01 02 26.51	+02 04 30.30	...
0107+015	PMN J0107+0133	01 07 26.97	+01 33 34.43	...
0108+015	4C +01.02	01 08 38.77	+01 35 04.32	2.0990
0108+028	4C +02.02	01 08 24.89	+02 49 52.70	...
0110+015	PMN J0110+0131	01 10 04.56	+01 32 14.81	...
0110+018	?PMN J0110+0153?	01 10 43.54	+01 52 06.59	...
0113+027	4C +02.03	01 12 17.11	+02 57 41.62	...
0108−006	4C -01.06	01 08 26.84	-00 37 24.10	1.3780
0113+024	PMN J0113+0222	01 13 43.15	+02 22 17.50	0.0470
0114+000	4C -00.07	01 14 29.61	+00 00 36.80	0.3890
0115+000	4C -00.07	01 15 27.71	+00 00 39.50	...
0125−000L	...	01 25 12.07	-00 01 53.40	...
0125−000U	...	01 25 11.25	-00 01 11.40	...
0059+001	4C -00.06	00 59 05.51	+00 06 47.70	0.7170

Table 5.7: Radio source position for each source in the control sample. For each radio position, the source identification and redshift is listed, where available.

Source J2000	ID	R.A. h m s	Dec. ° m s	z
0106−019	PMN J0106−0155	01 06 23.02	-01 55 39.00	2.2010
0122−063	MRC 0120−065	01 22 31.89	-06 19 58.90	...
0125−001	MRC 0122−003	01 25 28.86	-00 05 55.50	1.0700
0139+015	4C +01.04	01 39 57.30	+01 31 45.30	0.2600
0238+049	...	02 38 40.03	+04 55 16.50	...
0251+062U	4C +05.12	02 51 03.03	+06 12 19.50	...
0251+062L	4C +05.12	02 51 02.61	+06 11 35.70	...
0259+008	4C +00.11	02 59 00.41	+00 49 24.00	...
0259+077	PKS 0256+075	02 59 27.08	+07 47 39.64	0.8930
0301+074	4C +07.10	03 01 49.20	+07 25 13.40	...
0305+056	PMN J0305+0537	03 05 32.21	+05 36 37.50	...
0318+053R	PMN J0318+0518	03 18 26.45	+05 18 10.20	...
0318+053L	PMN J0318+0518	03 18 30.65	+05 18 59.40	...
0259+139	4C +13.17	02 59 38.29	+13 54 56.60	0.0748
0317+440R	IRAS F03144+4350	03 17 40.85	+44 00 52.30	...
0317+440L	IRAS F03144+4350	03 17 46.08	+44 01 34.30	...
0427−116	MRC 0425−117	04 27 23.97	-11 40 19.00	...
0430−130	MRC 0428−131	04 30 31.59	-13 01 23.84	...
0436−133	...	04 36 42.25	-13 22 09.89	...
0439−113	...	04 39 57.12	-11 22 11.30	...
0444−135	PMN J0444−1333	04 44 23.24	-13 33 53.70	...
0654+503	4C +50.19	06 54 10.56	+50 18 52.20	...
0658+492U	...	06 58 46.68	+49 12 51.00	...
0701+497	...	07 01 03.82	+49 43 20.00	...
0706+425B	...	07 07 03.20	+42 32 48.69	...
0713+488	4C +48.20	07 13 27.93	+48 49 21.30	...
0714+456	4C +45.13	07 14 31.06	+45 40 07.70	...
0728+505	4C +50.22	07 28 06.17	+50 34 43.60	0.3500
0712+565	...	07 12 57.97	+56 31 03.50	...
0713+579R	8C 0709+579	07 13 39.55	+57 51 09.90	...
0713+579L	8C 0709+579	07 13 42.74	+57 51 16.50	...
0723+548	...	07 23 52.02	+54 49 10.90	...
0906−090	PMN J0906−0905	09 06 18.50	-09 05 50.11	...
0906−103	PMN J0906−1020	09 06 05.02	-10 21 03.10	...
0908−107	MRC 0905−105	09 08 04.41	-10 42 38.90	...

Table 5.7 – *Continued*

Source	ID	R.A.	Dec.	z
J2000		h m s	° m s	
0913−092	...	09 13 37.82	-09 14 24.75	...
0915+320	7C 0912+3213	09 15 23.79	+32 01 16.20	...
0921+368L	MG2 J092130+3652	09 21 32.60	+36 52 52.90	...
0921+368R	MG2 J092130+3652	09 21 28.18	+36 52 39.70	...
1023−278	PMN J1023−2749	10 23 33.24	-27 49 07.50	...
1059+283	7C 1056+2836	10 59 32.56	+28 20 01.60	...
1106+300	7C 1103+3017	11 06 24.15	+30 00 44.15	...
1107+288	7C 1104+2910	11 07 01.78	+28 53 11.25	...
1108+279	7C 1105+2814	11 08 16.58	+27 58 05.64	...
1108+292A	7C 1105+2930	11 08 25.75	+29 15 06.02	...
1108+292B	7C 1105+2930	11 08 19.94	+29 13 50.03	...
1109+289	...	11 09 18.04	+28 55 45.17	...
1110+293	7C 1107+2936	11 10 18.41	+29 20 16.85	...
1118+279A	7C 1116+2810	11 18 59.37	+27 54 11.98	0.0672
1118+280B	...	11 18 46.68	+28 02 55.98	...
1121+501	...	11 22 44.35	+50 10 09.96	...
1147+545	...	11 47 17.25	+54 34 55.70	...
1125+261	7C 1123+2626	11 25 53.71	+26 10 19.98	2.3410

Table 5.7 – *Continued*

5.6 Summary

A detailed description of the rotation measure fitting, and error analysis for the radio sample was presented in this chapter. Plots of the rotation measure fits for each source were shown in Figures 5.3 and 5.4. The division of the sources into two samples was based on the impact parameter of the radio sources compared to the outer radius of the X-ray emitting intracluster gas. In order to determine the cluster contribution to the observed rotation measure, the Galactic rotation measure was calculated toward each cluster, and removed from the observed rotation measure for each source. Tables of the residual rotation measures for the sources were presented, as well as identifications for sources in the radio sample.

Chapter 6

Rotation Measure Analysis

Overview: This chapter presents the analysis of the Faraday rotation measure data. As explained in Chapter 3, the sample of extragalactic radio sources is divided into a **cluster** sample, and a **control**. Section 6.1 compares the width of the rotation measure distribution of the **cluster** sample to that of the **control** sample to search for the signature of an intracluster magnetic field. This section also investigates the radial distributions of the observed rotation measure samples. The location of the Faraday rotating medium is considered in § 6.2, where the observed properties of the radio sample are used to place constraints on the location of the medium responsible for the observed rotation measure distribution. Section 6.3 discusses the consequences of selection effects introduced by targeting NVSS sources. The final section, § 6.4, provides a summary of the main results determined from this chapter.

6.1 Rotation Measure Analysis

The radio source sample observed for this thesis can be split into two separate populations, based on the impact parameter of the radio source to the relevant galaxy cluster. Sources lying at impact parameters which are interior the edge of the X-ray emitting gas for a particular cluster are included in the **cluster** sample. The lines of sight to these sources pass through the intracluster medium, and thus provide a probe for the intracluster magnetic fields. The second population consists of radio sources at impact parameters beyond the edge of the X-ray emitting gas, and are designated as the **control** sample. These **control** sources provide the baseline for searching for excess Faraday rotation within the cluster

sample. They are also included in the determination of the Galactic contribution to the observed rotation measures. The dispersion in the RRM of the **control** sources also provides a measure of the intrinsic scatter in the rotation measure of extragalactic radio sources.

6.1.1 Comparing the Cluster and Control Samples

One point to keep in mind during the comparison of the **cluster** and **control** rotation measure samples is the large variation in sample sizes, which is largely a result of the different volumes sampled. The **cluster** sample contains 28 sources distributed across impact parameters between 3 and 1460 kpc. The median impact parameter for the **cluster** sample is 445 kpc. The **control** sample, on the other hand, contains 89 radio sources distributed at impact parameters between 610 and 8550 kpc. The median impact parameter of the **control** sample is 3460 kpc. Figure 6.1 displays RRM histograms of the **cluster** and **control** samples. This figure clearly shows that the RRM distribution of the **cluster** sample is much broader that that of the **control** sample. One potential source of such a broadening could be associated with the distribution of the errors in the two rotation measure samples. In Figure 6.2, the distributions of the errors in the two samples are shown. The errors in the **cluster** sample appear to be marginally broader, but this effect could not produce the excess broadening seen in Figure 6.1.

To determine the statistical significance of the excess broadening, the Kolmogorov-Smirnov (K-S) test was applied to the two data sets to test the null hypothesis that the two samples are drawn from the same population. The cumulative K-S probability distribution for the two samples is shown in Figure 6.3. Based on this cumulative distribution function, the K-S test rejects the null hypothesis for these two samples at the 99.4% confidence level, *confirming the detection of excess Faraday rotation within the* **cluster** *sample. This Faraday excess further indicates the presence of intracluster magnetic fields.*

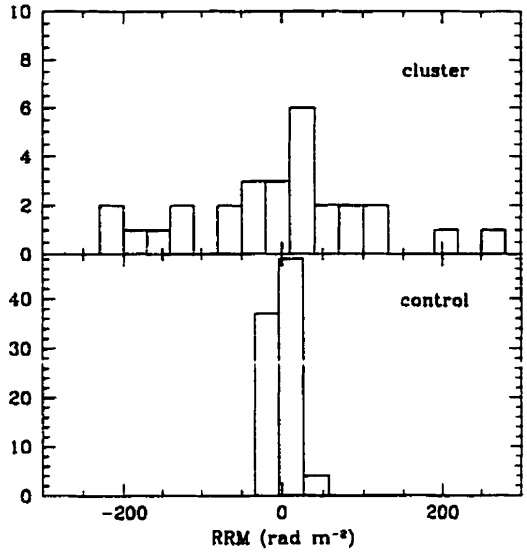

Figure 6.1: The top panel displays the histogram of the residual rotation measure distribution for the cluster sample, while the bottom panel displays that of the control sample. Comparing the width of these histograms reveals a statistically significant excess rotation measure distribution within the cluster sample.

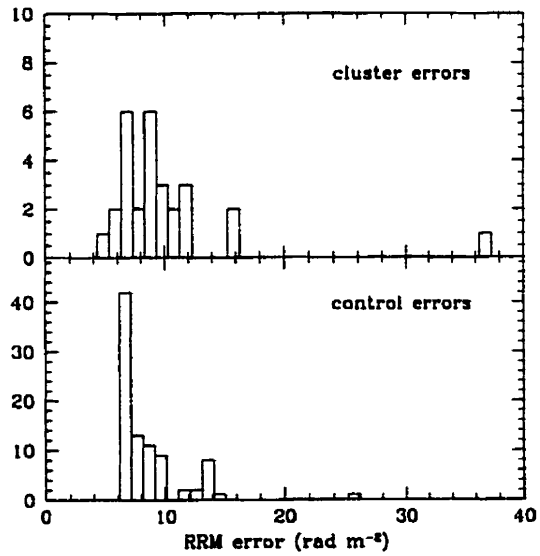

Figure 6.2: The top panel shows the distribution of the errors in the RRMs of the cluster sample while the lower panel shows that for the control sample. Although the cluster sample is slightly broader than the control sample, the difference cannot account for the observed RRM excess.

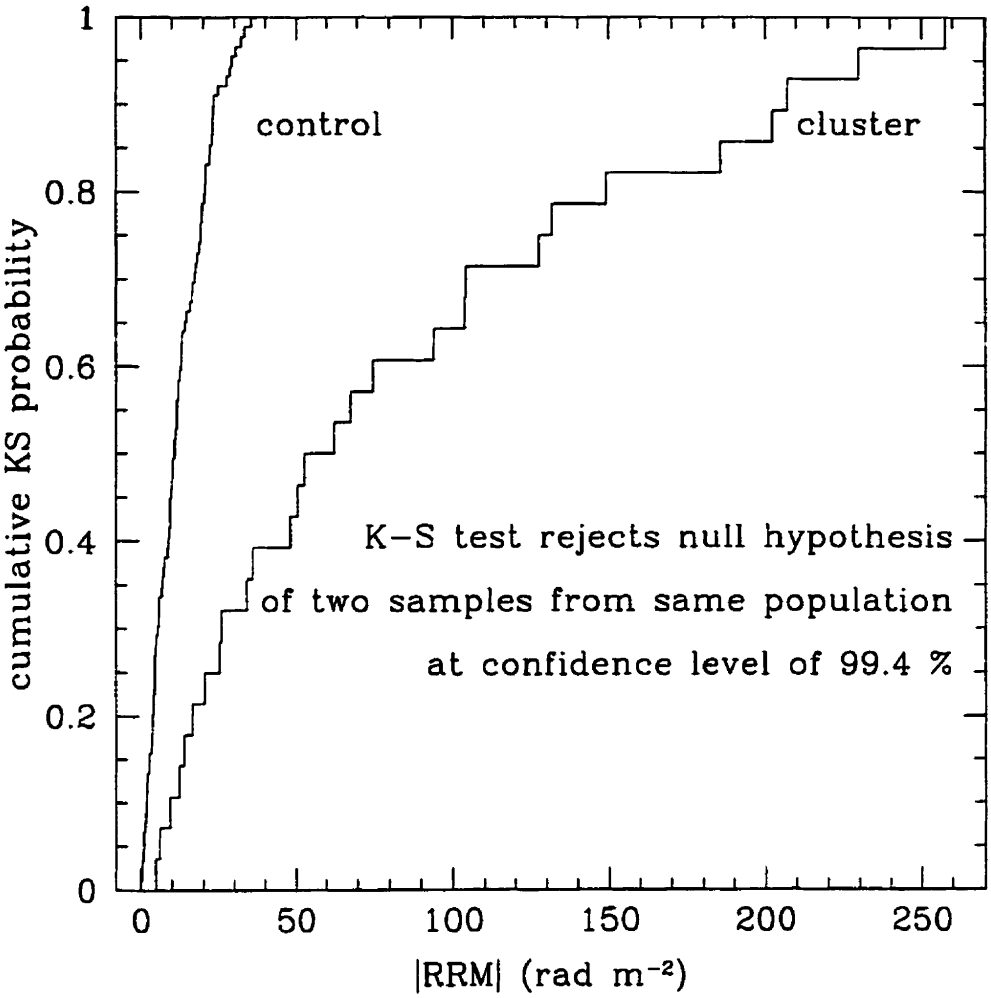

Figure 6.3: The cumulative Kolmogorov-Smirnov probability distribution is plotted for both the cluster and control samples. Based on this probability distribution, the K-S test rejects the null hypothesis of the two samples being drawn from the same population at a confidence level of 99.4%.

6.1.2 Rotation Measure Distribution

The rotation measure distribution of the radio sources falling at impact parameters out to 6 Mpc is shown in Figure 6.4. The open points represent the radio sources in the **cluster** sample, while the closed points represent the **control** sample. The error bars associated with the RRM points are the 1σ errors discussed in § 5.4. The residual rotation measure distribution of the **control** sample has a mean of 0.1 ± 1.6 rad m^{-2}, and a standard deviation of 15.1 rad m^{-2}. The standard deviation of the **control** sample sets the significance level for probing the radial distribution of the region of enhanced cluster-induced Faraday effects. Although the mean of the **cluster** sample, -4.6 rad m^{-2}, is not significantly different from that of the **control** sample, the standard deviation, 113.8 rad m^{-2}, is nearly an order of magnitude larger.

The magnitude of the residual rotation measure distribution clearly increases toward small impact parameters, reaching values of over 200 rad m^{-2} in the central regions of the clusters. Given the confirmed detection of excess Faraday rotation toward the **cluster** sample, the next question to consider is, to what impact parameter is the rotation measure excess observed?

Although Figure 6.4 clearly indicates that there is excess Faraday rotation toward lines of sight probing the central regions of galaxy clusters, it is difficult to determine the extent of this Faraday excess from this figure. Determining a measure of the extent of the excess rotation measure over a statistical sample of galaxy clusters is complicated by the intrinsic variations in the radial distributions of the intracluster medium in individual clusters. For instance, the RRM at a given physical impact parameter to an X-ray compact galaxy cluster is probing a completely different specimen of cluster gas when compared to a source at the same physical impact parameter to a cluster with very extended X-ray emission. To estimate the extent of the rotation measure excess, Figure 6.5 displays the magnitude of the RRM for the radio sample plotted as a function of the impact parameter expressed in units of R_{out}, the maximum extent of the X-ray gas. The solid line at 15 rad m^{-2} represents the 1σ intrinsic variation in extragalactic rotation measures as determined from the **control** sample. Note that the majority of the RRMs for the **cluster** sample ($b/R_o < 1$) are above the 1σ line out to the edge of the X-ray emitting gas. Although this statement is qualitative, it is important to note that *the rotation measure excess is not merely confined to the central*

fraction of the galaxy cluster, but, in fact, extends to large radii within the cluster sample.

At this point, it is useful to take note of a couple of individual points within Figure 6.5, which do not appear to follow the general trend.

- The source located at (b/R_o, |RRM|) $\sim$ (0.63, 202) is 0154+365, which probes Abell 262.
- The two sources falling at (b/R_o, |RRM|) $\sim$ (0.81, 104), and (0.95, 104) are 1039-273, and 1039-272, respectively. Both of these sources probe the intracluster medium in Abell 1060.

The residual rotation measure for these three radio sources appears to fall well above the general trend for sources at similar impact parameter within the **cluster** sample. Note, however, that these sources are probing the intracluster medium of the two lowest redshift galaxy clusters in the thesis sample. At the redshift of Abell 262, the PSPC field of view of 2° provides a maximum radial extent of 1080 kpc, while at the redshift of Abell 1060, the field of view probes a maximum radial extent of 780 kpc. The limitations provided by the PSPC field of view, combined with the low redshift of these two clusters, suggests that the maximum radial extent of the X-ray emitting gas in these clusters is underestimated. If this is the case, the three sources indicated above would be shifted inward in Figure 6.5. There is currently, however, no better estimate available for the radial extent of the X-ray emission in these two galaxy clusters.

In order to smooth out some of the variations introduced by the uncertainties in the measurement of R_{out}, the radial distribution of the dispersion of the rotation measure distribution has been plotted in Figure 6.6. The rotation measure dispersion was calculated through the use of Tukey's biweight estimator (Hoaglin et al. 1983), and is determined in bins each containing 9 sources. The figure plots the dispersion as a function of the mean value of the bin center in units of R_{out}, together with the 2σ confidence limits. Within this 2σ confidence interval, the three central bins, which cover the **cluster** sample, fall above the intrinsic dispersion in extragalactic rotation measures, as determined from the **control** sample.

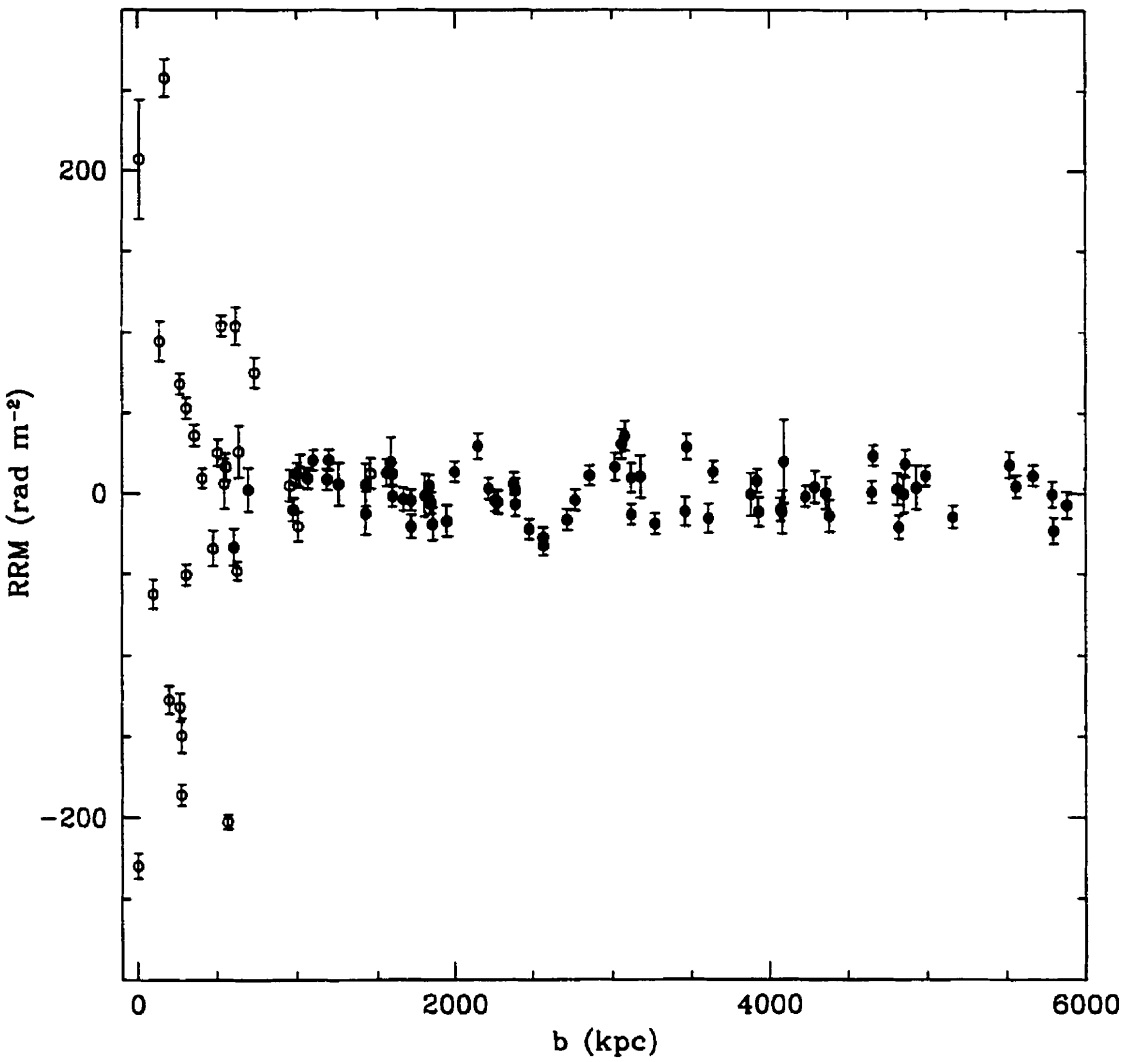

Figure 6.4: The residual rotation measure (RRM) is plotted as a function of the source impact parameter in kpc. The cluster sample is plotted with open points, and the control sample with filled points. The width of the distribution shows a clear increase toward small impact parameters.

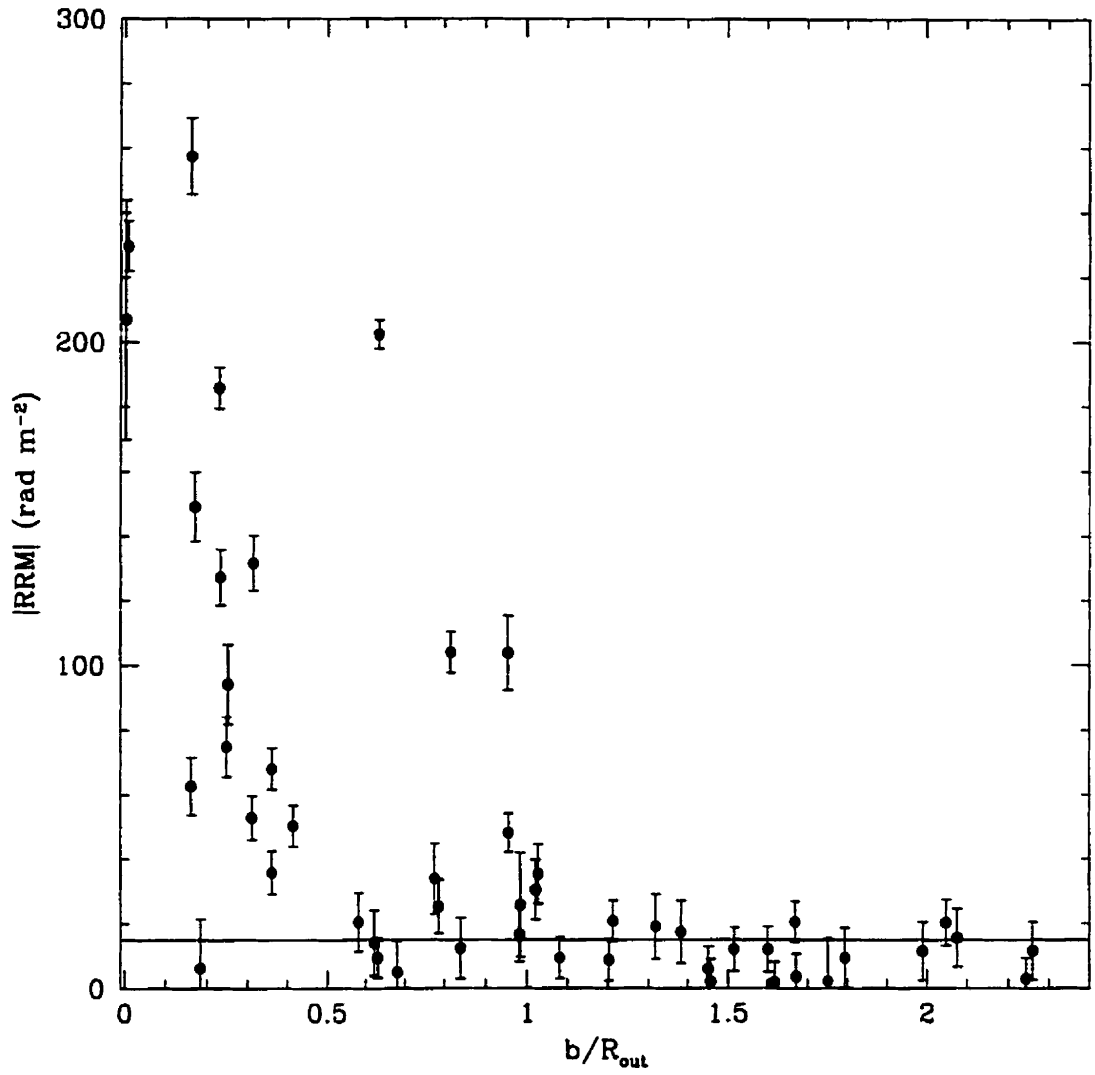

Figure 6.5: The magnitude of the residual rotation measure of the cluster sample is plotted as a function of the source impact parameter in units of R_{out}, the outer radius of the X-ray emission. The solid line at 15 rad m^{-2} indicates the intrinsic variation in the rotation measure distribution of extragalactic radio sources. The plot shows that the majority of the RRM measurements lie above the background level out to the edge of the cluster gas distribution (b/R_{out}=1).

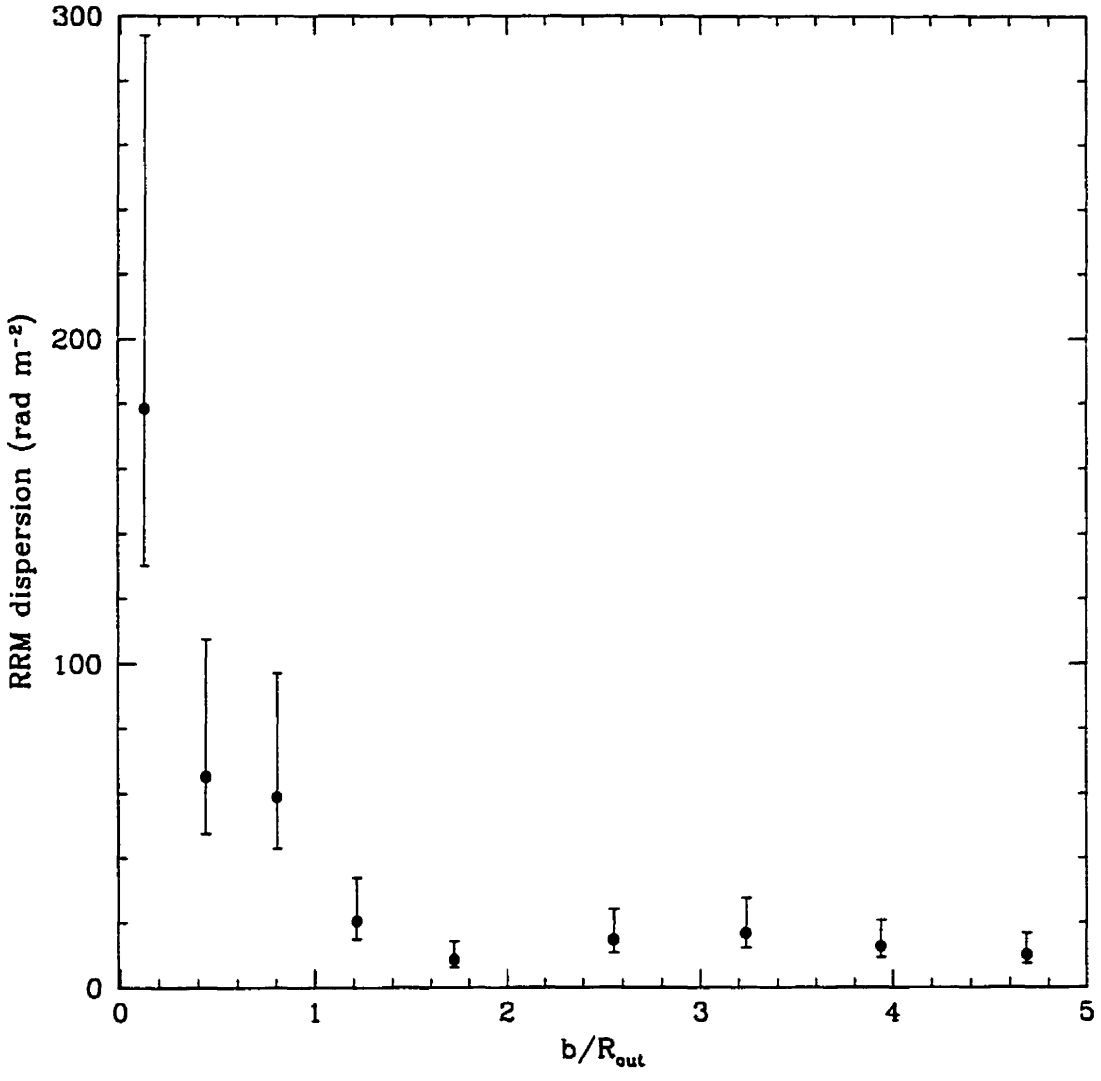

Figure 6.6: The dispersion in the RRM is plotted as a function of the mean impact parameter of the bin in units of the outer radius of the cluster gas (R_{out}). The dispersion is calculated for bins of 9 sources, and the error bars represent the 2σ confidence interval. The central three bins cover the sources in the cluster sample, with the remainder of the bins representing the control sample. Note that the dispersion in the cluster sample is well above that of the control sample, thus indicating that the Faraday excess (and hence magnetic field) extends to the edge of the intracluster gas.

6.2 Location of the Faraday Rotating Medium

Before estimating the magnetic field strength associated with the observed rotation measure excess, it is necessary to consider all plausible locations for the origin of the excess. Recall that the observed rotation measure is a sum of all rotation measure contributions along the line of sight between the source and the observer. The potential Faraday rotation media were briefly touched upon in § 5.4, where the Faraday rotation was considered to originate from any combination of the following media:

- the local environment within the radio source
- the local galactic medium
- the intercluster medium
- the intracluster medium
- the interstellar medium within our Galaxy
- Earth's ionosphere

Based on the arguments presented in § 5.4, and the clear correlation of the magnitude of the RRM with the source impact parameter, it is possible to rule out all media but the intracluster medium as the source of the observed Faraday excess. This does not, however, provide a unique physical location for the origin of the Faraday excess *within the clusters*, as there are several possible components within the intracluster medium which may generate Faraday rotation:

- a mixing layer, within the radio source, of thermal cluster gas and the radio source magnetic fields
- a dense sheath of thermal gas and intracluster magnetic fields surrounding embedded radio galaxies
- magneto-ionic plasma filling the intracluster medium

The potential contributions from each of these components are considered below.

6.2.1 Mixing Layer

The synchrotron emission from the radio sources under study indicates the presence of magnetic fields distributed within the sources (§ 2.1.1). For the sources embedded within the hot intracluster gas, it is possible that the thermal cluster gas may mix into the radio plasma, causing internal Faraday rotation (§ 2.4.3). In this case, the radio emission from the back of the source is rotated by a different amount from that on the near edge. In the simplest geometry of a uniform slab of constant density and magnetic field through the source, the Faraday depth increases uniformly from 0 at the forward edge of the radio source, to $n_e B \ell_{slab}$ at the far edge of the slab. The position angle of the polarized emission will follow a λ^2 law with increasing wavelength, as shown by the dashed lines in Figure 2.1. The solid lines in the figure show the decreasing behaviour of the polarized intensity in the case of internal Faraday rotation. Toward long wavelengths, the polarization amplitude drops to zero, and the position angle of the polarized emission jump discontinuously from $\pi/2$ to zero. This behaviour of internal Faraday rotation is characterized by severe depolarization of the radio sources. This simple picture of a uniform mixing layer for the origin of the Faraday excess can be ruled out by recalling that the radio sample does not display significant depolarization, even at the relatively long observing wavelengths of 20 cm, (Figure 5.1).

In a more realistic geometry, the magnetic field and the electron density vary along the line of sight through the radio source. The general trend found by Gardner & Whiteoak (1966), for these non-uniform geometries, is that the zeros in the polarization amplitude vanish, and the position angle no longer follows a λ^2 law, but turns over to approach 45°. Note that the non-vanishing polarized intensity means that the depolarization in this case is less severe than for the uniform slab. The majority of the sources in the **cluster** sample, however, follow a λ^2 law very closely over more than 90° in position angle. It can therefore be concluded that *the majority of the observed Faraday excess is external to the radio sources.*

6.2.2 Dense, Magnetized Sheath

Van Breugel et al. (1984) considered a shell of thermal cluster material surrounding embedded radio sources. This shell could be generated through the expansion of the radio source within the ICM. This expansion sweeps up the intracluster gas, and compresses it. The magnetic fields associated with the radio source serve to decelerate the accreting, ionized

gas in the Van Breugel model. This deceleration of the gas results in a clumpy boundary layer of relatively high density surrounding the radio source. According to the Van Breugel model, Rayleigh-Taylor and Kelvin-Helmholtz instabilities in the boundary layer mix the thermal and synchrotron plasmas, thus creating a Faraday rotating medium. A more detailed numerical simulation of this scenario, by Bicknell et al. (1990), predicts that there should be large rotation measure excursions across the radio source. The scale of the RM variations is the half-wavelength of the surface waves formed by the Kelvin-Helmholtz instabilities, where the typical scale is estimated to be of order 4 kpc.

The current observations of the radio source sample presented in this thesis do not provide the resolution necessary to detect these predicted rotation measure excursions, and thus cannot rule out this model as a source of at least some of the observed Faraday excess. Note, however, that a number of the high residual rotation measure sources in the **cluster** sample are currently unidentified. The lack of optical identification for the sources suggests that the sources are, in fact, high redshift background galaxies, and thus presumably not embedded within the intracluster gas. *Therefore, the high rotation measures of these sources must originate in the diffuse, foreground intracluster gas. Further, the foreground intracluster gas must also contain magnetic fields.*

6.2.3 Diffuse Intracluster Medium

The detection of cluster-wide synchrotron halos in a small number of galaxy clusters (Feretti & Giovannini 1996), provides evidence for the existence of magnetic fields distributed through the ICM in these galaxy clusters. It is not, however, known if the rarity of synchrotron halos results from a general lack of strong magnetic fields within clusters of galaxies, or from a paucity of energetic particles. Further evidence of the presence of magnetic fields within the diffuse intracluster medium is presented in the work of Kim et al. (1991). In their paper, Kim et al. find evidence, at a confidence level above 2σ, of excess Faraday rotation in the RRM distribution of a sample of background-only radio sources. Further evidence of the intracluster magnetic fields are provided by the observed rotation measure excess of the background sources within the sample of this thesis. Note, however, that the study by Hennessy et al. (1989) found no evidence of excess Faraday rotation toward galaxy clusters for a sample of background-only radio probes.

The question of what constraints the current sample places on the presence of an intr-

acluster magnetic field is considered next. This question is addressed through Figure 6.7, which shows the magnitude of the RRM plotted against the projected electron density at the impact parameter of the radio source for each source in the **cluster** sample. This figure shows that the RRM values are correlated with the intracluster gas density. This correlation further indicates that the RRMs are related to the intracluster medium, although the nature of this relation is not unique. One interpretation of this correlation could be that the lines of sight through the cluster gas are indeed probing the general intracluster magnetic fields. It is also possible, however, that the correlation is more directly related to the magnetized sheath model described above. To resolve this issue, the data for embedded sources are plotted in Figure 6.7 with open circles, while the remaining (background) source data are plotted with filled circles. This separation of the source population shows that both samples display similar correlations between the magnitude of the RRM and the projected intracluster electron density. This persistence of this correlation suggests that *the residual rotation measures are at least partially tracing an overall intracluster magnetic field.*

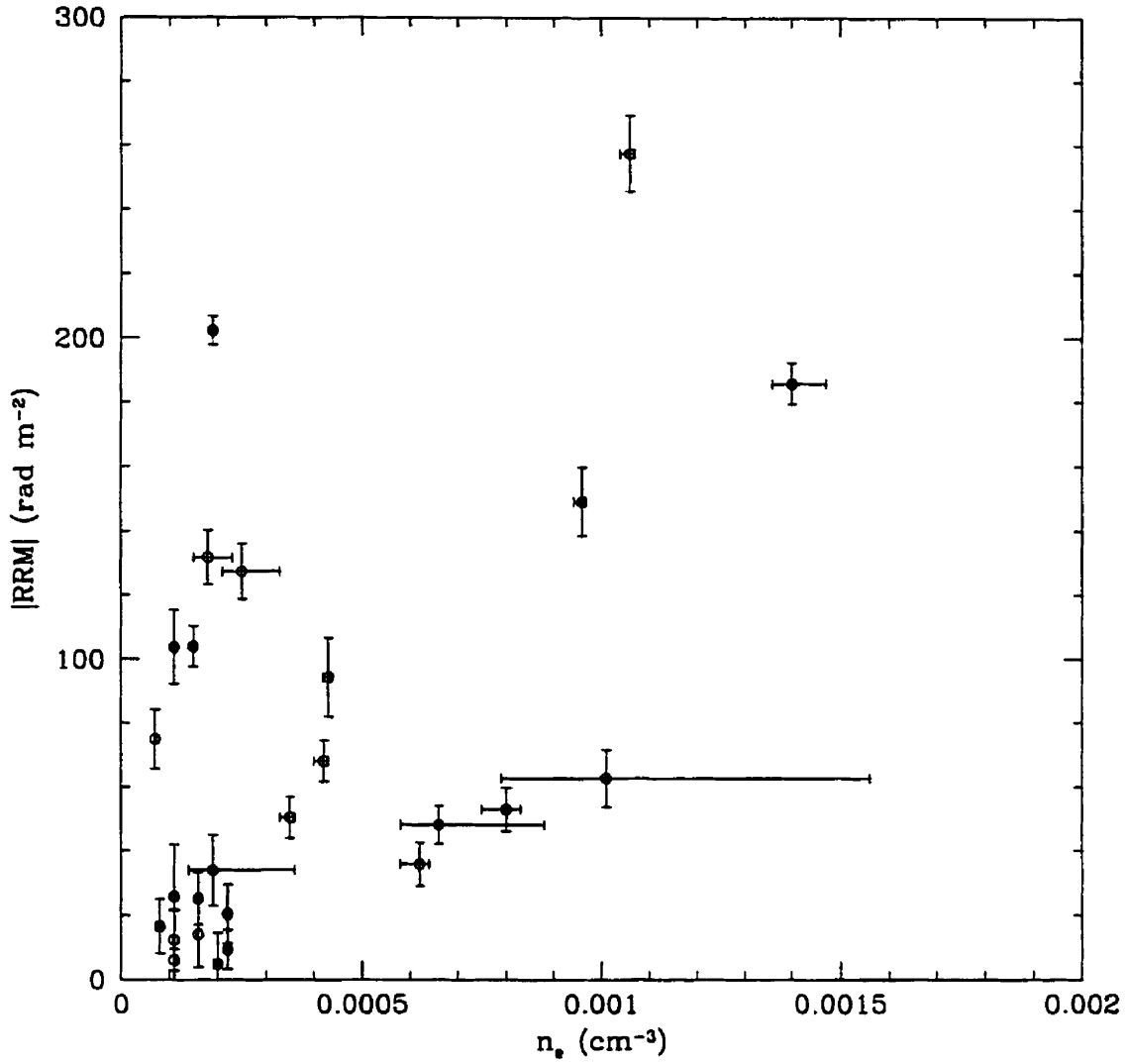

Figure 6.7: The absolute magnitude of the residual rotation measure is plotted as a function of the projected intracluster electron density at the impact parameter of the radio source for the cluster sample. The open points represent the embedded sources, and the closed points indicate the background sources. The similar trends of increasing |RRM| with increasing n_e for the embedded and background samples points toward the diffuse ICM as the origin of at least part of the observed Faraday excess.

6.3 Sample Selection Effects

The radio targets selected for follow up polarimetry for this thesis were identified from the NVSS survey. The observations for this survey were undertaken within the 20 cm band at the VLA, with a resolution of 45″. This combination of long wavelength, low resolution observations introduces a selection effect into the target sample. A radio source viewed through a foreground region of highly tangled magnetic cells would be severely depolarized in the NVSS survey. Such a source would not meet the polarization criteria required by the target selection in this thesis.

These highly depolarized sources are generally located in the central regions of galaxy clusters, with associated rotation measures of over 500 rad m^{-2}. It could be argued that selection against these high rotation measure sources results in a sample which is biased toward probing lines of sight through fairly ordered magnetic fields. As the magnetic field strength scales inversely with the square root of the coherence length of the field (for a given rotation measure) the field strengths presented in this thesis should be considered lower limits.

6.4 Summary

This chapter examined the rotation measure distribution of the radio source sample with a goal of providing a basic framework for understanding intracluster magnetic fields. The results from the chapter were mainly based on comparing the distribution of the RRMs of sources viewed through the intracluster gas (the **cluster** sample), to that of sources viewed beyond the detectable X-ray edge of the gas (the **control** sample).

Comparing the rotation measure distribution of the **cluster** sample to that of the **control** sample provided clear evidence of excess Faraday rotation toward the sources in the **cluster** sample. Further, the Kolmogorov-Smirnov test rejected the null hypothesis of the **cluster** and **control** samples being drawn from the same parent population at the 99.4% confidence limit. It was therefore concluded that the observed Faraday excess was indeed tracing the effects of a magnetic field associated with the intracluster medium.

The radial variation and extent of the observed Faraday excess helps to distinguish between models of the distribution of the intracluster magnetic fields. The residual rotation measures of the **cluster** sample showed a radially decreasing distribution from absolute

magnitudes of $\sim$ 200 rad m^{-2} in the central regions of the clusters, to background levels of around 15 rad m^{-2} near the outer edges of the clusters. The dispersion in the rotation measure distribution plotted as a function of radius indicated that the excess broadening of the distribution extends out to the edges of the X-ray emitting gas. This was therefore interpreted as indicating the widespread presence of magnetic fields, within the intracluster medium, out to the edges of the thermal cluster gas.

Although the data indicated a statistically significant excess Faraday effect toward lines of sight through the intracluster medium, there are several possible media which may be responsible for this excess. Based on the depolarization properties of the radio sample, and the fact that the data were well fit by a λ^2 relation, the mixing layer model of thermal gas within the synchrotron boundaries of the radio sources was rejected as the source of the majority of the observed Faraday excess. Another possibility for the Faraday rotating media was a dense sheath of magneto-ionic material built up around radio galaxies embedded within the intracluster gas. Although the resolution of the source sample was insufficient to detect the predicted Faraday variations for this model, the presence of excess Faraday rotation along lines of sight toward background radio probes indicated that these sources were tracing magnetic fields in the general ICM. Also, the absence of any small rotation measures at small impact parameter in the **cluster** sample further supports the diffuse ICM as the origin of the Faraday excess.

The conclusion that the Faraday excess originates in the diffuse intracluster medium was further supported by the comparison of the magnitude of the residual rotation measures with the projected intracluster electron density. The high redshift background radio sources followed the same distribution as sources embedded within the intracluster gas, indicating that the Faraday excess was not local to the source, but was universal to the foreground intracluster medium.

Based on the results from this chapter, the magnetic field estimates presented in the next chapter are determined under the assumption that the Faraday rotating medium is associated with the general intracluster gas. Note that for a given residual rotation measure, the inferred magnetic field strength for the intracluster origin model will be lower than that inferred from the magnetized sheath model, due to the longer path length through the Faraday rotating gas in the former model. The application of the intracluster origin model to the data therefore provides a conservative estimate for the associated magnetic field

strength.

Chapter 7

Intracluster Magnetic Fields

Overview: This chapter develops an overall picture of the distribution of the intracluster magnetic fields which produce the observed rotation measure excess. Section 7.1 investigates the nature of the geometry of intracluster magnetic fields. Several models for the distribution of magnetic fields within the ICM are considered, and the predictions from each model are compared to the observed properties of the cluster sample. Based on these models, a range of magnetic field strengths for lines of sight toward the radio sources are presented in § 7.2. Although the majority of the radio sources within the cluster sample are marginally resolved, there are a few sources which have sufficient resolution to permit Faraday mapping of the rotation measure structure. The rotation measure maps of four sources observed through the ICM of three Abell clusters are presented in § 7.3. The final section in this chapter, § 7.4, summarizes the main results from the analysis of the intracluster magnetic fields.

7.1 What is the Nature of the Intracluster Magnetic Field Distribution?

In order to interpret the RRM distribution for the radio sources, it is necessary to have a physical picture of both the electron density distribution, and the magnetic field structure within the intracluster medium. In this section, several possible models of the intracluster magnetic field structure will be explored. For each model, the underlying assumptions are discussed, and the predictions of the rotation measure distribution are compared to the

observed rotation measure distribution to assess the applicability of the model to the data. Note that the magnetic field strength referred to in Equation 2.40 is the component of the magnetic field parallel to the line of sight. The magnetic field distribution in the intracluster medium is likely to have components perpendicular to the line of sight, which would, on average, increase the overall field by $\sqrt{3}$ from $B_{||}$. The magnetic field strengths discussed within this chapter, therefore, refer to the total field, unless otherwise indicated.

7.1.1 "Uniform Slab" Intracluster Field

The simplest model for the magnetic field within the intracluster medium is the uniform slab model. In this model, the magnetic field has a constant strength and direction over the entire path through the intracluster medium. The electron density can also be assumed to be uniform, although more physically it is generally modeled as a King profile, Equation 2.29. The mean line of sight magnetic field strength at impact parameter b to the cluster centroid is given by

$$B(b) = \sqrt{3} < B_{||} >= \frac{\sqrt{3}|RRM|}{811.9\, n_e(b)\, \ell_{\rm path}} \ \mu{\rm G}, \tag{7.1}$$

where $\ell_{\rm path}$ is the path length in kpc through the intracluster gas. This model further assumes that the magnetic field within the intracluster gas has a filling factor of one. In this picture, the rotation measure distribution would be expected to increase, with increasing electron column density through the intracluster medium. This prediction can be compared with Figure 7.1, where the magnitude of the residual rotation measure for the **cluster** sample is plotted as a function of the electron column density along the line of sight to the radio source. This figure shows a clear trend of increasing magnitude of the RRM with increasing electron column density, as predicted by the uniform slab model. Note, however, that there does not appear to be a single field estimate which is appropriate for the sample of clusters studied. The three solid lines on the plot provide the range of magnetic field strengths required to constrain the majority of the observations under this model. This plot shows that the uniform slab model is broadly consistent with the observations, for magnetic field strengths between 0.1 and 1.5 μG. Note, however, that high resolution Faraday maps of extended radio sources often show small scale structure in the rotation measure, indicating that the field is not uniform on all scales.

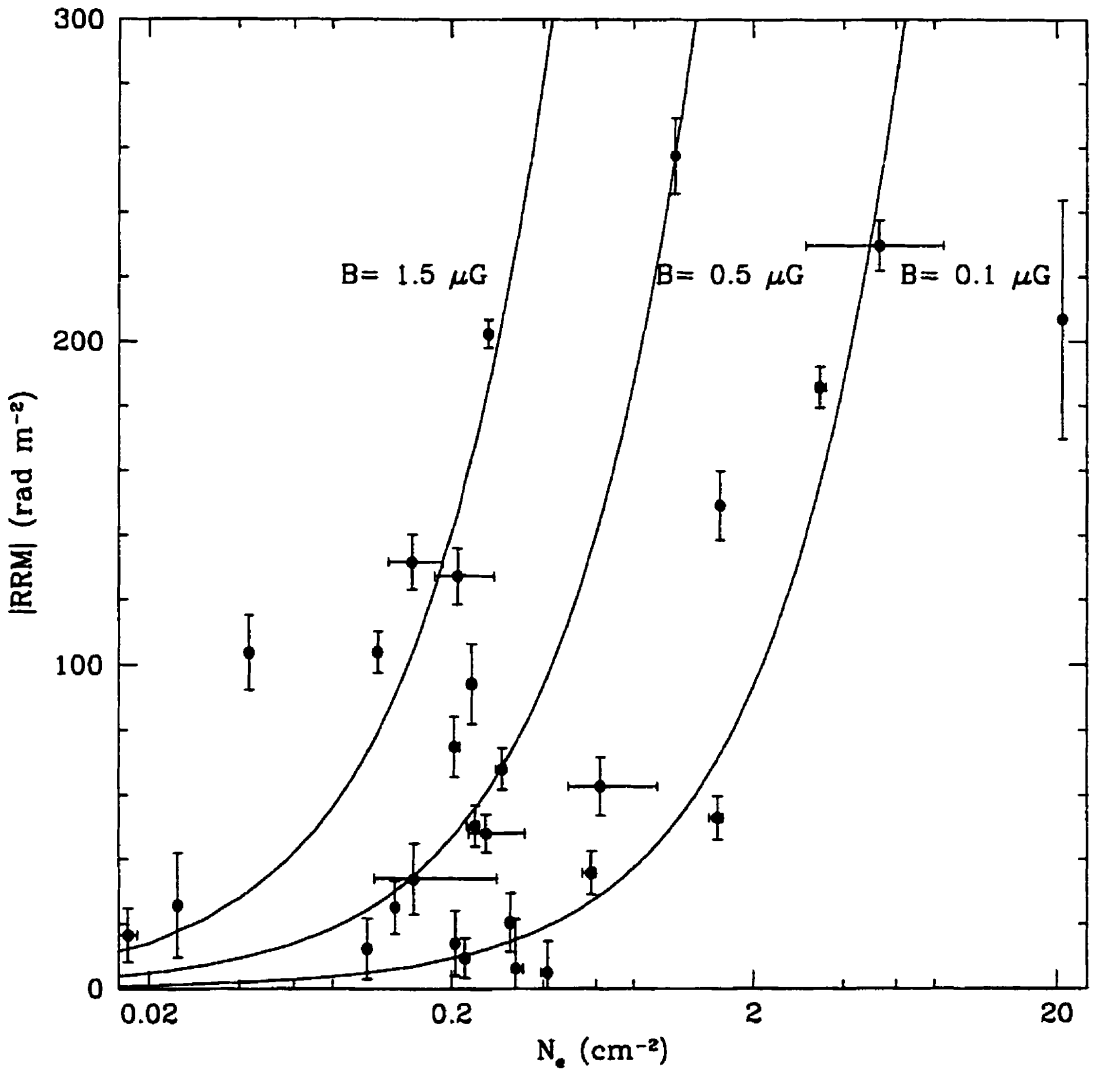

Figure 7.1: The absolute magnitude of the residual rotation measure is plotted as a function of the electron column density along the line of sight to the radio source. The error bars represent the 1σ errors on RRM, and N_e. The three solid lines at magnetic field strengths of 1.5, 0.5, and 0.1 μG show the predicted relation, at each of these field strengths, for the uniform slab model.

7.1.2 Tangled Cells

Perhaps a more realistic model for the distribution of intracluster magnetic fields is a geometry where the field direction is constant within some cell scale, $\ell_{\rm cell}$, and varies randomly from cell to cell. Such a field geometry was considered in the statistical rotation measure study of Lawler & Dennison (1982), and could be generated by galaxy motions as discussed by Jaffe (1980).

Rotation Measure Distribution

Consider, initially, a configuration where the magnetic field strength is uniform throughout the Faraday cells. The observed rotation measure in the tangled cell model is generated by a random walk process, where each cell along the line of sight contributes a rotation measure of

$$RM_{\rm cell} = 811.9\, n_e\, B_{||}\, \ell_{\rm cell}. \tag{7.2}$$

For a random distribution of many such cells, the average line of sight magnetic field will be zero as there will be an equal number of cells with fields pointed toward, and away from the observer. The expectation value for the observed rotation measure in an ensemble in this geometry is (Lawler & Dennison 1982)

$$< RM_{\rm obs} >= 811.9 n_e < B_{||} > L = 0. \tag{7.3}$$

The variance for a line of sight through a cluster which experiences a random walk in RM through many cells is (Lawler & Dennison 1982)

$$\sigma^2_{RM} = \frac{811.9^2}{3} \ell_{\rm cell} \int_o^L n_e^2(b) B^2_{\rm cell}(b) d\ell \quad \text{rad m}^{-2}. \tag{7.4}$$

For a random walk through $\mathcal{N}$ Faraday cells, the observed rotation measure is related to the rotation measure of the Faraday column with a uniform magnetic field by

$$RM_{\rm obs} = \frac{RM_{\rm col}}{\sqrt{\mathcal{N}}}, \tag{7.5}$$

while the Faraday column rotation measure is related to the individual cell rotation measure by $RM_{\rm col} = RM_{\rm cell}\mathcal{N}$, thus the observed rotation measure is related to the cell rotation

measure by

$$RM_{\rm obs} = RM_{\rm cell}\sqrt{N}. \tag{7.6}$$

This equation follows from Equation 7.4, and simply states that the typical rotation measure observed is the root mean square value.

For a path length of 1 Mpc through the ICM, and a typical cell size of 10 kpc, the observed rotation measures of 200 rad m^{-2} at small impact parameter corresponds to a magnetic field strength of order 5 μG in the cells. This cell field estimate places that magnetic pressure within the cell at 10% of the local ICM gas pressure. As the lines of sight toward radio sources probe larger impact parameters, the equipartition magnetic field strength within the cells would drop due to the declining ambient gas pressure. Further, if the tangling of the intracluster magnetic field is indeed a result of turbulence from galactic wakes, one would expect that the tangling frequency would increase toward the central regions of galaxy clusters, where the galaxy density is highest. Thus, in the turbulent wake model, the radially decreasing magnetic field strength would be accompanied by a radial increase in the cell sizes.

Next consider what the rotation measure distribution of a tangled cell model, with radially increasing cell size, would look like. For radio sources probing the outer regions of such a distribution, the line of sight would pass through a small number of randomly distributed cells, and, on average, the observed rotation measure would only be slightly higher than that produced in a single cell. On the other hand, lines of sight passing through the central regions of this distribution would encounter many Faraday cells. The observed rotation measure toward the central regions would therefore be increased by a larger amount, compared to that from individual cells. In this case, the rotation measure distribution would be expected to increase from moderate values near the outer edges of the cluster gas, to fairly large values at small impact parameters through the cluster core. This prediction is in agreement with what is seen in Figure 6.5, and observed toward the central regions of cooling flow clusters (Ge & Owen 1994; Taylor et al. 1994) where the observational trend is for the residual rotation measure to significantly increase toward small impact parameters. It is also interesting to note the lack of small rotation measures at small impact parameters. This distribution indicates that either the filling factor of the cells is near unity, or alternatively, that the cluster also contains a large scale, ordered field

such that all lines of sight experience Faraday rotation. Further evidence for a large scale field is discussed in § 7.3. The combination of tangled cells plus a uniform component is investigated below through the rotation measure dispersion.

Polarization Properties in the Tangled Cell Model

It is worth considering what effects a tangled cell model, with radially varying cell size, would have on the polarization properties of the radio sources. The main issue to consider is that an observation of a radio source through a region of many small-scale Faraday cells will be depolarized at long wavelengths, through beam depolarization (§ 2.6.1). This depolarization is not, however, observed within the **cluster** sample (Figure 5.1) which indicates that the lines of sight probed are not dominated by small scale Faraday features. A detailed discussion of the depolarization created by a foreground screen is given in Burn (1966). Note, however, that the study by Tribble (1991) indicates that the depolarization predicted by the Burn model was severely overestimated at long wavelengths. Based on the Tribble results, the tangled cell model is therefore not ruled out by the depolarization properties of the radio sample.

Rotation Measure Dispersion

For a line of sight passing through an intracluster medium filled with cells of randomly distributed magnetic field directions, the observed rotation measure distribution would be a Gaussian with a mean RM given by Equation 7.6, and the variance given by Equation 7.4.

The projected electron density, at the impact parameter of the radio sources, has been determined for each source in our sample. It is therefore possible to calculate the rotation measure dispersion of the sources in units of $B_{\rm cell}\sqrt{\ell_{\rm cell}}$. Using the 2σ confidence limits for the (binned) rotation measure dispersion of the **cluster** sample (the first three bins in Figure 6.6), the radial distribution of $B_{\rm cell}\sqrt{\ell_{\rm cell}}$ for the cluster sample can be determined. Assuming that the magnetic field strength within the ICM follows a radial distribution such that the magnetic pressure in the individual cells is some fraction of the ambient gas pressure:

$$\frac{B_{\rm cell}^2}{8\pi} \approx \alpha n k T, \tag{7.7}$$

the radial distribution of cell sizes can be recovered.

A reasonable approach to estimating the magnetic field strength would be to assume that throughout the cluster, the magnetic pressure reaches some uniform fraction of the ambient gas pressure. Taking the scaling constant α=0.1, the associated magnetic field represents the limiting case where the magnetic pressure begins to be dynamically important within the ICM. The field strengths determined for this scaling constant are given in Table 7.1 for each of the embedded sources. Using these field strengths, and binning the data into radial bins containing nine sources, as in Figure 6.6, the radial distribution of the cell sizes, and the associated bin centers (in units of the outer radius of the gas distribution) are estimated as

$$0.2 < \ell_{cell} < 1.1 \text{ kpc}, \quad < b/R_o >= 0.13 \tag{7.8}$$

$$21 < \ell_{cell} < 108 \text{ kpc}, \quad < b/R_o >= 0.44 \tag{7.9}$$

$$224 < \ell_{cell} < 1140 \text{ kpc}, \quad < b/R_o >= 0.81. \tag{7.10}$$

This predicted radial distribution of cell sizes is unique as it represents the first estimate of the radial distribution of Faraday cells within the ICM. Further, the cell scales presented herein represent the only estimate of cell sizes outside the cores of galaxy clusters. Note, however, that these cell scale estimates are based on a very simplified model and are simply intended to provide a first order estimate of the physical distribution of the Faraday cells.

Consider next, a situation where the magnetic pressure is in equipartition with the local gas pressure throughout the cluster. The cell estimates become

$$0.02 < \ell_{cell} < 0.08 \text{ kpc}, \quad < b/R_o >= 0.13 \tag{7.11}$$

$$2.1 < \ell_{cell} < 10.4 \text{ kpc}, \quad < b/R_o >= 0.44 \tag{7.12}$$

$$17 < \ell_{cell} < 86 \text{ kpc}, \quad < b/R_o >= 0.81. \tag{7.13}$$

The small cell sizes within the central regions of the ICM are consistent with estimates from high resolution Faraday mapping (Feretti et al. 1999).

7.1.3 Cluster Dynamo

A more complex model of the intracluster magnetic fields can be developed by invoking dynamo effects. Eilek (private communication) has pursued the possibility of a turbulent

dynamo within the intracluster medium. In the case of helical turbulence, inverse cascades could generate and support fields on scales much larger than the turbulence scale. The conditions required for helical turbulence are that $< \mathbf{v_t} \cdot \nabla \times \mathbf{v_t} > \neq 0$ or $< \mathbf{b_t} \cdot \nabla \times \mathbf{b_t} > \neq 0$, where $\mathbf{v_t}$, and $\mathbf{b_t}$ are the turbulent velocity and magnetic field, respectively. Eilek solves the dynamo equation, and finds that the magnetic fields for the higher order modes, $m \geq 2$, are

$$B(r) \propto (r/\lambda_D)^{m-1} \quad r < r_{\max} \tag{7.14}$$

$$B(r) \propto (r/\lambda_D)^{-1} \quad r > r_{\max}, \tag{7.15}$$

where λ_D is the length scale of the dynamo solution, and $r_{\max} = 1.4 m \lambda_D$.

The predicted rotation measure structure for the Eilek model has fluctuations on scales of 2–3 λ_D, which corresponds to 40–60 kpc. This model further predicts that there will be a rapid decrease in the rotation measures beyond the cluster core due to the r^{-1} scaling. Additionally, in all but the m=1 mode, the maximum field strength occurs at an impact parameter of several 10's of kpc from the cluster cores. The higher order modes, therefore, have a central hole in the magnetic field structure which produces a signature of maximum rotation measure at an impact parameter of several tens of kpc from the cluster core. Numerical simulations by Eilek also show that for a statistical sample of Faraday observations, the dynamo model predicts that the rotation measure distribution will range between zero and an envelope maximum which is determined by the properties of the dynamo. The observed distribution, on the other hand, shows that the central rotation measures fall on what appears to be an unfilled envelope, with the largest values observed at the smallest impact parameters. This discrepancy suggests that the dynamo model for intracluster magnetic fields is not the source of the majority of the observed Faraday excess.

7.1.4 Summary

Although the rotation measure analysis presented in Chapter 6 indicates that the majority of the observed Faraday excess originates within the intracluster medium, a model of the field distribution is necessary to interpret the RRM-impact parameter distribution. The simplest model for the magnetic field distribution is a geometry where a field of uniform direction fills the entire intracluster medium. The observed RRM distribution is constrained by the uniform slab model for field strengths between 0.1 μG and 1.5 μG.

The presence of turbulence within the intracluster medium (e.g. galactic wakes and merger effects) would tend to disrupt a uniform field and produce a distribution which can be characterized by Faraday cells. A line of sight passing through a simple tangled cell distribution would be characterized by a Gaussian distribution with a zero mean and radially decreasing rotation measure. The dispersion in the observed rotation measures places constraints on the product of $B_{\rm cell}\sqrt{\ell_{\rm cell}}$. Using the X-ray properties of the intracluster medium, the magnetic field strength at the impact parameter of an embedded radio source can be estimated from the local ICM gas pressure. By assuming that the magnetic pressure reaches some constant fraction of the gas pressure throughout the intracluster medium, the radial distribution of the magnetic field strength was estimated. Combining this field strength with the RRM distribution allowed the tangling scale of the field can be recovered. Although the estimated cell scales for the outer regions of galaxy clusters remain to be observationally verified, the small, $\lesssim 1$ kpc, cell scales estimated for the central regions are similar to the observed Faraday scales determined from high resolution Faraday mapping.

The final distribution considered for the intracluster magnetic fields relies on a dynamo effect to maintain the fields. The predictions of an offset in the maximum rotation measure, and a filled envelope of rotation measures, are not supported by the observed rotation measure distribution.

In conclusion, the observed rotation measure distribution was found to be broadly consistent with the predictions from a uniform slab model. In addition, the tangled cell model was also found to adequately reproduce the observed distribution, and was further used to make predictions about the radial distribution on cell scales within the intracluster medium.

7.2 Magnetic Field Estimates

In this section, the estimates of the intracluster magnetic field strength derived from the two models supported by the observations, the uniform slab model, and the tangled cell model, are provided.

7.2.1 Uniform Slab Model

The intracluster magnetic field estimates for the uniform slab model are determined from Equation 7.1. The field estimates across the **cluster** sample range from 0.02 to 5 μG for

lines of sight toward the radio probes. The magnetic field strength determined from this model for each source sightline is listed in Table 7.1.

7.2.2 Tangled Cell Model

The intracluster magnetic fields have also been modeled for a foreground screen composed of a number of Faraday cells. Based on the observed rotation measure dispersion, the scale length of the Faraday cells along the line of sight can be determined if the radial distribution of the magnetic field strength is known. The field strength, and associated cell sizes were determined from the assumption that the magnetic pressure within the individual cells reaches some fraction of the ambient gas pressure. The cell sizes in three radial bins were determined for the equipartition magnetic field strength, as well as the field strength derived from setting the magnetic pressure to be 10% of the local gas pressure. The magnetic field strengths determined for these two distribution are listed in Table 7.1.

						$P_B = 0.1P_{gas}$		$P_B = P_{gas}$	
Source	RRM	σ_{RRM}	b	$B_{\rm slab}$	$\sigma_{B_{\rm slab}}$	$B_{\rm cell}$	$\sigma_{B_{\rm cell}}$	$B_{\rm cell}$	$\sigma_{B_{\rm cell}}$
	rad m^{-2}		kpc	μG		μG		μG	
0039+212	-62.62	9.03	100	0.21	0.03	3.5	0.7	11.1	2.1
0040+212	-34.00	10.95	480	0.48	0.20	...	...	...	...
0042−092	4.88	9.77	960	0.02	0.02	...	...	...	...
0056−013	-149.16	10.68	280	0.21	0.02	4.8	0.3	15.1	0.2
0057−013	14.02	10.17	1020	0.14	0.10	1.9	0.1	6.2	0.03
0126−013a	94.22	12.25	140	0.87	0.10	1.6	0.2	4.8	0.1
0154+364	-202.36	4.31	570	1.63	0.03	...	...	...	...
0245+368	-48.06	5.92	630	0.40	0.05	...	...	...	...
0257+130	-185.89	6.47	280	0.12	0.003	...	...	...	...
0318+419	6.17	15.40	550	0.03	0.03	1.7	0.2	5.2	0.1
0319+415	206.94	37.04	10	0.02	0.003	13.3	0.01	41.9	0.03
0316+412	74.94	9.26	740	0.78	0.10	1.3	0.01	4.2	0.1
0434−131	52.91	6.69	310	0.07	0.01	...	...	...	...
0434−133	35.89	6.73	360	0.14	0.02	3.1	0.1	9.9	0.2
0709+486	-229.74	7.75	3	0.09	0.003	9.5	2.5	30.0	8.0
0908−100	12.35	9.43	1460	0.26	0.19	2.0	0.01	6.4	0.1
0909−093	-20.47	9.16	1010	0.14	0.07	2.8	0.03	9.0	0.2
0919+334	16.55	8.38	560	2.08	1.06	...	...	...	...
1036−267	25.76	16.23	640	2.20	1.39	...	...	...	...
1037−270	9.38	6.18	410	0.09	0.05	...	...	...	...
1037−281	25.21	8.19	510	0.42	0.14	...	...	...	...
1039−272	103.73	11.51	620	5.16	0.57	...	...	...	...
1039−273	103.99	6.33	530	1.96	0.12	...	...	...	...
1133+490	-50.38	6.40	310	0.45	0.05	2.7	0.1	8.3	0.2
1133+489A	68.05	6.42	270	0.50	0.05	2.9	0.1	9.2	0.2
1145+196	257.46	11.73	170	0.50	0.02	4.0	0.03	12.6	0.2
1650+815L	-131.75	8.56	270	1.91	0.12	1.8	0.2	5.7	0.7
1650+815U	-127.36	8.56	200	1.30	0.09	2.1	0.3	6.6	0.9

Table 7.1: Magnetic field estimates for the uniform slab model ($B_{\rm slab}$), and for the cell model ($B_{\rm cell}$) where the magnetic pressure traces the gas pressure. The field strength in the cell model has been calculated at two values of the scaling constant, $P_B = 0.1P_{gas}$, and $P_B = P_{gas}$.

7.3 Faraday Mapping of Extended Sources in Three Galaxy Clusters

The majority of the radio sources studied in this sample are only marginally resolved. Although ideally one would like to have a large sample of well resolved radio probes to study the intracluster medium, the increased integration times required for such a study make it unfeasible. There are, however, several sources within the sample which are sufficiently resolved to permit Faraday mapping of the rotation measure structure. Each of these sources is discussed briefly below.

The rotation measure maps for each source were determined from the individual-frequency position angle maps by blanking the final image where the flux in the total intensity image was less than five times the noise level on the map. Further blanking on the rotation measure map removed all regions where the position angle error in any one map was greater than 30°, unless otherwise indicated.

7.3.1 Abell 75

This section presents the Faraday maps of two polarized radio probes which are viewed through the intracluster medium of Abell 75. One source, 0039+212, appears to be a double lobed source, but is rather unique in that the lobes are very diffuse and weak, even at high resolution. The second source, 0040+212, appears very compact, with a slight east-west elongation visible.

0039+212

It is interesting to note that although this source displays a double-lobed morphology, there is no evidence of radio hotspots within the lobes, even at high resolution. An optical identification by Owen et al. (1995) places this radio source within the intracluster medium of Abell 75. This source is located at an impact parameter of 100 kpc from the cluster core. The rotation measure map for this source, Figure 7.2, shows a somewhat patchy RM distribution. The majority of the source is covered by rotation measures of order -100 rad m^{-2}, although there are several patches with rotation measures around 100 rad m^{-2}. The histogram of the rotation measure distribution, Figure 7.3, displays a double peaked distribution. The majority of the source is characterized by a distribution with a mean

of -62 rad m^{-2}, and dispersion of 40 rad m^{-2}. The small scale Faraday features seen in the figure are characterized by a distribution with mean $+99$ rad m^{-2}, and dispersion 15 rad m^{-2}. Note that the Galactic rotation measure toward this source is -14.5 ± 3.7 rad m^{-2}.

The overall properties of the RM map indicate the presence of large scale order, although there is a Faraday patch of significantly different rotation measure ($\sim$ 100 rad m^{-2}) located across the western lobe. The width of this Faraday feature is approximately 13″, which corresponds to a linear scale of approximately 14 kpc at the redshift of the source. The fact that this Faraday feature does not correspond with any features in the total intensity map of this source, suggests that the feature is generated in the foreground medium, and is superimposed on the source.

The dispersion in the rotation measure for a random walk through $\mathcal{N}$ cells is

$$\sigma_{RRM} = \frac{811.9}{\sqrt{3}} n_e < B^2 >^{1/2} \ell_{\rm cell} \mathcal{N}^{1/2}. \tag{7.16}$$

The line of sight to 0039+212, which is at an impact parameter of 100 kpc from the cluster core, passes through approximately 600 kpc of the intracluster medium. Assuming this foreground medium is filled with randomly distributed cells with a typical scale of 14 kpc, Equation 7.16 estimates a field strength of 1.0 ± 0.5 μG for each cell. This estimate places the field within the cell at approximately 20% of that required for dynamical importance within the ICM. Note, however, that the assumed distribution of the entire foreground path filled with cells of 14 kpc scale is fairly unlikely. A more realistic estimate of 200 kpc for the path through the region of cells tangled on a scale of 14 kpc increases the estimated field strength in each cell to approximately 1.7 μG.

0040+212

The second, more compact, source imaged in Abell 75, is 0040+212, which is seen at an impact parameter of 480 kpc from the cluster core. There is no optical identification available for this source, and an examination of the POSS plates does not reveal an optical counterpart. The lack of optical ID, and the compact size of this source suggest that it is a high redshift radio source which is being viewed through the foreground intracluster medium. The rotation measure map, Figure 7.4, shows a very smooth rotation measure over the majority of the source. There is some evidence on the northern edge of this source

of a small patch of positive rotation measure of order 50 rad m^{-2}. The rotation measure histogram for this source, Figure 7.5, shows a non-Gaussian distribution with a long tail to negative rotation measures. The mean rotation measure from the histogram is -51 rad m^{-2}, and the dispersion is 46 rad m^{-2}.

Once again, the overall rotation measure distribution is fairly uniform over this radio source. A slice through the Faraday patch in the northern region of the source estimates the observable width to be approximately $12''$, which corresponds to a scale of 13 kpc at the redshift of the galaxy cluster. Using the complete path length through the intracluster medium to 0040+212, Equation 7.16 yields a field strength of 5.1 ± 1.3 μG. At the point of highest intracluster gas density along the line of sight to this source, the magnetic pressure from a field of strength of 5.1 μG is in equipartition with the ambient gas pressure. A larger scale length for the Faraday cells toward this source, as might be expected for the larger impact parameter, would result in a decrease in the estimated field strengths.

Summary for Abell 75

Both radio sources probing the intracluster medium in Abell 75 display large-scale ordered rotation measures. Further, the sign, and magnitude of the rotation measures for the two sources are nearly identical. In fact, the rotation measure histograms in Figures 7.3, and 7.5 display remarkably similar distributions:

- The histograms of 0039+212, and 0040+212 indicate a large peak centered on rotation measures of -62, and -51 rad m^{-2}, respectively.
- The measured dispersions in the RM distribution for the two sources are 40 and 46 rad m^{-2}.
- Although both Faraday maps display a general trend of ordered RMs, there is also evidence with both maps of Faraday patches of significantly different RM.
- The Faraday patches observed across 0039+212 and 0040+212 have rotation measures of order $+100$ rad m^{-2} and $+50$ rad m^{-2}, respectively.
- The estimated scales of the Faraday patches calculated for the two sources, assuming that the feature is at the redshift of the galaxy cluster, are 14 kpc, and 13 kpc. Note,

however, that the location of the Faraday patch on the edge of 0040+212 only permits a minimum estimate of the scale.

The similar rotation measure distributions observed for these two sources located at widely different impact parameters within this cluster strongly argues for the origin of the Faraday excess within the foreground intracluster medium. The additional indication that one source is embedded within the ICM, while the other is a background source, together with the superimposed Faraday features, serve to further strengthen the arguments for a foreground Faraday screen which contains large scale, ordered magnetic fields.

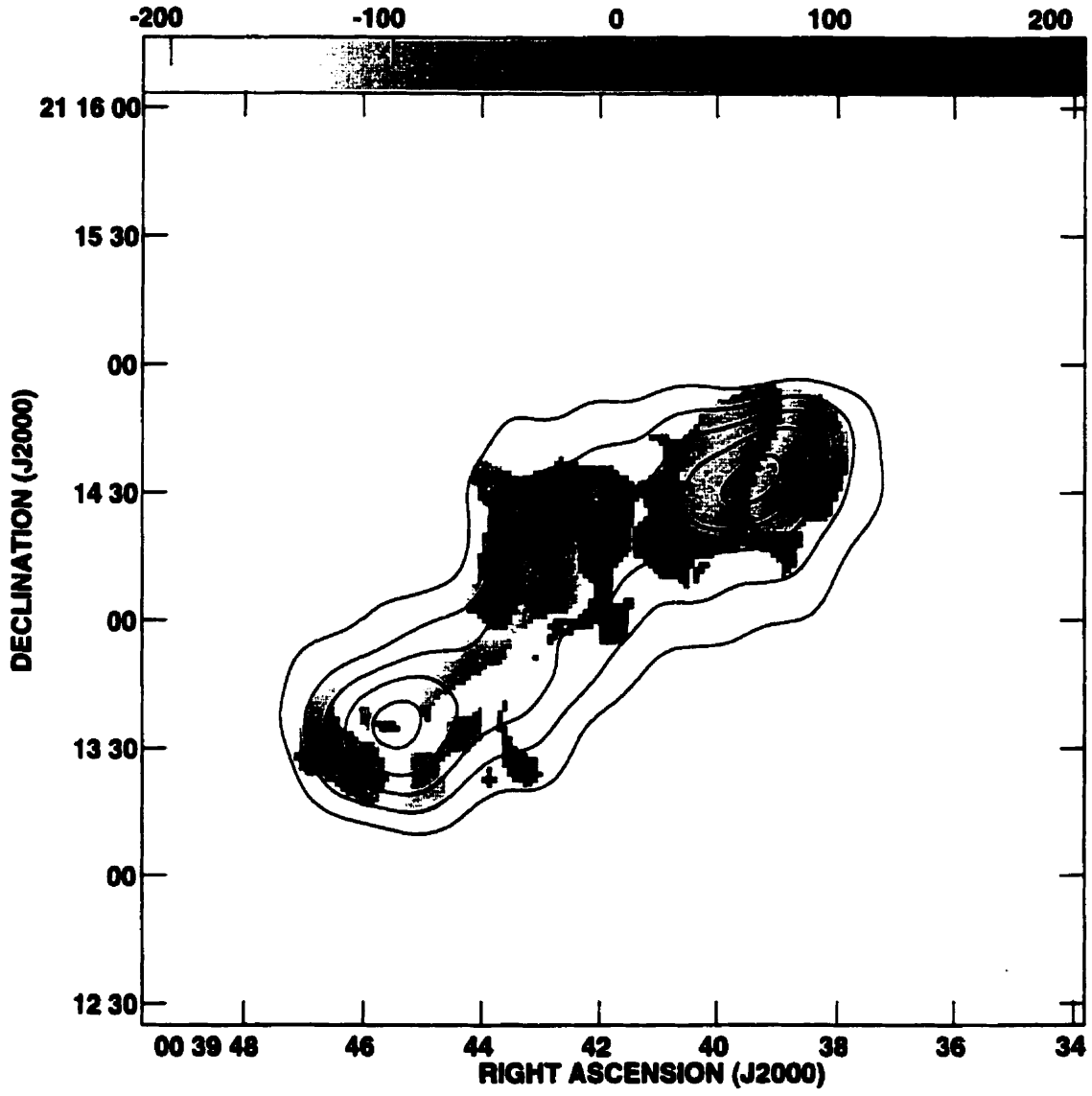

Figure 7.2: Rotation measure map of 0039+212 in Abell 75. Note that the majority of the radio source is covered by rotation measures of order -50 rad m^{-2}, although there is a rotation measure patch of $+100$ rad m^{-2} toward the upper hotspot.

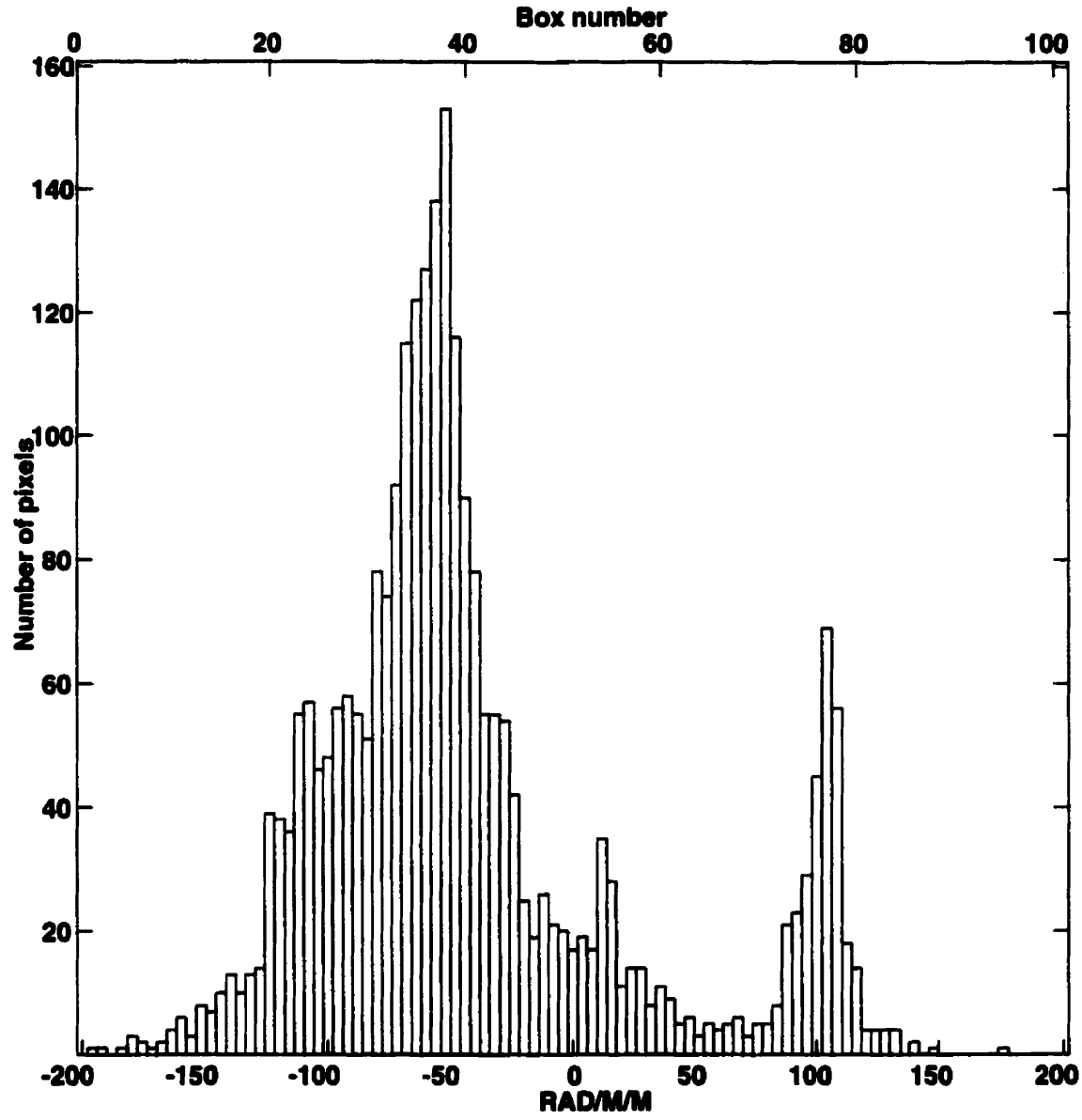

Figure 7.3: Histogram of rotation measure distribution for 0039+212 in Abell 75. This histogram clearly displays both the large negative rotation measure peak, and the small positive peak associated with the rotation measure patch.

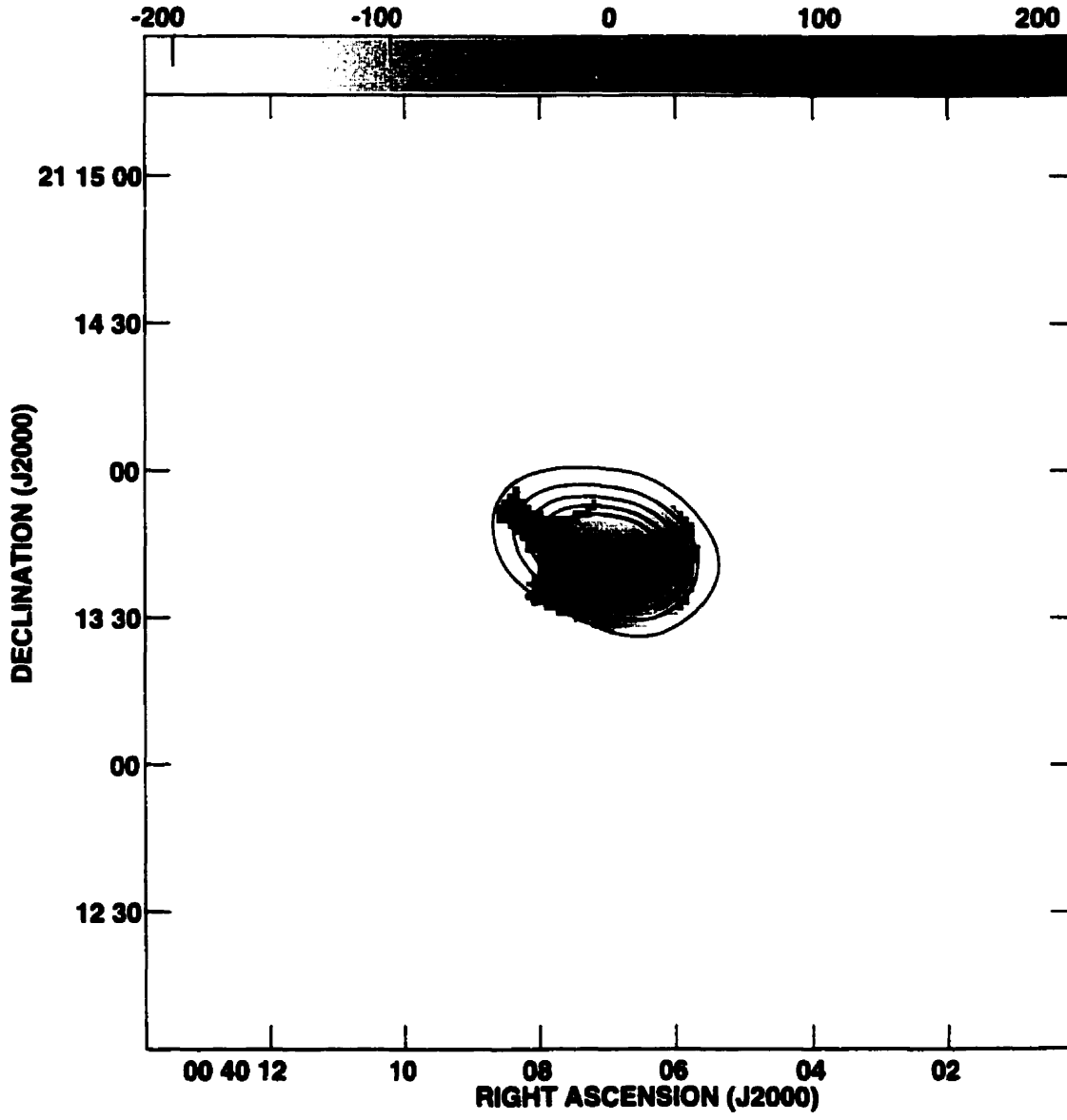

Figure 7.4: Rotation measure map of 0040+212 in Abell 75. The majority of this compact source displays rotation measures around -45 rad m^{-2}, although there is some evidence for a positive rotation measure patch on the edge of the source.

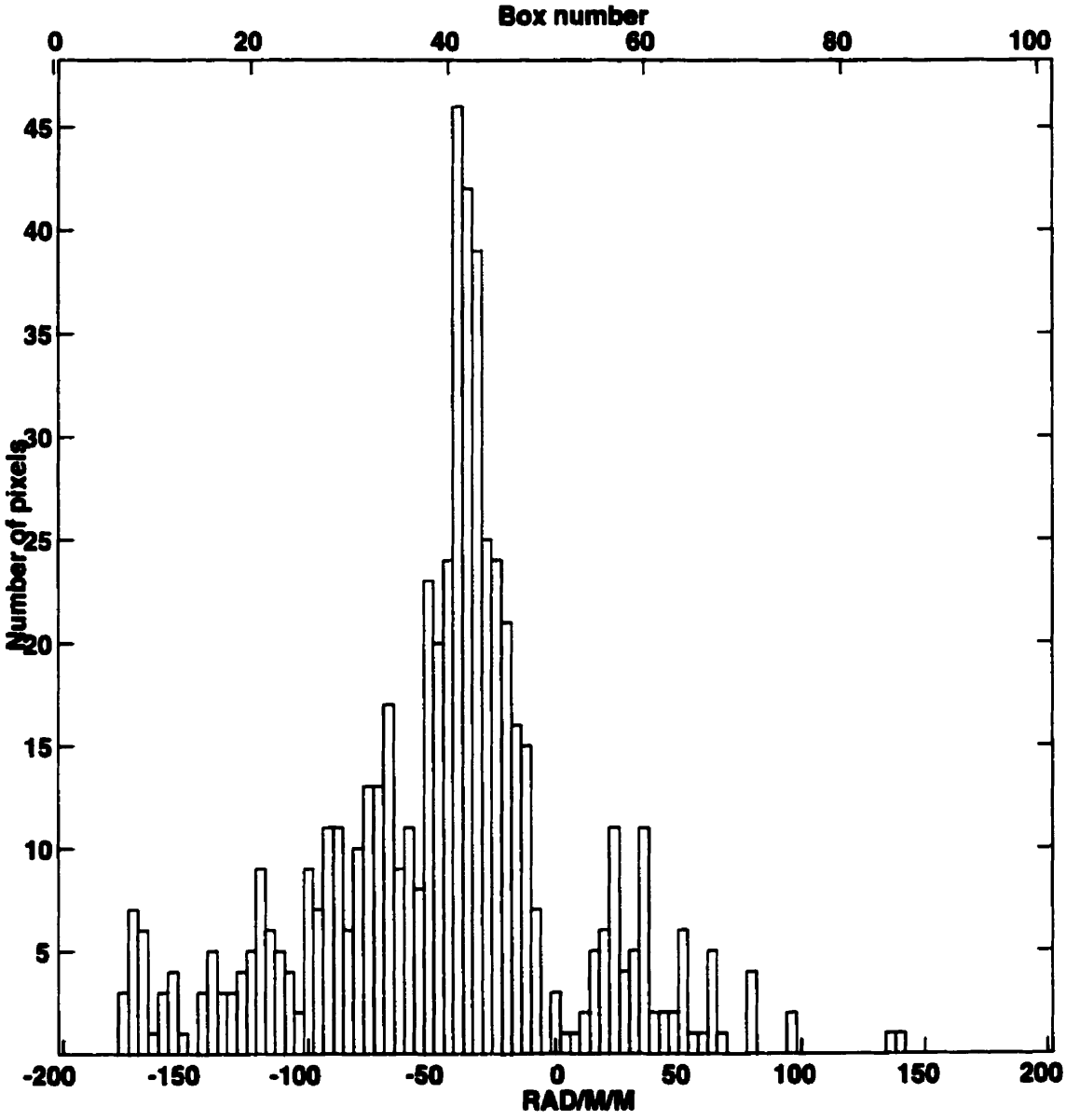

Figure 7.5: Histogram of rotation measure distribution for 0040+212 in Abell 75.

7.3.2 Abell 119

The presence of three extended, polarized radio sources at impact parameters within the boundary of the thermal cluster gas makes Abell 119 an ideal cluster for the study of the radial distribution of intracluster magnetic fields. Although a recent paper by Feretti et al. (1999) provides a more detailed analysis of the intracluster medium within this cluster, a brief outline is presented below of the rotation measure distribution of one of the central radio galaxies. Note that the blanking on the position angle error for this source was relaxed to 40°. The purpose of the relaxed blanking is to provide some insight into the rotation measure distribution in the outer regions of 0056−013, as the relaxation of the position angle error by 10° reveals rotation measure features in the tail of this source, but does not alter the rotation measure distribution of the central region of 0056−013. The results presented for the outer regions of this radio source should therefore be regarded with caution due to the increased uncertainties involved.

0056−013

This source displays a classical narrow-angle-tail morphology, and is identified as a cluster member. The source falls at an impact parameter of approximately 280 kpc from the X-ray centroid of Abell 119. The rotation measure distribution for this source, shown in Figure 7.6, has a fairly ordered structure across the source, to a distance of approximately 2.′5, or 118 kpc, from the cluster core. Beyond this region, there are large variations in the RM through the tail of the radio source. Figure 7.7 displays the rotation measure histogram of the central ∼120 kpc of this source. The central RM distribution is double peaked, and runs from −300 rad m^{-2} to +100 rad m^{-2}, with the majority of the pixels displaying negative rotation measures. The mean rotation measure in Figure 7.7 is −116 rad m^{-2}, and the dispersion is 75 rad m^{-2}.

Figure 7.8 displays the rotation measure histogram for the positive Faraday features within the tail of 0056−013. The choice of plotting only positive RMs in the histogram was designed to more clearly display the distribution of the positive features. The mean RM determined from the histogram is 486 rad m^{-2}, and the dispersion is 91 rad m^{-2}. The typical scale of the Faraday patches in the tail of this radio galaxy is 12″, which corresponds to a physical scale of 10 kpc at the redshift of the cluster. Using this scale

length in Equation 7.16, the rotation measure dispersion of the positive Faraday features predicts a magnetic field strength of 1.6 ± 0.6 μG in the tail region of this source. The RM dispersion across the head of this source finds a similar field strength of 1.3 ± 0.6 μG. Note, however, that this source is highly depolarized, which indicates that the true structure of the Faraday screen in not being resolved, thus these magnetic field estimates should be considered a lower limit on the field strength. Comparing these field strengths to the values calculated for dynamical importance, we find that the estimates are $\sim$ 20% of the dynamically significant field strength.

Summary for Abell 119

The embedded radio source 0056−013, probing the central regions of the intracluster medium in Abell 119, displays fairly ordered rotation measures over scales of over 100 kpc. The rotation measure distribution presented here can be compared to that presented in Feretti et al. (1999). Comparing the Faraday map in Figure 7.6, with their Figure 12, shows similar distributions of uniform negative RM in the central regions, with an increasing patchiness containing positive RMs through the tail region. The rotation measure histograms shown in Figure 7.7, and the Feretti et al. Figure 13, display a nearly identical double peaked RM distribution. Although both histograms show RMs ranging from −300 rad m^{-2} to +100 rad m^{-2}, the histogram presented herein displays a significant increase in the height of the more negative of the two peaks. The higher resolution available to Feretti et al. permit them to estimate the tangling scale of the Faraday screen to be 3 kpc.

The Feretti et al. paper also investigates two other radio sources in Abell 119. One source, 0056−012, is located closer to the X-ray centroid of the cluster, while the other source, 0057−013, is located on the periphery of the cluster. Feretti et al. find a maximum rotation measure of 450 rad m^{-2} for 0056−012, and 30 rad m^{-2} for 0057−013. They find an average rotation measure of 4 rad m^{-2} for 0057−013 which is consistent with the rotation measure of $\sim$ 10 rad m^{-2} presented in this thesis. Note, however, that 0056−012 was not included in the source sample for this thesis as it is severely depolarized at the NVSS wavelength of 20 cm, and thus did not fit the radio source selection criteria described in § 3.2.1. Feretti et al. point out that both the radio source depolarization and observed rotation measure increase with decreasing impact parameter for the sources in this cluster. They interpret this polarization behaviour as the results of a foreground, tangled intracluster

Faraday screen with a magnetic field strength of order 5-10 μG.

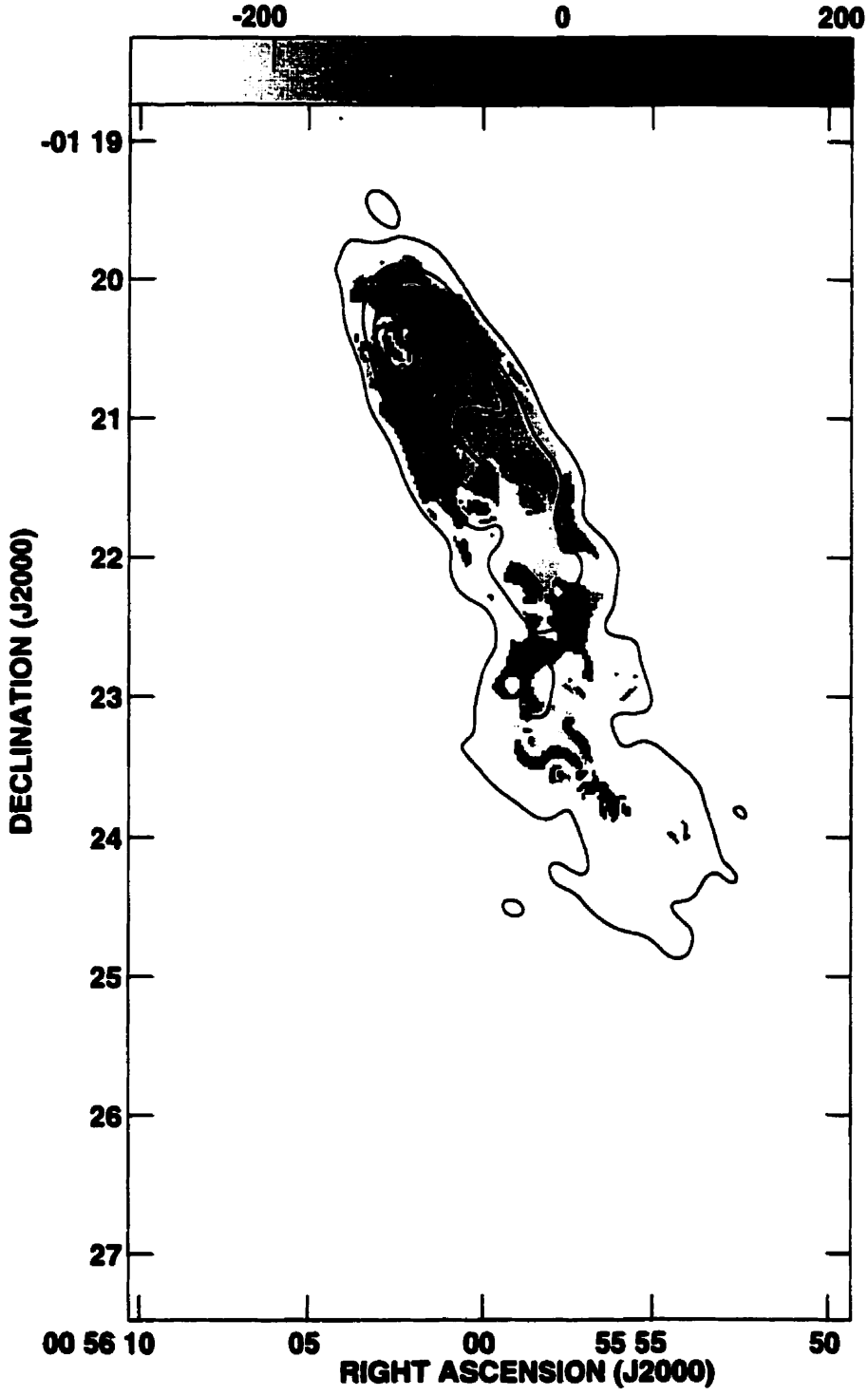

Figure 7.6: Rotation measure map of 0056−013 in Abell 119. The rotation measures in the head of this source range from approximately 0 rad m^{-2} to −200 rad m^{-2}, while the tail displays very complex rotation measure patches with large positive rotation measure regions visible.

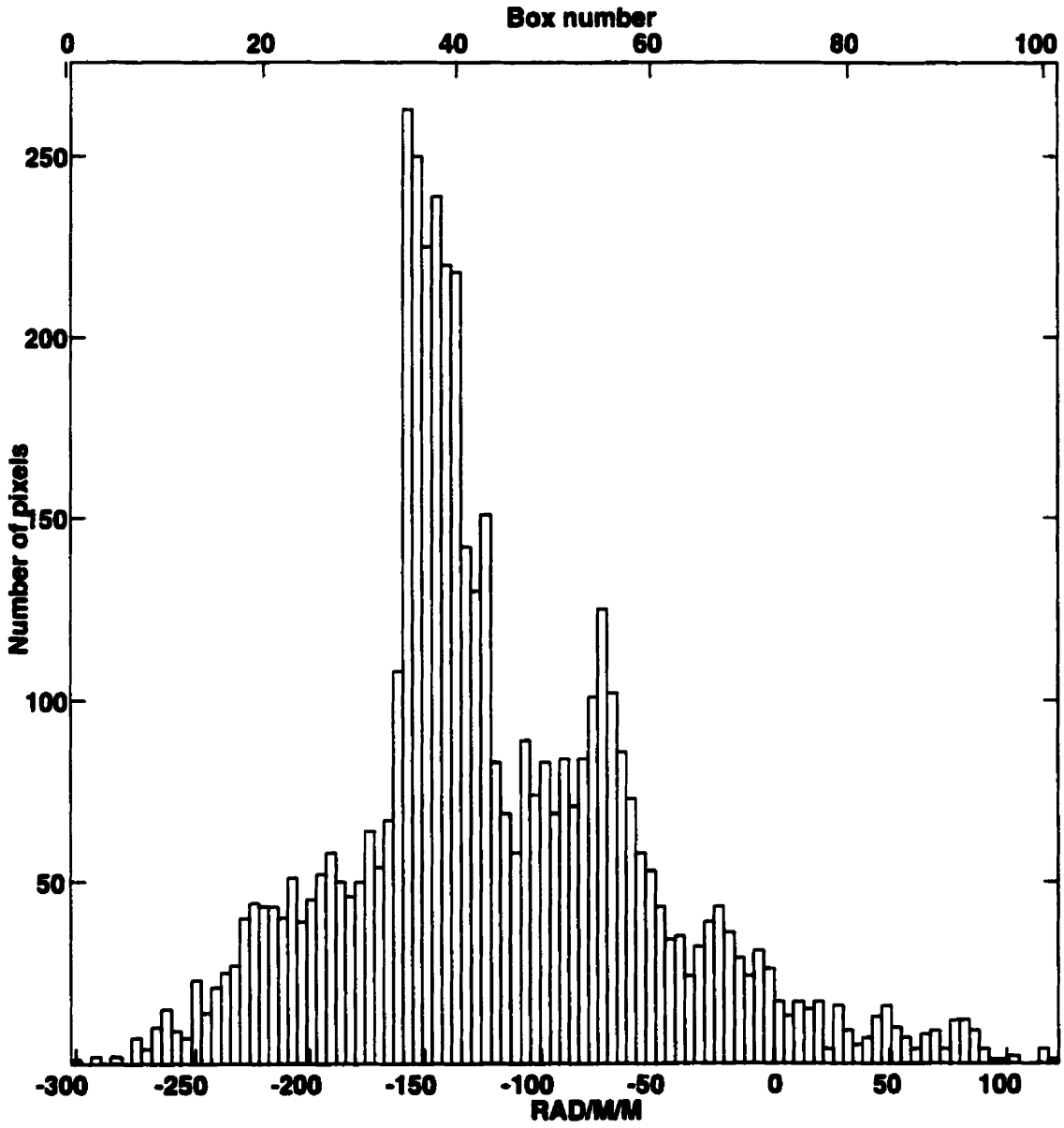

Figure 7.7: Histogram of rotation measure distribution for the central regions of 0056−013 in Abell 119.

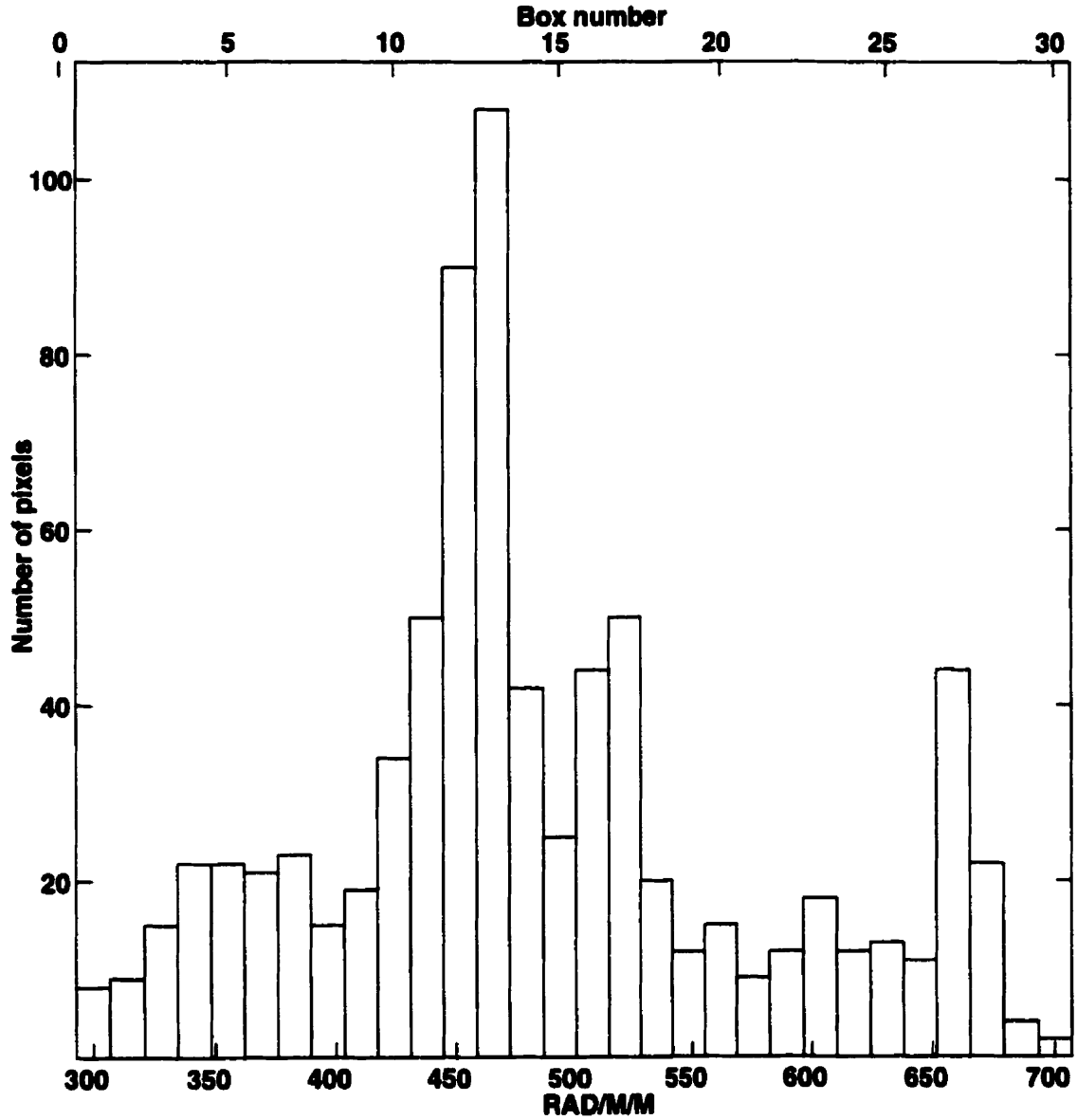

Figure 7.8: Histogram of rotation measure distribution for the tail of 0056−013 in Abell 119 scaled to display the rotation measure distribution across the positive Faraday patches.

7.3.3 Abell 2247

The X-ray image of Abell 2247 displays a very elongated, clumpy morphology. The radio probe for this cluster lies in a region near one of the X-ray clumps, and falls well within the boundary of the X-ray emitting gas.

1650+815

This source displays double lobed morphology, and is identified with a galaxy in the group UGC 10638, which lies at the redshift of A2247. The impact parameter for 1650+815 is 270 kpc. Unlike the previous sources, the Faraday map of this source, Figure 7.9, displays a significant patchiness, with only a few regions of fairly uniform rotation measure. The distribution of the Faraday features is similar for both the northern and southern lobes, although the features do not appear to correlate with any total intensity structure for the source. The histograms shown in Figures 7.10, and 7.11, display the RM distributions across the southern and northern lobes, respectively. Both histograms display a non-Gaussian distribution in rotation measure with the majority of the RMs concentrated around -100 rad m^{-2}. There is also a weak distribution in both lobes of RMs around 150 rad m^{-2}. The mean rotation measure in the southern lobe is -75 rad m^{-2}, and the dispersion in this lobe is 142 rad m^{-2}. The northern lobe has a mean RM of -35 rad m^{-2}, and a dispersion of 122 rad m^{-2}.

The typical scale of the rotation measure features in 1650+815 is $\sim 10''$, which corresponds to a physical scale of 7 kpc at the redshift of the cluster. The estimated magnetic field strengths from the rotation measure dispersions are 22 ± 3 μG, and 14 ± 2 μG, for the southern and northern lobes respectively. These field estimates correspond to a magnetic pressure which is well above the ambient gas pressure. Note, however, that both the rotation measure and X-ray distributions used in these calculations are very complex, thus the field estimates should be regarded with caution.

Summary for Abell 2247

The rotation measure distributions across the lobes of 1650+815 display similar, but complex, signatures. Each lobe contains several Faraday features, with only a fairly small region of uniform Faraday rotation visible. The complex nature of the Faraday distribution for

this source makes it difficult to determine reliable magnetic field estimates from the Faraday maps.

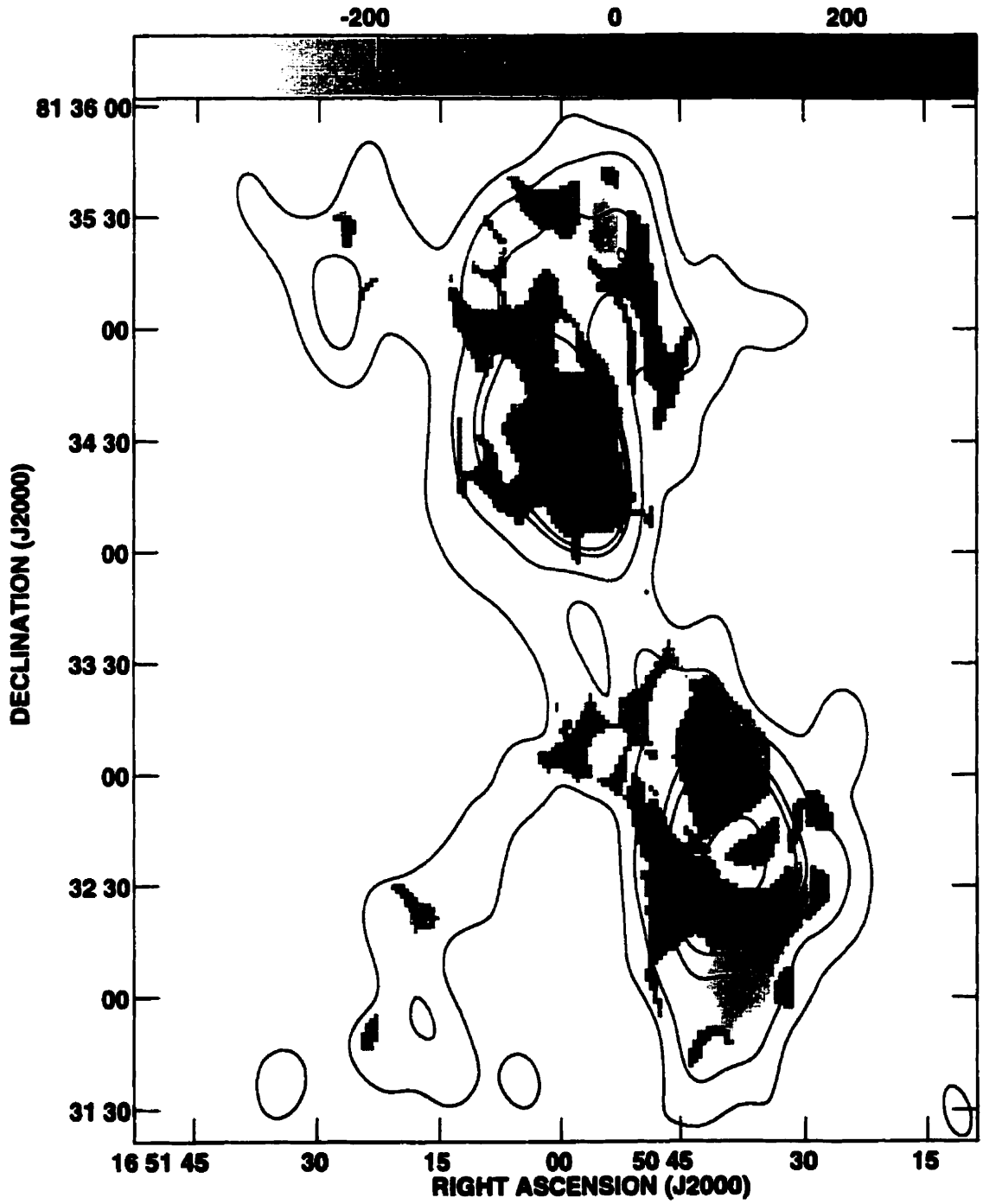

Figure 7.9: Rotation measure map of 1650+815 in Abell 2247.

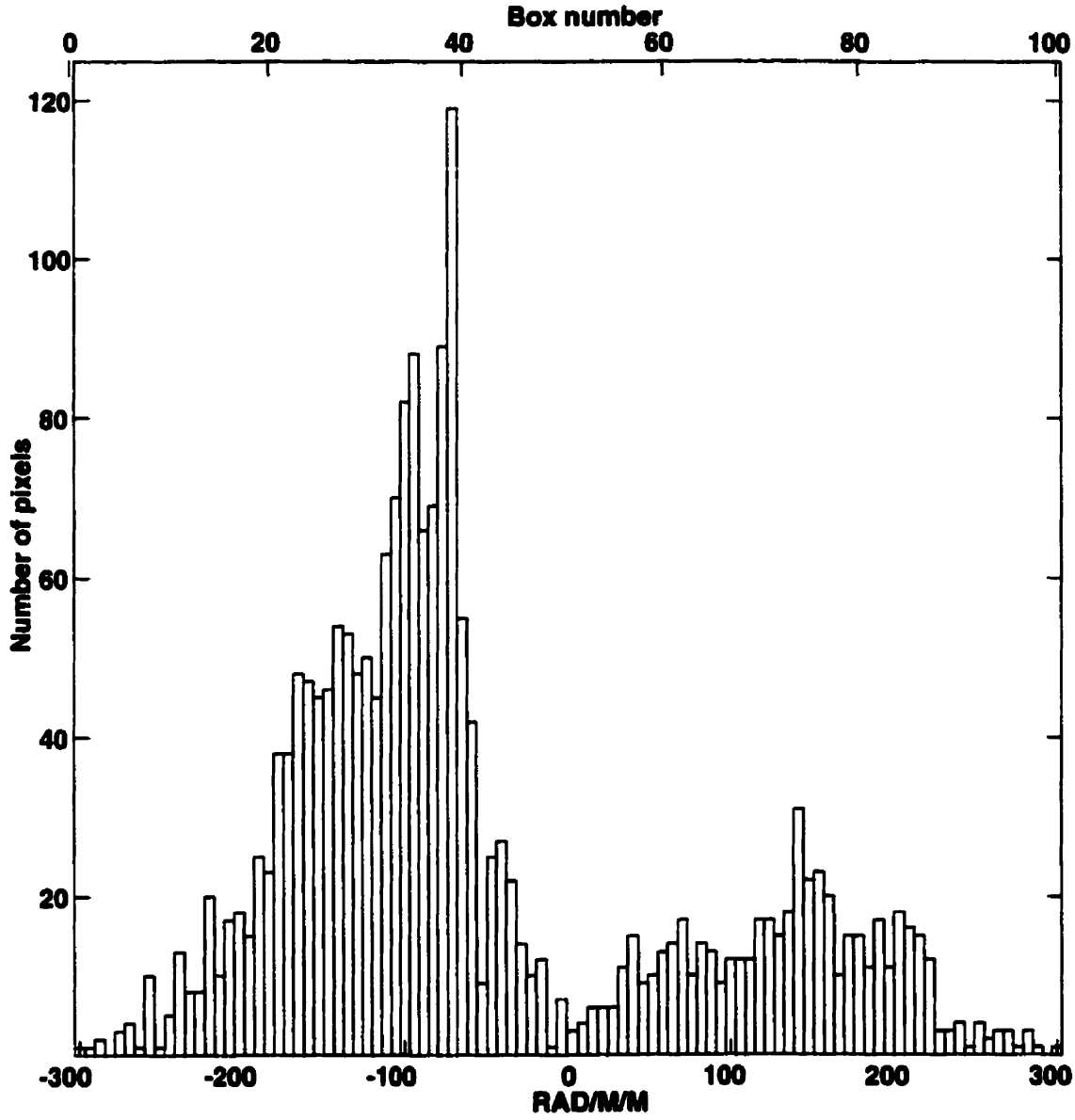

Figure 7.10: Histogram of rotation measure distribution for the southern lobe of 1650+815 in Abell 2247.

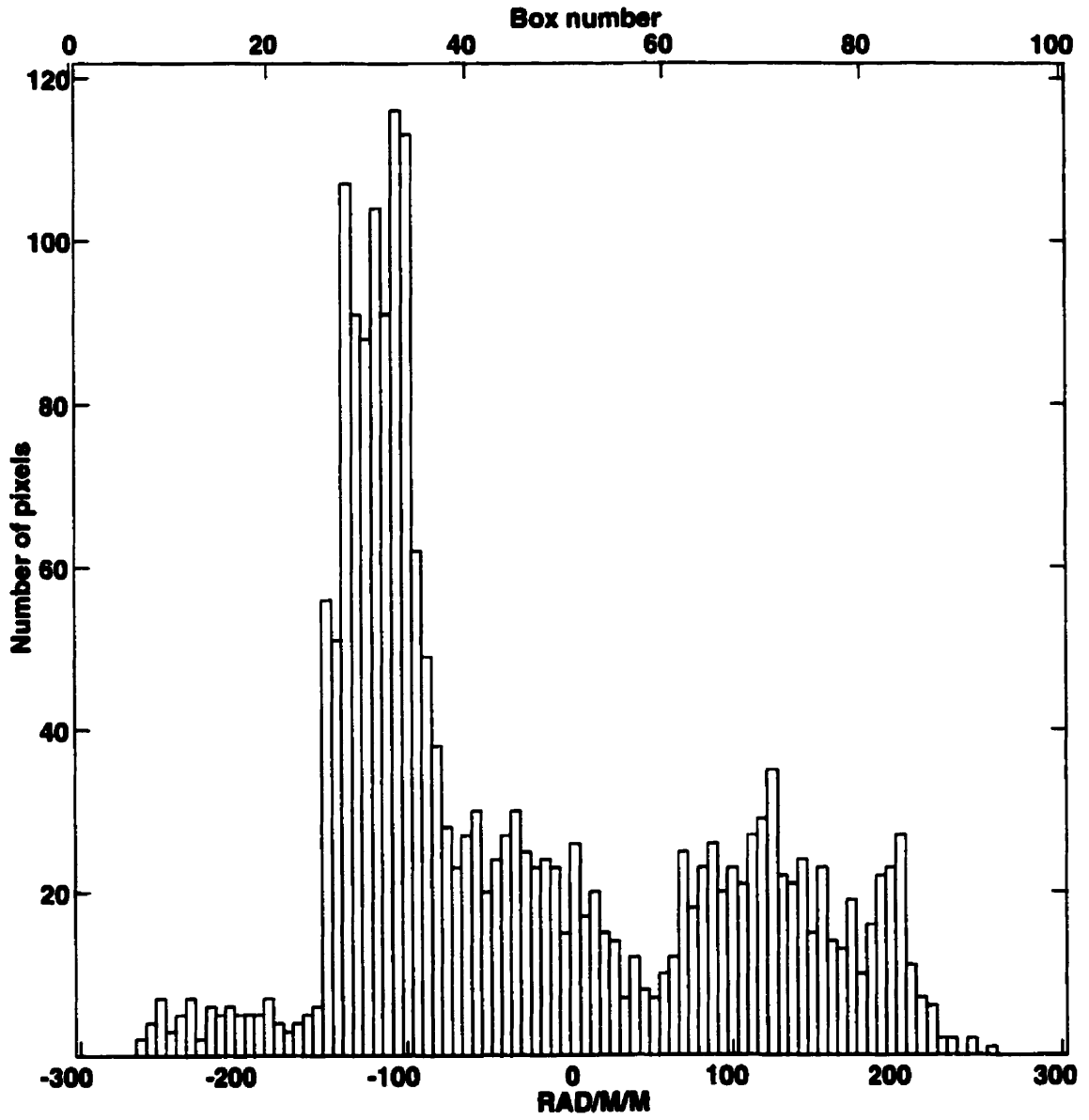

Figure 7.11: Histogram of rotation measure distribution for the northern lobe of 1650+815 in Abell 2247.

7.4 Summary

In this chapter, several possible models for the distribution of magnetic fields in the intracluster medium have been considered. The predictions from each model were compared to the observed rotation measure distribution. Fitting the RRM observations to a uniform slab model, which assumes that the ICM is filled with magnetic fields of constant strength and direction, provides a range of magnetic field strengths between ~ 0.5 μG, and ~ 1.5 μG for the majority of the sources. The presence of turbulence within the intracluster medium is, however, likely to disturb intracluster magnetic fields, and generate a tangled field distribution. A simplified view of this tangled field distribution considers the ICM to be filled with Faraday cells of uniform size, where the magnetic field varies randomly in direction from cell to cell. The rotation measure excess for the sample studied in this work, combined with the depolarization ratios calculated for the sources, argue for a magnetic field distribution which contains both large and small scale magnetic fields. Assuming the magnetic pressure in the region around embedded sources traces the gas pressure, the rotation measure dispersion indicates a radial increase in the cell size from the central regions to the edges of the galaxy clusters. Further, the cell sizes predicted for the central regions of the clusters are in agreement with the scales determined from high resolution Faraday mapping studies of cluster core sources. The final model considered for the field distribution was the dynamo model, however, the predicted rotation measure distribution for the model does not reproduce the observed distribution, thus this model was not further considered.

Estimates of the magnetic field strength for the uniform slab model can be compared to the field strengths required for dynamical importance in ($P_B \geq 0.1 P_{gas}$), or equipartition with ($P_B = P_{gas}$), the intracluster gas pressure. In general, a uniform slab model predicts magnetic pressures in the intracluster medium which are only a few percent of the local gas pressure. On the other hand, in a tangled cell model, dynamically significant magnetic pressures are predicted for Faraday cell sizes similar to those determined in the literature.

To further probe the structure of intracluster magnetic fields, Faraday maps were produced for four extended radio sources viewed through the ICM of three Abell clusters. Although the maps varied from source to source, the general trend across the four sources indicated a large scale ordered intracluster field (scales $\gtrsim 100$ kpc), in which smaller scale Faraday features (scales ~ 10 kpc) were embedded. The presence of the observed Faraday

patches, and ordered structures, support a model in which the intracluster magnetic field consists of tangled cells, or flux ropes, which have a variety of scales along the line of sight. The data in this Chapter confirms that the "uniform slab" model is ruled out. Hence $|B| < 1\ \mu$G is also ruled out.

Chapter 8

Discussion and Future Work

8.1 Summary of Thesis Results

This thesis investigates the nature of intracluster magnetic fields through the Faraday effect. The magnetic fields are revealed through the wavelength-dependent rotation of the position angle of polarized synchrotron emission, as it propagates through the magnetized, ionized region. Multi-frequency radio observations, toward polarized radio sources, provide a means of determining the magnitude of the Faraday rotation.

The observed rotation measure is a linear sum of the individual Faraday rotations from all magneto-ionic media along the line of sight between the radio source and the observer. In order to isolate any individual contribution to the rotation measure, all potential sources of Faraday rotation must be considered and removed (corrected), or otherwise accounted for. The presence and magnitude of an intracluster contribution to the corrected rotation measure is then determined by comparing the magnitude of the observed Faraday effect of sources viewed through the intracluster gas (**cluster** sources), to that of sources which are not influenced by the intracluster medium (**control** sources). Once the magnitude of the intracluster contribution to the Faraday excess has been determined, the magnetic field strength required to produce the observed excess can be estimated, provided that the geometric distribution of the magnetic fields is known.

8.1.1 Main Issues

Although evidence for the presence of magnetic fields within the intracluster medium is fairly common in the literature (Lawler & Dennison 1982; Kim et al. 1991; Goldshmidt & Rephaeli 1993; Ge & Owen 1994; Taylor et al. 1999), there are many important questions about the nature of these magnetic fields which remain unanswered. This section addresses three of these questions which have been investigated in this thesis:

- What is the location of the Faraday rotating component within the intracluster medium?
- What is the geometric distribution of the magnetic fields within the dominant Faraday component?
- What is the radial extent of the dominant Faraday component?

These issues have remained open due to the combination of sparse data, and the dependence of Faraday rotation on the product of the intracluster electron density and the line of sight magnetic field strength - parameters which are likely to display a radial dependence. A further complication introduced by turbulence within the intracluster medium is the tangling scale associated with the magnetic fields.

This thesis takes advantage of the relatively recent availability of the NRAO VLA Sky Survey (NVSS) archive, and the ROSAT archive, to resolve a number of the complications described above. Follow-up polarimetric observations, at four to six wavelengths, of NVSS targets provide a relatively large statistical sample of Faraday rotation measures. Unlike previous statistical studies which generally relied on (sometimes poorly determined) rotation measure estimates from the literature, the rotation measure estimates presented within this thesis have been systematically determined for a carefully selected set of wavelengths. The availability of sensitive ROSAT X-ray observations for each galaxy cluster presented in this thesis provides the first opportunity to incorporate the individual intracluster electron density distributions into the rotation measure analysis. This individual-source decoupling of the product of the electron density, and line of sight magnetic field, further simplifies the analysis of the magnetic field distribution. Finally, the results from Faraday mapping of four sources presented in this thesis, combined with Faraday mapping results from the literature, yield estimates of the tangling scale for comparison with the calculated radial

distribution.

8.1.2 Location and Extent of the Faraday Rotating Medium

Comparison of the width of the residual rotation measure distribution of the **cluster** sources, to that of the **control** sources, reveals a statistically significant Faraday excess in the cluster sample. The width of the residual rotation measure distribution of the **control** sample was found to be $\sim$ 15 rad m^{-2}, while the width of the **cluster** sample increased from this background level at the outer edge of the cluster, to a width of $\sim$ 115 rad m^{-2} in the central regions of the cluster. The radial distribution of the residual rotation measures indicates that the Faraday excess extends to the edges of the X-ray emitting intracluster gas. These results are the first strong evidence of the widespread distribution of intracluster magnetic fields to the boundary of the intracluster medium. Previous statistical studies of the Faraday excess toward galaxy clusters were not able to determine the radial limits of the excess, due to a lack of available X-ray distributions. Further, Faraday mapping has been mainly confined to sources in the central regions of clusters, thus, again, providing little information on the extent of the Faraday excess. An exception to this, is the work by Feretti et al. (1999) on Abell 119, where the large radial extent of the intracluster magnetic fields is suggested by the Faraday rotation measure images of three extended sources that are located at impact parameters between 190 and 1500 kpc.

Based on the excellent fits of the position angles to a λ^2 law across both thesis samples, and the lack of internal depolarization, the majority of the Faraday excess is concluded to originate external to the radio sources. Further, the similar radial distributions of the RRMs for the embedded and background radio sources indicates that the majority of the Faraday excess originates in the diffuse intracluster medium, rather than a magnetized sheath surrounding the radio sources. The origin of the Faraday excess in the foreground ICM is further supported by the correlation of the RRM with the projected electron density, as similar correlations hold for both the embedded, and background sources.

8.1.3 Intracluster Magnetic Field Distribution

The radial variation and width of the observed residual rotation measure distribution indicate that the intracluster magnetic field contains both small scale structure, and large scale order. The field distribution was investigated through a simple model which considered the

intracluster medium to be composed of tangled cells of magnetic field. In this model, the magnetic field direction varies randomly from cell to cell, and the field strength is uniform within a single cell, but varies radially throughout the cluster. Through a parameterization of the magnetic pressure by the X-ray determined gas pressure, the approximate radial distribution of the intracluster magnetic field strength was estimated. This magnetic field strength, combined with the residual rotation measure distribution, provides the first estimates of the radial variation of the cells sizes. In the central region of the clusters, the tangling length of the fields is found to be $\lesssim 1$ kpc. This tangling scale increases to over 100 kpc toward the outer regions of the cluster gas distribution. The small central tangling scale estimated from these results are in good agreement with the measured tangling lengths from Faraday mapping of extended radio sources in the central regions of clusters. For example, studies by Feretti et al. (1995, 1999), Taylor & Perley (1993), and Ge & Owen (1993) indicate that the foreground Faraday screen contains structure on scales of a few kiloparsec in the central regions of clusters. Note, however, that the tangling scale estimates presented in this thesis for the outer regions of the clusters represent the only information available on the Faraday cells at these large radii.

Faraday mapping of radio sources in three Abell clusters confirms the picture presented above. In general, the Faraday maps display ordered rotation measure structures over scales of $\sim$ 100 kpc, although the maps also display Faraday patches on scales of order 10 kpc. The magnetic field strength in the foreground intracluster medium, determined from the Faraday mapping results, was found to be $\sim$ few μG for sources in two of the clusters, while a field strength of $\sim$ 15 μG was estimated for the third cluster. Note that these magnetic fields may, in fact, be dynamically important within the intracluster medium.

8.2 Fitting the Pieces Together

Intracluster magnetic fields have been investigated through numerous techniques in the literature. There is now sufficient information available to begin considering how these observations fit together in the overall picture of the intracluster magnetic field distribution. Developing a detailed picture, and fitting these results into it, is, however, a complex undertaking, which is beyond the scope of this thesis. Instead, this section presents a summary of some of the results available in the literature, and considers a broad overview of how these

results might fit together.

8.2.1 Observations

There are several observational approaches to measuring the intracluster magnetic field. An overview of the theory behind these approaches is given in § 2.4. Below, the magnetic field strengths, or limits, determined from these observational approaches are summarized. Note, however, that this section is not intended to provide a complete review of the literature, but rather a sampling of a variety of the observations.

- **Synchrotron haloes, equipartition:** Minimum energy estimates of magnetic fields associated with synchrotron haloes find equipartition magnetic field strengths of order 0.5 μG (Feretti & Giovannini 1996) extend over regions of $\sim$ 500 kpc through the intracluster medium.

- **Synchrotron haloes and inverse Compton:** Upper limits on inverse Compton emission from clusters (Hanisch 1980; Ensslin & Biermann 1998) places lower limits of order 0.1 μG on the strength of the volume-averaged intracluster magnetic field strength. Recent evidence of the detection of IC from synchrotron halo clusters (Fusco-Femiano et al. 1999; Bagchi et al. 1998), predict volume-averaged field strengths of $\sim$ 0.15 μG.

- **Statistical Faraday Studies:** Comparing Faraday rotation measures of sources viewed through the ICM to those beyond the edge of the cluster gas (Lawler & Dennison 1982; Kim et al. 1990; Kim et al. 1991; Goldshmidt & Rephaeli 1993) yields intracluster magnetic field estimates of order 1 μG, tangled on scales of order 10 kpc. Further, these magnetic fields are generally found to extend to large cluster-centric distances. Note, however, the study by Hennessy et al. (1989), based on high redshift radio probes, found no evidence of intracluster magnetic fields.

- **Faraday Mapping:** High-resolution Faraday mapping directly images the structure of the Faraday screen. The majority of the Faraday mapping results (Dreher et al. 1987; Ge & Owen 1993; Taylor & Perley 1993) concentrate on extended sources embedded in the cores of cooling flow clusters. These results indicate magnetic field strengths of order 50 μG, tangled on scales of a few kpc. Feretti et al. (1999) find

similar field strengths and tangling scales for a source located at a slightly larger impact parameter in Abell 119.

8.2.2 Emerging Picture

The overall consensus from the results of this thesis and the literature appears to be that magnetic fields are a common property of all X-ray galaxy clusters, and probably all clusters. Further, these magnetic fields appear to extend from the cluster core out to the edge of the X-ray emitting gas. The geometry of the magnetic fields must contain both large scale ordered features (to produce non-zero RMs), and small scale tangled features (observed in Faraday mapping). The magnetic field strength associated with the uniform component of the fields is predicted to be of order 1 μG, while the highly tangled component probably reaches values of 50 μG, at least in the central regions of the clusters. Although a field strength of 1 μG is probably not dynamically important, a field strength of 50 μG almost certainly is. In general, these observations appear to be consistent with a picture of the intracluster medium filled with magnetic cells, where the cells have a radially increasing scale length.

The observational picture is similar to the picture emerging from the theory. Simulations of magnetohydrodynamic turbulence indicate that the magnetic fields are generally organized into elongated filaments or flux ropes through a plasma (Nordlund et al. 1992; Miller et al. 1996). A line of sight passing through a region containing magnetized filaments would likely experience a random walk in rotation measure similar to that in the cell model. Note, however, that the lack of observations of Faraday holes toward galaxy clusters indicates that the covering factor of the magnetized filaments must be near unity.

8.3 Future Directions

The overwhelming picture developing from a variety of observations is that the intracluster medium contains widespread magnetic fields. Despite, or perhaps because of, the growing body of observations, there are several fundamental questions which remain unanswered.

Does the Faraday excess truly originate from magnetic fields embedded in the diffuse intracluster medium? Although indications from this thesis and the literature point toward the diffuse intracluster medium as the source of the Faraday excess, the presence of embedded sources in the Faraday samples leaves the issue unresolved. A solution to the issue would be provided by a large Faraday sample of background radio probes, preferably located behind clusters in which embedded sources display a Faraday excess.

What is the radial distribution of the tangling length of the intracluster magnetic field? The first estimates of this distribution are provided in § 7.1.2 of this thesis. A more direct approach to determining the radial distribution of the field coherence length is to undertake high resolution Faraday mapping of extended sources located at impact parameters beyond the core radius of clusters. This approach provides a direct mapping of the Faraday scale at the impact parameter of the source.

Do magnetic fields influence the dynamical evolution of galaxy clusters, and if so how? The influence of intracluster magnetic fields on the dynamics of the cluster gas will depend on both the field strength and structure. A magnetic pressure $\gtrsim 10\%$ of the local gas pressure will likely have dynamical significance on the evolution of the intracluster medium. A partial answer to this question will therefore be determined by the answers to the two questions posed above. The question of how the fields influence the evolution of the clusters is best addressed through comparison of Faraday studies of high redshift galaxy clusters, to the currently available low redshift samples.

Further issues to address include: What is the origin of intracluster magnetic fields? What role to magnetic fields play in the development of cooling instabilities in clusters, and how do the cooling instabilities influence the magnetic fields? How is the morphology of embedded radio galaxies influenced by the intracluster gas? What effects do cluster mergers have on the intracluster magnetic field distribution?

Beyond the observational investigation of intracluster magnetic fields, the theory must also be developed. The growing awareness of the nearly universal presence and dynamical

importance of magnetic fields in astrophysics has been driven by observation. A full understanding of the implications of these observations on the inferred properties of galaxy clusters requires a combination of numerical and theoretical follow-up.

> **The larger one's ignorance, the stronger the magnetic field.**
> Woltjer, Noordwijk, 1966

References

Abell, G.O. 1958, ApJS, 3, 211

Abell, G.O., Corwin, H.G., Jr. & Olowin, R.P. 1989, ApJS, 70, 1

Allen, S.W. 1995, MNRAS, 276, 947

Amram, P., Marcelin, M., Balkowski, C., Cayatte, V., Sullivan, III, W.T. and Le Coarer, E. 1994, A&AS, 103, 5

Arnaud, K.A. 1988, *Cooling Flows in Clusters and Galaxies.* (Boston:Kluwer), 31

Aschenbach, B. 1988, Appl. Optics, 27, 1404

Baars, J.W.M., Genzel, R., Pauliny-Toth, I.I.K. & Witzel, A. 1977, A&A, 61, 99

Bagchi, J., Pislar, V. & Lima Neto, G. B. 1998, MNRAS, 296, L23

Begelman, M.C., Blandford, R.D., and Rees, M.J. 1984, Rev. Mod. Phys., 56, 255

Bicknell, G.V., Cameron, R.A., & Gingold, R.A. 1990, ApJ, 357, 373

Bignell, C. 1982, *Synthesis Mapping*, ed. Thompson and D'Addario, 6

Blandford, R.D. and Rees, M.J. 1974, MNRAS, 169, 395

Böhringer, H. 1995, Reviews of Modern Astronomy, 8, 259

Bridle, A.H., & Perley, R.A. 1984, ARAA, 22, 319

Briel, U.G., and Pfeffermann, E., 1986, Nucl. Instr. Methods, A242, 376

Broten, N.W., Macleod, J.M., & Vallée, J.P. 1988, Ap&SS, 141, 303

Burbidge, G.R. 1956, ApJ, 124, 416

Burn, B.J. 1966, MNRAS, 133, 67

Burns, J.O. 1998, Science, 280, 400

Chandran, B. 1999, in Proceedings of the Ringberg workshop on *Diffuse Thermal and Relativistic Plasma in Galaxy Clusters*, H. Böhringer, L. Feretti, P. Schuecker (eds.), MPE Report No. 271, MPE Garching

Clark, B.G. 1994, in *Synthesis Imaging in Radio Astronomy*, ed. R.A. Perley, F.R. Schwab, & A.H. Bridle, (California:ASP), 6, 1

Cleary, M.N., Haslam, C.G.T., and Heiles, C. 1979, A&AS, 36, 95

Condon, J.J., Cotton, W.D., Greisen, E.W., Yin, Q.F., Perley, R.A., Taylor, G.B., & Broderick, J.J. 1998, AJ, 115, 1693

Conway, R.G., Kronberg, P.P. 1969, MNRAS, 142, 11

Cornwell, T., and Braun, R. 1994, in *Synthesis Imaging in Radio Astronomy*, ed. R.A.

Perley, F.R. Schwab, & A.H. Bridle, (California:ASP), 167

David, L.P., & Bregman, J.N. 1989, ApJ, 337, 97

David, L.P., Slyz, A., Jones, C., Forman, W., Vrtilek, S.D., and Arnaud, K.A. 1993, ApJ, 412, 479

Dennison, B. 1979, AJ, 84, 725

Dreher, J.W. Carilli, C.L. and Perley, R.A. 1987, ApJ, 316, 611

Ebeling, H., Voges, W., Böhringer, H., Edge, A.C., Huchra, J.P., & Briel, U.G. 1996, MNRAS, 281, 799

Ensslin, T.A., & Biermann, P.L. 1998, A&A, 330, 90

Fanaroff, B.L., & Riley, J.M. 1974, MNRAS, 167, 31P

Fanti, R., Fanti, C., Schilizzi, R.T., Spencer, R.E., Nan Rendong, Parma, P., van Breugel, W.J.M., & Venturi, T. 1990, A&A, 231, 333

Felten, J.E., & Morrison, P. 1966, ApJ, 146, 686

Feretti, L., Dallacasa, D., Giovannini, G., & Tagliani, A. 1995, A&A, 302, 680

Feretti, L., Dallacasa, D., Govoni, F., Giovannini, G., Taylor, G.B., & Klein, U. 1999, A&A, 344, 472

Feretti, L., & Giovannini, G. 1996, IAU Symposium, 175, 333

Forman, W. 1988, *Cooling Flows in Clusters and Galaxies*, ed. A.C. Fabian, (Boston:Kluwer), p.17

Friaça, A.C.S., & Jafelice, L.C. 1999, MNRAS, 302, 491

Fusco-Femiano, R., Dal Fiume, D., Feretti, L., Giovannini, G., Grandi, P., Matt, G., Molendi, S. & Santangelo, A. 1999, ApJ, 513, L21

Gardner, F.F., and Whiteoak, J.B. 1966, ARAA, 4, 245

Ge, J.P., & Owen, F.N. 1993, AJ, 105, 778

Ge, J.P., & Owen, F.N. 1994, AJ, 108, 1523

Goldshmidt, O., & Rephaeli, Y. 1993, ApJ, 411, 518

Hanisch, R.J. 1980, AJ, 85, 1565

Hennessy, G.S., Owen, F.N., & Eilek, J.A. 1989, ApJ, 347, 144

Henriksen, M.J., and Markevitch, M.L. 1996, ApJ, 466, L79

Hjellming, R.M. 1992, *An Introduction to the NRAO Very Large Array*, Edition 2.0 (Socorro:NRAO)

Hoaglin, D.C., Mosteller, F., & Tukey, J.W. 1983, *Understanding Robust and Exploratory*

Data Analysis, (New York:Wiley)

Hogböm, J.H. 1974, A&AS, 15, 417

Jaffe, W. 1980, ApJ, 241, 925

Jones, C., & Forman, W. 1978, ApJ, 224, 1

Jones, C., & Forman, W. 1984, ApJ, 276, 38

Jones, C., & Forman, W. 1992, *Clusters and Superclusters of Galaxies*, NATO ASI Series, 366, 49

Kent, B.J., Reading, D.H., Swinyard, B.M., Spurrett, P.H., & Graper, E.B. 1990, SPIE proceedings, 1344, 255

Kim, K.-T., Kronberg, P.P., Dewdney, P.E., & Landecker, T.L. 1990, ApJ, 355, 29

Kim, K.-T., Tribble, P.C., & Kronberg, P.P. 1991, ApJ, 379, 80

Kraus, J.D. 1986, *Radio Astronomy*, Second Edition (Powell:Cygnus-Quasar Books)

Kronberg, P.P., & Simard-Normandin, M. 1976, Nature, 263, 653

Lawler, J.M., & Dennison, B. 1982, ApJ, 252, 81

Loeb, A., & Mao, S. 1994, ApJ, 435, L109

Longair, M.S. 1981, *High Energy Astrophysics*, (New York:Cambridge University)

Makino, N. 1997, ApJ, 490, 642

Mather, J. C., et al. 1990, ApJ, 354, L37

Meeus, J. 1991, *Astronomical Algorithms*, (Virginia:Willmann-Bell)

Miley, G.K. 1980, ARAA, 18, 165

Miller, R.S., Mashayek, F., Adumitroaie, V., & Givi, P. 1996, Phys. of Plasmas, 3, 3304

Miralda-Escude, J., & Babul, A. 1995, ApJ, 449, 18

Mohr, J.J., Mathiesen, B., & Evrard, A.E. 1999, ApJ, 517, 627

Nordlund, A., Brandenburg, A., Jennings, R.L., Rieutord, M., Ruokolainen, J., Stein, R.F., & Tuominen, I. 1992, ApJ, 392, 647

Ott, M., Witzel, A., Quirrenbach, A., Krichbaum, T.P., Standke, K.J., Schalinski, C.J. & Hummel, C.A. 1994, A&A, 284, 331

Owen, F.N., Ledlow, M.J., & Keel, W.C. 1995, ApJ, 109, 14

Pacholczyk, A.G. 1970, *Radio Astrophysics*, (San Francisco:W.H. Freeman)

Pearson, T.J., & Readhead, A.C.S. 1984, ARAA, 22, 97

Perley, R.A. 1998, "Very Large Array Observational Status Summary"

Perley, R.A., and Taylor, G.B. 1996, "The VLA Calibrator Manual"

Press, W.H., Flannery, B.P., Teukolsky, S.A., and Vetterling, W.T. 1988, *Numerical Recipes in C*, (New York:Cambridge University Press)

Raymond, J.C., and Smith, B.W. 1977, ApJS, 35, 419

Rees, M.J. 1971, Nature, 229, 312

Roettiger, K., Stone, J.M., and Mushotzky, R.F. 1998, ApJ, 493, 62

Ruzmaikin, A.A. and Sokoloff, D.D. 1979, A&A, 78, 1

Rybicki, G.B., and Lightman, A.P. 1979, *Radiative Processes in Astrophysics*, (Toronto:John Wiley & Sons)

Sarazin, C.L. 1988, *X-ray Emission from Clusters of Galaxies*, (New York:Cambridge University), 136

Sarazin, C.L. 1992, *Clusters and Superclusters of Galaxies*, NATO ASI Series, 366, 131

Shapley, H., and Ames, A. 1932, *Ann. Harvard College Obs.*, 88, 43

Simard-Normandin, M. & Kronberg, P.P. 1980, ApJ, 242, 74

Snowden, S.L., Egger, R., Freyberg, M.J., Plucinsky, P.P., Schmitt, J.H.M.M., Trümper, J., Voges, W., McCammon, D., and Sanders, W.T. 1997, ApJ, 485, 125

Snowden, S.L., Freyberg, M.J., Plucinsky, P.P., Schmitt, J.H.M.M., Trümper, J., Voges, W., Edgara, R.J., McCammon, D., and Sanders, W.T. 1995, ApJ, 454, 643

Snowden, S.L., MCCammon, D., Burrows, D.N., & Mendenhall, J.A. 1994, ApJ, 424, 714

Soker, N., & Sarazin, C.L. 1990, ApJ, 348, 73

Sokoloff, D.D., Bykov, A.A., Shukurov, A., Berkhuijsen, E.M., Beck, R., and Poezd, A.D. 1998, MNRAS, 299, 189

Spitzer, L. Jr. 1956, *Physics of Fully Ionized Gases*, (New York:Interscience)

Sramek, R.A., and Schwab, F.R. 1994, in *Synthesis Imaging in Radio Astronomy*, ed. R.A. Perley, F.R. Schwab, & A.H. Bridle, (California:ASP), 117

Stark, A.A., Gammie, C.F., Wilson, R.W., Bally, J., Linke, R.A., Heiles, C., and Hurwitz, M. 1992, ApJS, 79, 77

Stokes 1852, Trans. Camb. Phil. Soc., 9, 399

Struble, M.F., and Rood, H.J. 1987, ApJS. 63, 555

Taylor, G.B. 1991, Ph.D. Thesis, UCLA

Taylor, G.B. Allen, S.W. and Fabian, A.C. 1999, in Proceedings of the Ringberg workshop on *Diffuse Thermal and Relativistic Plasma in Galaxy Clusters*, H. Böhringer, L. Feretti, P. Schuecker (eds.), MPE Report No. 271, MPE Garching

Taylor, G.B., Barton, E.J. & Ge, J. 1994, AJ, 107, 1942

Taylor, G.B., & Perley, R.A. 1993, ApJ, 416, 554

Thompson, A.R. 1994, in *Synthesis Imaging in Radio Astronomy*, ed. R.A. Perley, F.R. Schwab, & A.H. Bridle, (California:ASP), 11

Tribble, P.C. 1991, MNRAS, 250, 726

Trümper, J. 1983, Adv. Space Science, 2, 241

Vallée, J.P. 1990, ApJ, 360, 1

Van Breugel, W., Heckman, T., & Miley, G. 1984, ApJ, 276, 79

Venturi, T., & Taylor, G.B. 1999, accepted in AJ

Voges, W., Aschenbach, B., Boller, Th., Bräuninger, H., Briel, U., Burkert, W., Dennerl, K., Englhauser, J., Gruber, R., Haberl, F., Hartner, G., Hasinger, G., Kürster, M., Pfeffermann, E., Pietsch, W., Predehl, P., Rosso, C., Schmitt, J.H.M.M., Trümper, J., and Zimmermann, H.-U. 1996, IAU Circ., 6420, 2

Voges, W., Aschenbach, B., Boller, Th., Bräuninger, H., Briel, U., Burkert, W., Dennerl, K., Englhauser, J., Gruber, R., Haberl, F., Hartner, G., Hasinger, G., Kürster, M., Pfeffermann, E., Pietsch, W., Predehl, P., Rosso, C., Schmitt, J.H.M.M., Trümper, J., and Zimmermann, H.-U. 1999, submitted to A&A

Wardle, J.F.C., and Kronberg, P.P. 1974, ApJ, 194, 249

Wells, A., Abbey, A.F., Barstow, M.A., Cole, R.E., Pye, J.P., Sims, M.R., Spragg, J.E., Watson, D.J., Willingale, R., Courtier, G.M. 1990, SPIE proceedings, 1344, 230

Welter, G.L., Perry, J.J., & Kronberg, P.P. 1984, ApJ, 279, 19

White, D.A., Jones, C., and Forman, W. 1997, MNRAS, 292, 419

Wolf, M. 1906, *Astron. Nachr.*, 170, 211

Wolter, H. 1952, Ann. Phys., 10, 94

Wright, W. 1973, Ph.D. thesis, Caltech

Zwicky, F., Herzog, E. & Wild, P. 1968, *Catalogue of Galaxies and of Clusters of Galaxies*, Pasadena: California Institute of Technology (CIT), 1961-1968